
THE UNIVERSITY *of* EDINBURGH

# High-resolution topography: tools and analysis of the life and death of salt marshes

Guillaume C. H. Goodwin


Submitted for the degree of Doctor of Philosophy

The University of Edinburgh

2020

.

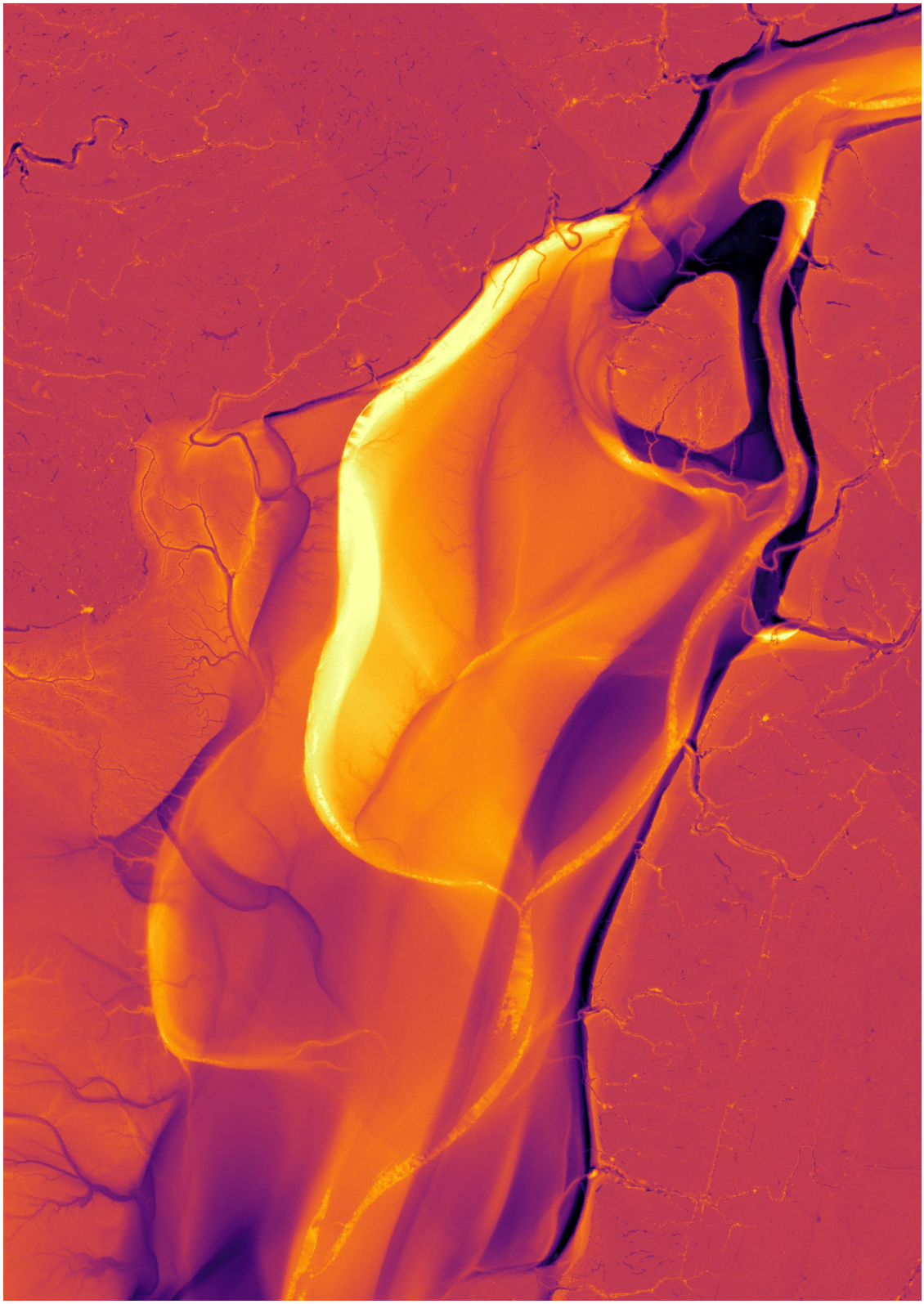

**Figure 1:** Difference in elevation between 2009 and 2017 in the Moricambe Bay salt marshes. Dark colours show erosion, bright colours show accretion. Pixel size $1m$.

.

I watched you
Swim backstrokes
Through all the consequences
Of *your* growth,
Until now you
And I
Tread water,
Delicate in our balance.
There is a push
And a pull to things.
You see that
When you grow with the tides.

Exerpt from *The Salt Marsh Speaks to the Scientist*, by Doug Garry

.

# Abstract

Salt marshes are grassy platforms that develop on sheltered coasts with high sediment supply. They may be found on sub-tropical shores where they often coexist with mangrove swamps, or in temperate climates where they might front brackish and fresh wetlands. These landscapes filter pollutants, protect coastlines against storm surges, and sequester carbon at high rates, making salt marshes some of the most valuable ecosystems on Earth. However, their survival is jeopardised by imbalance between formative and destructive processes: salt marshes rely heavily on external sources of sediment, and the poor sediment supply may prevent them from recovering from wave-driven erosion or from matching accelerating sea level rise. The sustained existence of a salt marsh ecosystem depends strongly on its topographic evolution. Hence, quantifying marsh platform topography is vital to improve coastal management, and the current development of high-resolution topographic data acquisition techniques presents geomorphologists with important opportunities to achieve this objective.

This thesis addresses the need for topographic analysis tools specific to the morphology of salt marshes and explores a selection of potential uses for these tools. First, I propose a novel, unsupervised method to reproducibly isolate salt marsh scarps and platforms from a Digital Terrain Model (DTM). This method takes the form of a multiple routing algorithms grouped under a single programme referred to as the Topographic Identification of Platforms (TIP). Field observations and numerical models show that salt marshes mature into subhorizontal platforms delineated by subvertical scarps. Based on this premise, the programme identifies scarps as lines of local maxima on a slope raster, then fills the DEM from the scarps upward, thus isolating mature marsh platform objects. I then test the TIP method using lidar-derived DTMs from six salt marshes in England with varying tidal ranges and geometries, for which topographic platforms were manually isolated from tidal flats. Agreement between manual and unsupervised classification exceeds 90 % for resolutions up to 3m. I also find that our method

allows for the accurate detection of local block failures as small as 3 times the DTM resolution. Ultimately, I show that unsupervised classification of marsh platforms from high-resolution topography is possible and sufficient to monitor and analyse topographic evolution over time. The relevance of such monitoring is however dependant on the frequency and time-span of data acquisition, a point which I discuss further in the conclusive chapter.

Second, I use the TIP method to extract the distribution of elevations of multiple marsh platforms in the United Kingdom and the United States. I compare marsh elevations relative to current sea level and run simple 0-dimensional settling simulations in order to explore constraints on suspended sediment concentration and particle size. These experiments set a basis for comparison with observed accretion rates from field sources, as lidar-derived accretion rates are found to be inaccurate. I find that the marsh platforms examined occupy a narrow range of elevations in the upper tidal frame, situated between Mean High Tide and the Observed Highest High Tide. At these elevations, accretion models using sinusoidal tidal forcing do not allow these platforms to be inundated nor experience deposition. However, when forced with year-long tidal records, I find not inconsiderable deposition rates that follow hyperbolic contour lines when expressed as a function of sediment concentration and median grain size. I find that the deposition of coarse, concentrated sediment is necessary for platforms in the upper tidal frame to immediately match sea level rise, suggesting a strong dependance on infrequent high-deposition events for short-term accretion. This is particularly true for marshes that are very high in the tidal frame, making accretion increasingly storm-driven as marsh platforms gain elevation. Finally, I reflect on the capacity of marshes to regenerate after erosion events within a context of changing sediment supply conditions and how this may affect the long-term, dynamic equilibrium of marsh platforms.

Finally, I add a module to the TIP method to determine the topographic signature of retreat and progradation on the edges of salt marsh platforms in mega-tidal Moricambe Bay (UK) in 2009, 2013 and 2017. I first describe the TIP method, and from the outlines it determines I generate transverse topographic

profiles of the marsh edge 10m long and 20m apart. Profiles are grouped into categories depending on whether they experienced erosion or accretion in the 2009-2013 or 2013-2017 periods respectively, and I find that profiles belonging to the same retreat or progradation event have distinctly similar morphologies, regardless of the event magnitude. Progradation profiles have a shallow scarp and low relief that decreases with event magnitude, facilitating more progradation. Conversely, steep-scarped, high-relief retreat profiles that dip away from levees as retreat reveals older platforms. Furthermore, vertical accretion of the marsh edge is found to be primarily controlled by elevation in the study site, suggesting an even distribution of deposition that would allow bay infilling were it not limited by the migration of creeks. The scope of this research within future research on marsh margins is further discussed in the conclusive chapter.

# Lay summary

Salt marshes are grassy platforms found on sheltered coasts with high sediment supply. They may be found coexisting with mangrove swamps on sub-tropical shores, or bordering brackish and fresh wetlands in temperate climates. These landscapes filter pollutants, protect coastlines against storms and waves, and store carbon from the atmosphere, making salt marshes some of the most valuable environments on Earth. However, their survival is endangered by the lack of sediment: without this important building material, marshes are more vulnerable to accelerating sea level rise and erosion due to waves. While marshes normally retreat inland, in many cases they are trapped between the sea and artificial structures like levees and roads. For salt marshes to survive, they need to stay high enough above mean sea level for plants to grow. Therefore, measuring marsh elevation is vital to improve their management. The recent explosion of high-resolution elevation data allows us to create accurate 3-dimensional models of salt marshes, opening exciting prospects for salt marsh science.

In this thesis, I design numerical tools to analyse the elevation of salt marshes and demonstrate their use for scientific research.

First, I propose a new method to isolate salt marshes from a map of elevation, which resulted in an suite of algorithms called the Topographic Identification of Platforms (TIP). Field studies and numerical models show that salt marshes mature into low-lying plateaux above the mudflats. Using this information, the programme identifies the edges of these plateaux, then numerically fills the flat areas of the elevation map from the edge inward, isolating mature marsh platforms. I then test the TIP method using high-quality elevation maps from six salt marshes on various coasts of England, by comparing the results of the TIP method to marsh outlines I had digitised manually. I find that agreement between manual digitisation and the TIP method exceeds 90 %. I also find that our method allows us to see blocs of marsh that had fallen on the mudflat if they were larger than 3 times the elevation map resolution. Ultimately, I show that

the TIP method used on high-quality elevation maps is possible and sufficient to monitor salt marshes in the future.

Second, I use the TIP method to analyse the variations in elevation in different marsh platforms in the United Kingdom and the United States. I compare marsh elevations relative to sea level and rates of elevation change to a simple numerical model of sediment deposition. This allows me to explore the influence of sediment size and concentration in the sea over marsh elevation change. I find that the marsh platforms I examined occupy a narrow range of elevations, situated between Mean High Tide and the Highest High Tide. Under sinusoidal tides, common in numerical models, marshes at these elevations are never flooded. However, when using real tidal records, deposition still occurs at these heights and is influenced by the properties of sediment in the sea. I find that the deposition of coarse, concentrated sediment is necessary for high platform elevation to match its contemporary rate of sea level rise, suggesting a strong influence of storms and river floods.

Finally, I add a module to the TIP method to determine the signature elevation patterns of retreat and advance of the edges of salt marshes. I do this in Moricambe Bay (UK) for high-resolution elevation data collected in 2009, 2013 and 2017. I generate elevation profiles of the marsh edge perpendicular to the marsh outline, 10m long and 20m apart. The behaviour of the marsh outline at its intersection with profiles produces noticeably different profile geometries. Profiles drawn on advancing outlines have a shallow edge that decreases with the size of the advance, facilitating more progression. Conversely, steep profiles drawn on retreating outlines have marsh platforms that dip away from edge levees as retreat reveals older marshes. Furthermore, vertical elevation gain of the marsh edge is controlled by elevation rather than lateral motion, suggesting evenly distributed sediment deposition that would allow the bay to fill were it not limited by the migration of creeks.

# Declaration

I declare that this thesis has been composed solely by myself, and that it contains only my work except where otherwise specified, or where the work is explicitly indicated below to have formed part of a jointly-authored publication. This work has not been submitted for any other degree or professional qualification.

For work that is part of a jointly-authored publication, I declare that I was the principal author of the publication and conducted the research content myself, with co-authors playing an instrumental supervision and advising role.

Guillaume C. H. Goodwin

February 2020

# Acknowledgements

Although the work in this Ph.D. is presented under my name, it would be ludicrous to claim that it was produced without profuse help and support from mentors, friends and family. Too many people have guided me trough these 1628 days and I realize that I will not be able to thank all of them appropriately, but I shall try nevertheless.

First, I must thank the National/Natural Environment Research Council (NERC) and the selection committee at the University of Edinburgh for funding my doctoral project.

Next I wish to thank my supervisor in Edinburgh, Simon Mudd, for his guidance, support, opportunism and investment in my work. He has never failed to offer wise advice about research and street-wise advice about the world of academia. It was his good-humoured passion for science that first made me apply to this PhD; since then it has encouraged me to push through (or walk around) difficult times and I have not looked back once. Of course, I cannot thank Simon without thanking his internet double, Pernicious Q. McStuggles, for passing on his great wisdom to the world.

I also wish to thank Andrea D'Alpaos, my supervisor in Padova. Andrea was always helpful despite the distance between Edinburgh and Padova, and always enthousiastic about my work through the twists and turns of its changing direction.

Thank you as well to my advisor Mikaël Attal. Mikaël had, in honesty, a fairly easy job as a moderator since I don't recall any acrimony between my supervisors and me. As an advisor, I might have given him more trouble, but Mikaël was always available to answer my sometimes irrelevant questions, regardless of how busy he was, and to support my goal to pursue a career in research.

Throughout my PhD I was fortunate to meet fellow academics who influenced my way of thinking about my work, and helped me develop more holistic vision

of coastal geomorphology. First I must thank Stéphane Costa from the university of Caen who first believed in my objective of entering the academic world and supported my candidacy to this PhD. Dimitri Lague from the Observatoire des Sciences de l'Univers de Rennes has been of inestimable help over the last 4 years in teaching me the use and limitations of Lidar both airborne and terrestrial. He has been a supportive critic of my strange ideas and a great mind to learn from. Giulio Mariotti of Louisiana State University was patient enough to teach me the rudiments of Delft3D, and was of great help to shape my understanding of a variety of salt marshes. Jaap Nienhuis of Florida State University was kind enough to share his holistic vision of coastal processes and help me develop outline tools, and made the 7-hour car ride from Tallahasse to New Orleans pass like a breeze. Fellow PhD students met at conferences make great friends and I very much look forward to meeting them again as fully-fledged colleagues.

My PhD experience might have been miserable without the fantastic people of the Land Surface Dynamics (LSD) group. The staff (Simon, Mikaël, Hugh, Anthony, Andy, ...) are a fun-loving, passionate gang; the students past and present (Fiona, Stuart, Lizzie, John, Noorzalianee, Louis, Monika, Lauren, Boris, Laura, Thomas, Zhui, Justine, Emma, Polly, ...) are the reason these four years sped by so fast. I especially want to thank: Fiona, for the good chats and making learning Python so easy; John, for the storm-chasing, outdoor adventures and floor inspections; Goris, for not chasing the bears and not complaining *too much* about the Schmidt hammer (or the car); Emma, for living next door and walking back home under the rain, snow and occasional hail; Louis and Lauren, for being the best field assistants in the worst conditions (comparatively, John, Laura, Boris, Emma and Flavia had it easy); Ashley, who is not a member of the group but made this mean LaTeXthesis template; the Brass Monkey on Drummond Street, which should by now have honorary membership of our group; the list goes on.

Luckily, LSD is not so addictive that I knew no one outside of it. The walls of the Harris and Saint Kilda suites (officially the Postgraduate Coffee Room) heard more than their share of "deep scientific musings" and slightly shallower sheep-

oriented discussions. I was blessed with inestimable friends in Lucas, Andy and Rowan: with them tough times blew over as simply as tickling a chilly or tossing a frisbee at a brand new Tesla. Among the many things I enjoyed in Edinburgh, I will always remember the Dirty Weekenders (and the Warties Morna, Martha and Other Will), the Sneeekys Ultimate Frisbee Club, the Edinburgh University Folk Society, the City of Edinburgh Pipe Band, ... But most of all I will always remember and love Scotland.

Finally, I deeply thank my parents Chantal and Kim for their unshakeable love and support, and Aline, my much better half, who somehow prevented my descent into madness during the final writing stages.

# Contents

# List of Figures

# List of Tables

# Chapter 1

# Introduction

# List of Abbreviations

| Abbreviation | Meaning |
|---|---|
| ALS | Airborne Lidar Survey |
| AoI | Area of Interest |
| BSS | Bottom Shear Stress |
| D-GNSS | Differential Global Navigation Satellite System |
| DEM | Digital Elevation Model |
| DSM | Digital Surface Model |
| DTM | Digital Terrain Model |
| GESLA | Global Extreme Sea Level Analysis |
| NDVI | Normalised Difference Vegetation Index |
| NOAA | National Oceanigraphic and Atmospheric Administration |
| RTK-GNSS | Real-Time Kinematic GNSS |
| SET | Surface Elevation Table |
| TIP | Topographic Identification of Platforms |
| TLS | Terrestrial Laser Scanner |
| UAV | Unmanned Aerial Vehicle |
| UK | United Kingdom |
| USD | United States Dollar |
| WoO | Window of Opportunity |

**Table 1.1:** Abbreviations used in this chapter

# List of Notations

| Notation | Meaning |
|---|---|
| $B$ | Width of control surface [L] |
| $h$ | water depth [L] |
| $\Delta V$ | Volume passing through in control surface [$L^3$] |
| $\Delta t$ | a short duration of time [T] |
| $u_c$ | Current velocity [$L.T^{-1}$] |
| $\tau_{cur}$ | Current shear stress [$M.L^{-1}.T^{-2}$] |
| $\rho w$ | Volumetric mass of water [$M.L^{-3}$] |
| $\rho s$ | Volumetric mass of sediment [$M.L^{-3}$] |
| $g$ | gravity constant [$L.T^{-2}$] |
| $Ch$ | Chézy constant [$\varnothing$] |
| $D_{50}$ | Median grain diameter [L] |
| $T$ | Wave period [$T^{-1}$] |
| $\lambda$ | Wavelength [L] |
| $u_m$ | Orbital wave motion [$L.T^{-1}$] |
| $H_s$ | Significant wave height [L] |
| $Re$ | Reynolds Number [$\varnothing$] |
| $U$ | Wind speed [$L.T^{-1}$] |
| $f_r$ | Rough bed friction coefficient [$\varnothing$] |
| $f_s$ | Smooth bed friction coefficient [$\varnothing$] |
| $\nu$ | Kinematic visosity of water [$L^2.T^{-1}$] |
| $\tau_{wav}$ | Wave shear stress [$M.L^{-1}.T^{-2}$] |
| $\tau$ | Total bed shear stress [$M.L^{-1}.T^{-2}$] |
| $\tau_c$ | Critical shear stress [$M.L^{-1}.T^{-2}$] |
| $e$ | Erosion rate factor [$\varnothing$] |
| $\mu$ | Dynamic viscosity of water [$M.T.L^{-1}$] |
| $w_s$ | Terminal Stokes settling velocity [$L.T^{-1}$] |

**Table 1.2:** Notations used in this chapter

## 1.1 General definition of a salt marsh

Salt marshes are grassy wetlands that are regularly flooded by the tide (Allen, 2000) (Figure 1.1). They are typically located in sub-arctic to sub-tropical climates (Figure 1.2), although in the latter they increasingly find themselves supplanted by mangrove forests (Saintilan et al., 2014). On their seaward side salt marshes are bordered by tidal flats, and on the landward side they merge into brackish marshes, coastal forests or sand dunes when infrastructure does not interrupt this natural succession (Fagherazzi et al., 2019).

The formation of a salt marsh platform is initiated by the establishment of pioneer halophytic plants on high tidal flats (Balke et al., 2014; Hu et al., 2015). Clusters of plants, provided they are not dislodged or buried, modify hydrodynamic conditions around and above themselves (Bouma et al., 2007; Finnigan et al., 2009), enhancing the settling of sediment ranging in size from mud to fine sands (Allen, 2000; Wentworth, 1922) within the vegetated area (Mudd et al., 2010). Such patches develop relief (Balke et al., 2012), expand and connect (Temmerman et al., 2007), all the time gaining elevation relative to the tidal flats surrounding tidal flats (Marani et al., 2013) while the dissecting creeks incise (D'Alpaos et al., 2005). Through this process, marshes acquire a distinctive platform-like morphology: as seen in Figure 1.1a.-c., they form sub-horizontal meadows that are most often separated from the neighbouring tidal flat by a scarp of variable height. Scarps are mostly visible in mature or actively accreting marshes, as newly formed or slow-evolving landscapes such as the one seen in Figure 1.1d. barely present any relief above their sandy substrate.

Salt marsh vegetation is specific to these environments, consisting of halophytic and almost exclusively herbaceous plants. Although communities vary regionally, commonly found genera are *Spartina*, *Salicornia*, *Juncus*, *Puccinellia*. This typical vegetation contributes to giving marshes their meadow-like appearance, an impression occasionally reinforced by the sight of grazing sheep or cattle on high marshes (Figure 1.1a.). Their unique morphology and vegetation are responsible for the many benefits provided by salt marshes to society, detailed in

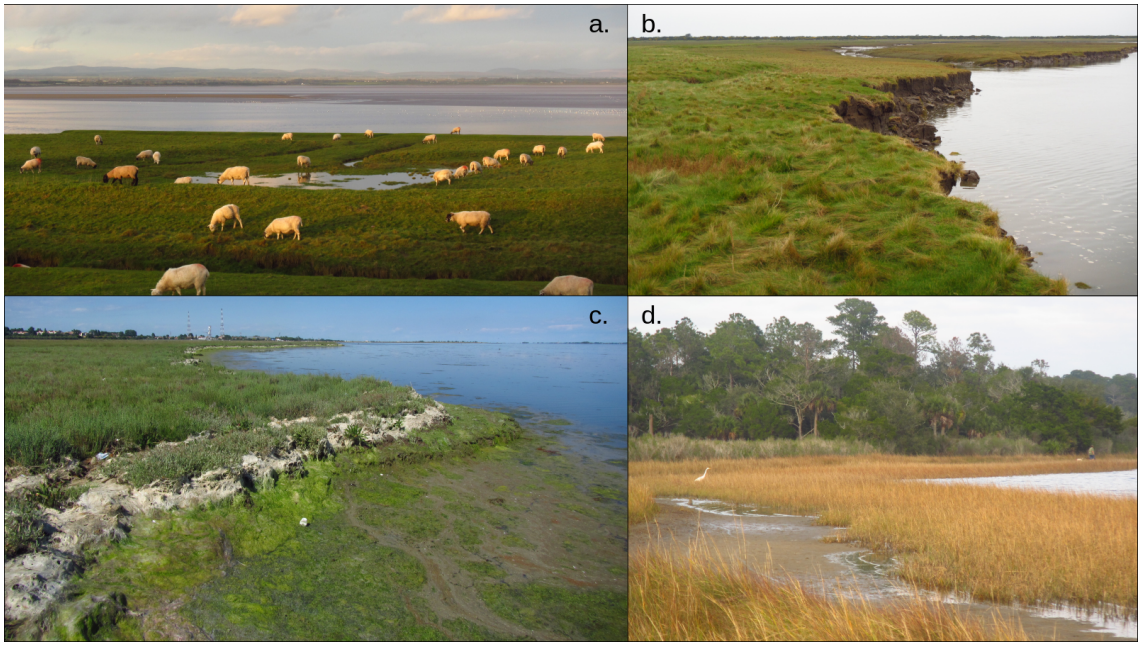


**Figure 1.1:** Examples of salt marshes; a. grazed salt marsh platform near Drumburgh, Cumbria, United Kingdom (UK); b. Salt marsh platform and retreat scarps in Skinburness, Cumbria, UK; c. Salt marsh with plant debris and scarp near Campalto, Venice, Italy; d. Salt marsh with high vegetation bordering a coastal forest on Wakulla Beach, Florida, United States. Images: G.C.H. Goodwin.

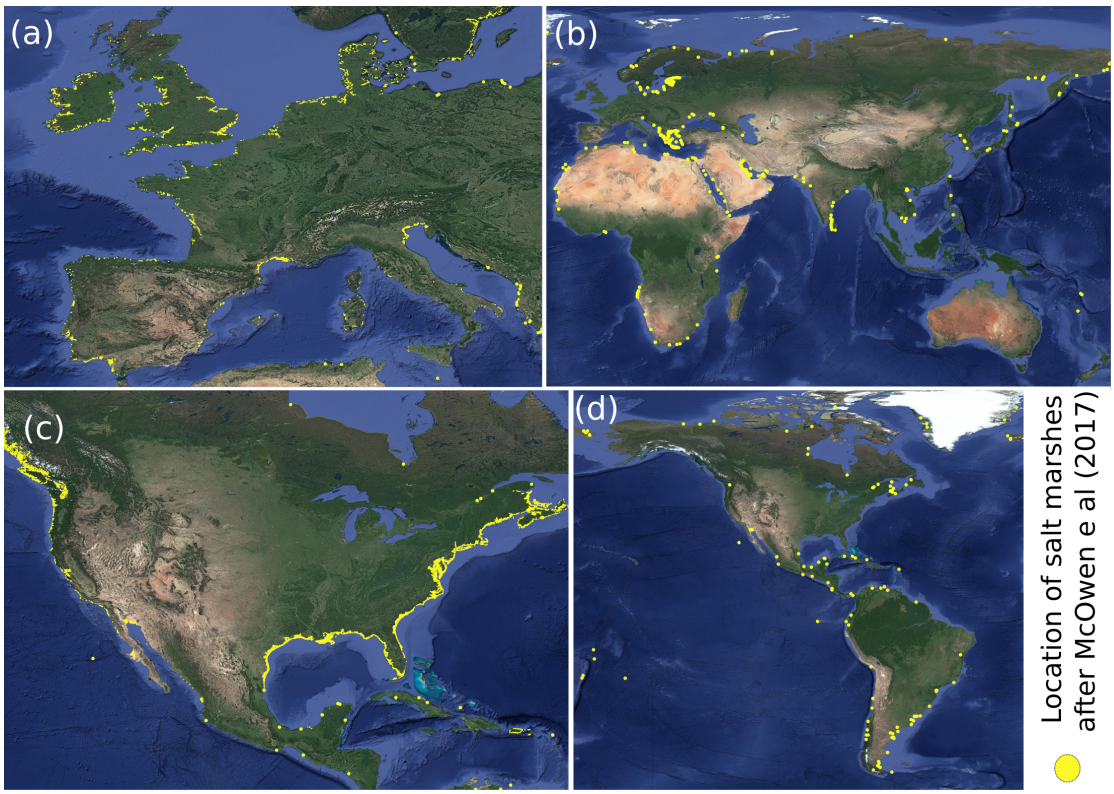


**Figure 1.2:** Map of salt marshes in the world. Data: Mcowen et al. (2017)

Section 1.2.1.

Classified as "soft" coasts, salt marshes are more mobile than "hard" coasts such as rocky platforms or cliffs, and have comparatively fast responses to external forcings such as variations in sea level, wave action and tidal flooding patterns. Consequently, they only develop on sheltered coasts, where they form in the intertidal zone (i.e. land that is higher than the lowest low tides and lower than the highest high tides). Figure 1.3 depicts an early classification of the types of coasts where salt marshes are found. Despite being typically located along protected coastlines, salt marshes exhibit dynamic responses at various time-scales depending on external influences: Section 1.2.2 outlines the threats they face and how this may impact their existence in the near future.

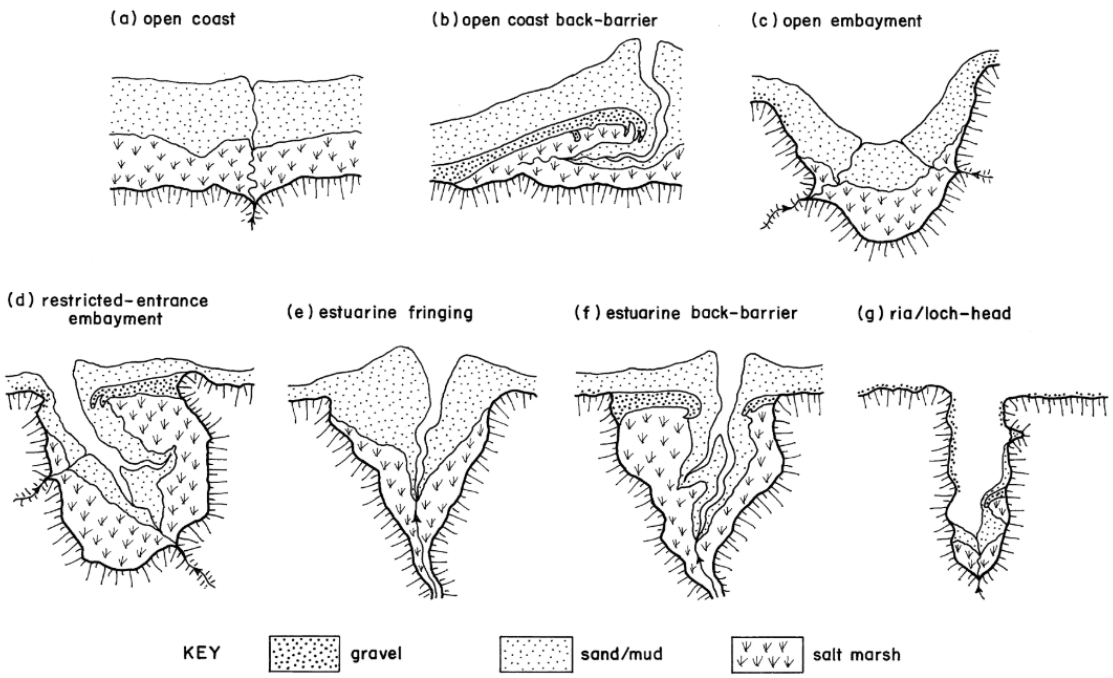


**Figure 1.3:** Types of salt marshes based on the coastal setting in which they develop. Source: Allen (2000)

## 1.2 Rationale

### 1.2.1 Ecosystem services provided by salt marshes

Historically, many salt marshes were drained and converted to agricultural land (Gedan et al., 2009), as they were perceived as insalubrious. Indeed, their local denomination of "paluds" in Southern France gave birth to the term "paludism", designating the disease found in populations bordering marshlands. This disease was originally thought to be contracted from exposure to the "bad air" or "malaria" of the marshes, and only later was the connection made between malaria and the mosquitoes breeding in stagnant water (Dobson, 1989; Packard, 2016).

Today, land conversion on marshlands is in decline because the ecosystem services they provide are better understood and valued. For this we must thank Costanza et al. (1997) amongst others; Costanza et al. (1997) initially valued the ecosystem services provided by salt marshes and mangrove forests at $9,990\ USD \cdot ha^{-1} \cdot y^{-1}$, making them the $4^{th}$ most valuable ecosystems after estuaries ($22,832\ USD \cdot ha^{-1} \cdot y^{-1}$), swamps and fluvial continental wetlands ($19,580\ USD \cdot ha^{-1} \cdot y^{-1}$) and seagrass meadows ($19,004\ USD \cdot ha^{-1} \cdot y^{-1}$).

Many contributions followed to further define the ecosystem services provided by salt marshes, highlighting their breadth (Barbier et al., 2011; Spivak et al., 2019) and high economic importance (Beaumont et al., 2008): these rich and sheltered environments are ideal nursing grounds for marine species, including species of high economic value such as the brown shrimp *Farfantepenaeus aztecus* (Haas et al., 2004; Lafleur et al., 2002). Marshes are instrumental in the nitrogen cycle (Nelson and Zavaleta, 2012) and sequester metallic pollutants such as mercury (Marques et al., 2011), but are better-known for their carbon sequestration capacity due to high biomass production and degradation in salt marsh soils. Accumulation rates in salt marshes average $210\ g \cdot m^{-2} \cdot y^{-1}$, an order of magnitude more than in peatlands (Chmura et al., 2003a) and approximately twice as much as in the declining Amazonian rainforest (Brienen et al., 2015).

Location exerts an important control over ecosystem services provided by salt

marshes: latitude, tidal range and elevation combine to control carbon accumulation rates (Ouyang and Lee, 2014), but strong variations exist between regions and within a single marsh (Roner et al., 2016). Likewise, the efficiency of salt marshes as natural barriers against waves and storm surges (Möller et al., 2014; Shepard et al., 2011) is conditioned by environments that allow them to develop (Van der Nat et al., 2016). Instrinsic properties also influence the impact of marshes on wave propagation: attenuation rates depend on scarp morphology and elevation (Möller and Spencer, 2002; Stark et al., 2016) as well as vegetation (Möller, 2006; Ysebaert et al., 2011).

Because of the many socio-economic benefits provided by salt marshes, the prospect of their degradation has become a cause of considerable concern, as loss of salt marsh systems is expected to cause significant losses in ecosystem services (Zedler and Kercher, 2005). Of course, losses as well as gains in surface area are to be expected over various time scales and in different environments as marshes tend toward dynamic equilibrium states (Zhou et al., 2017). Nevertheless, despite the cyclicity observed in some regions (Bouma et al., 2016), long-term net loss is already observed in multiple sites(see Section 1.2.2). Such long-term die-off is likely to impact the carbon cycle as carbon sequestration potential is lost (Chmura et al., 2003b) and large amounts of carbon are released from the marsh soil into the ocean (Coverdale et al., 2014; Kirwan and Mudd, 2012; Pendleton et al., 2012), reducing its capacity for carbon dioxide absorption.

### 1.2.2 Pressures on salt marsh survival

Being located at the interface between terrestrial and marine environments, salt marshes are exposed to destructive and constructive forces at both their landward and seaward boundaries. If during a given period of time when these forces are in net imbalance, loss or gain of salt marsh environment occurs. While I discuss the processes driving marsh accretion, progradation and erosion further in Section 1.3, here I give a preliminary account of the most commonly described threats to marsh survival.

Salt marshes are affected by variations in sea level at various time scales:

tidal amplitude and hydroperiod limit their vertical range, thus constricting their expansion both seaward (Balke et al., 2016; Hu et al., 2015) and inland (Morris et al., 2002). This vertical range is defined in relation to mean sea level (see Section 1.3.1), and marsh platform elevation lags behind its long-term variations (D'Alpaos et al., 2011; Kirwan and Murray, 2008). Hence, accelerating sea level rise observed around the world (Ipcc, 2014) is one of the better documented threats to salt marsh survival. Salt marshes have historically kept pace with sea level variations through feedback loops between flooding patterns and sediment settling and production (Kirwan and Temmerman, 2009) (see Section 1.3.2). However, there is concern that, in the near future, sediment supply will be insufficient to compensate for the combined effects of accelerated mean sea level variations (D'Alpaos et al., 2011) and subsidence (Day et al., 2011), further described in Section 1.3.1. In such cases, marshes would be more reliant on organic belowground production (see Section 1.3.2). This is particularly true of deltaic regions, where decreased sediment supply due to anthropogenic activities is set to accentuate these pressures (Syvitski et al., 2009).

The effects of relative sea level rise ($RSLR$, defined as the rise of sea level compared to a mobile salt marsh platform elevation) may cause salt marsh plants to die from hypersalinity or hypoxia (Morris et al., 2013; Morris et al., 2002; Morris, 2007), thus converting vegetated land into bare tidal flats (Voss et al., 2013), which eventually sink into open water (see Section 1.3.2). Changing sea levels, lack of sediment supply and subsidence at different depths are being felt across the world (Kirwan and Guntenspergen, 2010; Kirwan and Megonigal, 2013) and have cost coastal Louisiana $\approx 90\ km^2$ of wetlands per year since 1932 (Day et al., 2000; Jankowski et al., 2017), and it has been suggested that this degradation and the resulting reduction of storm surge attenuation contributed to the disastrous damage caused by hurricanes Katrina and Rita (Day Jr. et al., 2007; Jonkman et al., 2009). In Section 1.3.2, I discuss how the dependance of salt marshes on external sources of sediment may affect their response to sea level changes.

Human activites often are an aggravating factor of marsh die-off. Ecological ratchet models predict that the upland salt marsh boundary retreats inland un-

der rising sea levels (Fagherazzi et al., 2019), converting brackish marshes and coastal forests to salt marsh. However, built environments can prevent landward migration (Feagin et al., 2010), creating barriers that contribute to "squeezing" coastal marshes between a rising sea and hard infrastructure (see Borchert et al. (2018) in the Gulf Coast of the United States). Similarly, overfishing on he USA Atlantic Coast has been observed to cause excessive herbivory from crab populations, damaging salt marsh vegetation (Bertness et al., 2014).

In addition to vertical pressure from RSLR, salt marshes are impacted at their seaward margin by erosive waves and currents. Indeed, waves were found to remove considerable volumes of sediment from the marsh edge (Marani et al., 2011; McLoughlin et al., 2015; Priestas et al., 2015). Statistical analyses over marshes in the USA, Australia and Italy show that storms cause marshes to retreat proportionally to incident wave power (which in this case is calculated without consideration for local margin geometry) (Leonardi et al., 2016a). Simple cell models show that the energy released by breaking waves relative to soil strength defines the rate of erosion and the horizontal aspect of retreat outlines (Leonardi and Fagherazzi, 2014), and a link between erosion rate and outline geometry was confirmed on the field by Leonardi et al., 2016b.

Erosive waves are the product either of wind friction (Padilla-Hernández and Monbaliu, 2001), storm-generated swell (Alves, 2006; Hasselmann et al., 1973) or boat wakes (Bauer et al., 2002; Silinski et al., 2015) (See Figure 1.4). Increasing

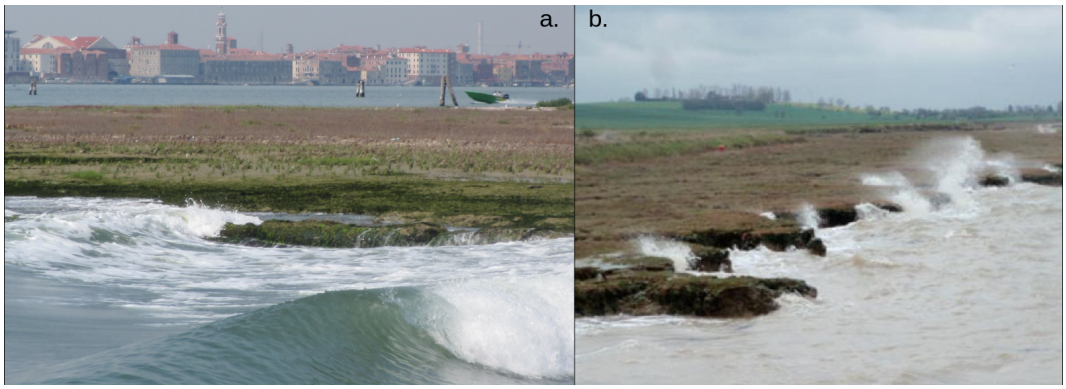


**Figure 1.4:** Waves breaking on salt marsh edges; a. wave induced by boat wake impacts along the marsh edge in the Venice Lagoon; b. wind waves impact a salt marsh in Essex. Images: G.C.H. Goodwin.(a.), James Tempest (b.)

sea levels are not always matched by rising bed elevations: in regions with poor sediment availability, the average depth in intertidal landscapes risks increasing, with risk of increasing the statistical prevalence of erosive waves (D'Alpaos et al., 2013), thus enhancing lateral retreat. This is observed in the dramatic retreat of the Venice Lagoon marshes (Carniello et al., 2009; Defina et al., 2007), accentuated by the deepening of the lagoon (Molinaroli et al., 2009).

The complexity of the settings in which marshes develop (see Figure 1.3) means that not all marshes experience RSLR in the same manner, even if the rate of RSLR is the same (Cowell and Thom, 1994): In closed bays, marsh retreat modifies hydroperiod and further reduces sediment delivery to the remaining marshes (Donatelli et al., 2018). Conversely, areas with strong sediment supply and little wave impact show little sign of generalised retreat (Goodwin and Mudd, 2020). Other effects of modern climate variations such as modified storminess initially caused concern, but have been shown to enhance the resilience of salt marshes to sea level rise (Hopkinson et al., 2018a; Schuerch et al., 2013). Much remains to learn on erosive processes: while marsh retreat is demonstrably linked to nearby channel deepening in a macro-tidal setting (Cox et al., 2003), the stochasticity of tidal effects on the erosive power of tidal currents is not well known; in the case on wind-waves, the difficulty in quantifying the combined impact of waves and tides is illustrated by (D'Alpaos et al., 2013); sightings of marsh surface being stripped of vegetation by waves or currents are also not unheard of, although the mechanics of this process are not yet well known.

The previous sections highlight the importance and precarity of salt marsh landscapes and environments, although the extent of their vulnerability is regularly debated and depends very much on local batyhmetry, tidal range, sediment supply and wave exposure (Ganju et al., 2017; Kirwan et al., 2016a; Saco et al., 2017; Schuerch et al., 2018). First, Section 1.2.1 showed that salt marshes provide a wide range of ecosystem services. These services only exist through the combined action of biological and geomorphological processes that make salt marshes co-evolve as landscapes and ecosystems. Second, Section 1.2.2 detailed the threats to continued salt marsh existence throughout and after the $21^{st}$ cen-

tury. Specifically, salt marshes are vulnerable to vertical drowning through an increase in sea level relative to the marsh surface and horizontal retreat through exposure to waves and currents.

This thesis aims to provide and demonstrate objective topographic tools for researchers and eventually land managers to monitor and understand the evolution of salt marshes worldwide under changing environmental constraints. To understand the scientific background and challenges that lead to the development of these tools, the following section will (1) detail the processes through which salt marshes establish, develop and disappear and (2) draw a state of the art of observation methods and their use in marsh evolution predictions.

## 1.3 Background

In this section, I cover the major scientific notions necessary to follow the narrative of this thesis. First, I summarily explain the mechanisms by which salt marshes acquire or lose their characteristic topography and vegetation. Second, I detail methods of topographic data collection used to study salt marshes.

### 1.3.1 Intertidal hydrodynamics

**Tides:** Tides are long-period waves that circumnavigate the Earth's oceans and seas as the gravitational pull of the Moon and the Sun lifts the free surface of water bodies (Kvale, 2006). As the Moon circles the Earth, it draws masses of water underneath it, creating high tides, and creates a smaller high tide at the antipode of its position. Meanwhile, water is drawn from other parts of the Earth, creating low tides (Figure 1.5 A). The cycles of high and low tides are half a lunar day, or 12 hours and 25 minutes. The position of the Moon relative to the Earth and Sun determines the succession of spring and neap tides (Figure 1.5 B). When the Earth, Moon and Sun are aligned in a phenomenon known as syzygy (which occurs at the new and full moon), high tides are at their maximum and low tides at their minimum: these tides are called spring tides. Conversely, at the first and third quarters of the moon, high tides are at their lowest and low tides at their

highest: these tides are called neap tides. Many more periodic cycles exist (Figure 1.5 C,D), making the astronomical tide the result of many harmonic constituents, first predicted by Lord Kelvin's "tide machine". The succession of astronomical high tides can be seen in Figure 1.5 E. Nowadays, predictions of astronomical tides are mostly numerical and easily accessible (Pawlowicz et al., 2002).

Locally, astronomical tides are not the only phenomena to influence the level of the sea. The propagation of tides is affected by bathymetry, such that some regions experience different tidal regimes and amplitudes (Figure 1.6). Regions under a semi-diurnal regime will experience approximately two tides of similar amplitudes in a day, while diurnal regimes cause only one tide a day. Regions under a mixed semi-diurnal regime experience two tides of different amplitudes in a day. The periodical succession of astronomical tides is further altered by meteorological events: for example, a drop in atmospheric pressure will cause an increase of the water level at the rate of $1cm$ for every millibar; low pressure fronts moving landward such as storms or hurricanes propagate a bulge of water called a storm surge, further increasing water levels (Lagomasino et al., 2013; Muller et al., 2014; Mulligan et al., 2014). Conversely, high pressures decrease tidal elevations. These meteorologically induced deviations from the astronomical tide predictions in any given location are called anomalies.

As their name suggests, intertidal habitats such as tidal flats and salt marshes are situated at elevations between most high tides and most low tides, making their evolution dominated by the ebb and flow of the tide. Tide gauges installed around the world measure and record water levels at sea and on the coast and some of these gauges have been recording water levels since the 1830s. Many services distribute predicted and observed tidal data as well as real-time tidal levels for their own country, like the United Kingdom Tide Gauge Network (https://www.ntslf.org/data/uk-network-real-time) or the National Oceanographic and Atmospheric Administration (NOAA, https://tidesandcurrents.noaa.gov/), or globally, like the Global Extreme Sea Level Analysis (GESLA, https://gesla.org/). These data are frequently used to determine the flooding frequency and depth on tidal flats and salt marshes (Reed and Cahoon, 1992),

248 although tidal propagation means that inundation properties on salt marshes
249 on the salt marshes themselves often differ from those measured at tide gauges,
250 particularly for tidal extremes (Mossman et al., 2011).

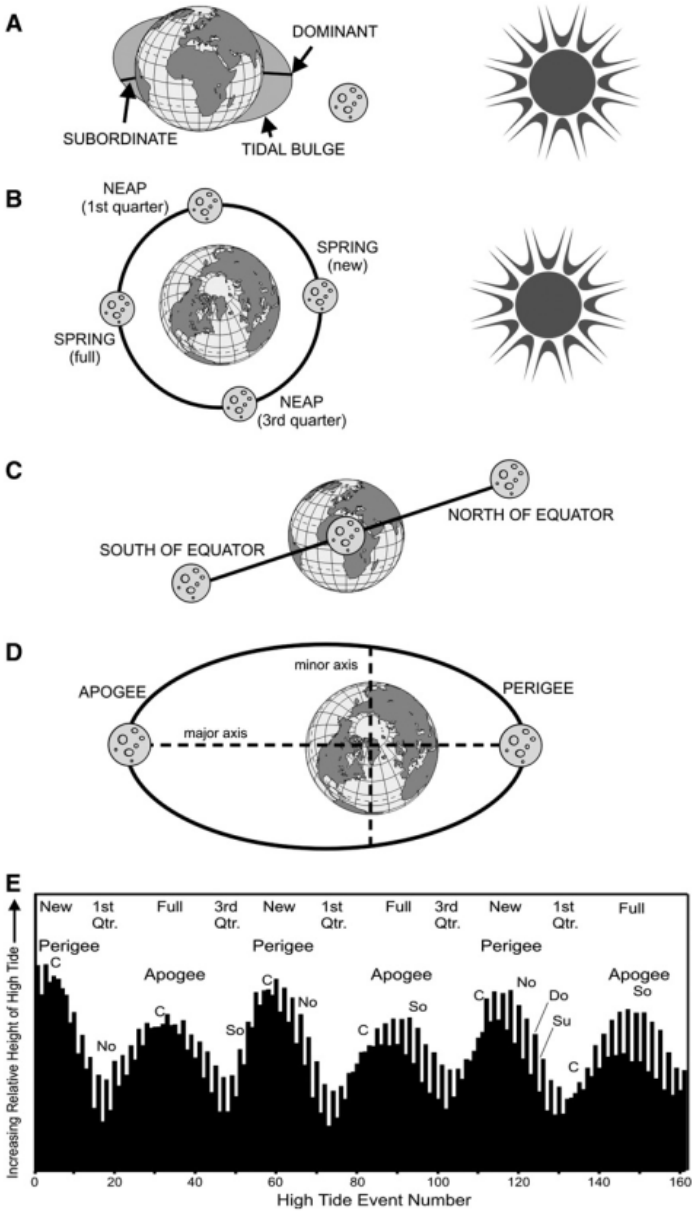


**Figure 1.5:** Idealized equilibrium tidal models that illustrate semidiurnal tides (A), the synodic month (B), the tropical month (C), and the anomalistic month (D). (E) depicts a segment of the 1991 predicted high tides from Kwajalein Atoll, Pacific Ocean. " Su"— Subordinate semidaily tide; "Do"— Dominant semidaily tide; "C"— Denotes the tides that occurred when the Moon crossed the Earth's equator (crossover) and the semidiurnal tides were equal in height; "No"— Moon at maximum northern declination; "So"— Moon at maximum southern declination. Source and caption: Kvale (2006)

As they rise and fall, tides generate currents which may be combined with nearby fluvial currents. As water passes through a control surface of width $B$ and depth $h$, the volume $\Delta V$ passing through the control surface over a time $\Delta t$ determines the current velocity $u_c$ according to Equation 1.1 (Hu et al., 2015):

$$u_c = \frac{\Delta V}{\Delta t \; hB} \tag{1.1}$$

Tidal currents are often separated into cross-shore (perpendicular to the coastline) and long-shore (parallel to the coastline).

**Wind-Waves:** The waves referred to in Section 1.2.2 are part of the larger group of ocean waves (which themselves are gravity waves), which were first classified according to their period by Munk (1950). Wave period is defined as the the time elapsed between two wave crests, measured in seconds. The waves most often observed on the shore are wind-and ocean-waves, which typically have a period of less than $12s$ (Figure 1.7). Waves of longer period such as tides and storm surges (Munk, 1950) influence the propagation of wind-waves by changing the depths of waters in which they propagate.

Wind-waves are generated by pressure fluctuations caused by wind shearing on

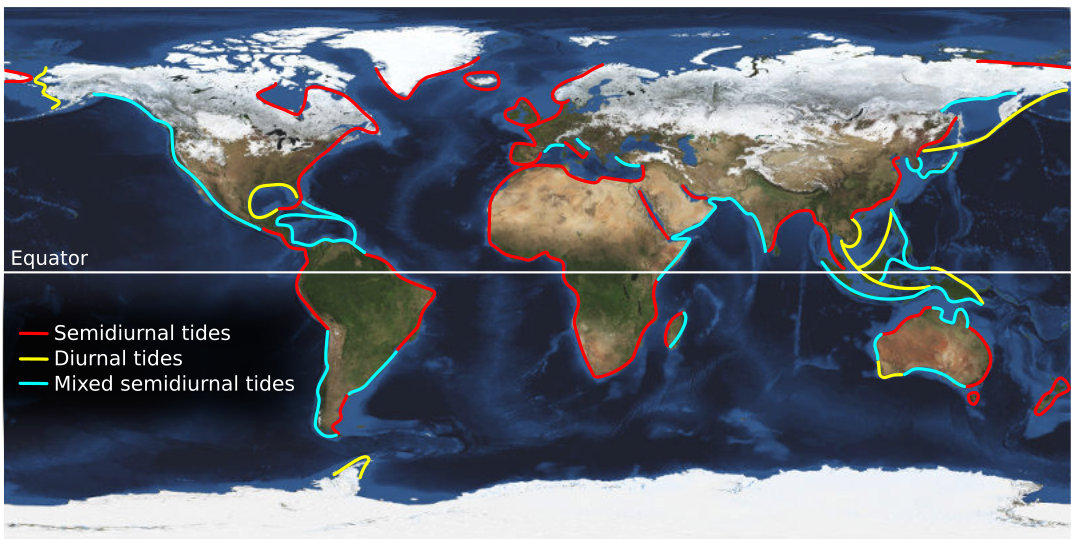


**Figure 1.6:** Tidal regimes of the world. Source: https://web.archive.org/web/20180918123631/https://oceanservice.noaa.gov/education/kits/tides/media/supp_tide07b.html

a water surface. The resulting vibrations of the water surface are then amplified (Young, 1999). The propagation of this disturbance causes groups of waves to form on the water surface, which in open water organise themselves into sea-waves or swell (Hasselmann et al., 1973). While salt marshes may also be affected by swell, they often develop on sheltered coasts (see Figure 1.3), where the distance over which wind affects the water surface is limited. Combined with the shallow depths characteristic of environments harbouring salt marshes, waves affecting salt marshes are more often than not fetch-limited (Mariotti and Fagherazzi, 2013b), fetch being a function of distance and depth (Karimpour et al., 2017). Most of our knowledge on transformation of wind friction into waves in fetch-limited settings comes from empirical measurements on Lake George, New South Wales, Australia (Breugem and Holthuijsen, 2007; Young and Verhagen, 1996).

**Bottom shear stress:** Bottom shear stress (BSS) is a force exerted parallel to the surface of the sediment, and is most often designated as $\tau$. BSS is generated by the combined effects of currents and waves on the sea bed (Dalyander et al., 2013). The magnitude of the bottom shear stress $\tau_{cur}$ exerted by a tidal current $\overrightarrow{u}$ of velocity $u$ is defined by Roberts et al. (2000) as:

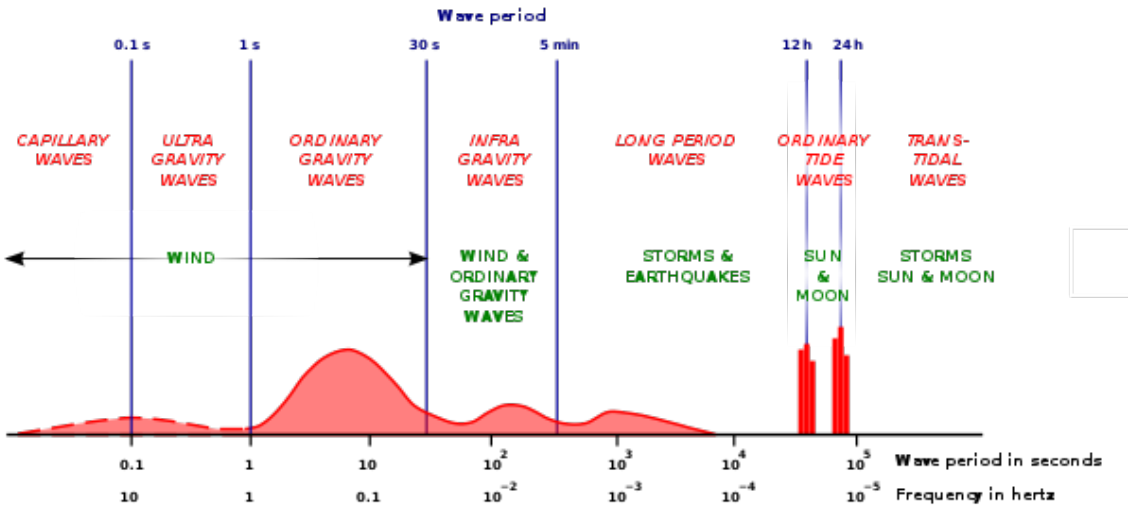


**Figure 1.7:** Tentative classification of ocean waves according to wave period. The forces responsible for various portions of the spectrum are shown. The relative amplitude is indicated by the curve. Source and caption: https://www.wikiwand.com/en/Infragravity_wave, adapted from Munk (1950)

$$\tau_{cur} = \rho_w \frac{g}{Ch} u^2 \tag{1.2}$$

where $\rho_w$ is the volumetric mass of water ($\rho_w = 1000\ kg \cdot m^{-3}$) and $g = 9.81\ m \cdot s^{-2}$ is the gravitational constant. In Roberts et al. (2000), $\frac{g}{C} = 0.002$, however this was updated in Hu et al. (2015) so that:

$$Ch = 18\ log_{10} \frac{12\ h}{2.5\ D_{50}} \tag{1.3}$$

where $h$ is the water depth and $D_{50}$ is the median grain diameter on the bed.

BSS generated by waves is aptly described in Carniello et al. (2005), where the orbital velocity $u_m$ of a wave of significant wave height $H_s$, wave period $T$ and wave number $k = \frac{2\pi}{\lambda}$ (where $\lambda$ is the wavelength) propagating in water of depth $h$ is defined thus:

$$u_m = \frac{\pi\ H_s}{T\ sinh(k\ h)} \tag{1.4}$$

Wave friction against the bed is then calculated for rough and smooth beds (cf. Nikuradse (1950)), according to the method of Soulsby and Clarke (2005):

$$f_r = 1.39 * (\frac{u_m\ T}{2\pi \frac{D_{50}}{12}})^{-0.52} \tag{1.5}$$

$$f_s = 2\ Re^{-0.5}, Re < 5000 \tag{1.6}$$

$$f_s = 0.0521\ Re^{-0.187}, Re > 5000 \tag{1.7}$$

, where the wave Reynolds number $Re$ is defined as below, with $\nu = 1.0533 \cdot 10^{-6} m^2 \cdot s^{-1}$ the kinematic viscosity of water :

$$Re = \frac{u_m^2\ T}{2\pi\ \nu} \tag{1.8}$$

The BSS generated by waves $\tau_{wav}$ is then :

$$\tau_{wav} = 0.5\ \rho_w\ max(f_r, f_s)\ u_m^2 \tag{1.9}$$

The value of $\tau_{wav}$ is related to the determination of deep or shallow water conditions. If $\tau_{wav} = 0$, then the wave orbitals are circular and do not reach the bottom: these are deep water conditions for wave stress. Conversely, in shallow water, wave orbitals are elliptical and $\tau_{wav} > 0$. Figure 1.8 illustrates the regions in which wave shear stress does or does not occur, stressing the importance of the timing of tidal water level and wind conditions in the determination of BSS (D'Alpaos et al., 2013; Fagherazzi and Wiberg, 2009). If bottom shear stress is sufficient to cause sediment resuspension (see below), suspended material will move in the direction of the resultant of waves and tidal/fluvial currents.

**Erosion processes:** While BSS determines the strength of hydraulic stresses on the bed, the resistance of the bed to these stresses will ultimately determine whether sediment will be put into suspension. This resistance is typically referred to as the critical shear stress $\tau_c$. In numerical models used to predict erosion, it is customary to consider that erosion occurs if $\tau = \tau_{cur} + \tau_{wav} > \tau_c$. When erosion occurs, the rate of erosion is often considered proportional to the relative

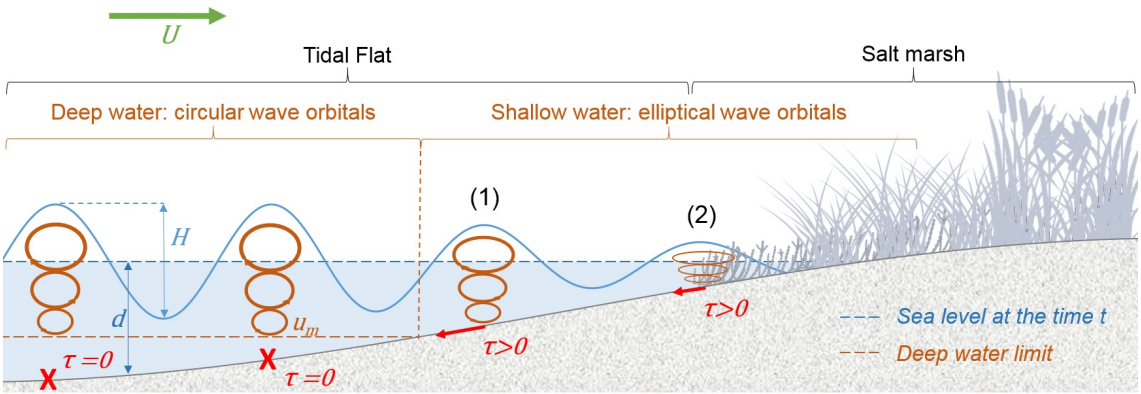


**Figure 1.8:** Diagram depicting the mechanism of wave-scouring. At a given location and time t in the tide cycle, the water depth is $d$. Wind blowing at the speed $U$ generates waves of significant height $H$. The size of wave orbitals decreases with depth, and in deep water the orbital velocity at the bottom u m is null and no erosion occurs. However, when $d$ decreases or $H$ increases, $u_m$ is no longer null and generates a positive bottom shear stress $\tau$. Source: G.C.H. Goodwin

difference between the shear stress and the critical shear stress, as shown below:

$$e = \frac{\tau - \tau_c}{\tau_c} \tag{1.10}$$

However, determining an appropriate value of $\tau_c$ to use in numerical simulations of intertidal environments is complex, as it varies greatly with the size of the surface sediment (Houwing, 1999), its heterogeneity (Ahmad et al., 2011; Wiberg and Smith, 1987), organic content (Mehta et al., 2015), and local and seasonal sediment supply variations (Amos et al., 2004; Amos et al., 2010). Despite these variations, several authors consider the soil of salt marsh platforms to be sufficiently stabilised by vegetation and neglect erosion in morphodynamic models (D'Alpaos et al., 2011; Morris et al., 2002), however occurrences of platform plants being stripped away are not unheard of. This assumption is concordant with the work of Julian and Torres (2006), who estimate that grassy vegetation multiplies by a factor of 2 the critical shear stress. In situations such as that described by Marani et al. (2010), applying this factor would put critical shear stress at $0.8Pa$, which is only slightly smaller than the maximum value of shear stress obtained for a wind speed of $20m \cdot s^{-1}$ or $72km \cdot h^{-1}$ under unlimited fetch.

**Deposition processes:** When hydraulic conditions are calm, suspended sediment can settle onto intertidal surfaces. The amount of sediment deposited has previously been modelled as depending on BSS (Fagherazzi et al., 2006), however this approach does not capture the complexity of sediment settling and capture. The settling of a particle in still water may be described by the balance of buoy-

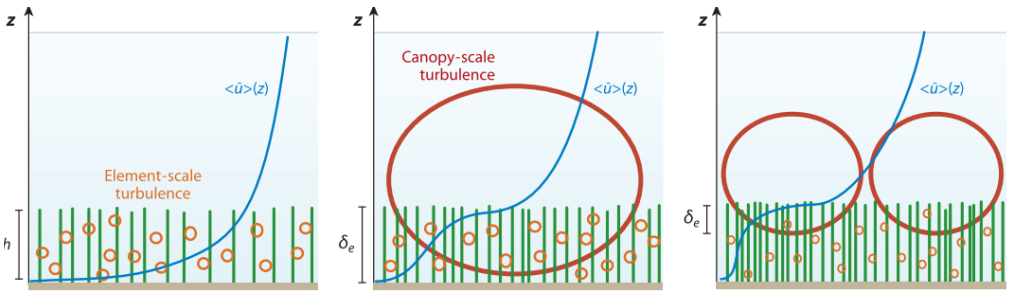


**Figure 1.9:** Velocity profiles and turbulence scales for tidal flats with increasing stem density left to right. Source: Nepf (2012).

ant forces and gravitational forces. Hence, the shape and density of particles play an important role on the velocity at which they fall in the water column. In simplified cases, the falling velocity of a particle is determined by Equation 3.3:

$$w_s = \frac{2}{9} \left(\frac{\rho_s - \rho_w}{\mu}\right) g \left(\frac{D_{50}}{2}\right)^2 \tag{1.11}$$

where $w_s$ is the terminal settling velocity calculated using Stoke's law for a spherical particle of diameter $D_{50}$ and volumetric mass $\rho_s = 2650\ kg\ m^{-3}$ in unagitated water of volumetric mass $\rho_s = 1000\ kg\ m^{-3}$ and dynamic viscosity $\mu = 0.0010518\ kg\ s\ m^{-1}$.

While this equation is often used in numerical models of settling on marsh platforms (see Chapter 3), real deposition on salt marsh platforms departs from this simplified vision. Fine sediment such as muds tend to flocculate, forming agglomerates of varying stability (Eisma, 1986). These flocs appear in sand-mud mixtures and their size greatly affects their settling velocity (Manning et al., 2010), with experiments showing that flocs consistently settle slower that spherical particles of similar size (Strom and Keyvani, 2011) Furthermore, the behaviour of settling particles on vegetated surfaces is made yet more complex by the fact that tidal currents interact with vegetation to generate turbulence at various scales, as shown by Nepf (2012) in Figure 1.9.

**Compaction and subsidence:** Once deposited on a marsh platform (or a tidal flat), sediment compacts through dewatering and under the weight of overlaying strata (Temmerman et al., 2003). This may cause a loss of volume of around 50% (D'Alpaos et al., 2011). Compaction has been found to be at its highest during the first few centuries after deposition (Eugene Turner et al., 2006), in the upper layers of soil were organic matter is found in greater proportion (Bartholdy et al., 2014). Shallow compaction is accompanied by deeper compaction caused by water, gas and oil extraction (Dijkema, 1997; Kennish, 2001), with notable examples including the Holocene compaction of the Mississippi Delta (Törnqvist et al., 2008). Compaction plays such a large role in the long-term evolution of marsh topography that it is taken into account when reconstructing past sea

level from salt marsh cores (Brain et al., 2015) along with deeper subsidence and eustatic land movements (Shennan and Horton, 2002). The combined effects of compaction and subsidence are determinant in the calculation of relative sea level rise.

### 1.3.2 Development of salt marsh platforms

**Tidal flat colonisation:** Salt marsh platforms are initiated when pioneer plants establish a foothold on an unvegetated tidal flat. These species are often *Spartina anglica*, *Spartina alterniflora*, or species of the genus *Salicornia*. Plants only establish under favourable hydrodynamic conditions, named Windows of Opportunity (WoO) after initial work on mangrove seedlings by Balke et al. (2011). WoO are an ubiquitous concept in disturbance-driven ecosystems like salt marshes (Balke et al., 2014). Hu et al. (2015) later detailed this notion for the establish-

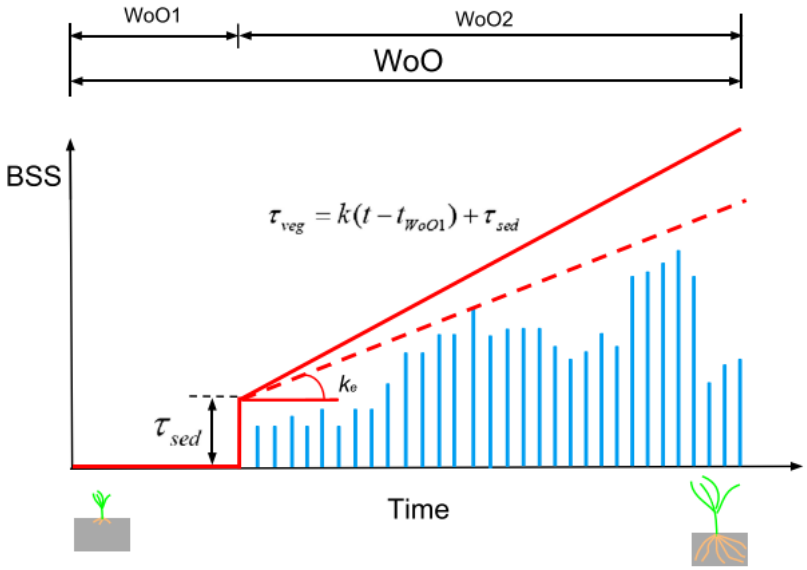


**Figure 1.10:** Diagram of plant establishment; WoO1 controls seedling establishment, and is an inundation-free period with a critical minimum duration (bottom shear stress (BSS) is zero); WoO2 is a period following WoO1, when the seedlings are experiencing BSS disturbance (the blue line). If during WoO2 the external BSS stays lower than the minimum BSS for vegetation uprooting $\tau_{veg}$ (red solid line), then WoO events occur for seedling establishment. $\tau_{sed}$ represents the minimum BSS for bed erosion. $\tau_{veg}$ increases with seedling age because of seedling roots development at the rate $k$. $k_e$ is the maximum slope derived from the BSS time series, which incorporates both magnitude and timing of the external forcing. Source: Hu et al. (2015).

371 ment of salt marsh plants, as shown in Figure 1.10.

372 **Platform growth through eco-geomorphic feedbacks:** Plants established
373 on the tidal flat form patches in which current velocities and shear stress on
374 the bed are reduced (Ma et al., 2014). This protects the patches from further
375 erosion in a positive feedback loop where vegetation protects itself from being
376 broken or dislodged from its substrate. Conversely, flow velocity is higher on
377 the side of vegetation patches (Bouma et al., 2013), prompting a development
378 of salt marshes as platforms (former patches) dissected by channels and pools
379 (Temmerman et al., 2007). When the plant canopy is completely submerged,
380 velocities are higher above the canopy than in the vegetation patch (Neumeier
381 and Ciavola, 2004), and turbulence is generated between stems and at the scale
382 of the patch, as shown in Figure 1.9. These factors contribute to faster accretion
383 rates on salt marsh platforms than on tidal flats. While some sources mention
384 suspended sediment capture or trapping by leaves and stems (Fagherazzi et al.,
385 2012; Mudd et al., 2010) as an added factor to enhanced settling, there is little

**Figure 1.11:** Photographs of salt marshes at different stages of topographic development. Left: pioneer plants (*Suaeda maritima*) established on the mudflat in the Mont-Saint-Michel Bay, France; centre: emergent marsh platform, barely elevated above the sandy substrate of Belhaven Bay, Scotland; Mature salt marsh platform, well above the tidal flat and exhibiting erosion features (saltings) in Skinburness, UK. Images: G. C. H. Goodwin.

evidence that "captured" sediment truly settles; moreover, the individual effect of sediment trapping has not been quantified.

Plants also contribute to the vertical accretion of salt marsh platforms over tidal flats: By modifying their root-to shoot-length ratios in response to elevation, plants also generate feedbacks between organic material build-up and sediment capture (Mudd et al., 2009). Furthermore, the species present and their productivity is influenced by flooding and salinity (Belliard et al., 2017; Pennings et al., 2003; Silvestri et al., 2005), with both of these factors being influenced by the elevation of the marsh platform relative to sea level. Hence, plant productivity has been expressed as following a bell curve with a minimum at high and low elevations, where a given species disappears, and an productivity maximum in between (Marani et al., 2013; Morris et al., 2002). This model presents an efficient description of marsh die-off: when all the species on the marsh platform reach a low-elevation productivity minimum, then the marsh is entirely drowned. While elevation relative to sea level (and by proxy flooding patterns) is identified as the primary control on vegetation prodictivity, other parameters such as interspecific competition also play a significant role in macro-tidal marsh plant distribution (Pennings et al., 2005; Suchrow and Jensen, 2010).

Through organic production, detritic deposition and self-protection against erosion, marsh platforms gain elevation relative to the surrounding tidal flats. From an initial state of vegetated tidal flats (Figure 1.11, left), emergent marsh platforms appear (Figure 1.11, centre) and mature into high marsh platforms (Figure 1.11, right). The relative proportion of organic production versus inorganic settling that contribute to the accretion of the marsh platforms defines the the allochtonous (dominated by detritic imports) or autochtonous (dominated by organic production) character of the marsh. This character may be measured in salt marsh soils through loss on ignition tests (LOI) and may find proportions of organic matter varying from less than 10% to more than 50% (Neubauer, 2008; Roner et al., 2016; Sebag et al., 2006). Autochtonous marshes tend to have soils of lower bulk density (Neubauer, 2008) and depend more strongly on plant production to maintain their elevation, whereas allochtonous marshes tend to build

upon external sources of sediment and a particularly sensitive to variations in available sediment. Nevertheless, it is important to note that the structure of a salt marsh is conditioned by the presence of vegetation: under conditions that do not allow vegetation survival, the unvegetated surface loses the platform-like structure and returns to a tidal flat (Defina et al., 2007; Fagherazzi et al., 2006). Indeed, the marsh and tidal flat are each one of two alternate stable states of low-energy intertidal landscapes (Schroder et al., 2005) maintained through the eco-geomorphic feedbacks described above. The variable intensity of these eco-geomorphic feedbacks enables salt marshes to accrete in response to variations in sea level, thus maintaining their place in the tidal frame under variable sea levels (Crosby et al., 2016; Kirwan and Temmerman, 2009).

The geographic context largely affects the development of vegetation and topography, as illustrated in Figure 1.12. Indeed, it is the local conditions and

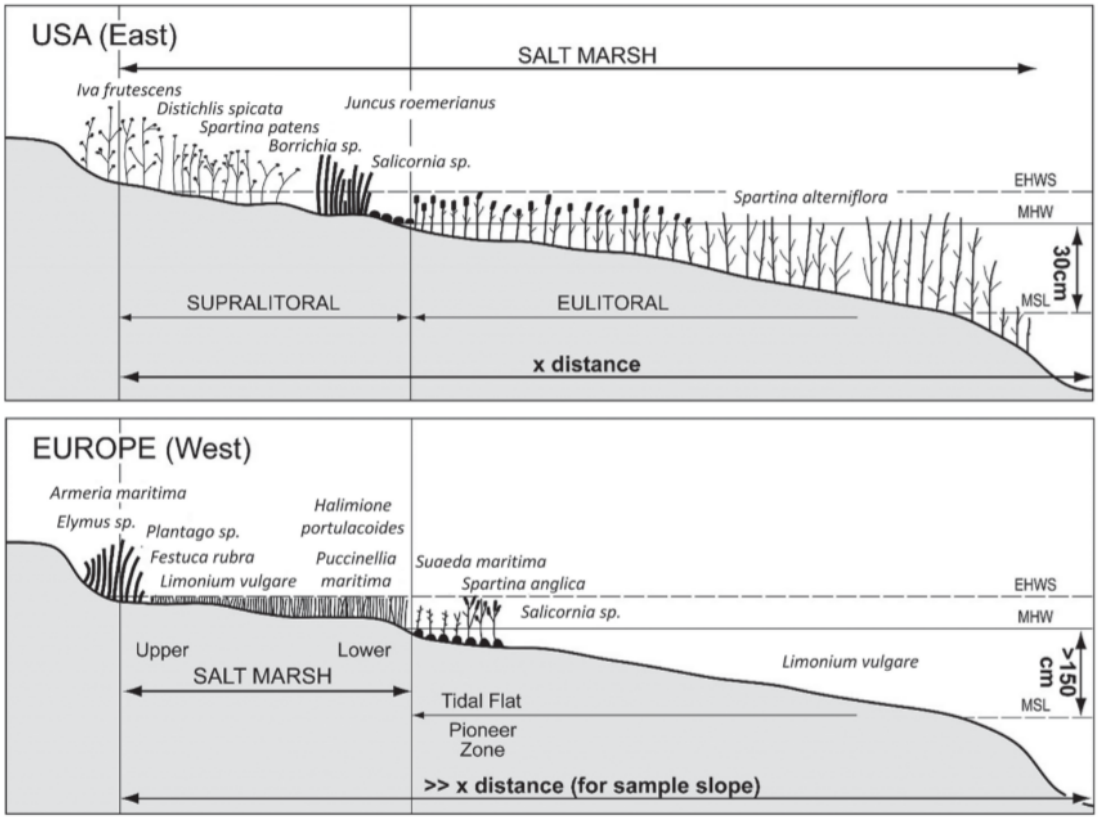


**Figure 1.12:** Comparison between northwest European marshes and those on the eastern coast of the United States. Source: Brooks et al. (2020) modified from Dame and Lefeuvre (1994).

features (tidal range, sediment cells, fluvial outlets, plant distribution, ...) that determine which plants will establish and how they will affect the development of marsh platforms. To this day, the early classifications of Allen (2000) are our best attempt at defining the influence of local context. Although it does not form an objective of this thesis, a possible avenue for salt-marsh research would be to attempt a more fluid, physically oriented classification of marsh systems, similar to the approach adopted by Nienhuis et al. (2015) to qualify the dominance of waves in delta formation.

### 1.3.3 Observation of relevant salt marsh properties

The most closely monitored properties of salt marsh ecosystems are vegetation and elevation, as they are both essential to understand eco-geomorphic processes (Reed and Cahoon, 1992). Nolte et al. (2013) and Webb et al. (2013) summarise the different methods used to observe topography in salt marsh studies (Figure 1.13). While field-based surveys were historically dominant, the exponential growth of remote sensing has offered a variety of methods to observe both elevation and vegetation distribution, most of which still require field calibration.

**Data acquisition in the field:** Field observations are often used as calibration data for the analysis of remotely acquired images or records, which allow for a better analysis of the spatial patterns that may not be captured by fieldwork

| | Field | Field | Field | Airborne | Satellite | Satellite |
|---|---|---|---|---|---|---|
| | RSET-MH | d/RTK-GPS | Total station | LiDAR | ASTER | SRTM data products |
| Vertical accuracy (RMSE) (m) | 0.0010–0.0015[19] | 0.02–0.12[94] | 0.0005–0.005 at 100 m* | 0.14–0.29[23] | 9–11, 10–25[95] | 3.3–9.73[95,96] |
| Spatial resolution (m) | Fine within instrument reach (point measurements) | Depends on survey effort; can be fine over site scale | Depends on survey effort | Variable (m scale) | 15[96] | 30–90[97] |
| Spatial coverage ($m^2$) | Point (but easily replicable) | Small | Small | Medium | Large | Large |
| Cost (magnitude of $ per site) | $10^3$ | $10^3$–$10^5$ | $10^3$–$10^5$ | $10^5$–$10^6$ | Free† | Free† |
| Other issues | Marker horizons can be affected by bioturbation and trampling | Time- and labour-intensive | Time- and labour-intensive | Poor vegetation penetration; requires high level of expertise | Few time-steps available; requires high level of expertise | |

*Calculated from specification sheets of several commercial total station manufacturers. †Data products are freely available, though platform cost is considerable. d/TRK-GPS, Differential/real time kinematic global positioning system; ASTER, Advanced spaceborne thermal emission and reflection; SRTM, Shuttle radar topography mission; RMSE, Root mean square error.

**Figure 1.13:** Observation methods for salt marsh elevation. Source: Webb et al. (2013).

alone. These methods will be detailed in the following paragraphs. Other field methods are still very much in use to provide high-accuracy data on salt marsh properties.

For example, terrestrial laser scanners (TLS) are used to collect very high resolution topographic data. Figure 1.14 shows a composite image collected using a TLS in Campfield Marsh (Cumbria, UK), subsampled to only show points $5cm$ apart (the original dataset has more than $10pts \cdot cm^{-3}$). The accuracy of the elevation of each point after georeferencing is $\approx 1cm$. In the top panel, points with low intensity (blue) are bare tidal sandflats, while those with higher intensity (green to red) are associated with vegetation. In this 3-dimensional scene, the shape and relief of individual patches of pioneer plants *Spartina anglica* are clearly visible, as is the ridge-and-runnel morphology of the low marsh and the higher, continuous mature platform. The same scene coloured by elevation is seen in the bottom panel and distinctly illustrates the elevation gap between the mudflat and pioneer marsh, the low marsh and the high marsh. TLS data can be used to construct precise 3D models of marsh topography and plant occupation (Leroux, 2013), which enables monitoring of erosion, progradation, vegetation encroachment and vertical variations superior to twice the Z-accuracy of the point cloud data (usually $2 - 3cm$).

Other methods are specifically designed to measure changes in ground elevation. Accretion markers are flat clay or plastic objects or coloured markers placed flush with the sediment surface (Cahoon and Reed, 1995; Cahoon et al., 2001; Cahoon et al., 1996). The elevation of the marker is usually measured with a Differential Global Navigation Satellite System (D-GNSS). After a given period of time, the height of the sediment above the marker is measured to obtain total deposition (which is different from total elevation difference). Likewise, Surface Elevation Tables (SET) (Anisfeld et al., 2016; Cahoon, 2015; Cain and Hensel, 2018; Kirwan et al., 2016a) are used to give a precise measurement of changes in ground elevation. Like accretion markers, SET precision for the initial elevation is that of the D-GNSS used (usually around $1cm$), and their precision on elevation change is millimetric, allowing Cahoon et al. (2000) to study the differences

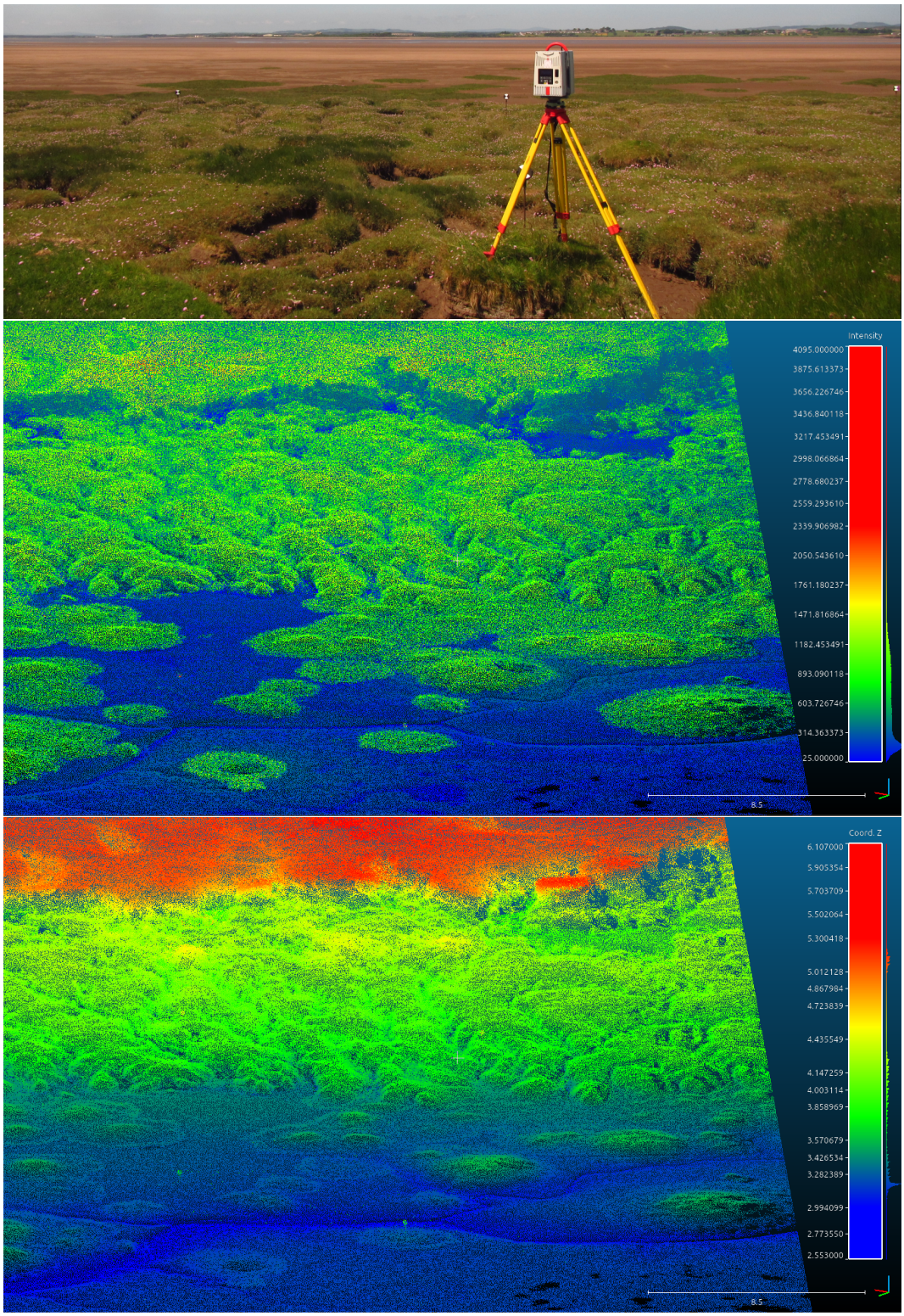


**Figure 1.14:** Composite model of 12 TLS scans of Campfield Marsh in Cumbria, UK (photo on top). Each point in the dataset is on average 5 *cm* apart from any other. Points are coloured by intensity (middle) and elevation (bottom). Source: G.C.H. Goodwin.

between accretion through deposition and elevation change, thus highlighting the impact of organic production and shallow subsidence on marsh elevation. The functioning of a SET is shown in Figure 1.15.

**Remote sensing for habitat and elevation mapping:** Despite their great accuracy, field methods have the disadvantages of a small footprint and high labour intensity (Webb et al., 2013). For instance, the data shown in Figure 1.14 were collected over the course of 4 hours and processed for another 4 hours. Instead, remote sensing (either airborne of via satellite) is often used to take advantage of its relatively large spatial coverage.

Habitat mapping is a common application of hyperspectral satellite images, through the analysis of spectral properties such as the Normalized Difference of Vegetation Index (NDVI) (Jucke van Beijma, 2015). NDVI mapping has developed to the point where only a minimum of ground-truthing is required to determine the presence and type of vegetation (Hladik and Alber, 2014). This

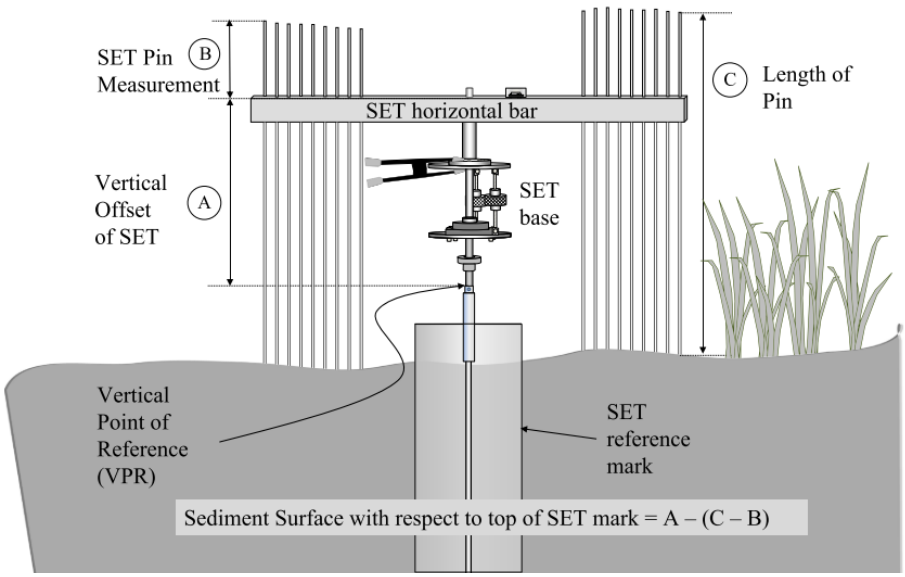


**Figure 1.15:** Conceptual diagram of a Surface Elevation Table (SET) showing the deployment of the horizontal reference bar atop the SET base, which is locked onto the SET bench mark during a measurement session. The SET benchmark is a deep driven rod, the top meter of which is encased in PVC. The figure also shows how SET pin height measurements are used to compute the elevation of sediment surface with respect to the top of the SET mark, which is also the Vertical Point of Reference, or VPR. Source and caption: Cain and Hensel (2018).

index has been shown to consistently differentiate vegetated areas from tidal flats (Tuxen et al., 2008) and flooded channels from dry land despite the sensitivity of classification algorithms (Belluco et al., 2006; Wang et al., 2007). However, knowledge of vegetation coverage is not sufficient to analyse or predict the elevation of salt marshes. Although Digital Terrain Models (DTMs) have been successfully generated from habitat maps in the specific context of the Venice lagoon (Silvestri et al., 2003), additional influences on halophyte distribution such as groundwater circulation (Moffett et al., 2010, 2012) can lead to mismatches between topography and habitats (Hladik et al., 2013). Furthermore, marshes experiencing a higher tidal range than the micro-tidal Venice Lagoon tend to have more complex topography, which further prevents the reliable use of spectral data to infer topography.

In this thesis, we use direct methods of observation of topography in intertidal

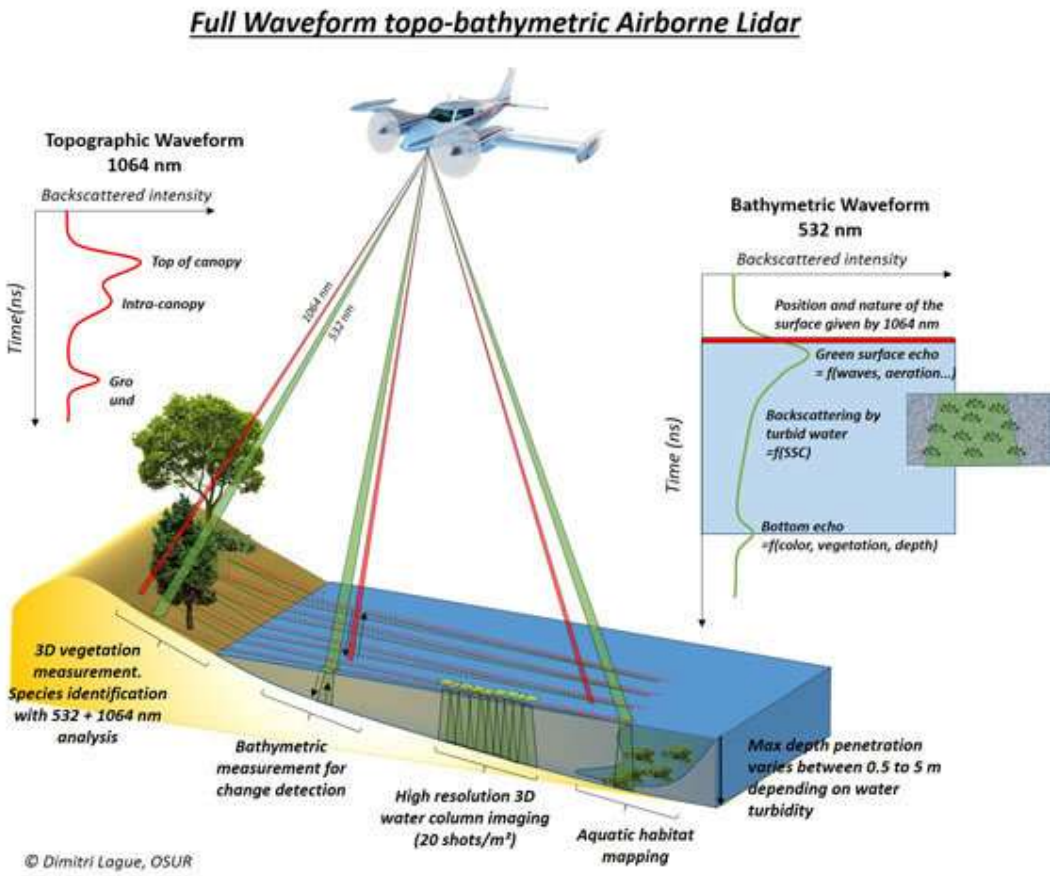


**Figure 1.16:** Schematic description of a full waveform topobathymetric lidar acquisition. Image: Dimitri Lague.

environments. Particularly, we focus on airborne lidar surveys (ALS), which produce the most accurate and highest resolution data (Figure 1.13). Lidar is the abbreviation of LIght Detection And Ranging, and measures distances by timing the return of a projected laser pulse. In this sense, a TLS is effectively a ground-based lidar sensor. However, most lidar sensors are airborne, being carried either on airplanes or Unmanned Aerial Vehicles (UAV). Because ALS are the centre-piece of this thesis, we detail the acquisition and processing of airborne lidar data.

In the case of an ALS, an aircraft flies over the area of interest, its position being tracked by a GNSS, most often a Real-Time Kinematic (RTK) GNSS, and its orientation (roll, pitch and yaw) tracked by the onboard computer. The lidar sensor, most often nadir-facing, emits multiple laser pulses of around 10 $ns$ along swathes orthogonal to the flight path of the aircraft (Figure 1.16). Each pulse is reflected by elements of the landscape such as trees, grass or bare ground, forming a return signal of varying intensity, or waveform (Figure 1.17(a)). This waveform may be processed to output the first and last peak returns (Figure1.17(a)) or conserved to preserve the signatures of different layers of reflective objects (Figure 1.17(b,c)). The analysis of the full waveform is very useful to establish the

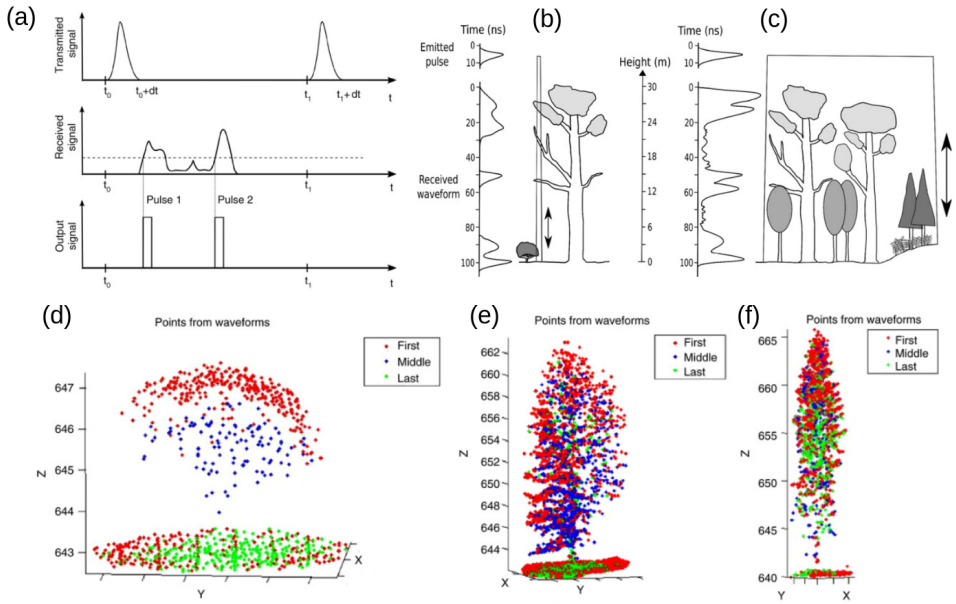


**Figure 1.17:** Schematic description of full waveform topographic lidar outputs. Source: Mallet and Bretar (2009).

structure of tree canopy, as seen in Figure 1.17(d-f)). Lidar can be topographic (red emitted pulse at 1064 $nm$) or bathymetric (green emitted pulse at 532 $nm$). As shown in Figure 1.16, full waveform analysis on bathymetric lidar data allows 3D imaging of the water column, and may also be combined with red lidar to identify canopy types.

**Quality of lidar data:** In the context of salt marshes, the desired data is often ground elevation. In Figure 1.17 (b)-(f), this means that the last (and lowest) return is retained. Gridding such data produces a Digital Terrain Model

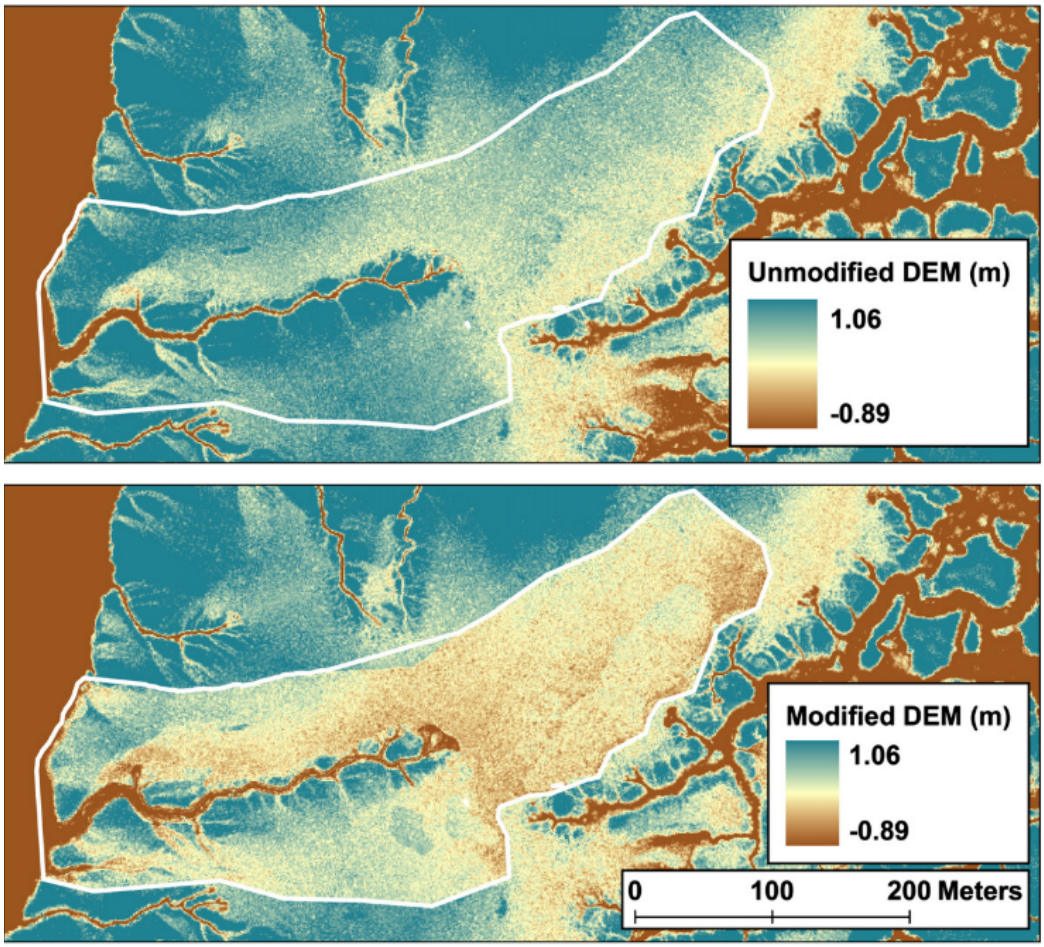


**Figure 1.18:** Map of a marsh on Sapelo Island, GA, USA, used as a test site for LIDAR-derived DTM corrections showing unmodified (top) and modified (bottom) DTM elevations (m). Cooler blue colors indicate higher elevations and warmer dark browns indicate lower elevations. Note the decrease in elevation associated with creek heads surrounded by tall and medium *Spartina alterniflora* in the modified DTM. Total area mapped and modified at location 2 was 0.078 km$^2$ (outlined in white). Source and caption: Hladik and Alber (2012a)

(DTM), as opposed to Digital Surface Models (DSM) which are obtained by keeping the first return and show the top of infrastructure and vegetation. If the last return has effectively reached the ground, then ground elevation is known with an accuracy close to that of the position of the aircraft. However, the density of salt marsh vegetation often prevents the laser pulse from finding bare ground (Sadro et al., 2007), meaning that the last return will overestimate ground elevation (Chassereau et al., 2011; Schmid et al., 2011).

This vegetation-induced bias generates a positive measurement error to the elevation of almost all of the marsh platform (i.e. the measured elevation is higher than the true ground elevation). Its magnitude varies with vegetation height (Hladik and Alber, 2012a; Rogers et al., 2016a), with plants such as *Spartina alterniflora* causing an error upward of 70 *cm* at the end of summer. The consequences of such an error are dependant on the usage of the DTM, however they almost systematically include an impossibility to monitor elevation change over stable portions of salt marsh (see Chapter 3), as the error propagates over several data acquisitions. Moreover, subtle topographic features and elevation changes that are critical in calculations of drainage, sediment deposition and plant growth may be occluded by vegetation.

Vegetation bias may be corrected at the expense of spatial resolution or footprint of the resulting DTM (Wang et al., 2009) or by using full waveform processing (Parrish et al., 2014; Rogers et al., 2018), but there is no guarantee that the resulting elevation will indeed be the ground level. Figure 1.18 provides an example of a DTM before (top) and after (bottom) vegetation bias correction performed by on-site ground-truthing with a GNSS. Such results are also achieved using TreeNet (Rogers et al., 2018), however the cost and duration of implementation of such methods is prohibitive. In Chapter 5, I further discuss potential solutions to the monitoring of salt marsh surfaces.

## 1.4 Research objectives

### 1.4.1 Design a modular topographic analysis method

Section 1.3.3 shows that the means to acquire topographic data of salt marshes are plentiful and of increasingly easy access. In such a data-rich field, the lack of topographic analysis tools for salt marsh geomorphology stands out sorely. Such tools are present, although arguably not yet widespread, in other field of geomorphology, notably in the analysis of hillslopes and river networks (Mudd et al., 2014; Schwanghart and Scherler, 2014), where they are used to reproducibly identify key features of mountainous landscapes, such as channel heads (Clubb et al., 2014), floodplain terraces (Clubb et al., 2017) or knickpoints (Gailleton et al., 2019), and to determine the consistency of river network properties such as concavity (Mudd et al., 2018). While basic principles of topographic analysis such as the determination of slope and curvature may be universally applicable, the metrics described above may not apply to salt marsh landscapes: for example, although channel heads do exist in salt marshes, the Clubb et al. (2014) method cannot be applied to find them and extract channel networks since some channels intersect with ditches or abandoned reaches. While the developments of tidal creek analysis tools by Chirol et al. (2018), Fagherazzi et al. (1999), and Liu et al. (2015) and topographic classification of marsh edge analyses (Evans et al., 2019) begin to address this need, tools to classify and describe the marsh platform and its features are still lacking.

Many studies rely on the delineation of the marsh outline, particularly on the seaward side: indeed, it is important in the determination of different roughness values for hydraulic models of flooding patterns and wave propagation on the marsh surface. It is also primordial in determining rates of retreat or progradation. A significant number of these studies digitise the outline of marsh platforms from satellite or aerial photography (Gedan et al., 2011; Leonardi et al., 2016a; Pringle, 1995) or spectral analysis to discriminate vegetated platforms from bare tidal flats (Belluco et al., 2006; Collin et al., 2010). Spectral analysis in particular offers many advantages: the high frequency of data acquisition and multiple

sources of easily accessible data (e.g. from NASA, ESA or Planet) contrast with the relative temporal sparcity of high-resolution topographic data. However, despite these attractive properties, they present two major disavantages:

- Both digitisation and spectral analysis have subjective and non-reproducible components. Digitising the outline of a salt marsh from an image is sensitive to variable image lighting, coloration and to operator experience and fatigue. Similarly, the calibration used to calculate vegetation indices like the NDVI requires experienced appreciation of threshold values, and may be influenced by organic matter lying on the tidal flat. Furthermore, outlines of the same marsh digitised at different dates are difficult to compare if the digitising conditions change or if they were digitised by different operators.
- Using spectral data to identify marsh platforms only provides a two dimensional (2D) observation. Thus, even if the marsh outline is correctly identified, the elevation of the platform will not be known. If the outline is to be used in a hydrodynamic model, additional elevation data will be necessary. Unless spectral and topographic data were collected simultaneously, this will be a source of error for predictions of marsh evolution.

Hence, this thesis aims to develop a topographic analysis tool tailored to the specific features of salt marshes. Such a tool is meant to improve the reproducibility and portability of studies on salt marsh landscapes. This will be achieved by addressing the issues detailed above. First, I will describe a method to detect seaward salt marsh outlines without any input by the user other than the Digital Elevation Model (DEM) and the Area of Interest (AoI) in which the marsh is located. Second, I will add the possibility of retrieving several features of the identified salt marsh platform according to the needs of the user, thus making the tool modular. This step will ensure that the necessary inputs for models will be provided, as well as volumetric measurements of change for platform monitoring. Combining topographic and spectral data analysis is key to the accurately monitoring salt marshes and will be addressed separately in Chapter 5.

### 1.4.2 Investigate platform elevation within the tidal frame

As shown in Section 1.2.2, drowning is a threat to salt marsh survival, especially in micro-tidal settings. The need to better know the elevation of marsh platforms relative to sea level and understand its response to changing flooding patterns has never been more pressing, particularly since marshes that are not at risk of drowning may hold clues to increased resilience. Several answers to this long-standing issue have been proposed, both in the form of numerical models (D'Alpaos et al., 2011; Morris et al., 2002) or field observations (Kirwan et al., 2016b). However, most of these approaches make three major assumptions:

- Due to the sub-horizontal geometry of many salt marsh platforms, it is often considered a viable assumption to describe a marsh platform by a single elevation data point. While this assumption may hold for some sites, many salt marshes show some overall gradient due to cycles of progradation and retreat (Allen and Rae, 1988). These cycles generate new platforms at lower elevations, and a single-point representation that misrepresents the distribution of elevations may affect predictions of future marsh evolution.
- While many modelling approaches consider variable tidal forcing, multiple studies concerned with the effects of sea level rise focus on micro-tidal marshes, and thus use sinusoidal tidal records as inputs, giving them a constant amplitude equal to the mean tidal range. This assumption neglects astronomical variations in tidal amplitude as well as the effect of meteorological surges on tidal levels.
- Likewise, suspended sediment concentrations and settling velocity are often considered constant and calculated for spherical particles of constan median diameter, even though it is known that for sandy substrates grain size and concentration vary greatly in space and time (see Section 1.3.2). This approximation is even more likely to misrepresent deposition for clay-rich marshes where flocculation causes further variations in settling velocity.

The method I developed to objectively identify marsh platforms within a landscape provides coastal researchers with the means to measure the distribution of elevations on a marsh platform where aerial lidar is available. The description

of the salt marsh platform elevation will form the first additional module of the initial topographic analysis tool designed in Section 4.4.2. Combined with world-wide high-frequency tidal records, this module will yield the necessary data to verify the effects of the assumptions described above, and explore the effects of removing these assumptions.

### 1.4.3 Determine typical morphologies for platform edges

Aside from sea level variations, tidal currents and waves also created changes in salt marsh morphology. While considerable effort has been devoted to the determination of wave power and its effect on marsh retreat (see Section 1.2.2), only a few studies like that of Evans et al. (2019) focus on the morphology of marsh edges and their potential influence on retreat and progradation. In this particular case, 3 morphological types of margings were identified along sections of marsh and related to progradation and erosion. It has however been shown that wave thrust against marsh scarps is sensitive to scarp slope and terracing (Tonelli et al., 2010). Furthermore, objectively classified morphologies of marsh edges have been linked to their evolution: scarps have been tied to retreat, while ramped edges are more often associated with progradation, and ridge-runnel edges with complex evolution patterns (Evans et al., 2019). This last example is to date the only topographic analysis tool devoted to marsh edges, contrasting with the multiple works on tidal creek identification (Chirol et al., 2018; Fagherazzi et al., 1999; Liu et al., 2015). Despite this method's quality, its choice to classify marsh edges and evolution patterns rather than quantify them does not allow for a nuanced approach to retreat and progradation of the marsh outline.

I propose to use the TIP method developed in Section 4.4.2 to separate marsh platforms from tidal flats using free topographic records in a mega-tidal bay. This method is particularly well fitted for mega-tidal environments where scarps are easily detectable from lidar data. I will enrich this method with a module that identifies the marsh outline and describes it with series of transverse profiles. By using this new module on large, dynamic salt marsh systems over several years, I aim to establish a functional relation between marsh edge morphology and the

magnitude of erosion or progradation.

## 1.5 Thesis progression

The objectives of this thesis are (1) to develop a reproducible method to detect salt marshes and identify some of their topographic features, and (2) to demonstrate the method's scientific value by using it to predict topographic evolution and describe geomorphic features relevant to future salt marsh evolution. In this chapter, I have presented the necessary background to understand the development of salt marsh platforms as well as the means available to observe them, with a particular focus on the observation of topography and topographic change. In the rest of the thesis, I describe the achievement of our research objectives through three chapters of original research material produced during the PhD.

In chapter 2, I describe the design and testing of the Topographic Identification of Platforms (TIP) method. First, I develop the rationale and methodology of this method designed to isolate salt marsh platforms from tidal flats, using exclusively high resolution topographic data within an area of interest, with minimal input from the user. I then test the method on six salt marshes in the United Kingdom and explain the potential and limits of the method, as well as our choice of default calibration.

In chapter 3, I develop the TIP method to focus on platform elevation. I add a module to identify and characterise the elevation of eight marsh platforms in the UK and the USA. Using high-frequency tidal records and remotely-sensed as well as field-based sediment supply data, I build a simple accretion model to explore the limits of common assumptions of time-invariance in model inputs.

In chapter 4, I further develop the TIP method to investigate the topography of salt marsh edges. I add a module to identify the most seaward marsh edge and describe its topography with a series of regularly spaced transverse profiles. I then examine the variation of these profiles with the magnitude of erosion and progradation events in a large salt marsh system in Moricambe Bay, UK, and link basic metrics of marsh edge topography to marsh outline mobility.

In chapter 5, I reflect upon the potential and limits of our method and results. Namely, I assess the opportunity that a modular topographic analysis tool offers for researchers and land managers to produce reproducible results, and address the two principal threats to salt marsh survival: drowning and erosion.

# Chapter 2

# Detecting salt marsh platforms

The work presented in this chapter was published in Earth Surface Dynamics:

Goodwin, G. C. H., Mudd, S. M., and Clubb, F. J.: Unsupervised detection of salt marsh platforms: a topographic method, Earth Surf. Dynam., 6, 239–255, https://doi.org/10.5194/esurf-6-239-2018, 2018.

The software used and developed in this chapter is available at: Goodwin, Guillaume C. H., Mudd, Simon M., & Clubb, Fiona J. (2017, October 10). LSDtopotools Marsh Platform Identification Tool (Version v0.2). The Zenodo link is: http://doi.org/10.5281/zenodo.1007788

This research was conducted in collaboration with the named co-authors, who helped to edit the final manuscript and contributed to software development. I wrote the topographic analysis algorithms, performed the analyses, created the figures, and wrote the manuscript.

# List of Abbreviations

| Abbreviation | Meaning |
|---|---|
| ALS | Airborne Lidar Survey |
| AoI | Area of Interest |
| BSS | Bottom Shear Stress |
| DEM | Digital Elevation Model |
| DI | Dissection Index |
| $K_n$ | Square kernel, n cells in length |
| $Pc_n$ | n-th order platform cell |
| pdf | Probability distribution function |
| D-GNSS | Differential Global Navigation Satellite System |
| $Sc_n$ | n-th order scarp cell |
| SfM | Structure from Motion |
| $Ss_1$ | First search space |
| UK | United Kingdom |

**Table 2.1:** Abbreviations used in this chapter

# List of Notations

| Notation | Meaning |
|---|---|
| $R_i$ | Relief of a pixel $i$ [L] |
| $z_i$ | Elevation of a pixel $i$ [L] |
| $z_{max}$ , $z_{min}$ | Maximum and minimum elevation of a raster [L] |
| $R_i^*$ | Dimensionless relief of a pixel $i$ [∅] |
| $S_i$ | Slope of a pixel $i$ [∅] |
| $S_{max}$ , $S_{min}$ | Maximum and minimum slope of a raster [∅] |
| $Rs_i$ | Slope relief of a pixel $i$ [∅] |
| $Rs_i^*$ | Dimensionless slope relief of a pixel $i$ [∅] |
| $P_i^*$ | Dimensionless product of a pixel $i$ [∅] |
| $TP$ | Number of true positives [∅] |
| $TN$ | Number of true negatives [∅] |
| $FP$ | Number of false positives [∅] |
| $FN$ | Number of false negatives [∅] |
| $Acc$ | Accuracy value [∅] |
| $Pre$ | Precision value [∅] |
| $Sen$ | Sensitivity value [∅] |
| $Sp_{thresh}$ | Threshold slope parameter value [∅] |
| $ZK_{thresh}$ | Threshold kernel elevation parameter value [∅] |
| $rz_{thresh}$ | Threshold elevation distribution parameter value [∅] |

**Table 2.2:** Notations used in this chapter

# Abstract

Salt marshes filter pollutants, protect coastlines against storm surges, and sequester carbon, yet are under threat from sea level rise and anthropogenic modification. The sustained existence of the salt marsh ecosystem depends on the topographic evolution of marsh platforms. Quantifying marsh platform topography is vital for improving the management of these valuable landscapes. The determination of platform boundaries currently relies on supervised classification methods requiring near-infrared data to detect vegetation, or demands labour-intensive field surveys and digitisation. We propose a novel, unsupervised method to reproducibly isolate salt marsh scarps and platforms from a digital elevation model (DEM), referred to as Topographic Identification of Platforms (TIP). Field observations and numerical models show that salt marshes mature into subhorizontal platforms delineated by subvertical scarps. Based on this premise, we identify scarps as lines of local maxima on a slope raster, then fill landmasses from the scarps upward, thus isolating mature marsh platforms. We test the TIP method using lidar-derived DEMs from six salt marshes in England with varying tidal ranges and geometries, for which topographic platforms were manually isolated from tidal flats. Agreement between manual and unsupervised classification exceeds 94% for DEM resolution of $1m$, with all but one site maintaining an accuracy superior to 90% for resolutions up to $3m$. For resolutions of $1m$, platforms detected with the TIP method are comparable in surface area to digitised platforms and have similar elevation distributions. We also find that our method allows for the accurate detection of local block failures as small as 3 times the DEM resolution. Detailed inspection reveals that although tidal creeks were digitised as part of the marsh platform, unsupervised classification categorises them as part of the tidal flat, causing an increase in false negatives and overall platform perimeter. This suggests our method may benefit from combination with existing creek detection algorithms. Fallen blocks and high tidal flat portions, associated with potential pioneer zones, can also lead to differences between our method and supervised mapping. Although pioneer zones prove difficult to classify using a

topographic method, we suggest that these transition areas should be considered when analysing erosion and accretion processes, particularly in the case of incipient marsh platforms. Ultimately, we have shown that unsupervised classification of marsh platforms from high-resolution topography is possible and sufficient to monitor and analyse topographic evolution.

## 2.1 Introduction

Salt marshes are highly dynamic ecosystems, sequestering on average 210 g $CO_2$ $m^{-2}$ $yr^{-1}$ through plant growth and decay (Chmura et al., 2003b) and capturing additional inorganic sediment when they are submerged (Nardin and Edmonds, 2014). This productivity has allowed salt marshes to match historic sea level rise (Kirwan and Temmerman, 2009) and laterally expand when sediment inputs were sufficient (Kirwan et al., 2011). It also places them among the most valuable ecosystems in the world (Costanza et al., 1997), and they provide diverse ecosystem services such as flood attenuation (Möller and Spencer, 2002; Shepard et al., 2011), blue carbon sequestration (Chmura et al., 2003b; Coverdale et al., 2014), and contaminant capture (Nelson and Zavaleta, 2012). Their economic value combined with their alarming retreat (Day et al., 2000; Duarte et al., 2008; Kirwan and Megonigal, 2013) makes monitoring the evolution of salt marshes crucial for developing management strategies that maintain the health of these ecosystems. The most closely monitored properties of salt marsh ecosystems are ecological assemblages and elevation, as they are both essential to understand eco-geomorphic processes (Reed and Cahoon, 1992). For instance, elevation determines flooding frequency and therefore influences pioneer vegetation encroachment (Hu et al., 2015), which in turn affects vertical accretion through inorganic sediment capture (Mudd et al., 2010; Mudd et al., 2004; Pennings et al., 2005). Individual plants also react to elevation by modifying their root to shoot length ratios, generating feedbacks between organic material build-up and sediment capture (Mudd et al., 2009). The variable intensity of these eco-geomorphic feedbacks enables salt marshes to accrete in response to variations in sea level, thus maintaining their place in the

tidal frame (Crosby et al., 2016; Kirwan and Temmerman, 2009).

The objective detection and analysis of vegetation patterns is a mature field, with habitat mapping commonly undertaken through the analysis of spectral properties such as the Normalized Difference of Vegetation Index (NDVI) (Jucke van Beijma, 2015). NDVI mapping is now developed to the extent that it requires only a minimum of ground-truthing to determine the presence and type of vegetation (Hladik and Alber, 2014). This index has been shown to consistently differentiate vegetated areas from tidal flats (Tuxen et al., 2008) and flooded channels from dry land despite the sensitivity of classification algorithms (Belluco et al., 2006; Wang et al., 2007).

However, spectral data sources do not provide the topographic information necessary to fully understand morphodynamic processes: although Digital Elevation Models (DEMs) have been successfully generated from habitat maps in the Venice lagoon (Silvestri et al., 2003), additional influences on halophyte distribution such as groundwater circulation (Moffett et al., 2010, 2012) can lead to mismatches between topography and habitats (Hladik et al., 2013). These additional influences on habitat distribution prevent the reliable use of spectral data to infer topography. Furthermore, delineating salt marsh platforms exclusively from spectral sources encourages morphological studies to define salt marshes dominantly from an ecological perspective, whereas the physical setting, most notably the elevation within the tidal frame, plays a key role in maintaining ecosystem health (e.g., Morris et al., 2002).

The topographic data necessary to identify marsh platforms already exist: the proliferation of freely available high resolution topographic datasets from lidar or structure from motion (SfM) techniques means that DEMs with a grid cell size below 1 m are increasingly common on salt marshes, and offer vertical accuracies below 20 cm even without correcting for vegetation (Chassereau et al., 2011; Sadro et al., 2007; Wang et al., 2009). At these resolutions, most scarps and channels are detectable on a DEM, and several automated topographic methods already allow the identification of tidal channel networks (Fagherazzi et al., 1999; Liu et al., 2015). However, contrary to spectral datasets, tools designed to accurately

delineate the extent of salt marshes through means other than manual digitisation are lacking.

In this study, we propose an unsupervised method to topographically differentiate marsh platforms from tidal flats, which we refer to as Topographic Identification of Platforms (TIP). The TIP method aims to reproducibly and accurately delineate marsh platforms using only a DEM as input, while also reducing identification costs and enabling systematic topographic analyses of multiple salt marshes.

We here define salt marsh platforms as sub-horizontal surfaces in the coastal landscape, separated from surrounding intertidal flats by steep scarp features. The processes that form salt marsh platforms can be described by ecological alternate stable states theory (Schroder et al., 2005) and geomorphic bifurcation models (Defina et al., 2007; Fagherazzi et al., 2006). These processes cause salt marshes to develop a distinctive, biologically-mediated topographic structure consisting of several sub-horizontal platforms, separated from tidal flats and from each other by a subvertical scarp and dissected by incising channels (Marani et al., 2007, 2013; Temmerman et al., 2007). The TIP method exploits this characteristic topography, which is clearly visible on high-resolution DEMs and their associated slope rasters, to identify scarps and steep channel banks. As our method uses topographic signatures of marsh platforms, it will reflect the interplay between sedimentation, erosion, and biomass (Fagherazzi et al., 2012) rather than the distribution of specific macrophyte species. It should therefore be complementary to, rather than a replacement for, methods used to detect plant biomass or zonation (in cases where it is present) on marshes. We compare TIP-detected platforms with six manually digitised platforms from English marshes at varying grid cell sizes, demonstrating the potential of this method for quantitative topographic analyses and short to mid-term monitoring.

## 2.2 Methodology

The TIP method automatically detects scarps and platforms of salt marsh systems from a DEM with no manual calibration requirements. Its general process is described in Fig. 2.1, and includes the possibility of filtering (step 1) and degrading (step 2) the DEM; the effects of both treatments are examined in the discussion. A slope raster is then generated by fitting a polynomial surface to topographic data and taking the derivative of this surface (Grieve et al., 2016a; Hurst et al., 2012) (step 3). Steps 4 and 5 are novel algorithms developed in this study to isolate scarps and platforms. The results of the isolation process are compared to manually generated platforms (step 6) to draw a comparison map (step 7).

### 2.2.1 Test sites

We test the TIP method on six sites in England, selected for the availability of airborne lidar data in the form of gridded 1 m resolution rasters, provided by the UK Environment Agency (http://environment.data.gov.uk/ds/survey/), and for the diversity of their morphologies and tidal ranges. Dataset metadata is available freely on the Environment agency website (https://data.gov.uk/dataset/lidar-composite-dtm-1m1). For each site, marsh platforms were digitised on an unfiltered and non-degraded DEM at a scale of 1: 500, using the open-source software QGIS (step 6 in Fig. 2.1). Source data were flown in 2012 for all sites, unless noted otherwise. The locations of the selected sites are shown in Fig. 2.2.

Shell Bay, Dorset (S1) is a shallow bay with a spring tidal range of 2.4 m, located in Poole Harbour, a limited entrance bay (*sensu* Allen, 2000) protected from strong waves. The marshes in Shell Bay display jagged outlines, which were shown in theoretical experiments to be indicative of retreat under low wave and tidal current stress (Leonardi and Fagherazzi, 2014). The Stour Estuary marshes (S2) 6 km upstream of the meso-tidal Stour mouth are subject to a spring tidal range of 3.8 m and fluvio-tidal currents due to their estuarine fringing position (*sensu* Allen, 2000), and therefore display more linear boundaries. The Stiffkey

875 marshes (S3) are back-barrier marshes (Allen, 2000), which experience a 4.7 m
876 spring tidal range and display signs of erosion and accretion. These recent per-
877 turbations to the marsh surface provide an interesting challenge for topographic
878 detection of marsh extents. The macro-tidal Medway estuary marshes (S4, spring

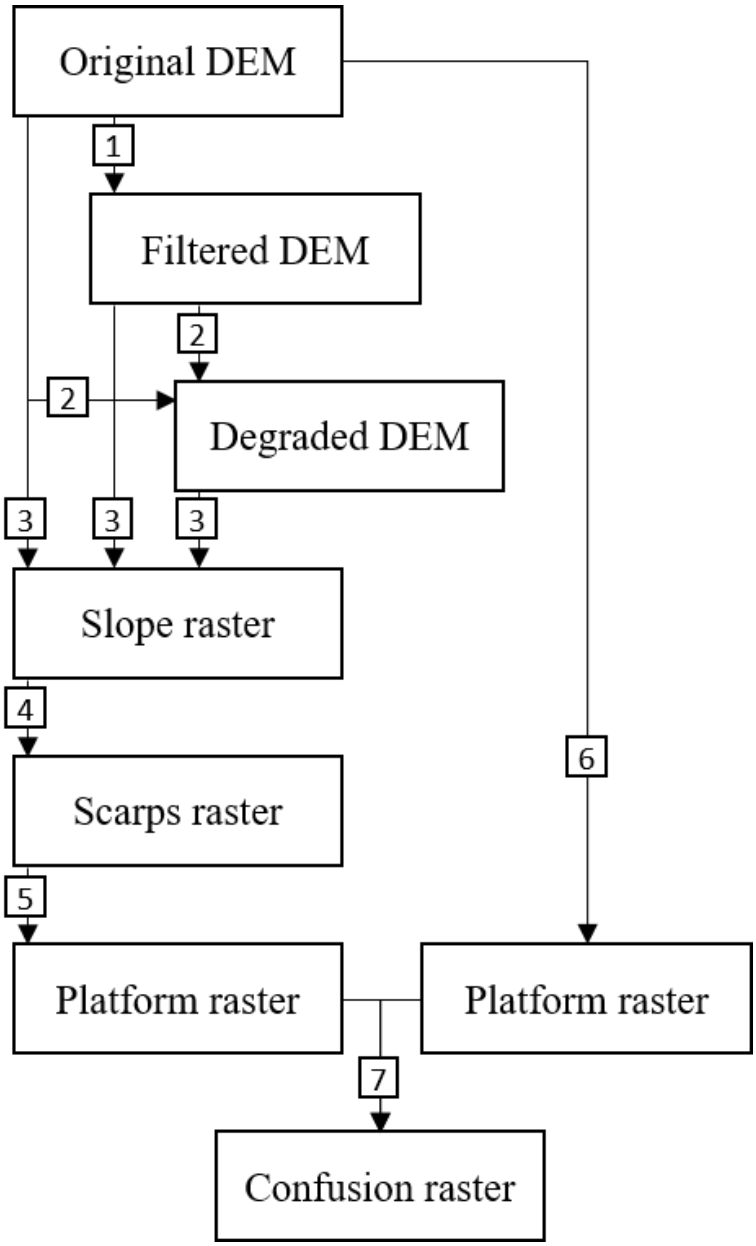


**Figure 2.1:** Flow chart showing the overall structure of the TIP method and its validation. Each object (rectangle) is obtained by implementing a routine (square), numbered as follows: 1. Implementation of a Wiener filter (optional); 2. Subsampling by average value (optional); 3. Calculation of slope by fitting a second order polynomial surface; 4. Scarp identification by routing; 5. Platform identification by dispersion; 6. Manual digitisation of a marsh platform; 7. Comparison of the objectively detected platform to the manually digitised platform.

879 tidal range of 6.4 m) were chosen due to the presence of numerous channels in
880 the tidal flats. Tidal range greatly affects the morphology of salt marshes, and
881 particularly the dimensions and slopes of the retreat scarp. Hence, we also anal-

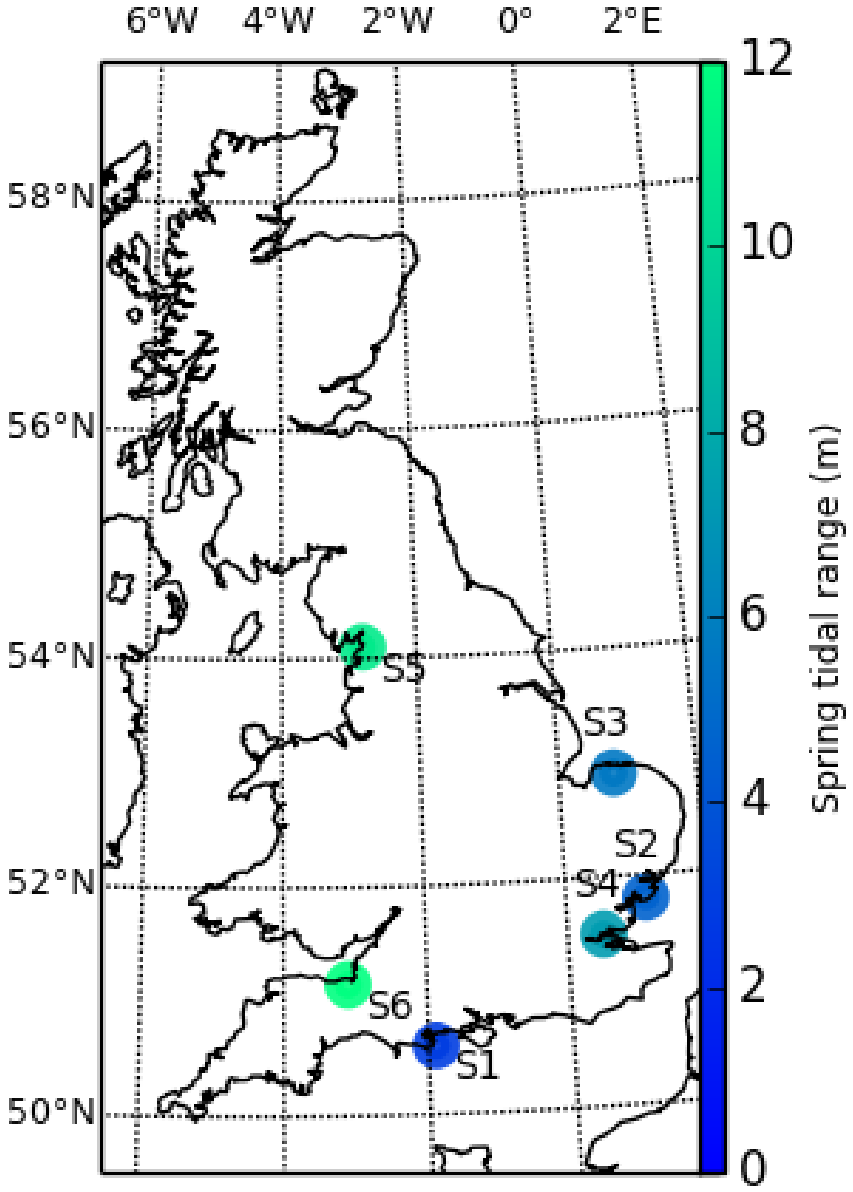


**Figure 2.2:** This map shows the six sites selected from the lidar collection of the UK environment agency, coloured by spring tidal range. The sites are numbered as follows: S1: Shell Bay, Dorset; S2: Stour Estuary, Suffolk; S3: Stiffkey, Norfolk; S4: Medway Estuary,Kent; S5: Jenny Brown's Point, Lancashire; S6: Parrett Estuary, Somerset.

ysed two mega-tidal sites: Jenny Brown's Point marshes (S5, spring tidal range of 9.2 m) and the Parrett estuary (S6, spring tidal range of 11.8 m), where sand dunes, different elevations inside the tidal flats, fallen blocks and sunken platforms will test the limits of the method's ability to correctly delineate marshes in these environments.

### 2.2.2 Preprocessing Topographic Data

The TIP method isolates marsh platforms from a DEM up to their seaward limits by detecting the topographic signature generated by the development of salt marshes. The definition of landward boundaries can vary significantly with context, and may be defined by a vegetation zonation change (Mo et al., 2015), agricultural parcels, or infrastructure (Feagin et al., 2010). Topographic input data is therefore clipped to the landward limit of the platform, at the discretion of the user. In the preparation stage, local slope is calculated from the DEM by fitting a second order polynomial surface (Hurst et al., 2012) with a window radius of three times the horizontal resolution of the DEM, selected because it is the minimum radius needed to calculate slope with this method. The DEM may be passed through a Wiener filter (Robinson and Treitel, 1967; Wiener, 1949) to reduce noise from lidar datasets and/or degraded by averaged subsampling before the determination of slope to match complementary datasets. The effect of enabling these optional treatments is further discussed in the results section. Although methods exist to account for vegetation cover in the DEM (Chassereau et al., 2011; Hladik and Alber, 2012a; Montané and Torres, 2006; Sadro et al., 2007; Wang et al., 2009), we chose not to apply these corrections as we wanted to ensure that the TIP method can be applied without information on the vegetation assemblages at a given site.

### 2.2.3 Scarp routing

Tidal flats and salt marshes occur mostly on dissipative coasts (Allen, 2000), characterised by low local relief and slopes. They therefore display similar local

slope values, and this parameter alone is insufficient to differentiate between tidal flats and marsh platforms. Likewise, although marsh platforms are locally higher than tidal flats and channels, this may not be the case for complex depositional environments (e.g. marshes sheltered by a sand spit), where long-shore declivity may cause portions of the tidal flats to be higher than distant emergent platforms. Therefore, elevation alone, though it may be used to visually identify salt marsh platforms, is insufficient for objective platform detection. We address this problem by investigating transition features such as channel banks and erosion scarps, which are outliers in both slope and elevation rasters. These features are commonly defined by steep local slopes, particularly in mature and eroding systems (Defina et al., 2007; Marani et al., 2013). Furthermore, scarps connect marsh platforms to tidal flats, and therefore represent a distinct break in elevation between the two. In this study, we focus on the identification of scarps and steep channel banks as a precursor to the detection of platforms, referred to as step 4 in Fig. 2.1.

To reduce computational costs, we delineate an initial search space to initiate the detection of scarps by isolating steep areas of the landscape, weighted by their elevation. We first calculate the relief of each pixel, $R_i$,

$$R_i = z_i - z_{min}, \tag{2.1}$$

where $z_i$ [dimensions L] is the elevation of the pixel and $z_{min}$ [L] is the minimum elevation in the DEM. We then divide this relief by the maximum relief in the DEM to get a dimensionless relief at each pixel, $R_i^*$:

$$R_i^* = \frac{R_i}{z_{max} - z_{min}} \tag{2.2}$$

A similar procedure is followed for slope, where $Rs$ [dimensionless] is determined by the slope at a pixel, $S_i$ minus the minimum slope $S_{min}$:

$$Rs_i = S_i - S_{min}, \tag{2.3}$$

and the dimensionless version is calculated as:

$$Rs_i^* = \frac{Rs_i}{S_{max} - S_{min}} \tag{2.4}$$

We then multiply these two metrics at each pixel to create the dimensionless parameter $P_i^*$ at each pixel:

$$P_i^* = R_i^* Rs_i^* \tag{2.5}$$

This dimensionless product is useful for highlighting steep areas at high elevations (Fig. 2.3): the higher the value of $P_i^*$, the steeper and higher the pixel is. $P_i^*$ could vary between 0 and 1, where a value of 0 would mean that a pixel was at both the lowest elevation and gradient in the DEM, and vice-versa for a value of 1.

We use the properties of the probability distribution function (pdf) of $P^*$ to define the first search space, which we call $Ss_1$. With the exception of macrotidal sites S5 and S6, the pdf of $P^*$ decreases monotonically with increasing $P^*$, and at sites S5 and S6 the pdf decreases monotonically after a peak value (Fig. 2.3a). When $f(P^*) < \max(f(P^*))$ and $P^* > \max(P^*)$, the derivative of the pdf is negative and increasing, i.e., the slope of the pdf curve becomes gentler with increasing $P^*$. We therefore define the threshold value ${P^*}_{th}$ where the slope of the pdf is equal to a threshold slope, $Sp_{thresh}$, on the declining limb of the pdf curve (Fig. 2.3a). In this study we optimize the threshold value $Sp_{thresh}$ to improve the classification of each site, as described in the Results section. The first search space, $Ss_1$, is defined as those pixels where $P^* > {P^*}_{th}$, as shown in Fig. 2.3b. The search space $Ss_1$ is also schematically represented as grey cells in Fig. 2.4a (step 4.1)

We then define a square kernel $K_3$ of 3 cells in width around each cell in $Ss_1$. If more than one cell of $K_3$ is included in $Ss_1$, the cell containing the local slope maximum in $K_3$ is flagged as a first order scarp cell $Sc_1$. If one given $K_3$ already contains an $Sc_1$ cell that is not the central cell, the central cell will be flagged as an $Sc_1$ if and only if it is the next local maximum in $K_3$. This results in a patchwork of first order scarp cells (step 4.2 in Fig. 2.4a).

For each first order scarp cell $Sc_1$, we then flag two second order cells $Sc_2$

960 as neighbouring cells with the next steepest slopes contained in the search space
961 and not in contact with each other (red outlines in Fig. 2.4b). If two $Sc_1$ cells

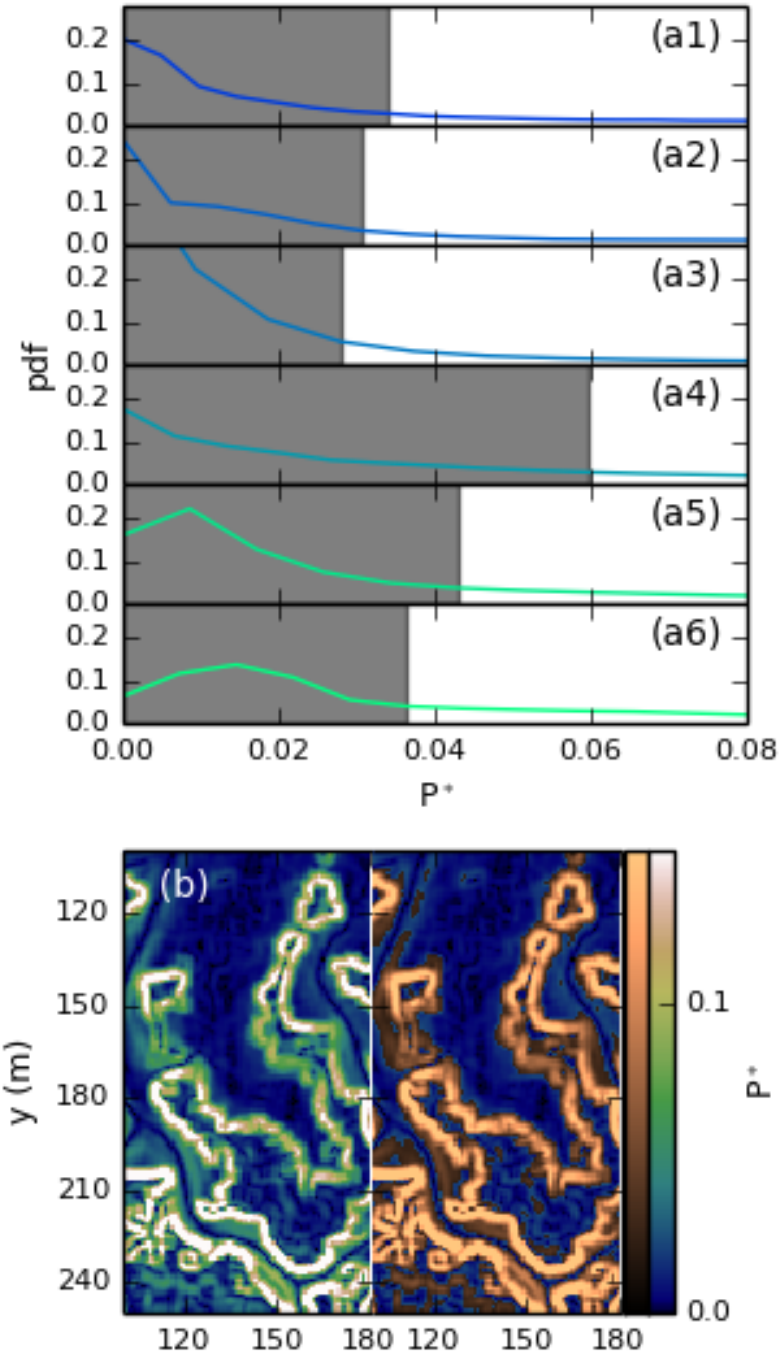


**Figure 2.3:** a1-6. Frequency distribution of $P^*$ for sites S1-6. The greyed portion of the plot represents pixels that are not included in the initial search space $Ss_1$; b. raster representation of $P^*$ for site S1: Shell Bay. Values of $P^*$ under $P^*_{th}$ use the topographic colour scheme, while values above $P^*_{th}$ use the copper colour scheme and are included in $Ss_1$.

are adjacent, only the cell with the higher slope will be flagged as a $Sc_2$ cell (step 4.3 in Fig. 2.4b). This generates a patchwork of first order cells (black outlines Fig. 2.4b) flanked by one or two second order cells (red outlines in Fig. 2.4b). Starting from the second order cells $Sc_2$, we prolong the scarps by finding the cell with the steepest slope that is not adjacent to another identified scarp cell of two lesser orders, within a $K_3$ kernel centred on the previously identified cell. For example, on the third iteration $Sc_3$ cells are identified in a $K_3$ kernel centred on a $Sc_2$ cell and must not be adjacent to an $Sc_1$ cell. Generally, $Sc_n$ cells are identified in a $K_3$ kernel centred on a $Sc_{n-1}$ cell and must not be adjacent to an $Sc_{n-2}$ cell. This routing procedure is applied in all kernels containing no more than two scarp cells and repeated until no cells fit the conditions or the order $n$ is equal to 100 (blue outlines, step 4.4 in Fig. 2.4b).

This procedure produces a large number of potentially misidentified scarps, as small creeks within the platform and in higher portions of the tidal flat tend to be selected during this procedure. We use a further algorithm to thin these scarps and eliminate creeks. The first procedure eliminates low elevation scarps. We first define a kernel of 9 cells in width $K_9$ (i.e., a square kernel of 81 pixels with the pixel being interrogated at its centre) and compare its maximum elevation $\max(ZK_9)$ to the 75th percentile $q_{75}$ of the entire DEM. Cells that do not satisfy the condition $\max(ZK_9) > ZK_{thresh} \times q_{75}$ are discarded from the finale ensemble of scarps (step 4.5 in Fig. 2.4c), where $ZK_{thresh}$ is a parameter which we optimize below. Each $K_9$ kernel containing less than 8 flagged cells is then discarded from the ensemble of scarps; after this procedure finishes we are left with the final ensemble of scarps (step 4.6 in Fig. 2.4d).

### 2.2.4 Platform identification

We identify marsh platforms based on the final ensemble of scarps (step 5 in Fig. 2.1). The final ensemble of scarps becomes a new search space $Ss_2$. We then create a square kernel 3 cells in width ($K_3$) around each cell in this new search space. Using this kernel we identify first order platform cells, $Pc_1$, which are defined as all cells within $K_3$ that have higher elevation values than the central cell of the

kernel (i.e., those that are higher in elevation than the cells in the final scarp ensemble). We do this because platform cells are located at higher elevations than the scarp cells separating them from tidal flats, even though levees found at the edge of creeks and old marsh margins introduce a small decrease in elevation toward the interior of the platform. We use a kernel rather than a simple blanket elevation threshold over the entire DEM because longitudinal elevation variations may cause some tidal flat cells to be higher than scarp cells. Each $Pc_1$ cell that is not adjacent to at least 2 other $Pc_1$ cells is considered a product of isolated

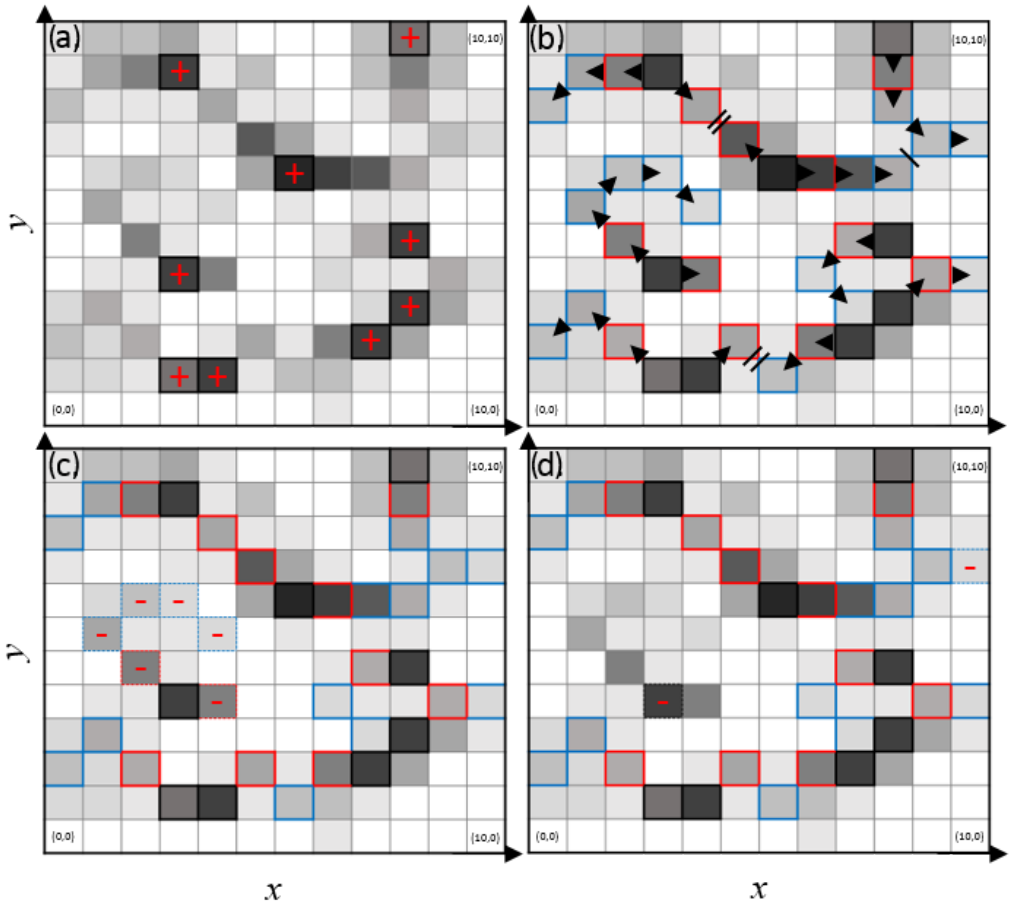


**Figure 2.4:** Schematic example of the scarp detection process through maximum slope routing. Panel a. shows two steps. Step 4.1: determination of the search space $Ss_1$ (greyed cells, darker with arbitrary slope). Step 4.2: Determination of local maxima $Sc_1$ (black outlines with a plus sign); b. Step 4.3: Determination of $Sc_2$ cells (red outlines). Step 4.4: Determination of $Sc_n$ cells, $n$>2 (blue outlines); c. Step 4.5: Elimination of cells where $max(Zk_9) < Zk_{thresh} \times q_{75}$ (dashed outlines with a minus sign); d. Step 4.6: Elimination of isolated cells (dashed outlines with a minus sign). The arrows represent the progressive selection of scarp cells.

situations and eliminated from the ensemble of platform cells.

Following this initial selection of platform cells, we proceed to iteratively fill the platforms. At this point, the initial ensemble of platform cells, $Pc_1$, is clustered around the final ensemble of scarps since we have only used a 3 pixel wide kernel centred on scarp cells to create the ensemble of $Pc_1$ cells. We then iterate using a filling algorithm. The first iteration uses the cells $Pc_1$, the second $Pc_2$, and so on. In each iteration of $Pc_n$ cells, new cells are identified using two kernels, one being larger than the other. First, we define a local elevation condition using an 11 pixel wide kernel $K_{11}$: we find the maximum elevation in this kernel and then subtract 20 cm to define the minimum local elevation for a platform pixel. The 20 cm leeway is applied to account for local elevation variations on the platforms. The algorithm will not identify as separate platforms separated by scarps less than this elevation threshold, so on microtial marshes this threshold can be lowered. We address this limitation in the discussion and appendix. The threshold is necessary to prevent the algorithm from excluding pools and slight depressions in the platform surface.

We then use a 3 pixel wide kernel $K_3$ within $K_{11}$ to identify any cells in the next iterations' platform ensemble ($Pc_{n+1}$). These cell must meet two conditions: i) that they are higher than the local elevation threshold identified with the 11 pixel kernel, and ii) that their distance to the nearest cell in the final scarp ensemble is greater than their distance to platform cells from previous iterations. The first condition is simply to ensure the platform is indeed a low relief surface, and the second is to ensure the iterative process fills the platform away from the scarps. The second condition is also necessary to ensure the platform filling process does not cross scarps. This iterative process is repeated until $n$ reaches an arbitrary value of 100, found to be sufficient to fill the entirety of the platform surface area for our sites.

This process results in platforms surfaces that are spatially continuous, but in some instances sections of the tidal flat with relatively high elevations may also have been identified as marsh platforms. These areas are lower than marsh platforms by the height of the scarp separating them. We filter these cells by

using the elevation properties of the entire DEM. A number of authors have shown that there is a gap in the probability distribution of elevations in intertidal landscapes that separates the majority of tidal flats from the majority of marsh platforms in micro-tidal environments (e.g., Carniello et al., 2009; Defina et al., 2007; Fagherazzi et al., 2006). Such a separation, demonstrated by the decrease in probability between the grey and blue surfaces in Fig. 2.5, is also observed in our meso- and macro-tidal sites, including mega-tidal environments such as the Parrett estuary (Fig. 2.9). We search for this separation using the probability distribution of elevation, $pdf(z)$ of all cells $Pc_n$, divided in 100 elevations bins. We determine that the most frequent elevation bin $z_{max(pdf(z))}$ is the most likely to contain cells correctly assigned to the platform ensemble, as the low relief of marsh platforms is expected to produce a local mode in the elevation distribution. This selection process is sensitive to the choice of the area of interest, which for optimal results should not include less than $\approx 50\%$ of marsh surface area. Therefore, only elevations lower than $z_{max(pdf(z))}$ may contain cells misidentified as marsh platforms.

We then must identify which cells from the population of cells lower than $z_{max(pdf(z))}$ form part of the platform, and which do not. To do this, we truncate low elevations that have a low probability (red curves in Fig. 2.5), to remove the long tail of low elevations from our initial platform identification. We take the probability distribution of the elevation of the remaining platform cells and calculate the mean probability $\bar{pdf}$ (i.e., we average the probability from the 100 bins). We then search for $rz_{thresh}$ consecutive elevation bins that lie below the elevation of the maximum probability elevation that have lower probabilities than this average. The reason we use consecutive bins is that we do not want the minimum elevation to be determined by a single low probability elevation that has spuriously arisen from the binning process. Once we find $rz_{thresh}$ consecutive elevation bins meeting these criteria we remove all cells lower and including the highest cell that lies within the $rz_{thresh}$ consecutive bins. We optimize the parameter $rz_{thresh}$ below.

Having eliminated these low elevation, low probability cells, we also mark all

cells higher than $z_{max(f(z))}$ as platform cells. This may still leave out pools and pans and platform edges remain jagged. Our final procedure aims to eliminate these artifacts using the following procedure: for a given value of the order $n$, we search in the ensemble of $Pc_n$ cells for cells that are surrounded by more than 6 $Pc$ cells of any order within a $K_3$ kernel. The 2 or less empty cells in $K_3$ are then attributed the order $n$-1. By iterating through values of $n$, starting with the order

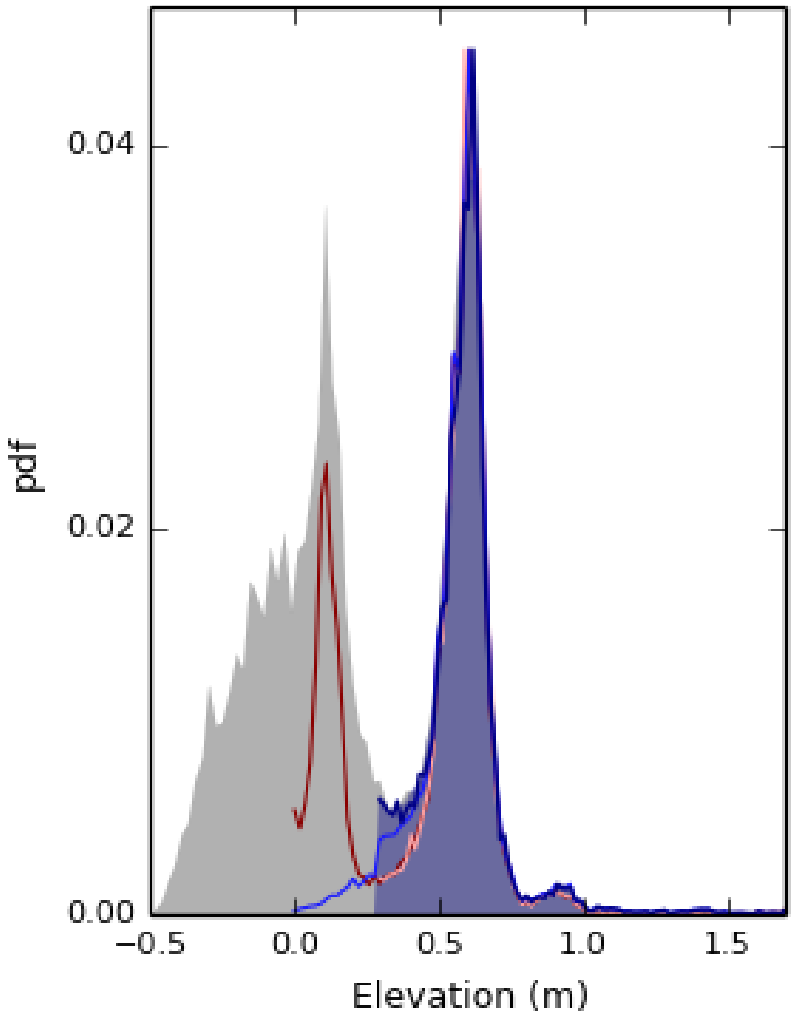


**Figure 2.5:** Diagram describing the elimination of the tail of the elevation probability distribution function for site S1. The grey filled surface is the pdf of elevation for the original DEM. The dark red line is the pdf of elevation of the platform after the dispersion process. The orange line is the pdf of elevation of the platform after truncation of the tail of the distribution. The blue line is the pdf of elevation of the platform after filling pools and jagged outlines and after the addition of scarps in the platform ensemble. The dark blue line, associated to the blue filled surface, is the pdf of elevation for the final platform, after the tail of its distribution is truncated a second time. All distributions in this plot are forced to display the same maximum for clarity.

100 and finishing with the order 2, we progressively fill pools and jagged borders of the platform (Fig. 2.6a). Choosing 6 as the minimal number of platforms cells in each $K_3$ necessary to execute this "reverse filling" procedure, we ensure that no headlands are generated. We then integrate scarp cells that are connected to platform cells into the platform ensemble with an order greater than 100. We then repeat the "reverse filling" process (Fig. 2.6b) and execute low-elevation elimination procedure (See blue curves in Fig. 2.5) to obtain the final platform ensemble.

### 2.2.5 Performance metrics

In order to evaluate the performance of the TIP method, we compare its outputs to manually digitised platforms for all of our test sites (step 7 in Fig. 2.1). For each grid cell in the detected (automatically processed) and the reference (manually digitised) outputs, we assign the boolean value True to the marsh platform and False to the tidal flat. The results are classified as follows: true positives correspond to matching True cells in the tested and reference outputs, true negatives to matching False cells, false positives to True cells in the tested output that are False in the reference output, and false negatives to False cells in the tested output that are True in the reference output. The performance of the method is then evaluated using three metrics based on the numbers of true positive ($TP$), true negative ($TN$), false positive ($FP$), and false negative ($FN$) cells respectively. The accuracy $Acc$ (Fawcett, 2006) describes the likelihood of cells in the tested raster corresponding to the reference raster:

$$Acc = \frac{TP + TN}{TP + TN + FP + FN} \tag{2.6}$$

We also test the performance of the method by reporting two other metrics: the precision, $Pre$, and the sensitivity, $Sen$ (Fawcett, 2006). The precision represents the likelihood of the tested raster overestimating the positives compared to the reference:

$$Pre = \frac{TP}{TP + FP} \tag{2.7}$$

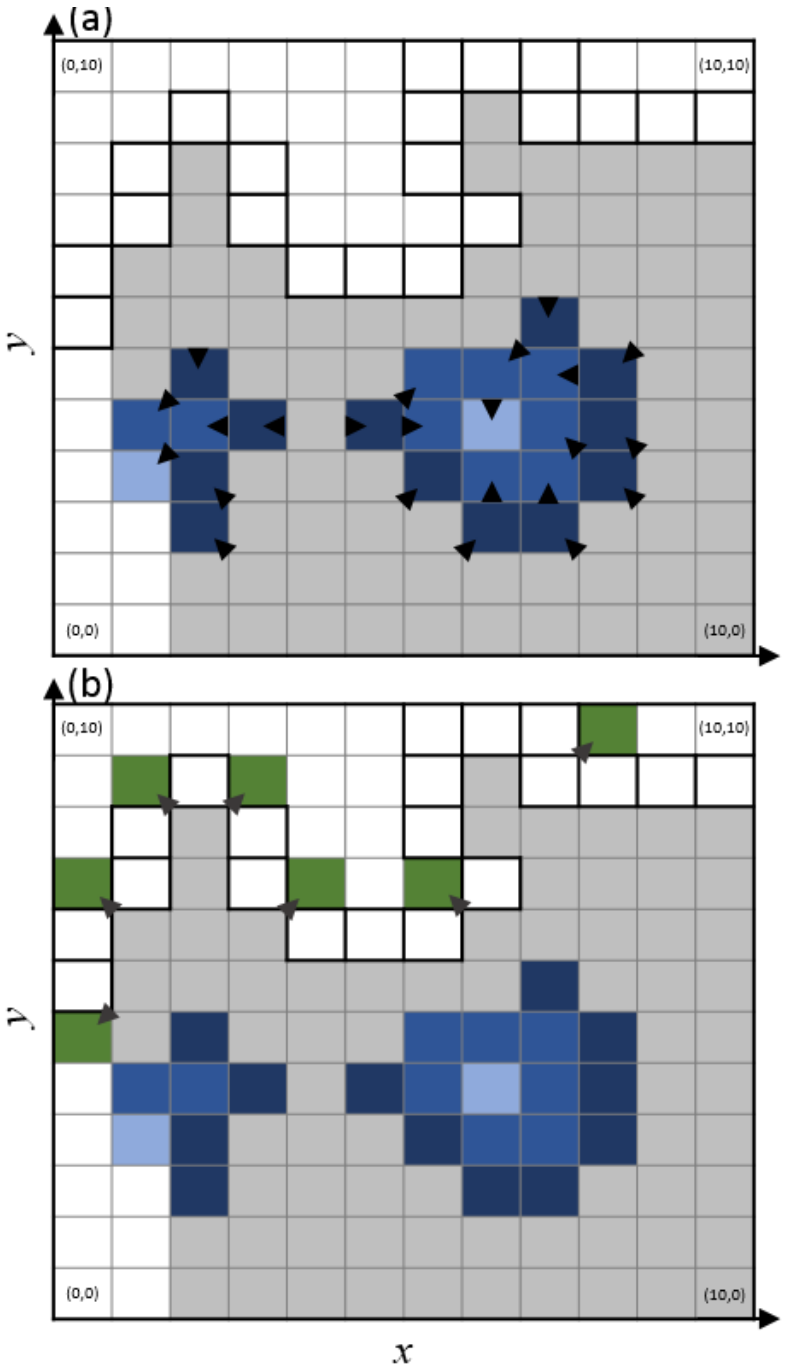


**Figure 2.6:** Schematic example of the reverse platform filling process. a. Step 5.1: Filling of empty cells adjacent to $Pc_n$ cells (grey, dark blue and blue cells) with and order *n-1* (dark blue, blue and light blue cells); b. Step 5.2: Filling of empty cells adjacent to $Pc_n$ cells (grey cells) with and order *n-1* (green cells) when scarp cells (black outlines) are included in the platform ensemble. The arrows indicate the dispersion pattern.

Conversely, the sensitivity $Sen$, represents the likelihood of the tested raster missing positives compared to the reference:

$$Sen = \frac{TP}{TP + FN} \tag{2.8}$$

If the results of the TIP method perfectly matched that of the manual digitisation, all three metrics would have a value of 1.

## 2.3 Results

### 2.3.1 Parameter optimisation

The TIP method contains three user-defined, non-dimensional parameters occurring in sequence during the detection process. The first parameter, $Sp_{thresh}$, determines the threshold value ${P^*}_{th}$ for the high-pass filter leading to the selection of the initial search space, shown in Fig. 2.3a. The parameter $Sp_{thresh}$ influences the solution of the equation $\frac{df}{dP^*} = Sp_{thresh}$. The second parameter, $ZK_{thresh}$ determines the condition on the refinement of existing scarps in the high-pass filter $max(ZK_9) > ZK_{thresh} \times q_{75}$, schematically represented in Fig. 2.4. The third parameter, $rz_{thresh}$ is used in the platform dispersion process to determine which percentage of the elevation range below $\bar{pdf}$ is maintained in the platform ensemble. In this study, these parameters were set to maximize the average accuracy $\bar{Acc}$ across test sites (Fig. 2.7): the optimized values ($Sp_{thresh}$=-2.0, $ZK_{thresh}$=0.85, $rz_{thresh}$=8) were used for the subsequent performance analysis. Users may modify these parameters as directed in the code documentation to better fit their study sites.

### 2.3.2 Validation and applicability

Figure 2.8 shows the performance of the TIP method for all six sites, discriminating between the use or absence of a Wiener filter and evaluating how the resolution of the topographic data influences the results. We also provide the full performance metrics in Appendix A (Tables 6.1 to 6.6). We find the method's

accuracy to be on average 94.8% at the data's native resolution of 1 m, whether we apply a Wiener filter (Fig. 2.8a2) or not (Fig. 2.8a1). Degrading the DEM resolution still results in accuracy of above 90%, although it decreases to around 60% for microtidal site S1 at a resolution of 3 m. Applying a Wiener filter to the data causes a slight decrease in accuracy and precision (Fig. 2.8b2), but an increase in sensitivity (compare Fig. 2.8c2 to Fig. 2.8c1). Examining the results

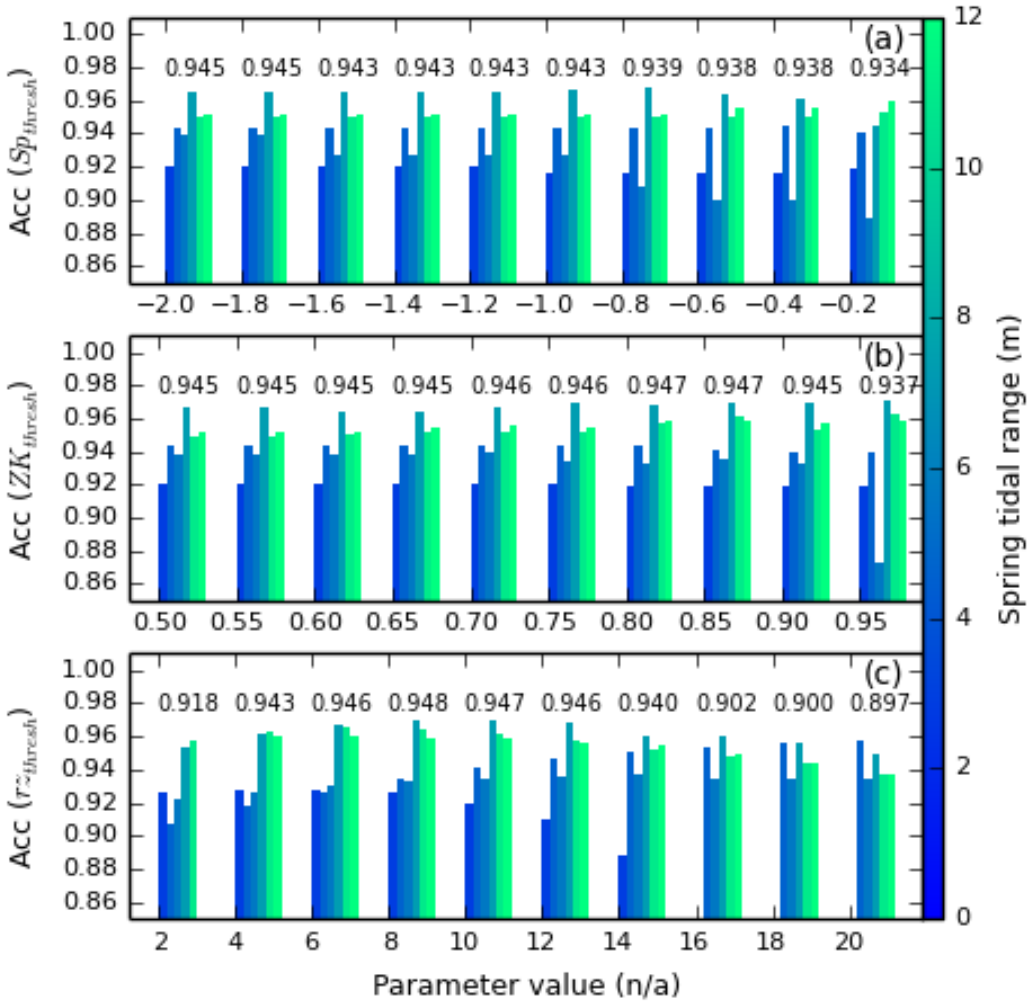


**Figure 2.7:** Accuracy charts used to optimize the three user-defined parameters for the six test sites, each site being coloured by spring tidal range, with no filter. Each group of bars represents the accuracy for one parameter value when applied to all the test sites. The mean accuracy appears above each group; a. Accuracy for the parameter $Sp_{thresh}$. The retained value for $Sp_{thresh}$ is -2.0; b. Accuracy for the parameter $Zk_{thresh}$. The retained value for $Zk_{thresh}$ is 0.85; c. Accuracy for the parameter $rz_{thresh}$. The retained value for $rz_{thresh}$ is 8.

of all of the metrics shows that resolution degradation up to 3 m, well as the use of a Wiener filter, primarily causes an increase in false positives and therefore an overestimation in the extent of the marsh platform. For sites S2 to S6, we observe little change in performance metrics with resolution degradation up to 3 m.

We suggest that all three performance metrics should be used when optimising the TIP method for a study site, as no combination of two metrics provides

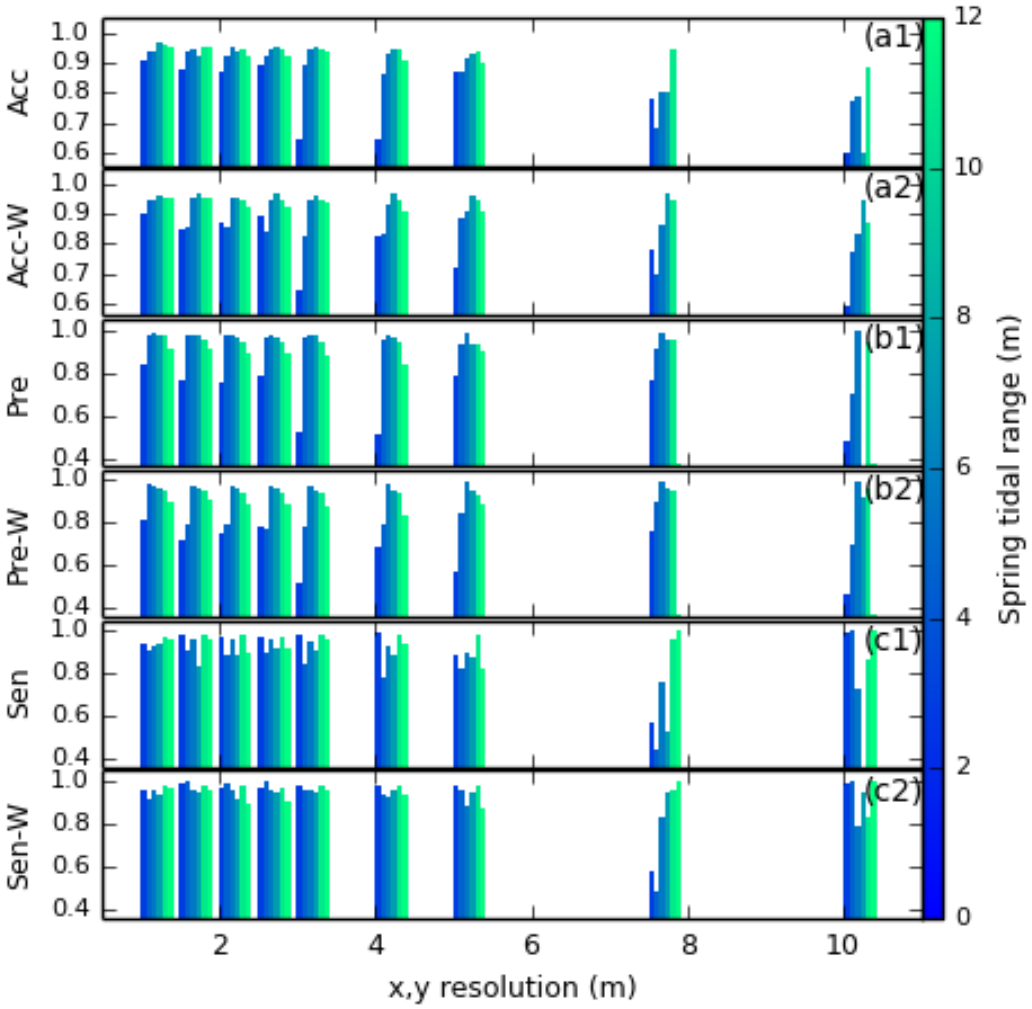


**Figure 2.8:** Performance of the platform detection method for all sites, coloured according to their spring tidal range; a1. Accuracy of the method when no filter is used; a2. Accuracy of the method when using a Wiener filter; b1. Precision of the method when no filter is used; b2. Precision of the method when using a Wiener filter; c1. Sensitivity of the method when no filter is used; c2. Sensitivity of the method when using a Wiener filter.

comprehensive insight into TIP uncertainties. Furthermore, although average accuracies remain above 85% for resolutions of 4 to 5 m, we recommend caution when using the method at these resolutions, particularly in micro- to meso-tidal settings where features may be smoothed beyond the method's recognition capacities. Use of the TIP method is not recommended for resolutions coarser than 5 m due to the very low accuracies observed for our test sites, making this method adapted to high-resolution data sources such as airborne lidar or photogrammetry.

## 2.4 Discussion

### 2.4.1 Influence of site morphology on the TIP method

In order to examine the performance of the method in sites with varying morphological characteristics, we compare the probability distribution functions (pdf) of elevation from the digitised platforms to the platforms detected using the TIP method (Fig. 2.9). Figures 2.9a to f show that a left-hand tail is present for the digitised platforms, whereas platforms detected by TIP show a sharp decrease in the pdf at these elevations: this indicates the presence of more false negatives than false positives at the lowest elevations of the marsh platform. This suggests that the TIP method excludes more features with a low elevation than manual digitisation, which correspond to tidal creeks and sunken terraces at the edge of the platform. However, this does not imply that the TIP method cannot identify multiple terraces within a platform, as shown by the multiple local maxima in the detected pdf in Fig. 2.9d and f.

We also show maps of the TIP method's performance for each test site in order to explore this spatial variability in feature detection (Fig. 2.10). For instance, the dominance of false positives over false negatives in Fig. 2.10a (site S1) suggests that the method tends to overestimate the extent of jagged, low-relief marsh platforms, which are common in the sheltered microtidal bays characterising this site. This is the product of two factors: (i) identified scarps are not always complete in micro-tidal environments, as scarps tend to be small and therefore liable to elimination by our elevation threshold (see Fig. 2.4, step 4.5); and (ii)

1160 the reverse dispersion process (see Fig. 2.6) is then likely to encroach on the tidal
1161 flat. This phenomenon is exacerbated by coarse grids or de-noised datasets (e.g.
1162 Fig. 2.8a1 and a2) where high slope values are smoothed and filtered out in the

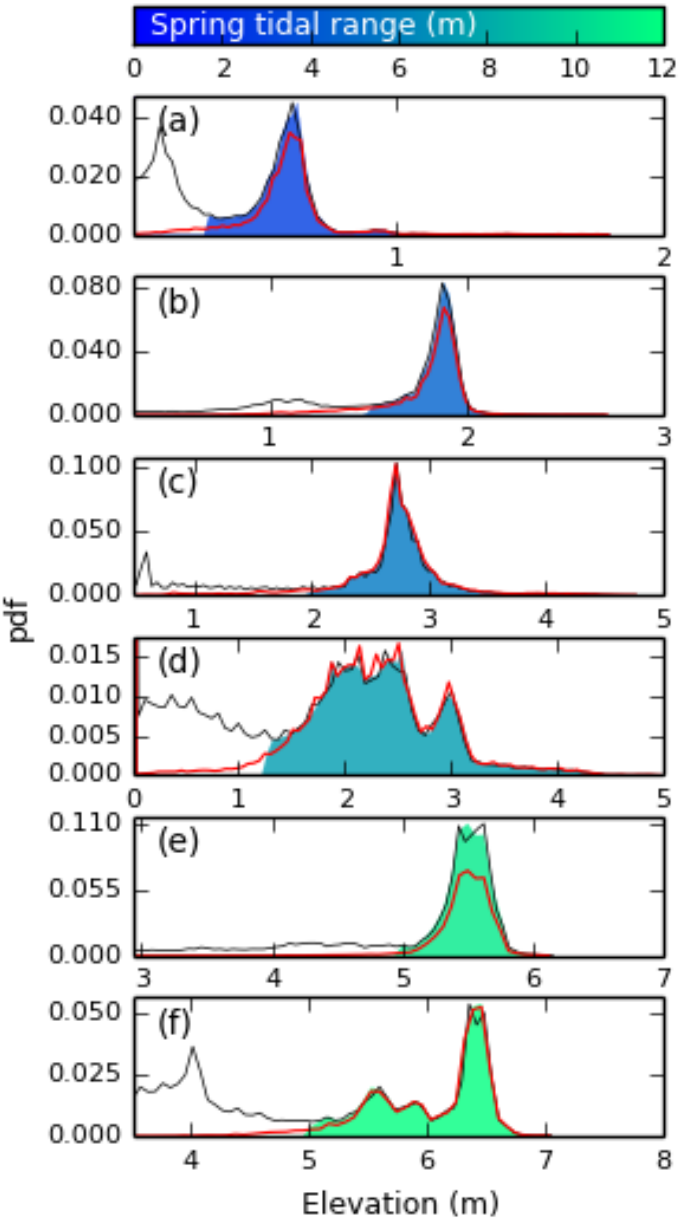


**Figure 2.9:** Elevation distribution functions for sites S1 to S6 (plots a. to f. respectively). The red line corresponds to the elevation distribution for the reference rasters. The filled area corresponds to the elevation distribution of the automatically processed rasters, coloured according to their spring tidal range. The grey line represents the elevation distribution of the original DEM, with frequency maxima set to match those of the automatically processed rasters so as to nullify the effect of empty cells.

scarp detection process. In our meso- to macro-tidal sites S2 to S4 (Fig. 2.10b-d), the method results in false negatives corresponding to the location of tidal creeks. These creeks were purposefully included in the marsh platform during the digitisation process, but were identified as part of the tidal flat by the TIP method. This result indicates that our method often characterises creek banks as platform scarps due to their morphological similarity.

Other coastal landforms may generate false positives, as seen in Fig. 2.10 c-f. In these cases, the position of the scarp line differs between the digitised and the TIP-detected platforms due to elevated portions of the tidal flat being adjacent to the marsh platform. This suggests that some areas of the tidal flat are topographically closer to the platform than to the rest of the tidal flat and may represent areas likely to be colonised by pioneer vegetation, even though they might not be vegetated at the time of data acquisition. Conversely, sunken platforms, areas of recently stripped vegetation or fallen blocks that are not delineated by scarps may generate false negatives, as seen in the central area of Fig. 2.10e.

Although the TIP method was tested using salt marshes located in England, the scarp and platform association is a common feature to many salt marshes around the world, making the TIP method applicable over a wide range of geographic areas. Furthermore, the TIP method does not require the precise topography of the platform to function, making it relatively insensitive to unequal removal of vegetation between different DEM sources. The presence of vegetation, when it is not stripped or grazed, induces positive errors in the DEM, which counter-intuitively may be useful when applying the TIP method, as this artificially increases the platform height and therefore the scarp slope. Examples of sites outside the United Kingdom are included in Fig. 6.2, and were selected to demonstrate the versatility but also the limits of the TIP method.

### 2.4.2 Future developments

As discussed in Section 2.4.1, the TIP method currently excludes tidal creeks from the marsh platform, leading to discrepancies when compared to manual digitisation. Therefore, we would expect the TIP method to underperform on

1193

1194

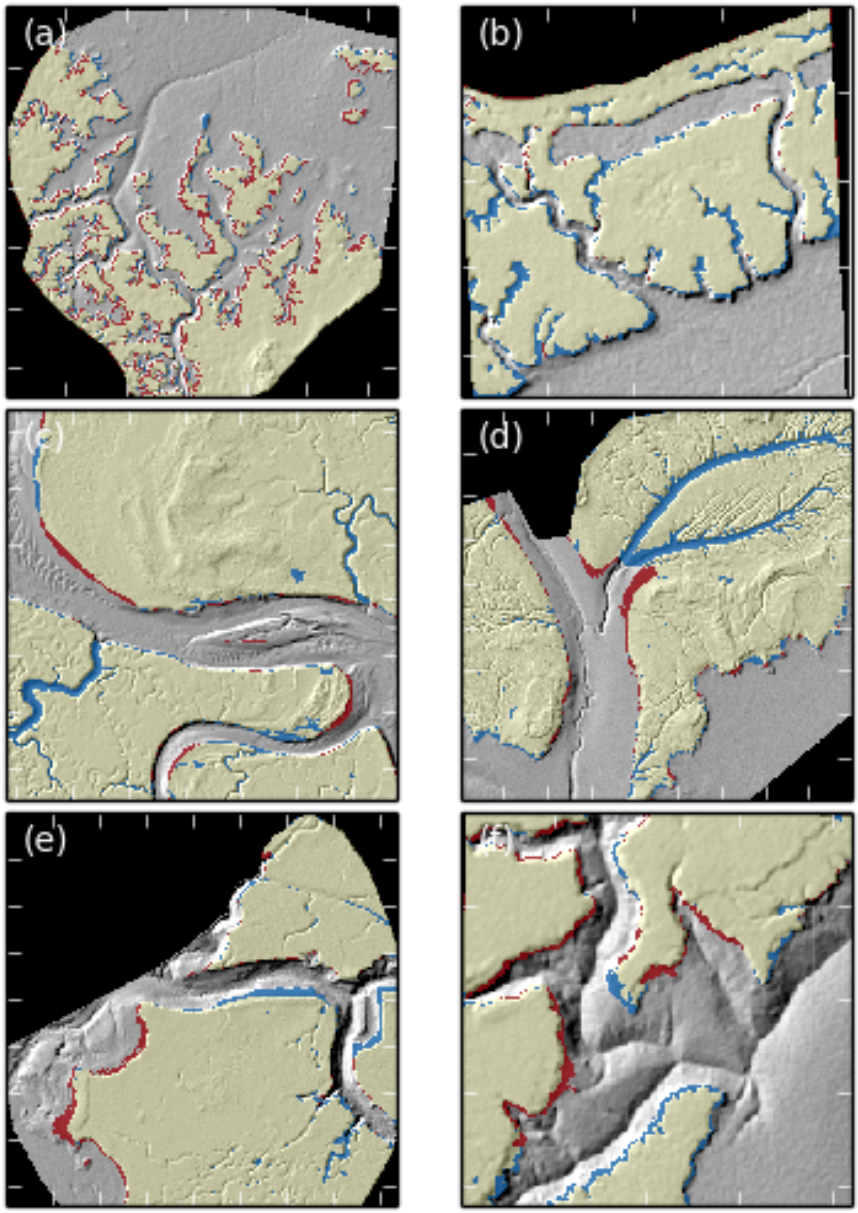


**Figure 2.10:** Rasters comparing digitised versus extracted marsh platforms superimposed on hillshade data for all six sites after detection with no Wiener filtering. Black areas are outside of the detection domain and contain no data. Yellow areas correspond to True Positives (TP) and transparent areas to True Negatives (TN). Red areas correspond to False Positives (FP) and blue areas to False Negatives (FN). Ticks are placed 50m apart. The sites are numbered as follows: a: Shell Bay, Dorset; b: Stour Estuary, Suffolk; c: Stiffkey, Norfolk; d: Medway Estuary,Kent; e: Jenny Brown's Point, Lancashire; f: Parrett Estuary, Somerset.

the marsh platform that were visible on the DEM (at 1 $m$ pixel size) were digitised. We then calculate the total length of tidal creeks included in the digitised platform divided by the platform surface area. We refer to this quantity as the Dissection Index (DI). In Fig.2.11, we examine the capacity of the TIP-method to determine the area and perimeter of marsh platforms according to their dissection index. We find that for all test sites, TIP-detected area remains within 10% of the digitised area, whereas TIP-detected perimeter increases steadily with Dissection Index, confirming that the exclusion of tidal creeks by the TIP method is consistently stricter than by digitisation. However, neither the TIP method nor manual digitisation offer an optimal solution to detect tidal creeks. For a comprehensive analysis of marsh platforms, we recommend that objective platform detection be used in conjunction with objective creek detection methods such as those developed by Fagherazzi et al., 1999 and Liu et al., 2015. Furthermore, future developments of the TIP method will include an objective creek detection method adapted from these publications, as well as channel network extraction methods developed for fluvial channels by Clubb et al., 2014, to ensure that tidal creeks are detected as separate objects.

The morphological characteristics of prograding marshes are different from those of established platforms: consequently, vegetation patches and pioneer zones are not the object of the TIP method. Specifically, prograding margins and vegetation patches tend to have a relief and slope that are close to those of the tidal flat, making their outlines invisible to the scarp routing process. The combined absence of scarps and low relief of prograding marshes then interfere with the 20 cm leeway included in the platform filling process and cause an excess of false positives. Users may reduce this leeway to improve accuracy (see Fig. 6.2b1), but we discourage the use of the TIP method to identify vegetation patches and prograding margins. However, these dynamic features are the most active in progradation and retreat processes and would benefit from reproducible monitoring methods. Future research may build on the works of Balke et al., 2012 to determine characteristic morphologies of prograding marshes, thus providing the necessary groundwork to enable reproducible monitoring.

### 2.4.3 Potential for monitoring

As well as providing us with the ability to automate the delineation and analysis of marsh platforms across multiple sites, our method also allows the objective detection of change in marsh extent through time, with important implications for habitat monitoring or carbon storage evaluation. We test the capacity of the TIP method to monitor temporal change through the example of site S6, which

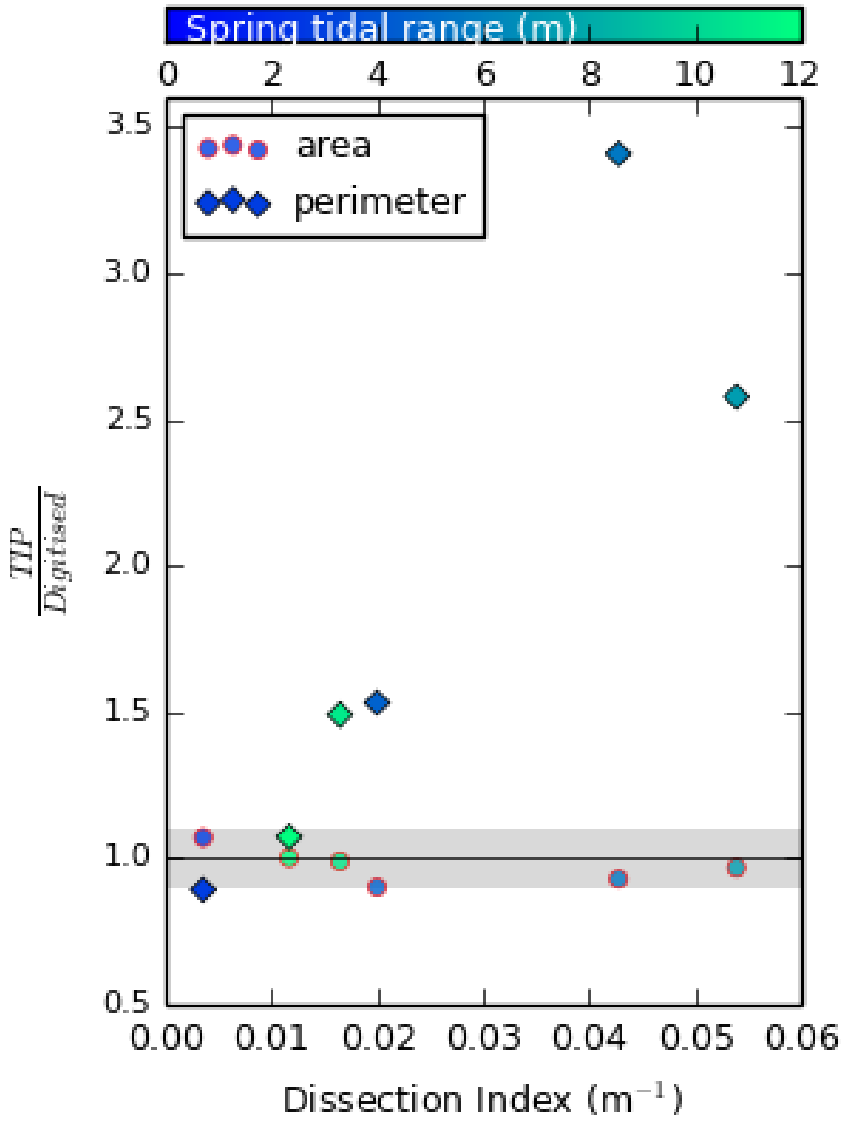


**Figure 2.11:** Ratio of TIP over digitised area (circles, red outlines) and perimeter (diamonds, black outlines) for sites S1 to S6 at the native resolution of 1 m, with no Wiener filtering, as a function of dissection index. Here, dissection index is defined as the ratio of the total length of tidal channels within the digitised marsh platform over the area of the digitised marsh platform, and is not bounded by drainage basins. The greyed area corresponds to a 10% buffer around the line of equation $y=1$.

was affected by heavy rainfall in the summer of 2007, resulting in high discharge in rivers such as the Parrett. 1 m lidar data distributed by the Environment Agency shows that between March and October 2007 the North-Eastern corner of site S6 underwent significant erosion. Blue pixels indicating loss of elevation (between March and October) in Fig. 2.12a bear the characteristic shape of slope failures and intersect both the automatically- and manually-detected platform outline of March 2007, showing that the October platform outline is further inland.

This retreat of the marsh platform is observed both by the objectively classified (Fig. 2.12b) and the manually digitised platforms (Fig. 2.12c). However, whereas the digitisation effort focuses on the large bank failures, the TIP method also detects small changes in the DEM at the platform margin (visible in Fig. 2.12a and b), and may detect them as changes in marsh platform extent. Consequently, despite a close correspondence between TIP-determined marsh outlines and digitised outlines (Fig. 2.12a) near the bank failures, the digitised volume loss is only 81% of the objectively detected volume loss. Pioneer zones, characterized by shallow slopes and rapid, uneven elevation changes, are also likely to generate small topographic differences between the DEMs.

## 2.5 Conclusions

In this study we have presented a novel method which uses the topographic signature of salt marsh platforms to determine their seaward extent on high resolution DEMs. By combining non-dimensional search parameters and empirical calibration, it separates marsh platforms from tidal flats with over 90% accuracy for source data of up to 3 m in grid resolution, a result sufficient to allow quantitative morphology analyses and monitoring, particularly for eroding marshes where scarps are clearly defined. Independence from environmental variables means that our method can be used to complement spectral data for identifying plant types, to better understand feedbacks between sedimentation, deposition and biomass. We tested our method on six sites with a wide range of spring tidal ranges and found that tidal range has no significant impact on the detection accuracy up to

a 3 m pixel size. Furthermore, the presence of algae, kelp or duckweed as well as varying vegetation reflectance properties, which may induce specific calibrations with spectral methods (Morris et al., 2005), do not affect our results (barring mounds of stranded algae large enough to affect topography). Although we did not test the performance of the TIP method on DEM resolutions finer than 1

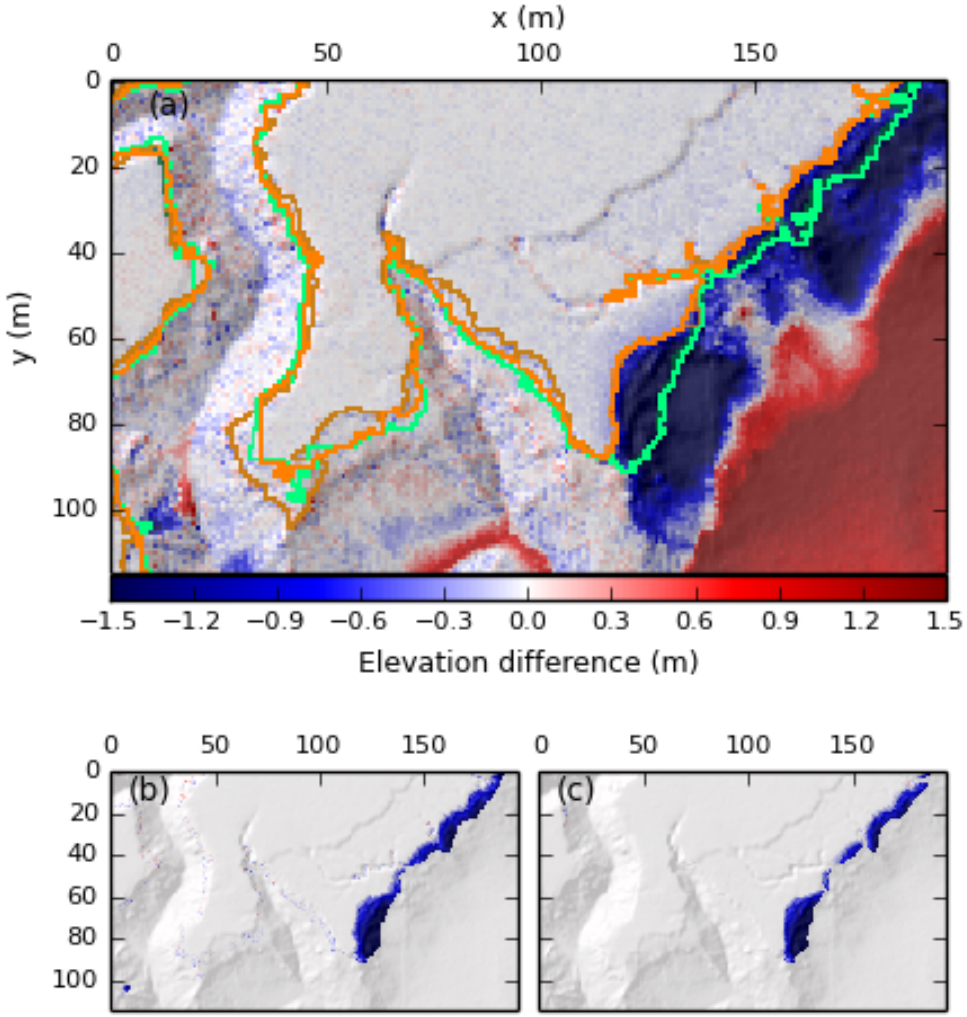


**Figure 2.12:** a. Comparison of marsh areas for a portion of S6 between March (green lines) and October (orange lines) 2007, surperimposed on hillshade data of October 2007. Bright lines correspond to the automatically detected marsh boundary, whereas faded lines correspond to digitised marsh boundaries. Green faded lines are mostly covered by bright green lines. Coloured surfaces indicate elevation gain or loss between March and October 2007; b. Map of elevation loss and gain associated to marsh platform evolution, according to the TIP method. Total volume loss is 1188 $m^3$; c. Map of elevation loss and gain associated to marsh platform evolution, according to manual digitisation. Total volume loss is 966 $m^3$.

m, the option of applying a Wiener filter to reduce DEM noise is available to accommodate DEMs generated from unclassified point clouds, which have higher surface roughness. When combined with creek detection methods, we expect the performance of the TIP method to improve with fewer false negatives. This would also allow the discrimination of channel evolution within the marsh platform and on the tidal flat, allowing us to simultaneously explore the development of marsh platforms and tidal creeks (D'Alpaos et al., 2007b, 2010) in sites with strong tidal forcing.

Furthermore, the unsupervised detection of marsh platforms from their topography alone reduces the computational cost of topographic analysis compared to spectral studies. This promotes the consideration of salt marshes as topographic objects as well as ecological systems, facilitating holistic, data-driven studies on salt marsh eco-geomorphic responses, and testing existing models of eco-geomorphic feedback (e.g. Fagherazzi et al., 2012). It also encourages us to think of the topographic object separately from the ecological system: mismatches in their respective boundaries may therefore be used to investigate accretion processes and pioneer zone growth in continuation with the works of Balke et al., 2014 and Hu et al., 2015. The examination of such processes at smaller scales, such as those obtained with terrestrial lidar stations, may also reveal characteristic accretion patterns (Balke et al., 2012) which topographic methods may objectively detect. Other developments of this method may, in time, enable the detection of the spatial extent of other ecosystems, such as riparian wetlands and mangrove limits.

# Chapter 3

# Platform elevation and sediment supply

The work presented in this chapter was published in Frontiers:

Goodwin GCH and Mudd SM (2019) High Platform Elevations Highlight the Role of Storms and Spring Tides in Salt Marsh Evolution. Front. Environ. Sci. 7:62. doi: 10.3389/fenvs.2019.00062

This research was conducted in collaboration with the named co-authors, who helped to edit the final manuscript and contributed to software development. I wrote the topographic analysis algorithms, performed the analyses, created the figures, and wrote the manuscript.

# List of Abbreviations

| Abbreviation | Meaning |
|---|---|
| ADCP | Acoustic Doppler Current Profiler |
| BODC | British Oceanographic Data Centre |
| BSS | Bottom Shear Stress |
| D-GNSS | Differential Global Navigation Satellite System |
| DEM | Digital Elevation Model |
| DSM | Digital Surface Model |
| DTM | Digital Terrain Model |
| GESLA | Global Extreme Sea Level Analysis |
| MHT | Mean High Tide |
| MHWS | Mean High Water Spring |
| MLT | Mean Low Tide |
| MSL | Mean Sea Level |
| MTR | Mean Tidal Range |
| NDVI | Normalised Difference Vegetation Index |
| NOAA | National Oceanigraphic and Atmospheric Administration |
| OHHT | Observed Highest High Tide |
| RMSE | Root Mean Square Error |
| RSLR | Relative Sea Level Rise |
| SET | Surface Elevation Table |
| TIP | Topographic Identification of Platforms |
| TSM | Total Suspended Matter |
| UK | United Kingdom |

**Table 3.1:** Abbreviations used in this chapter

# List of Notations

| Notation | Meaning |
|---|---|
| $\Delta t$ | a short duration of time [T] |
| $\Delta z$ | a small variation in elevation [L] |
| $Q_{dep,\Delta t}z$ | Deposition fluxes over $\Delta t$ [L] |
| $Q_{org,\Delta t}$ | Organic belowground production fluxes over $\Delta t$ [L] |
| $Q_{eros,\Delta t}$ | Erosion fluxes over $\Delta t$ [L] |
| $R_{\Delta t}$ | Change in sea level elevation over $\Delta t$ [L] |
| $T$ | Tidal cycle period [$T^{-1}$] |
| $w_s$ | Terminal Stokes settling velocity [$L.T^{-1}$] |
| $D_{50}$ | Median grain diameter [L] |
| $\rho w$ | Volumetric mass of water [$M.L^{-3}$] |
| $\rho s$ | Volumetric mass of sediment particles [$M.L^{-3}$] |
| $\rho b$ | Bulk density of deposited sediment [$\varnothing$] |
| $\lambda$ | compaction factor [$\varnothing$] |
| $\mu$ | Dynamic viscosity of water [$M.T.L^{-1}$] |
| $C$ | Depth-averaged suspended sediment concentration [$\varnothing$] |
| $C_0$ | Forcing depth-averaged suspended sediment concentration [$\varnothing$] |
| $D$ | water depth [L] |
| $H$ | Sinusoidal tidal half-amplitude [L] |
| $N$ | Number of tidal cycles [$\varnothing$] |
| $Z_{min}$ | Minimum pixel elevation [L] |
| $Z_{max}$ | Maximum pixel elevation [L] |
| $z_{eq}$ | Equilibrium elevation value [L] |
| $k$ | Sum of deposition and organic production [L] |
| $z^*$ | Normalised elevation within the tidal frame [$\varnothing$] |
| $z_0$ | Starting elevation [L] |

**Table 3.2:** Notations used in this chapter

## 3.1 Abstract

We combine sea level records and repeat lidar surveys at 8 sites in the United Kingdom and the United States to explore controls on marsh accretion. We compare marsh elevations relative to sea level as well as lidar-derived marsh accretion rates to simple 0-dimensional settling simulations in order to explore constraints on suspended sediment concentration and particle size. We find that the marsh platforms examined occupy a narrow range of elevations in the upper tidal frame, situated between Mean High Tide $MHT$ and the Observed Highest High Tide $OHHT$. Under sinusoidal tidal forcing, common in marsh accretion models, marshes at these elevations are never inundated, highlighting the inadequacy of sinusoidal forcing in numerical models of salt marshes. Forcing the model with year-long tidal records, deposition rates follow hyperbolic contour lines when expressed as a function of sediment concentration and median grain size. We also observe that when using a median sediment grain size $D_{50} = 50\ \mu m$ and sediment concentrations derived from satellite data, modeled deposition rates are much lower than when using field data. We find that the deposition of coarse, concentrated sediment is necessary for platforms in the upper tidal frame to withstand sea level rise, suggesting a strong dependance on infrequent high-deposition events. This is particularly true for marshes that are very high in the tidal frame, making accretion increasingly storm-driven as marsh platforms gain elevation. Finally, we reflect on the capacity of marshes to regenerate after erosion events within a context of changing sediment supply conditions.

## 3.2 Introduction

The issue of salt marsh elevation change is one that preoccupies coastal geomorphologists and land managers alike. Often measured relative to mean sea level, elevation determines the frequency and depth of flooding of the marsh surface, both from astronomic tides and storms (Cahoon and Reed, 1995). Flooding frequency in turn determines salinity, which influences the type and productivity of the plant communities on the marsh (Belliard et al., 2017; Pennings et al.,

2003; Silvestri et al., 2005), and therefore underpins the functioning of the entire ecosystem. Coastal marshes around the world face accelerating rates of sea level rise (Ipcc, 2014). Decreased sediment supply due to anthropogenic activities is set to accentuate the pressure of sea level rise on coastal wetlands, particularly in deltaic systems (Syvitski et al., 2009). Furthermore, subsidence caused by water, gas and oil extraction add to the existing stress on wetland ecosystems (Kennish, 2001). Factors that influence marsh growth are less favorable now than in the past (Kirwan et al., 2011), and so determining if salt marshes will maintain their elevation within the tidal frame is an intensively studied research question(Crosby et al., 2016; Kirwan et al., 2016a; Lerberg, 2016).

One approach to explore the future evolution of salt marsh elevation is numerical modeling, and several models of salt marshes have been created over the past decades to address the question (Fagherazzi et al., 2012). Models of salt marsh elevation change may be divided into point-based models (0-D), profile models (1-D) or spatially distributed models (2-D). Whereas 2-D models are effective at predicting the evolution of topographic or ecological patterns on the marsh surface (Belliard et al., 2016; D'Alpaos et al., 2005; Temmerman et al., 2007), their high computational cost often precludes their use for long-term simulations or large regions. 1-D models are often used to represent the marsh scarp and simulate salt marsh and mudflat interactions (Mariotti and Fagherazzi, 2010) and lateral erosion processes (Tonelli et al., 2010).

Contrary to these approaches, 0-D models do not take into account the propagation of hydrodynamic forcing, nor do they account for the spatial heterogeneity of marsh topography. These models often use synthetic elevations, simplified tidal forcings and assume constant suspended sediment concentration and median grain size. With these assumptions, they have been used to explore the response of marshes to various sea level rise scenarios (D'Alpaos et al., 2011) or the variations in vegetation productivity (Marani et al., 2013; Morris et al., 2002; Mudd et al., 2010). More recently, Schuerch et al., 2018 used a 0-D model to assess the potential of salt marshes to adapt to projected sea level rise over the 21st century, assuming that all coastal wetlands occupy the same continuous vertical

space between Mean Sea Level ($MSL$) and Mean High Water Spring ($MHWS$). However, due to the scarcity of local sediment size and concentration data, few studies using 0-D models consider variability in sediment supply.

Simulations of salt marsh change may be compared with observations of salt marsh elevation change, measured in the field or via remote sensing. Sediment Elevation Tables (SET) allow for highly accurate measurements (Anisfeld et al., 2016; Cahoon, 2015), but lack the spatial coverage provided by less accurate lidar surveys (Nolte et al., 2013; Webb et al., 2013). While they are affected by false ground returns due to vegetation (Hladik and Alber, 2012a; Rogers et al., 2016a, 2018; Schmid et al., 2011), their large footprint enables lidar surveys to account for the variability of salt marsh elevation in a way that would be too costly to implement on the field.

In this contribution, we use lidar-derived marsh platform elevations and local tidal records to simulate yearly settling fluxes for 8 salt marshes in the United Kingdom and the United States of America. We then compare the calculated settling rates under various sediment size and concentration conditions to various rates of sea level rise. Finally, we investigate the potential of pioneer platforms for rapid accretion. Our aim is not to perfectly simulate sediment settling on these marshes, but rather to use observed marsh elevations and tide records to constrain some of the conditions of sedimentation.

## 3.3 Materials and methods

### 3.3.1 Numerical framework for settling fluxes

Following Exner's equation, 0-dimensional numerical models describe the change in elevation of a point on the marsh surface as the sum of deposition and erosion fluxes (D'Alpaos et al., 2011; Kirwan and Temmerman, 2009; Marani et al., 2007, 2013). Over a given period of time $\Delta t$, the average variation of elevation relative to sea level $\Delta z$ is the sum of positive deposition fluxes $Q_{dep,\Delta t}$ and belowground organic production $Q_{org,\Delta t}$, and negative erosion fluxes $Q_{eros,\Delta t}$ on the platform surface, minus the relative sea level rise $R_{\Delta t}$, which for the purposes of this study

includes eustatic sea level variations, isostatic land movements (Shennan and Horton, 2002) and local subsidence, both shallow and deep (Cahoon et al., 2006). If $dt$ is an infinitesimal time period, the change in elevation $dz$ over $dt$ is therefore expressed by equation (3.1):

$$\frac{dz}{dt} = Q_{dep,dt} + Q_{org,dt} + Q_{eros,dt} - R_{dt} \tag{3.1}$$

where it is assumed that $Q_{eros,dt} = 0\ m\ yr^{-1}$, as the dampened currents and waves on elevated platforms are unlikely to erode a vegetated surface (Carniello et al., 2005; Möller et al., 2014).

Deposition fluxes on vegetated surfaces are expressed as the sum of particle settling and capture by stems and leaves. Here, capture fluxes are considered significantly smaller than settling fluxes (Marani et al., 2010; Mudd et al., 2010). Over a tidal cycle of period $T$, we therefore express $Q_{dep,T}$ according to equation (3.2) (D'Alpaos et al., 2011):

$$Q_{dep,T} = \frac{1}{T}\int_T \frac{w_s \cdot C(z,t)}{\rho_b}\,\mathrm{d}t \tag{3.2}$$

$$w_s = \frac{2}{9}\,(\frac{\rho_s - \rho_w}{\mu})\ g\ (\frac{D_{50}}{2})^2 \tag{3.3}$$

where $w_s$ is the terminal settling velocity calculated using Stoke's law for a spherical particle of diameter $D_{50}$ and volumetric mass $\rho_s = 2650\ kg\ m^{-3}$ in unagitated water of volumetric mass $\rho_s = 1000\ kg\ m^{-3}$ and dynamic viscosity $\mu = 0.0010518\ kg\ s\ m^{-1}$. The assumption of low turbulence on the marsh surface implicitly assumes low velocities, as vegetation increases turbulence on the surface (Nepf, 1999). Furthermore, flocculation of muddy sediment (under $50\mu m$ (Wentworth, 1922)) is expected to noticeably reduce settling velocity (Schwarz et al., 2017). We therefore anticipate settling fluxes obtained through this model to overestimate real settling. $\rho_b = \rho_s(1-\lambda)$ is the bulk density where $\lambda = 0.5$ is a parameter accounting for compaction (D'Alpaos et al., 2011; Marani et al., 2010).

The depth-averaged instantaneous suspended sediment concentration $C(z,t)$

is the solution of the first order differential equation (3.4):

$$\frac{d(DC)}{dt} = -w_s \cdot C + \tilde{C} \cdot \frac{dh}{dt} \tag{3.4}$$

with

$$\tilde{C}(z,t) = \begin{cases} C(z,t), & \text{if } \frac{dh}{dt} < 0. \\ C_0, & \text{if } \frac{dh}{dt} \geqslant 0. \end{cases} \tag{3.5}$$

where the instantaneous water depth $D(z,t)$ is the difference between the water level $h(t)$ and the elevation $z(t)$. In equation (3.5), $C(z,t)$ is dependent on flooding conditions during ebb ($\frac{dh}{dt} < 0$), but is forced by the boundary sediment concentration $C_0$ during flood ($\frac{dh}{dt} > 0$). Equation (3.4) is solved for positive values of $D(z,t)$ under the assumption that at any given time $t$, either $\frac{dz}{dt}$ is negligible in front of $\frac{dh}{dt}$ or both are null. The solution of equation (3.4) under these conditions is then:

$$C(z,t) = \begin{cases} C_0 \cdot e^{D(z,t)-D_{max}}, & \text{if } \frac{dh}{dt} < 0. \\ C_0, & \text{if } \frac{dh}{dt} \geqslant 0. \end{cases} \tag{3.6}$$

where $D_{max}$ is the maximum flooded depth for a given tidal cycle. Since dry areas cannot accrete through mineral deposition, we consider $\frac{w_s \cdot C(z,t)}{\rho_b} = 0$ for negative values of $D(z,t)$.

### 3.3.2 Modified forcing and representation of elevations

Due to their exploratory nature, 0-D models seldom represent any particular marsh platform elevation or vegetation association. Likewise, maritime forcing parameters are often synthetic, using a sine wave of amplitude $H = MHT - MSL$ as a tidal signal, and considering the forcing sediment concentration $C_0$ or the median grain size $D_{50}$ as time-invariant (D'Alpaos et al., 2011) (Figure 3.1a.). Figure 3.1b. illustrates the parameters required to force a more realistic model. Such models are usually implemented for a particular marsh platform and calibrated to simulate observed accretion values (e.g. D'Alpaos et al., 2007a;

Temmerman et al., 2007).

We examine the effects of using observed rather than sinusoidal or predicted tidal forcing to simulate the vertical accretion on marsh platforms extracted from lidar topographic data. This approach is implemented in the model by describing the mineral accretion flux over a period $\Delta t$, $Q_{dep,\Delta t}$, as the sum of settling fluxes over each of the $N_{\Delta t}$ tidal cycles in $\Delta t$ (3.7).

$$Q_{total,\Delta t} = \sum_{i=0}^{i=N_{\Delta t}} Q_{dep,T_i} \tag{3.7}$$

We initially consider fixed values for $C_0$ and $D_{50}$, as detailed in section 3.3.3. Our aim is to determine whether these parameters can be used to explain observed

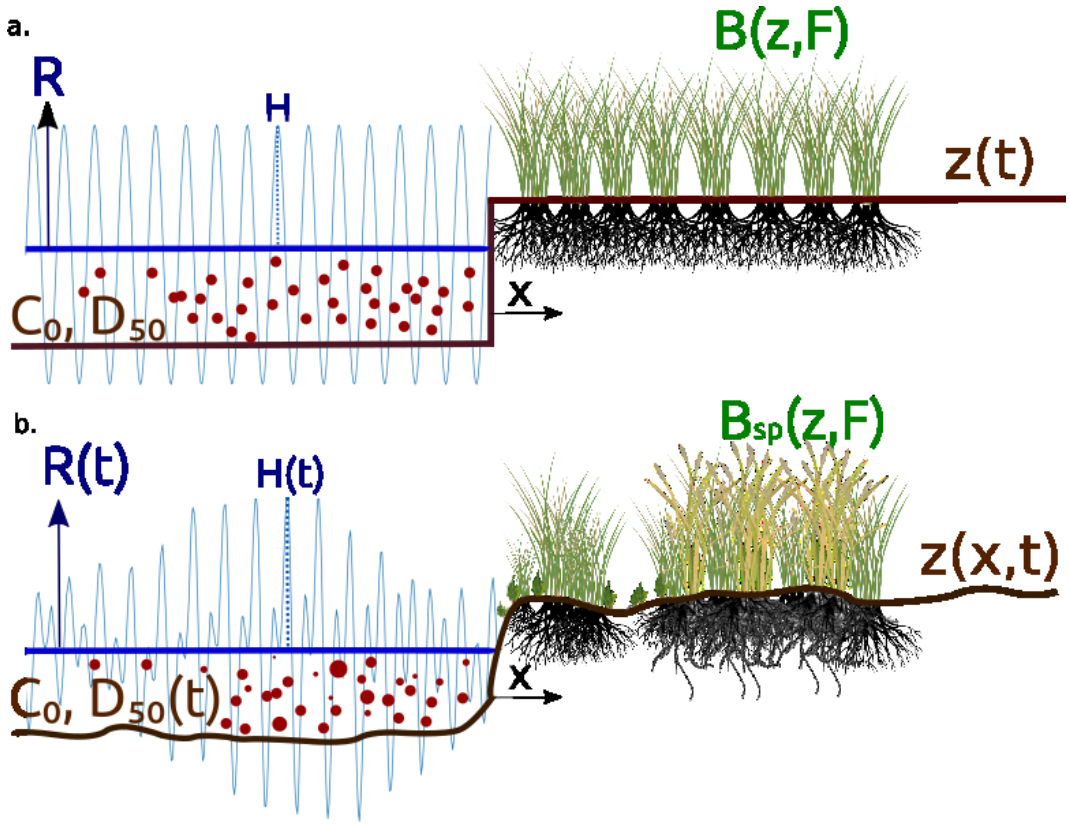


**Figure 3.1:** Schematic diagrams of the inputs of a 0-dimensional accretion model. a. Simplified model with time-invariant maritime forcing (left) and uniform topography and vegetation (right); b. Model with more realistic, time-dependent maritime forcing and variable topography and plant associations. $R$ is the rate of sea level rise, $C_0$ is the suspended sediment concentration, $D_{50}$ is the median sediment grain size, $H$ is the maximum tidal elevation for a given tidal cycle, $B$ is the biomass of a given species, and $F$ is the fitness function for that species.

marsh elevations and accretion rates, as well as the conditions necessary for platform elevations to match rising sea levels. Later in this contribution, we relax our assumptions about $C_0$ and $D_{50}$ and allow them to vary as free parameters.

### 3.3.3 Site description and sediment supply conditions

In this study, we examine 8 marsh sites where two lidar topographic surveys acquired at least 4 years apart are located in close proximity to a tidal gauge with a long-term record of hourly data. For each site, we obtain total suspended matter ($TSM$) using the GlobColour MERIS product (Barrot et al., 2007), which contains monthly values $TSM$ in the Earth's oceans and lakes between 2002 and 2012. Monthly coverage of MERIS, however, is incomplete. Consequently, we use the averaged $TSM$ between 2002 and 2012 in order to cover our sites. The angular resolution of MERIS products is $1/24°$ at the equator. While this is insufficient to observe the exact $TSM$ value at our sites, MERIS data has already been used to calculate local sediment availability in global estimates of wetland response to sea level rise (Schuerch et al., 2018). In this study, we therefore use MERIS data in combination with field data on sediment supply conditions sourced from the literature, as described below. The location of each site is given in Figure 3.2.

**Boston Harbor** The marsh studied in Boston Harbor is located in Squantum, MA, and borders Quincy Bay, approximately 6 $km$ from Boston Harbor tide gauge. Flume experiments conducted by Ravens and Gschwend, 1999 show tidal flat sediments to range between 30 and 60$\mu m$ in $D_{50}$, and to contain $3 - 4.5\%$ of organic matter. In these same experiments, under shear stresses of 0.05 $Pa$, $TSM$ oscillates around 25 $g\ m^{-3}$, peaking around 160 $g\ m^{-3}$ under stresses of 0.5 $Pa$. These values are slightly superior to those found by Hopkinson et al., 2018b in the nearby Plum Island Sound (median $SSC$ around 15.6 $g\ m^{-3}$ and peaks around 40 $g\ m^{-3}$), however organic content is much lower than the 30% assumed in Plum Island.

**Morro Bay** The marsh studied in Morro bay is located North of Morro Bay State Marine Reserve, CA, on the Chorro Creek estuary, approximately 20 $km$ from Port San Luis tide gauge. Few data on sediment size, concentration and organic content was found for Morro Bay. Instead, we use data for San Francisco Bay, CA. There, acoustic backscatter was used to estimate sediment grain size between 50 and 90 $\mu m$ and suspended solids to $20 - 300$ $g\ m^{-3}$ (Gartner, 2004).

**Morecambe Bay** The marsh studied in Morecambe Bay is located South of Jenny's point, Lancashire, approximately 15 $km$ from Heysham tide gauge. Few data were found for sediment concentrations. Instead we use data for the Mersey estuary. Aldridge, 1997 finds sandy sediments around 150 $\mu m$ and Pringle, 1995 finds silts of around 31 $\mu m$. Gray and Scott, 1977 mention loss on ignition of 8%. Modern measurements might find different values.

**Mersey Estuary** The marsh studied in the Mersey Estuary is located in Ellesmere Port, Cheshire, approximately 15 $km$ from Gladstone tide gauge. Acoustic Doppler

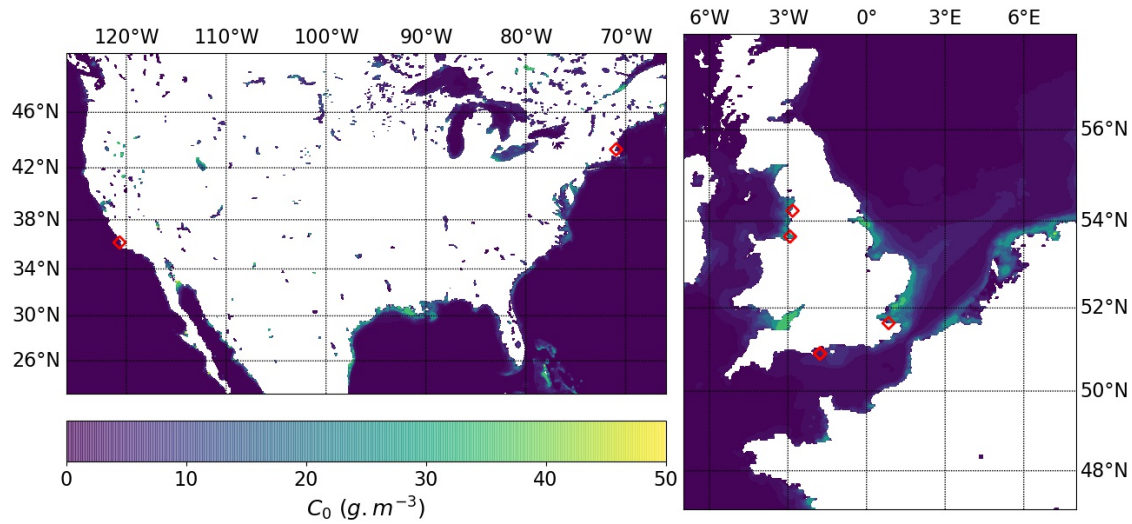


**Figure 3.2:** Location of the selected tidal stations over a map of averaged monthly Total Suspended Matter concentration between 2002 and 2012. In the United States, the stations are Port San Luis for the Morro Bay marsh (California) and Boston for the Boston Harbor marsh (Massachusetts). In the United Kingdom, the stations are: Heysham for the Morecambe Bay marsh, Gladstone for the Mersey Estuary marsh, Bournemouth for the Poole Harbour Shell Bay, Wych Lake and Arne Bay marshes, and Sheerness for the Swale Estuary marsh.

Current Profiler (ADCP) measurements in the Mersey river near Liverpool found $D_{50}$ in the channel to be approximately 9 $\mu m$, and were found up to approximately 50 $\mu m$. Suspended solids concentrations vary between 10 and 650 $g\ m^{-3}$ (Holdaway et al., 1999).

**Poole Harbour** The three marshes studied in the Poole Harbour, Dorset, are all under 7 $km$ from the Bournemouth tide gauge. Gao and Collins, 1994 show in the neighbouring Christchurch Harbour that sediment grain sizes vary between 65 and 250 $\mu m$ in the proximity of marshes, with concentrations measured around 120 $g\ m^{-3}$ but known to reach 600 $g\ m^{-3}$ during storm events (Green, 1940).

**Sheerness** The marsh studied in the Swale Estuary, Kent, is approximately 16 $km$ from the Sheerness tide gauge. Wharfe, 1977 reports $D_{50}$ values ranging from 50 to 90 $\mu m$, while Zhou and Broodbank, 2013 report concentrations ranging from 100 to $2,000\ g\ m^{-3}$.

### 3.3.4 Collection and processing of topographic data

Topographic surveys are sourced from either the NOAA Digital Coast archive or the United Kingdom Environment Agency. All datasets are referenced to their respective national topographic datum: the North American Vertical Datum 1988 in the USA and Ordnance Datum at Newlyn in the UK.

Errors in elevation measurements may stem from the georeferencing of the lidar point clouds. Vertical error margins are determined by comparing lidar elevations to the elevation of multiple ground control points. The root mean square error (RMSE) of this comparison is available on demand by both data providers. Vegetation is another factor of error when measuring salt marsh ground elevation (Parrish et al., 2014; Rogers et al., 2018; Schmid et al., 2011). On Sapelo Island, GA, Hladik and Alber, 2012b found that low plants such as short *Spartina alterniflora* and *Batis maritima* yielded positive errors of less than +0.05 $m$. Conversely, Chassereau et al., 2011 compared RTK-GPS and lidar elevations on Maddieanna Island, SC, a marsh dominated by *Spartina alterniflora*, with stem

heights of $0.15 - 0.55\ m$ on the platform and levees and up to $1.70\ m$ on the lower marsh and creek banks. The study found positively skewed histograms of signed error, with the lowest positive errors (under $+0.15\ m$) being far from creek banks, confirming the influence of stem height on the error in lidar elevation. To minimise the error due to vegetation, our selection of marshes excludes sites with dominant tall vegetation species (Table ??).

| Site | Dominant plant species | References |
|---|---|---|
| Boston Harbor | *S. patens*, *S. alterniflora*, *Distichlis spicata* | Buynevich et al., 2001 |
| Morecambe Bay | *Puccinellia maritima*, *Festuca rubra* | Gray and Scott, 1977 |
| Morro Bay | *Spartina sp*,*Salicornia subterminalis* | Kuhn and Zedler, 1997 |
| Mersey Estuary | *F. maritima*, *Suaeda maritima*, *Obione portaculoides* | Stopford, 1951 |
| Arne Bay | *Spartina sp.* | Hubbard, 1965 |
| Shell Bay | *Spartina sp.* | Hubbard, 1965 |
| Wych Lake | *Spartina sp.* | Hubbard, 1965 |
| Swale Estuary | *Spartina sp.* | Cundy et al., 2005 |

**Table 3.3:** Dominant plant species for the selected sites, sourced from literature on regional marsh systems and analog marshes.

From the downloaded point clouds, we use CloudCompare (https://www.cloudcompare.org/) to generate rasters of minimum and maximum elevations within a grid cell, respectively $\boldsymbol{Z}_{min}$ and $\boldsymbol{Z}_{max}$. Grid cell size is determined to fit a minimum of 6 points per cell, up to a maximum of $3\ m$. The marsh platform elevation is then extracted from $\boldsymbol{Z}_{min}$ using the Topographic Identification of Platforms (TIP), which accurately delineates marsh platforms for grids of up to $3\ m$ in horizontal resolution (Goodwin et al., 2018). For each survey, we select a a low-relief, non-vegetated structure (road, car park, etc.) for which we calculate the $1^{st}$, $2^{nd}$ and $3^{rd}$ quartile of the difference $\boldsymbol{Z}_{max} - \boldsymbol{Z}_{min}$. Two subsampling methods are then applied to the marsh platform. First, pixels classified as marsh platforms for which $\boldsymbol{Z}_{max} - \boldsymbol{Z}_{min}$ is inferior to the median of $\boldsymbol{Z}_{max} - \boldsymbol{Z}_{min}$ of the reference structure are preserved, as shown for the Mersey Estuary in Figure 3.3a.-c. (red pixels). Similar figures for other sites are available in the appendix

(Figures 6.3 to figure 6.10). This subsampling ensures that high elevation gradients do not exist within the pixel, whether they are due to topographic features (hummocks or pools), locally high vegetation or because pixels reside on the scarp and include points measure on marsh and creeks alike. Pixels classified as marsh platforms that are also levee points are selected by the second method (green pixels). Due to the larger spread of elevation and the potentially large errors in elevation associated with levee pixels, we do not use them further in this study (Figure 3.3d.).

Vertical offset between the two selected surveys is accounted for as the average difference of $\boldsymbol{Z}_{min}$ for the reference structure, the first survey being taken as reference by default. The values of vertical offset are given in Table ??.

| Site | Survey 1 | Survey 2 | Offset (m) |
|---|---|---|---|
| Boston Harbor | 2010-12 | 2014-12 | 0.094 |
| Morecambe Bay | 2008-01 | 2017-01 | -0.226 |
| Morro Bay | 2011-03 | 2015-09 | -0.034 |
| Mersey Estuary | 2006-01 | 2011-01 | 0.197 |
| Arne Bay | 2006-01 | 2013-01 | -0.119 |
| Shell Bay | 2007-01 | 2011-01 | 0.038 |
| Wych Lake | 2007-01 | 2016-01 | 0.052 |
| Swale Estuary | 2007-01 | 2016-01 | -0.122 |

**Table 3.4:** Date of surveys and elevation offset for a stable structure between $S2$ and $S1$. Column 3 shows the offset in elevation between reference structures.

### 3.3.5 Collection and processing of sea level data

Each selected marsh site is associated with a tidal station in its close vicinity. For these stations, we download sea level observations from the GESLA-2 dataset, a global collection of hourly sea level data from the time when each tide gauge started acquiring data at a frequency superior or equal to 1 hour up to the year 2015 (Woodworth et al., 2016), or the British Oceanographic Data Centre (BODC) data repository. From these records we extract the monthly mean high and low tides $MHT_m$ and $MLT_m$. We fit a linear trend to each of these times series, the difference of which constitutes the mean tidal range $MTR$. The same

process is applied to determine the trend of monthly observed highest high tide $OHHT$. Time series of monthly mean sea levels ($MSL_m$) were collected from the NOAA sea level trend dataset. For stations in the United Kingdom that do not have a long-term record of $MSL_m$, we choose the closest long-term tide gauge as a substitute. From this record we extract the linear trend of $MSL_m$, named $MSL$, the slope of which constitutes the rate of sea level rise $RSLR$ (NB: in this

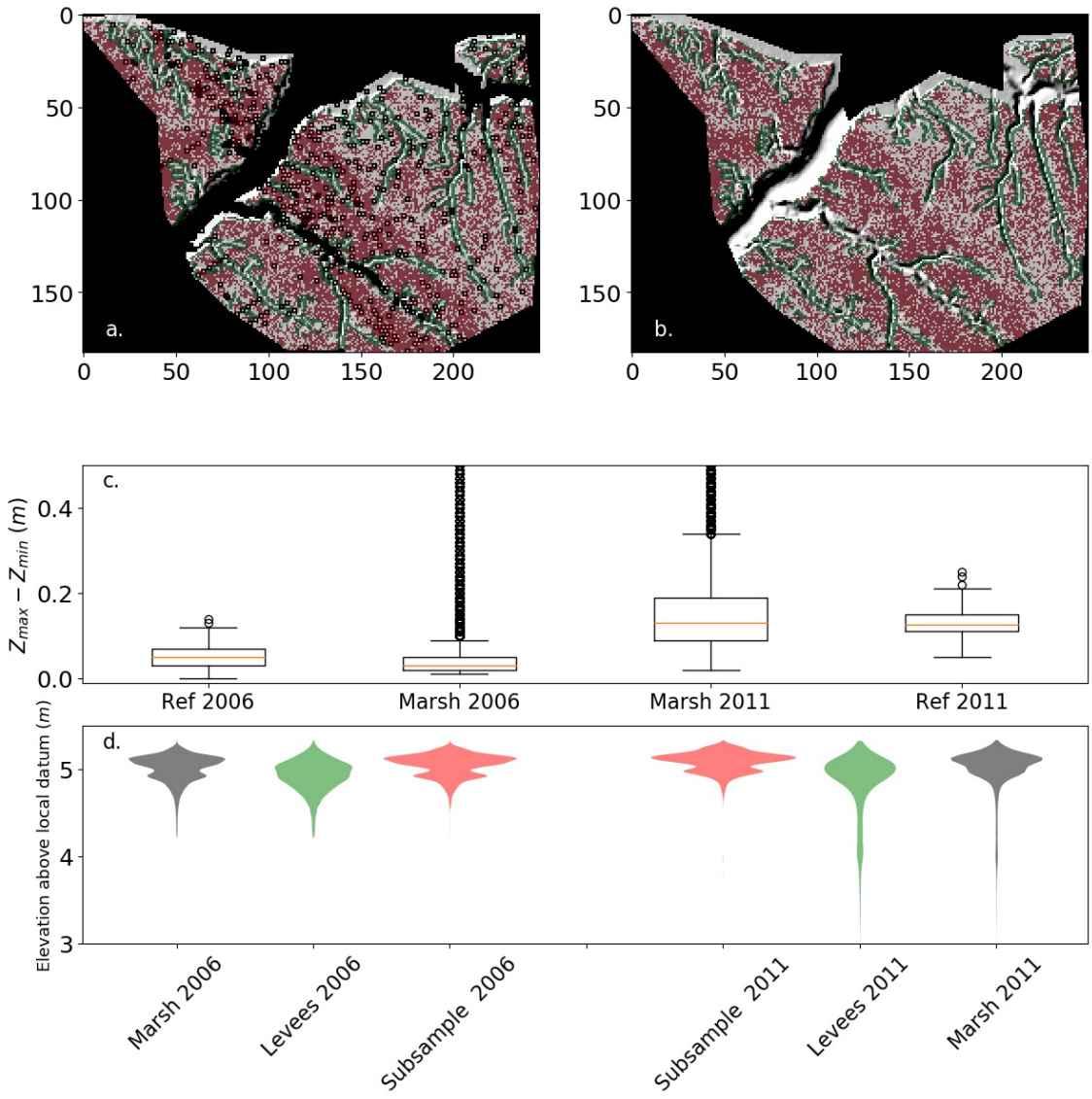


**Figure 3.3:** Mash platform subsampling results for the Mersey Estuary Marsh; a. and b. show the marsh hillshade (respectively for $S1$ and $S2$) overlayed with subsampled pixels (red) and levee pixels (green); c. boxplot of differences $Z_{max} - Z_{min}$ for the reference infrastructure and the marsh platform; d. probability distribution functions for the entire marsh platform (grey), levee pixels (green) and subsample pixels (red).

particular instance RSLR does not refer to relative sea level rise). Figure 3.4a. shows the tidal records with their associated metrics, as well as the 1-year subset of data used to calculate yearly deposition fluxes (see section 3.4). Figure 3.4b. shows the cumulative distribution function of flooding time at each station, for both the whole record and the selected subset.

## 3.4 Results and Discussion

### 3.4.1 High platform elevations cannot be explained by sinusoidal tidal forcing

For each of the 8 selected marshes, Figure 3.5 shows the probability distribution function of elevation $f_z$ of the marsh platform at the dates $S1$ (left of bar) and $S2$ (right of bar). Grey filled areas $f_z$ represent the subsampled marsh platform (see Figure 3.3c.). Grey lines represent the same pixel sets plus or minus half the RMSE reported by ground truthing reports. For each survey, marsh elevation is relative to its contemporary sea level. In all of the sites, irrespective of measurement error, the major part of the marsh platform lies within the upper tidal frame, defined here as the range of elevations between $MHT$ and $OHHT$.

While megatidal marshes show a wider distribution, no platform occupies more than half of the upper tidal frame. This observation is supported by surveys of vegetation populations relative to tidal levels (Belliard et al., 2017) and refines the approach of Schuerch et al., 2018, where marshes are assumed to occupy the entire range of elevations between $MSL$ and $MHT$.

In models using a sinusoidal tidal forcing of amplitude $H = MHT - MSL$, the equilibrium elevation $z_{eq}$ relative to $MSL$ is given by equation (3.8) (D'Alpaos et al., 2011):

$$z_{eq} = H \cdot (1 - \frac{R_y}{k_y}) \tag{3.8}$$

where $k_y = Q_{dep,y} + Q_{org,y}$ $[mm\ yr^{-1}]$ is the sum of yearly deposition and belowground production rates over the period of time $y$. This accounts for compaction

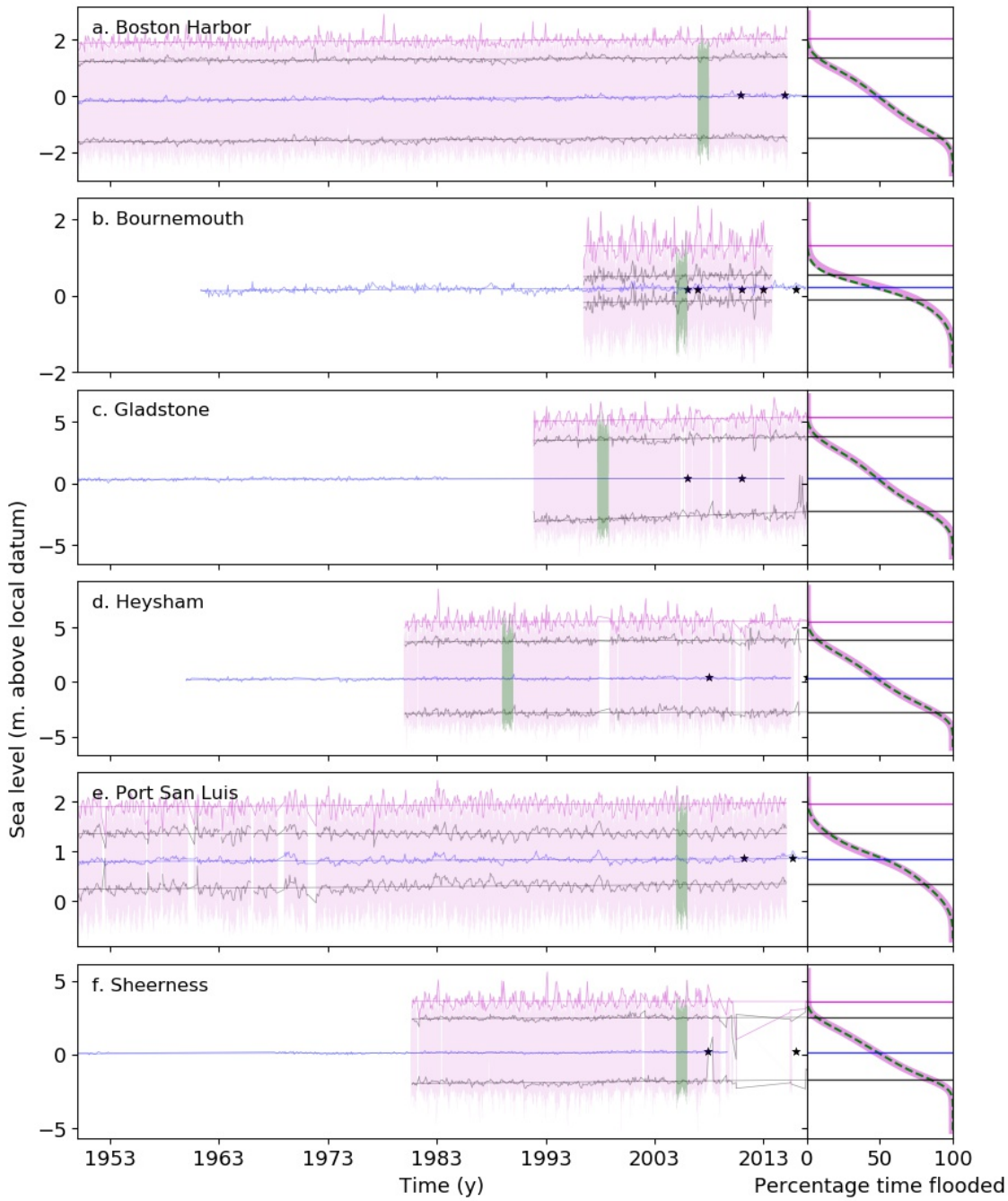


**Figure 3.4:** left: Hourly sea level record (pink) and monthly Mean Sea Level $MSL$ (blue) for each station between 1950 and 2017. Black lines are respectively the monthly Mean High Tide $MHT$ and Mean Low TIde $MLT$. Thicker pink lines are monthly Observed Highest High Tide $OHHT$. Straight lines are monthly linear trends for each metric. Green areas represent the most recent complete year of record; right: Cumulative distribution function of flooded time for a given elevation for the whole tidal record (pink), and for the chosen representative year (dashed green). Horizontal lines are the most recent value of the linear monthly trends. Black stars indicate the dates of lidar surveys.

effects but not for shallow subsidence. While $z_{eq}$ is seldom truly reached, it gives an indication of the elevation toward which marsh platforms converge. Equation (3.8) suggests that, under sinusoidal forcing, a marsh platform may reach only elevations higher than $MHT$ under high $Q_{org}$, which is rarely observed (Morris et al., 2016). This constraint is relaxed by the fact that platform elevation tends to lag behind sea level variations (Kirwan and Temmerman, 2009): salt marshes that have experienced higher sea levels may then be found at higher elevations.

All of the marshes examined in this study are higher than both their equilibrium elevations and their maximum elevation $H + MSL$. However, no stations other than Gladstone and Heysham have experienced late quaternary uplift (Bromirski et al., 2011; Donnelly, 2006; Shennan and Horton, 2002; Shennan et al., 2012) and no stations show significant negative modern variations in monthly $MSL$ (see figure 3.4). Hence, the high elevation of the examined marsh platforms cannot be explained by a sinusoidal forcing of amplitude $H$, notwithstanding the use of this forcing by several studies on marsh elevation change for lower marshes (e.g. D'Alpaos et al., 2011; Da Lio et al., 2013; Marani et al., 2007; Morris et al., 2002; Tambroni and Seminara, 2012).

Furthermore, platforms that are higher than $z_{eq}$ are predicted by equation (3.8) to lose elevation, as they are not flooded frequently enough to allow accretion rates that match sea level rise. However, figure 3.5 shows that in all but two sites, platforms are gaining elevation on $MSL$. This affirmation stands for all but when extreme positive error in $S1$ and extreme negative error in $S2$ are considered, which is unlikely since the ground-truthing given by data providers shows errors on ground-control points to be either consistantly positive or negative through time. All the examined platforms therefore experience deposition, and may be considered active, rather than relics of higher sea levels. This result strongly suggests that the marsh platforms in our study depend on deposition of concentrated coarse sediment to maintain their position in the tidal frame, typically provided by spring tides and storms. The latter are shown by Castagno et al., 2018 to positively influence sediment import into back-barrier bays. The same study shows this effect to be less important for fine sands ($D_{50} \geq 125\ \mu m$),

which hints at a potential depletion in this size fraction, which may in turn lead to marshes failing to keep pace with $RSLR$. Dependance on infrequent deposition events is also consistent with the findings of Mariotti et al., 2010 in micro-tidal back-barrier marshes, who showed that storm surges contribute to the erosion of scarps as well as to the recycling of eroded marsh sediment onto the platform.

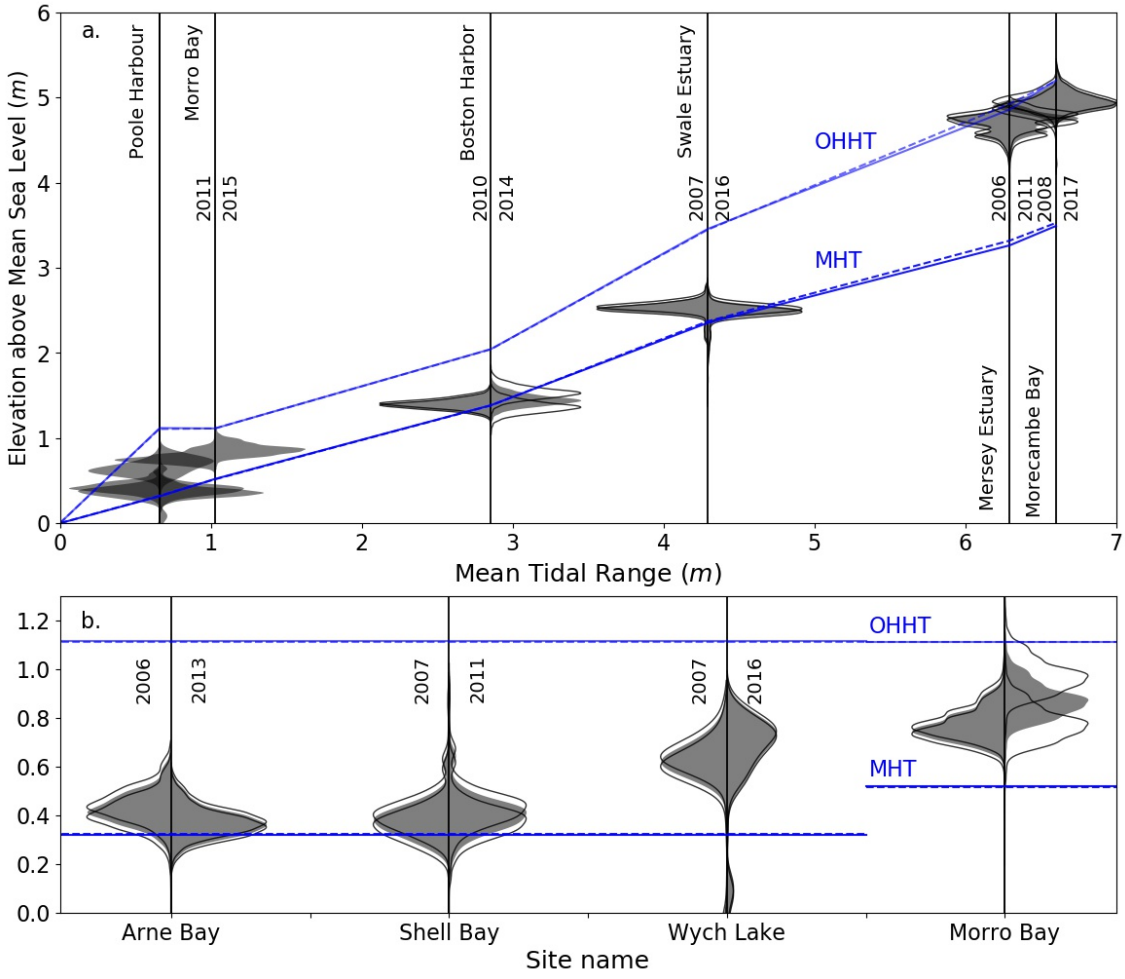


**Figure 3.5:** Probability distribution functions of marsh platform elevations relative to $MSL$ for each examined marsh at the dates $S1$ (left - grey fill) and $S2$ (right - grey fill); Black lines indicate the possible vertical offset of the probability distribution functions due to lidar vertical error; Blue lines show the monthly trend for $MHT$ and $OHHT$ a the dates $S1$ (full) and $S2$ (dashed); a. Marsh sites organized by Mean Tidal Range; b. detail of micro-tidal sites.

### 3.4.2 Modelling accretion rates with real tidal forcing highlights the influence of elevation, grain size and concentration

Following the observations of Section 3.4.1, we examine the effect of using a realistic tidal forcing by simulating deposition fluxes over a year for each marsh site. The sea level record used to force accretion is a subset of the full tidal record for each station, shown as the green highlighted data in Figure 3.4. In this experiment, we use three sets of values for $C_0$ and $D_{50}$. Lower values for $C_0$ and $D_{50}$ referenced in Section 3.3.3 are the first set. The second set is $D_{50} = 50\ \mu m$, which is within the higher range of values used in long-term modeling studies (D'Alpaos et al., 2011; Marani et al., 2007). $C_0$ is determined by the values obtained from the MERIS Total Suspended Sediment (TSM) dataset at the location of the tidal station. In the third set, higher values for $C_0$ and $D_{50}$ referenced in Section 3.3.3 are selected. Table ?? summarises sediment supply conditions used in the simulations.

| Site | Field $C0$ bounds ($g\ m^{-3}$) | Field $D_{50}$ ($\mu m$) | MERIS $C0$ ($g\ m^{-3}$) |
|---|---|---|---|
| Boston Harbor | 25-160 | 30-60 | 25.2 |
| Morecambe Bay | 10-650 | 31-150 | 25.7 |
| Morro Bay | 20-300 | 50-90 | 6.8 |
| Mersey Estuary | 10-650 | 9-50 | 28.9 |
| Arne Bay | 120-600 | 65-250 | 10.5 |
| Shell Bay | 120-600 | 65-250 | 10.5 |
| Wych Lake | 120-600 | 65-250 | 10.5 |
| Swale Estuary | 100-2,000 | 50-90 | 33.3 |

**Table 3.5:** Sediment conditions used for the production of Figures 3.6 and 3.8.

Figure 3.6 compares the observed and modelled elevation change of the dominant platform elevation $z_{max(f_Z)}$ relative to the terrestrial datum, with relative sea level rise as a reference. Despite the precautions taken to reduce error in the elevation samples (see Figure 3.3), observed accretion rates (red bars) are visibly unreliable. For instance, Arne Bay exhibits negative accretion rates while Wych Lake and Shell Bay, located less than 5 $km$ away, exhibit accretion rates close to

1641 those recorded at Wax Lake Delta, one of the fastest accreting marshes in the
1642 world. Morro Bay and Boston Harbor also exhibit unrealistic accretion rates,
1643 particularly in regard to the low rates of associated sea level rise. While such
1644 rapid elevation variations have been observed using SETs (Kirwan et al., 2016a),
1645 they may also be the product of uncertainty in elevation values. Indeed, errors
1646 in the measurement of elevation for both $S1$ and $S2$ lead to considerable error in
1647 rates of accretion, as shown by the error bars in Figure 3.6.

1648 However, the elevation error in $S1$ typically leads to errors of 5% or less on the
1649 modelled accretion rate (brown bars). Although variations in sediment supply and
1650 flooding patterns prevent a direct comparison between sites, we observe an overall
1651 decrease in modelled deposition rates with increasing tidal range and platform
1652 elevation. Conversely, we note a significant positive response of accretion rates
1653 to the combined increase in sediment size and concentration, as shown by the

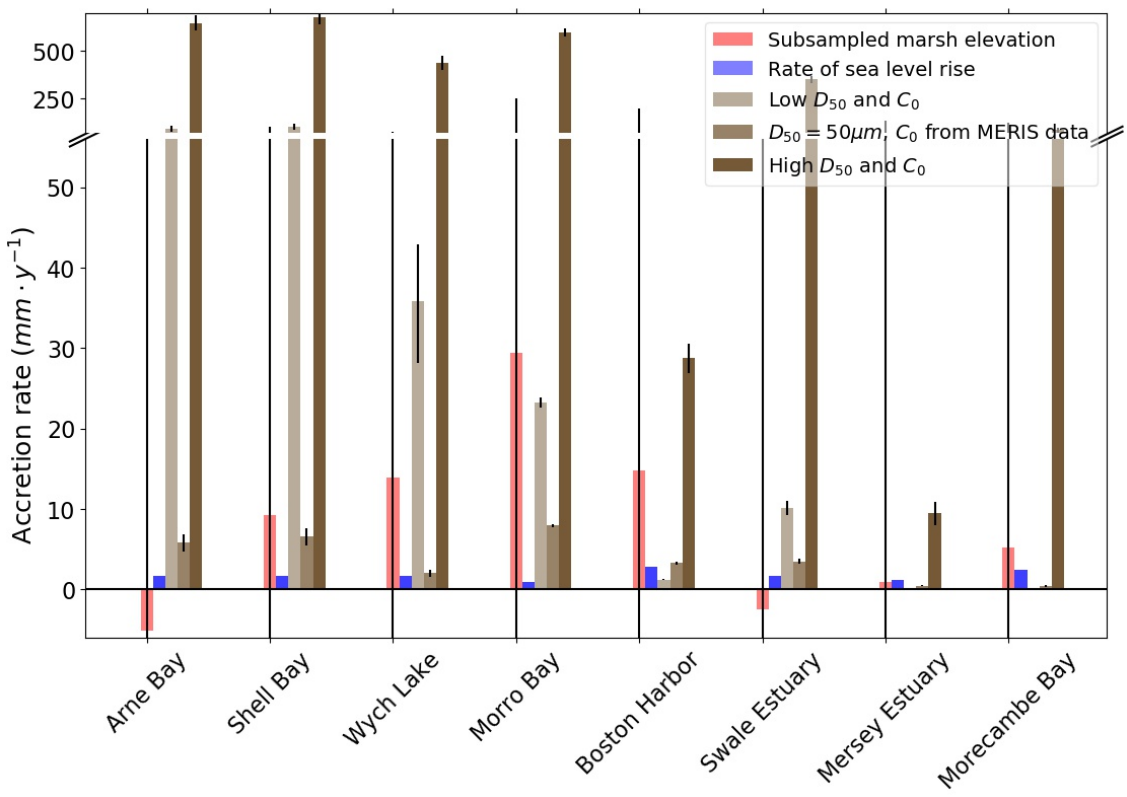


**Figure 3.6:** Magnitude of deposition rates (red and brown bars), with relative sea level rise $RSLR$ for reference, for each site; the initial elevation is the normalized dominant elevation of the platform $z_{max(f_Z)}$; Black lines indicate vertical error.

differences in accretion rates between low $C_0$ and $D_{50}$ and high $C_0$ and $D_{50}$. This response leads us to postulate that the low values of $C_0$ are the cause for the low modelled accretion rates when using MERIS data. Indeed, the MERIS dataset has a spatial resolution of 300 $m$ and is primarily an oceanic dataset. It does not account for complex coastal inlets, estuaries and bays where salt marshes are found, and where higher concentrations are likely to be found (Amos and Alfoldi, 1979). Furthermore, Fagherazzi et al., 2014 find strong spatial variations in sediment size within the tidal creeks of a single site at Plum Island Sound. In this respect, the site-specific data collected in Section 3.3.3 is likely representative of the spatial variability of sediment supply found in the sites examined. The relative influence of $C_0$ and $D_{50}$, however, is not discernable at this point.

### 3.4.3 Constraints on sediment supply and consequences for platform equilibrium

Whether a marsh keeps pace with sea levels has been suggested to depend on forcing sediment concentration (D'Alpaos et al., 2011; Kirwan et al., 2010; Kirwan and Megonigal, 2013). We establish in Section 3.4.2 that deposition is also conditioned by the initial platform elevation, as suggested by Cahoon and Reed, 1995, and the grain size of the deposited sediment. We calculate $Q_{dep}$ for a range

**Figure 3.7:** *left:* gravel from a nearby creek backed-up against marsh margins in Aberlady Bay; *right:* trail bar behind *Suaeda maritima* in Mont-Saint-Michel Bay. Images G. Goodwin

of $C_0$ and $D_{50}$, assuming a contribution of 6% from below-ground production $Q_{org}$. This value is the lower bound of a range estimated from loss on ignition organic matter contents for several marshes around the world (Crooks et al., 2002; Neubauer, 2008; Roner et al., 2016), and approximates to local data in Boston Harbor and Morro Bay (see Section 3.3.3). While it is not included in this chapter, we must bear in mind that increases in temperature and atmospheric $CO_2$ are likely to increase organogenic production in salt marshes (Reef et al., 2017). For each site, Figure 3.8 shows the contour lines of $C_0$ and $D_{50}$ values that yield given values of $k = Q_{dep} + Q_{org}$. The dashed blue line corresponds to conditions on $C_0$ and $D_{50}$ for marsh accretion to match the current $RSLR$. Dashed red lines indicate the accretion rates derived from lidar data, but do not represent the associated error. Sediment supply conditions corresponding to low and high $C_0$ and $D_{50}$ bound the grey box, and the black star represents the concentration determined using the MERIS data and $D_{50} = 50\ \mu m$. We remind the reader that due to the assumption of negligible turbulence on the marsh surface and the inconsideration for flocculation processes, $Q_{dep}$ is likely overestimated and therefore the required sediment supply to match a given $RSLR$ is likely under estimated.

In all cases, the contours follow a hyperbolic curve. This behaviour implies that at high sediment concentrations, variations in $C_0$ have less impact on $Q_{dep}$ than variations in $D_{50}$, and vice versa. Conversely, the point of the contour line that is closest to graph origin represents the conditions where variations in each parameters exert an equal influence on accretion rates. This behaviour is preserved along the 1:1 diagonal. High sediment concentrations require high shear stress at the bed to mobilise sediment (Fagherazzi et al., 2006) if generated in situ. If the sediment is sourced from either offshore or rivers, high turbulence is needed to keep sediment in suspension. High suspended sediment concentrations are associated with strong currents or high waves, increasingly so for large particle sizes (Yang et al., 2008). Consequently, we may expect higher sediment concentrations to be associated with larger particle sizes. Such conditions are typical of storm events, spring tides or fluvial flood discharges. They may be observed in rare instances on the field, for instance when gravel is backed-up against marsh

scarps after storm events, or when strong tides leave sandy trail bars on the lee side of pioneer plants (see Figure 3.7).

Figure 3.8 a.-c. represent three neighbouring marshes in Poole Harbour,

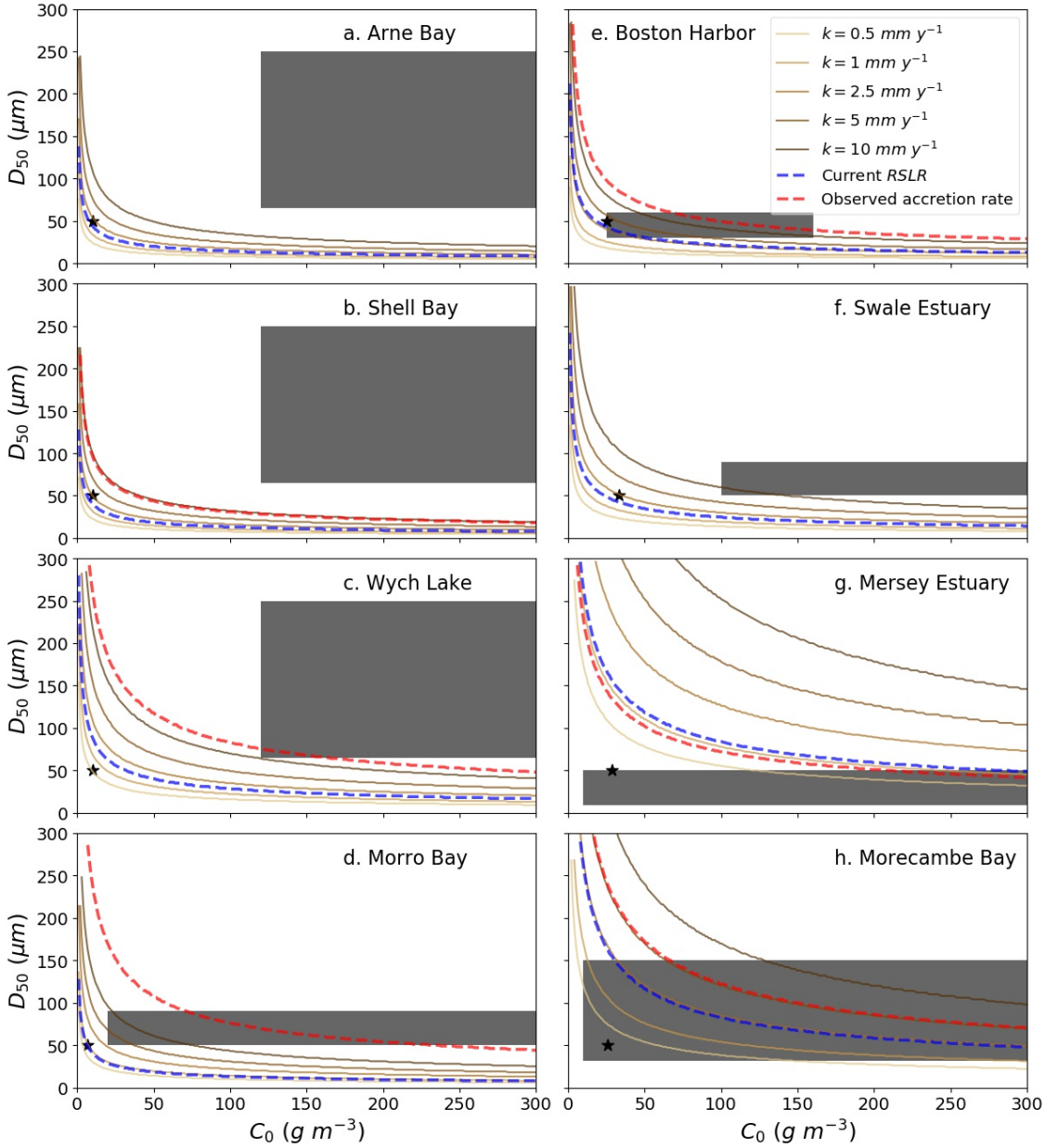


**Figure 3.8:** Contour lines representing conditions on $C_0$ and $D_{50}$ for total accretion $k = Q_{dep} + Q_{org}$ to reach the indicated values. Here, $Q_{org} = 0.06 \cdot Q_{dep}$; Grey boxes bound sediment supply conditions from low $C_0$ and $D_{50}$ to high $C_0$ and $D_{50}$; Black stars represent $C_0$ conditions obtained from MERIS data, with $D_{50} = 50\ \mu m$. Blue dashed lines represent the conditions required to match $RSLR$, and red dashed lines the conditions to match observed accretion rates.

Dorset, UK, for which tidal and sediment conditions are considered identical. Wych Lake (Figure 3.8c.) is higher in the tidal frame than the other sites, and as a consequence, the contour lines are both further from the origin and further apart. Hence, for equal sediment supplies and tidal forcing, increasing elevation reduces deposition rates and increases the demand in sediment to maintain elevation within the tidal frame. For example, platforms in Morecambe Bay and the Mersey Estuary (Figure 3.8g.-h.) are close to $OHHT$, and are seldom flooded. As a consequence, not only do these sites require more sediment to match current rates of sea level rise, but they would also require a greater increase in $C_0$ or $D_{50}$ if $RSLR$ increased. This situation is hinted at by Pringle, 1995, who finds medium to coarse silts (31 $\mu m$) and very fine sands of up to 100 $\mu m$ in Morecambe Bay marshes. Conversely, ranges of $20 - 40$ $\mu m$ were observed by Roner et al., 2016 in the Venice Lagoon, where salt marshes are notoriously low in the tidal frame (Da Lio et al., 2013).

We show the conditions necessary to match observed positive accretion rates (dashed red lines), but recommend caution when considering these data (see Section 3.4.2). Indeed, though it seems that most sediment supply condition boxes (grey boxes) contain the dashed red lines, the existence of negative accretion when conditions predict more than 10 $mm\ y^{-1}$ of accretion demands a critical view of the observed accretion values. Regardless, all field-measured sediment supply conditions generate enough accretion in all sites, except the Mersey Estuary and Morecambe Bay (Figure 3.8g.-h.), for the platform to keep up with current $RSLR$ (dashed blue lines) in the model. Aside from Boston Harbour (Figure 3.8e.), even the lower bounds of measured sediment supply are sufficient to match more than 10 $mm\ y^{-1}$ of sea level rise. Our application of Stokes' law with negligible current and turbulence may explain this overestimation of $k$. However, we must also consider that field measurements provide only a snapshot of sediment supply conditions at any given location.

Leroux (2013) highlighted the high temporal variability of sediment supply; they measured peak concentrations of up to $5,000\ g\ m^{-3}$ during a spring tide, while base concentrations were $500\ g\ m^{-3}$ in tidal creeks of the Mont-Saint-

Michel Bay, France. The high shear stresses caused by storms also generate peaks in sediment concentrations (Fagherazzi and Priestas, 2010). In this respect, averaged MERIS data (black stars) does not represent the temporal variability of sediment supply. To further improve our understanding of sediment supply, we suggest that $k$ contour lines may be combined with accretion monitoring through marker horizons and grain size distribution (GSD) analyses to determine average sediment concentrations during deposition events. While our 0-D model does not account for distance to creeks, the results of Zhang et al., 2019 show that it is an important factor of marsh deposition, and we suggest that these results should orient future methods of deposition measures.

### 3.4.4 Insight on the roles of elevation and tidal range

In this section, we compare the 8 marsh sites to better understand the interaction between platform elevation and tidal records. In Figure 3.9, we calculate $k$ for the same range of sediment supply conditions as in Section 3.4.3 and represent the conditions leading to $k = 2.5\ mm\ y^{-1}$. Each subplot shows the accretion contour lines for each site for various initial elevations $z_0$. Indeed, elevation within the tidal frame determines the 1) proportion of $N_{\Delta t}$ tidal cycles for which the platform floods (Equation 3.6), and 2) the maximum depth $D_{max}$ of each flooding event, thus influencing deposition within each cycle (Equation 3.7). Although below-ground production is known to vary with elevation, these variations are not well quantified above elevations of $MHT$ (Morris et al., 2002), and we therefore maintain $Q_{org} = 0.06 \cdot Q_{dep}$.

In Figure 3.9a., the initial elevation is the observed main platform elevation $z_{max(f_Z)}$. Regardless of mean tidal range, the normalised elevation in the upper tidal frame, defined as $z^*$ in Equation (3.9), exerts a positive influence on the sediment supply necessary to meet $k = 2.5\ mm\ y^{-1}$.

$$z^* = \frac{z - MHT}{OHHT - MHT} \tag{3.9}$$

We note that for $z_0 = OHHT$ (Figure 3.9b.), sediment requirements are so

high that for Boston Harbor and the Swale Estuary, sediment larger than fine sand would be needed for marshes to be at equilibrium of moderate sea level rise rates. Such conditions are typical of beaches and sand dunes rather than marshes (Hayden et al., 1995), suggesting that flooding patterns at these sites do not allow marshes to reach these elevations.

Conversely, if $z_0 = MHT$, very little variations between sites of different tidal ranges is observed, confirming that the effect of tidal range on accretion rates increases with platform elevation. Hence, similar sediment supply conditions shown (Figure 3.9c.) may allow low marsh platforms around the world to with-

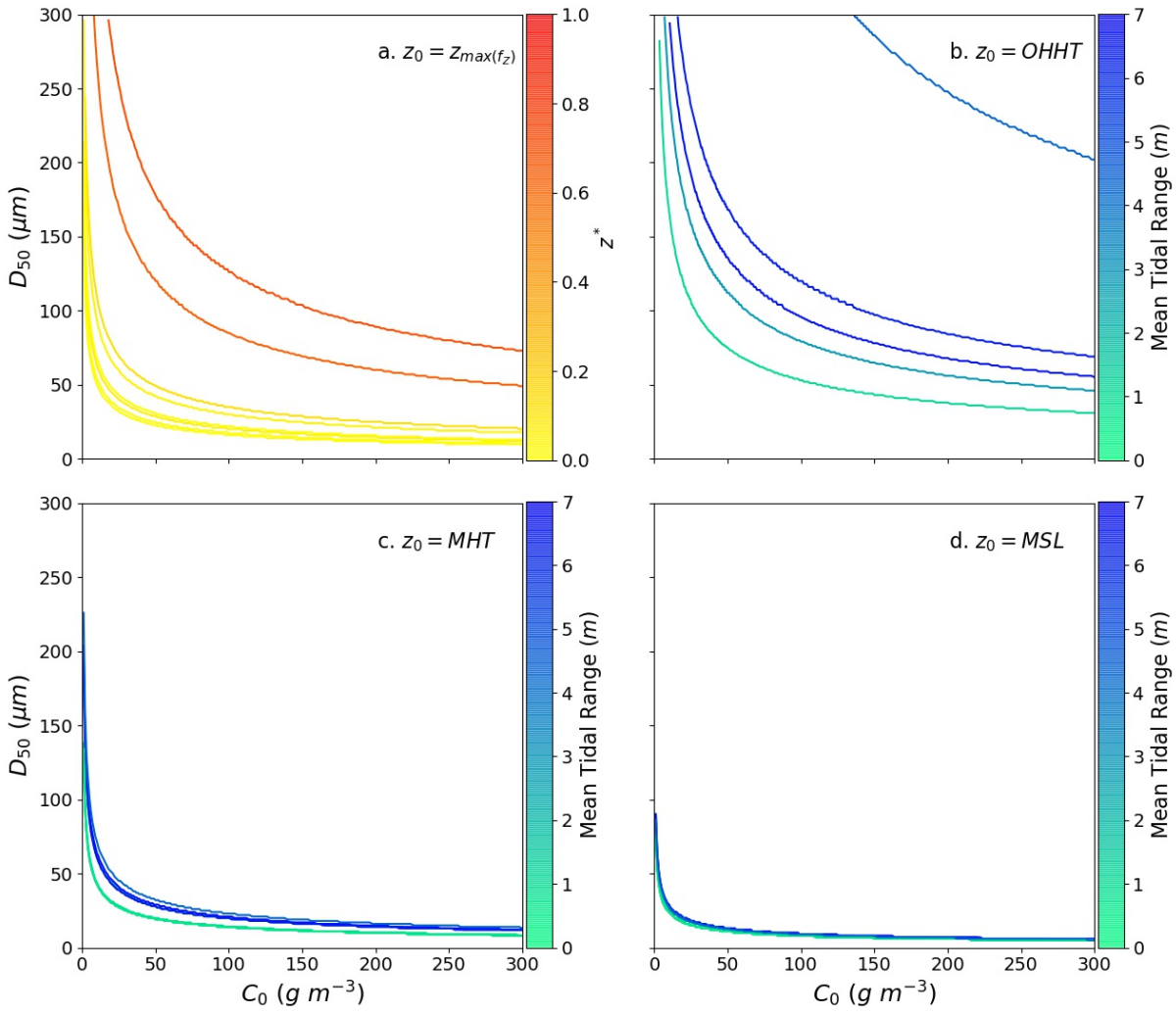


**Figure 3.9:** Necessary values of $C_0$ and $D_{50}$ for total accretion to reach $k = 2.5\ mm\ y^{-1}$; a. initial elevation $z_0 = z_{max(f_Z)}$, coloured by increasing $z^*$; b. $z_0 = OHHT$; c. $z_0 = MHT$; d. $z_0 = MSL$; the last three subplots are coloured by mean tidal range.

stand moderate sea level rise rates of $RSLR = 2.5\ mm\ y^{-1}$, whereas local tidal regimes would affect high platforms more strongly. Interestingly, low marshes across the world are more often observed to drown, suggesting that the drowning is caused by a lack of sediment supply and/or organic production rather than initial elevation. This low sediment demand is similar to that observed in Figure 3.9d., where initial elevations are $z_0 = MSL$. For these low elevations, mean tidal range also exerts a weak influence on accretion rates. More importantly, the little difference in accretion rates between $z_0 = MSL$ and $z_0 = MHT$ imply that pioneer platforms are likely to reach $MHT$, thus ensuring the regeneration of marsh surface area after lateral erosion events. We note that our model does not account for variable sediment concentrations on the platform, and is likely to overestimate deposition on parts of the platform that are far from creeks or scarps. Indeed, Temmerman et al., 2005 show that deposition rates decrease with distance from creeks and marsh edges. Pioneer platforms with different creek network properties, due for example to vegetation development (Kearney and Fagherazzi, 2016), may grow at different rates.

## 3.5 Conclusions

In this contribution, we test a 0-dimensional settling model to estimate elevation change on real salt marsh platforms, and compare these results with accretion fluxes derived from DEM surveys taken at least four years apart. While elevation changes observed through lidar have too high errors to yield accurate results, initial elevation measurements are sufficiently accurate provide initial data for model runs and assess the results' sensitivity to sediment supply conditions. We find that using a sinusoidal tidal forcing to simulate elevation evolution cannot explain the current elevation of the marshes we examined, which were located between $MHT$ and $OHHT$. While we did not examine enough sites to draw general conclusions on the distribution of salt marsh platforms within the tidal frame, our results suggest that simplified sinusoidal tides cannot account for the full evolution of salt marshes.

Using a representative subset of real tidal forcing, we calculate settling fluxes that better explain current platform elevations. When accounting for a 6% contribution of belowground organic production to accretion fluxes, modelled accretion rates for marshes that are low in the upper tidal frame (but still above $MHT$) are mostly sufficient to keep pace with current rates of relative sea level rise under most observed sediment supply conditions determined by MERIS. Conversely, sites that are closer to $OHHT$ require coarser or more concentrated sediment. The low hydroperiod associated with such high platforms suggests that small or light flocs do not have time to settle in sufficient quantity for the platform to maintain its elevation. Under storm surge conditions, however, advection of higly concentrated fine material and prolonged hydroperiod may counteract the effect of elevation.

It follows that marshes that reach a high position in the tidal frame should contain coarser sediment than platforms that do not attain this elevation, unless they are subject to frequent storms. The existence of such high platforms is therefore conditioned by the availability of coarse sediment or finer material in high volumes (or very high organic matter production), typically mobilised during storms, floods and spring tides. Conversely, we find that low platforms require a weaker sediment supply conditions to keep pace with $RSLR$. Further investigation into accretion rates with low starting elevations ($MHT$ and $MSL$) suggests that established low platforms are likely to contribute to long-term marsh regeneration regardless of tidal regimes, but also that plant establishment is likely the bottleneck of marsh progradation processes.

The results obtained in this chapter show a close similarity to the work of French (2006). There, the author describes the increase in accretion rates with increasing SSC and the lesser accretion rates obtained for higher marsh surfaces, which lead to an inexorable lowering of these high platforms. The results of this chapter show that where salt marsh platforms have developped to high elevations (close to OHHT), spring tides and storms may combine to supply sediment in sufficient concentrations and of sufficiently high settling velocity to maintain these high platforms.

To add weight to the conclusions drawn above, further research may investigate the relationship between marsh elevation and tidal records over a larger dataset. Furthermore, measuring sedimentation and back-calculating sediment concentration from field samples in different sites would allow to confirm the behavior suggested by the model. Future work may also investigate the size of deposited particles at various distances from scarps and tidal creeks to determine the detailed mechanisms of settling on wide vegetated platforms.

# Chapter 4

# Morphology of salt marsh margins

The work presented in this chapter was published in Remote Sensing:

Goodwin, G.C.H.; Mudd, S.M. Detecting the Morphology of Prograding and Retreating Marsh Margins—Example of a Mega-Tidal Bay. Remote Sens. 2020, 12, 13.

This research was conducted in collaboration with the named co-authors, who helped to edit the final manuscript and contributed to software development. I wrote the topographic analysis algorithms, performed the analyses, created the figures, and wrote the manuscript.

# List of Abbreviations

| Abbreviation | Meaning |
|---|---|
| CE | Change Event |
| DTM | Digital Elevation Model |
| DTM | Digital Terrain Model (A DTM of the ground surface) |
| DEFRA | UK Department for Environment and Rural Affairs |
| PE | Progradation Event |
| RE | Retreat Event |
| RMSE | Root Mean Square Error |
| TIP | Topographic Identification of Platforms (a software package) |

**Table 4.1:** Abbreviations used in this chapter

# List of Notations

| Notation | Meaning |
|---|---|
| $A_{CE}$ | Area of a change event |
| $V_{CE}$ | Volume of a change event |
| $h_{CE}$ | Average elevation change during a change event |
| $\tilde{X}$ | the median value of a set X |
| $P$ | A set of profiles |
| $pi$ | The $i^{th}$ profile in a set |
| $pi_j$ | The $j^{th}$ vertex of the $i^{th}$ profile in a set |
| $pi_{j,x}$ | Distance to landward vertex of the $j^{th}$ vertex of the $i^{th}$ profile in a set |
| $pi_{j,z}$ | Elevation of the $j^{th}$ vertex of the $i^{th}$ profile in a set |
| $p_{ma}$ | the first 4 vertices in a profile |
| $p_{mu}$ | the last 4 vertices in a profile |
| $\Delta_{P,N}$ | Mean absolute difference in elevation between N profiles of a set P |
| $D_{P,N}$ | Mean distance between N profiles of a set P |
| $R$ | Relief: difference in elevation between |
| $Smax$ | Maximum slope of the scarp |
| $S_{ma}$ | Overall slope of $p_{ma}$ |
| $S_{mu}$ | Overall slope of $p_{mu}$ |

**Table 4.2:** Notations used in this chapter

## 4.1 Abstract

Retreat and progradation make the edges of salt marsh platforms their most active features. If we have a single topographic snapshot of a marsh, is it possible to tell if some areas have retreated or prograded recently or if they are likely to do so in the future? We explore these questions by characterising marsh edge topography in mega-tidal Moricambe Bay (UK) in 2009, 2013 and 2017. We first map outlines of marsh platform edges based on lidar data and from these we generate transverse topographic profiles of the marsh edge 10 m long and 20 m apart. By associating profiles with individual retreat or progradation events, we find that they produce distinct profiles when grouped by change event, regardless of event magnitude. Progradation profiles have a shallow scarp and low relief that decreases with event magnitude, facilitating more progradation. Conversely, steep-scarped, high-relief retreat profiles dip landward as retreat reveals older platforms. Furthermore, vertical accretion of the marsh edge is controlled by elevation rather than its lateral motion, suggesting an even distribution of deposition that would allow bay infilling were it not limited by the migration of creeks. While we demonstrate that marsh edge geometry can be quantified with currently available DTMs, oblique observations are crucial to fully describe scarps and better inform their sensitivity to wave and current erosion.

## 4.2 Introduction

The alarming landward retreat of well-known salt marsh systems such as those of the Mississippi delta's "Bird Foot" (Day et al., 2000; Jankowski et al., 2017) or of the Venice Lagoon (Carniello et al., 2009) has sparked concern for the future of these highly valuable landscapes (Barbier et al., 2011; Costanza et al., 1997; Spivak et al., 2019). Salt marshes filter organic and metallic pollutants (Marques et al., 2011; Nelson and Zavaleta, 2012) and provide important nursing grounds for wildlife, including commercially exploited species such as Brown Shrimp (Haas et al., 2004). Furthermore, their high productivity makes salt marshes important sites of blue carbon sequestration (Chmura et al., 2003a) and their vegetation

and topography reduce storm surges and damp waves (Möller, 2006; Möller and Spencer, 2002; Möller et al., 2014; Shepard et al., 2011; Stark et al., 2016). The loss of salt marshes to the sea is predicted to cause significant losses to the ecosystem services they provide (Zedler and Kercher, 2005) and release stored carbon into the ocean (Coverdale et al., 2014; Kirwan and Mudd, 2012), diminishing its capacity to siphon atmospheric carbon.

Although the extent of their vulnerability is regularly debated (Ganju et al., 2017; Kirwan et al., 2016a; Saco et al., 2017), studies repeatedly show that some salt marsh environments are at risk of drowning due to sea level rise (Kirwan and Guntenspergen, 2010; Voss et al., 2013) despite the bio-geomorphic feedbacks (D'Alpaos and Marani, 2016; Mudd et al., 2009) that led to the emergence of marsh platforms from bare mudflats in the first instance (Marani et al., 2013). Frequently, this drowning has been attributed to insufficient sediment supply (Syvitski et al., 2009; Weston et al., 2014).

Vertical challenges to salt marsh survival are matched by lateral retreat, notably driven by waves and tidal currents. Multiple studies have focused on the impact of external forcing on the landward constriction of salt marsh habitat (Leonardi and Fagherazzi, 2014; Leonardi et al., 2016a; Mariotti and Fagherazzi, 2010), as well as the mutual interaction between wave impact, retreat processes and the morphology of retreating marsh margins (Bendoni et al., 2014; Francalanci et al., 2013; Tonelli et al., 2010). While marsh retreat is also demonstrably linked to nearby channel deepening in a macro-tidal setting (Butzeck et al., 2016; Cox et al., 2003), the action of tidal currents on marsh margins remains poorly understood relative to wave action.

Likewise, remote observation of salt marsh margins are scarce in the literature, in contrast with the wealth of documentation on the use of light detection and ranging (lidar) and hyperspectral data to characterise marsh platform elevation and vegetation (Farris et al., 2019; Hladik et al., 2013; Sadro et al., 2007; Silvestri et al., 2003). This knowledge gap hampers our understanding of present coastal mobility in general but also our predictions of the future retreat or advance (which we refer to as progradation) of salt marshes. The mobility of marsh edges is often

studied through the determination of wave- or current-generated stresses rather than direct observation of marsh edges. This lack of observation data prevents us from contextualising results on the influence of scarp topography on wave action (Tonelli et al., 2010).

The paucity of data on marsh edge topography may be due to technical difficulties: in many micro-tidal systems and some meso-tidal systems the foot of the marsh scarp is rarely exposed (Carniello et al., 2016) and few sites have as good topo-bathymetric data as the repeatedly studied Venice Lagoon in Italy (Molinaroli et al., 2009) and Plum Island in Massachussets, USA (Fagherazzi et al., 2014), both of which are the object of long-term monitoring campaigns. Moreover, the spatial resolution of airborne lidar images is usually in the range of 1–5 m, which reduces the perceived slope of scarps, despite being the most fine-grained remote sensing method used to cover large marsh systems (Webb et al., 2013). More importantly, scarps cannot be observed by nadir-facing airborne lidar surveys due to their sub-vertical face. Finally, many salt marsh are dominated by *Spartina alterniflora* or *Spartina anglica*, plants that lead to errors of $15 - 55$ cm on lidar elevations, with errors of up to 1.70 m along creek banks (Chassereau et al., 2011). For low-lying micro-tidal marshes (and to a lesser extent, meso-tidal marshes), such errors are of the order of scarp heights. These factors combined complicate the study of marsh margin morphology.

Conversely, macro- to mega-tidal mudflats are more frequently exposed, increasing the opportunities for purely topographic surveys. In these conditions marsh platforms are often higher in the tidal frame than their microtidal cousins (Goodwin and Mudd, 2019), with retreating margins often taking the shape of scarps more than $1m$ in height fronted by degrading fallen blocks, locally known as saltings (Figure 4.1c). These scarps contrast sharply with prograding margins, which exhibit shallow or non-existent scarps fronted by pioneer species like *Salicornia sp.* or *Sarcocornia sp.* (Figure 4.1b). As illustrated by these images of Skinburness Marsh in Moricambe Bay (Cumbria, United Kingdom), grazed marshes dominated by *Puccinellia maritima* have low vegetation near their margin, thus reducing the typical elevation bias caused by vegetation cover (Parrish

et al., 2014; Rogers et al., 2018; Schmid et al., 2011).

Under such conditions, we assume that salt marsh margins are sufficiently well defined to discern their morphology with lidar data. In this contribution, we use modern feature detection methods to extract salt marsh outlines from three lidar surveys covering the sheltered mega-tidal Moricambe Bay. From these outlines, we produce regularly spaced transverse profiles of the marsh margin topography. The profiles are attached to unique change events corresponding to localised and contiguous retreat or progradation between two observation times. Using these data, we detach margin profiles from their spatial context to examine the morphological difference between retreating and prograding margins. We

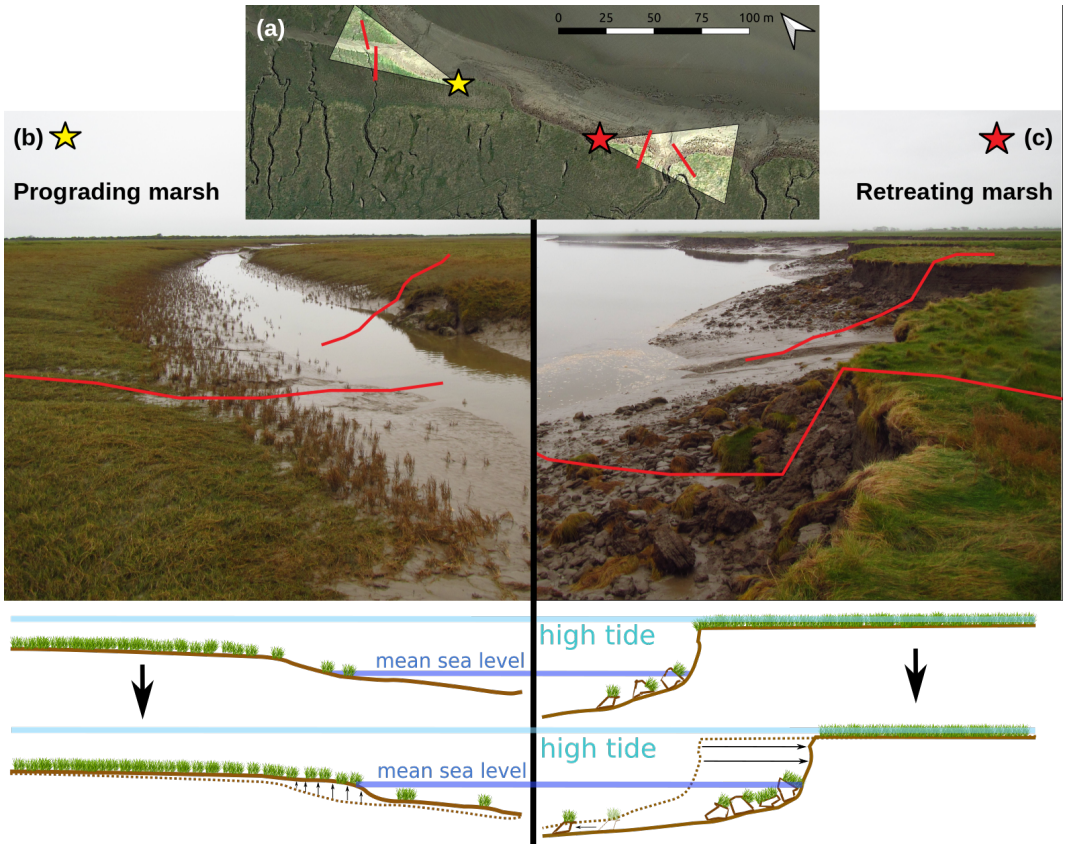


**Figure 4.1:** Aerial and ground views of salt marsh margin profiles. (**a**) aerial view of photography point of views and location of profiles; (**b**) photography of prograding margins (G. Goodwin, November 2016) and schematic profiles. The diagramme below provides a schematic view of the process of progradation; (**c**) photography of retreating profiles (G. Goodwin, November 2016) and schematic profiles. The diagramme below provides a schematic view of the process of retreat. Profiles on the photographs in panels (**b**,**c**) are deliberately drawn with low resolution to illustrate the perspective from $1m$ lidar data.

then focus on the properties of marsh margin relief to examine the distinctive properties of prograding and retreating margins with respect to the volume of displaced sediment, as well as the response of marsh margin elevation to retreat or progradation. The variety of retreating and prograding marsh margins in Moricambe Bay allows us to examine the morphology of a wide range of active margins for the years 2009, 2013 and 2017.

## 4.3 Site Description

The Solway Firth is a mega-tidal estuary separating Dumfries and Galloway in Scotland from Cumbria in England (Figure 4.2b). The Northern Cumbrian coastline is renowned for its active salt marshes, which show evident signs of both retreat and progradation (Figure 4.1). The bay of Moricambe, its North-West facing entrance enclosed between the Grune Cast sand spit and Cardurnock Flatts, is no excepti on and provides a sheltered environment where wide marshes have developed (Figure 4.2a). There, the meandering of the tidal rivers Wampool (North) and Waver (South) appear to be the main constraint on the development of salt marshes, generating autocyclic retreat and progradation (Singh Chauhan, 2009), of which the terracing of Skinburness Marsh (see Figure 4.5a) is a remnant. Likewise, the southern part of Newton Marsh shows signs of progradation enabled by the further distance of channels.

Such diversity in the active marsh margins is central to our study. The main activity on the salt marshes is cattle grazing, with both dairy cows and sheep regularly being kept in pastures on the marsh platforms. Hence, the dominant vegetation in Moricambe Bay is grazed *Puccinellia maritima* which seldom exceeds 1–5 cm in height. This makes it an ideal site upon which to study marsh evolution using high resolution topographic data, as the low vegetation minimizes errors in topographic data. High resolution lidar topography covering the whole of Moricambe Bay is freely available through the UK Department for Environment and Rural Affairs (DEFRA), allowing for the implementation of feature-based marsh platform detection.

## 4.4 Materials and Methods

### 4.4.1 Collection and Pre-Processing of Topographic Data

We download point cloud topographic data from airborne lidar surveys of Morecambe Bay within the area of interest (red polygon in Figure 4.2a) from the DEFRA data repository for 2009, 2013 and 2017 (https://environment.data.gov.uk/DefraDataDownload/?Mode=survey). DEFRA provides the last return for every point (the density of which does not exceed 6 pts·m$^{-2}$). This does not necessarily imply that the last return is the ground or bare earth, as dense vegetation on the marsh platform may prevent the laser from hitting the ground (Hladik and Alber, 2012a; Rogers et al., 2016b, 2018). However, thanks to pastoral activities in Moricambe Bay, vegetation rarely exceeds 5 cm and does not cause significant errors in measured elevations such as those reported reported by Hladik and Alber (2012a) on marshes with tall vegetation. The grazing of cattle observed in Moricambe Bay also incidentally causes compaction of deposited sediment on the marsh soil, to a degree which is still difficult to estimate (Elschot et al., 2013). This is not accounted for in the generation of the DEM since it is unlikely to affect ground elevation through DEM texture. We convert the point clouds to rasters with a grid resolution of 1 m, generating Digital Terrain Models (DTMs) for each year. At the ground-truthing points within the Ordnance Survey tile NY15 (https://environment.data.gov.uk/DefraDataDownload/?mapService=EA/LIDARGroundTruthSurveys&Mode=spatial), we find that the mode of the 2017 DTM is higher than the mode of the 2013 DTM by 7 cm and than the mode of the 2009 DTM by 5 cm (Figure 6.11).

For the purposes of this contribution, we are more interested in short-term sediment deposition or removal than long-term land movements caused by post-glacial uplift. We correct for long-term land movements by comparing stable infrastructure (e.g., roads) between DTMs. For these corrections, we use the 2017 DTM as reference. After correction, the Root Mean Square Error (RMSE) between GPS-acquired points and the lidar DTM are the following: for the 2009 DTM, the RMSE is 6.8 cm (Figure 6.12a); for the 2013 DTM, the RMSE is 6.5

cm (Figure 6.12b); for the 2017 DTM, the RMSE is 3.1 cm (Figure 6.12c). Each DTM is then clipped to the area of interest illustrated in Figure 4.2a. Because of the low vegetation ($< 3cm$ in height) shown in Figure 4.1, we do not apply an additional elevation correction to account for vegetation on the salt marsh platforms.

### 4.4.2 Determination of Marsh Outlines and Profiles

For each of the DTMs, we isolate marsh platforms using the Topographic Identification of Platforms (TIP) method (Goodwin et al., 2018), described in detail in Chapter 2. The TIP method uses a high-resolution DTM in raster format (e.g., from lidar data) to classify pixels as "marsh platform" or "tidal flat" within an area of interest. The TIP method proceeds in two major steps: (i) the determination of marsh outlines and (ii) the filling of marsh platforms.

For step (i), the product of dimensionless relief and slope is calculated as shown in Equation (4.1):

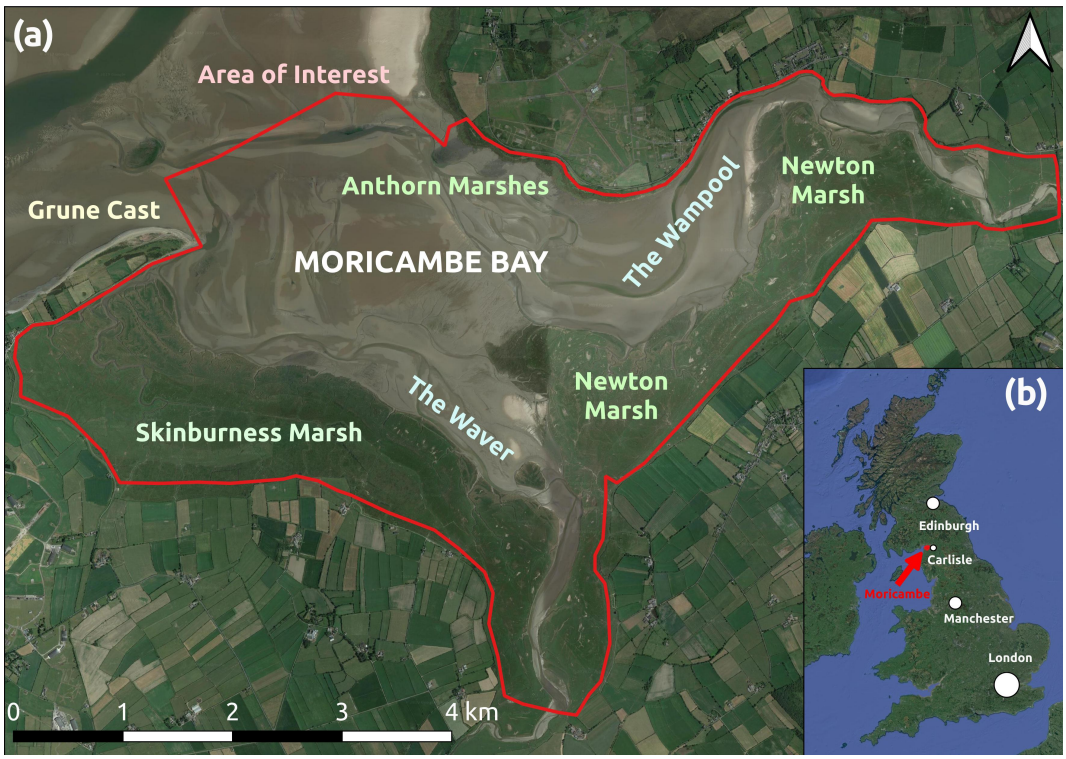


**Figure 4.2:** Satellite view of Moricambe Bay (**a**) and location within the United Kingdom (**b**). Image credit Google Earth (30 June 2018).

$$P^* = \frac{z - z_{min}}{z_{max} - z_{min}} * \frac{s - s_{min}}{s_{max} - s_{min}}, \tag{4.1}$$

where $z$ is the elevation of the pixel, $z_{min}$ is the minimum elevation in the DTM and $z_{max}$ is the maximum elevation in the DTM. The same notation applies to the pixel slope $s$, determined from the DTM after Hurst et al. (2012). The distribution of $P^*$ in a salt marsh DEM is typically exponentially decreasing: hence, pixels for which the slope of the distribution of $P^*$ is lower than $Sp_{thresh}$ are retained as potential marsh scarps. Local maxima of $P^*$ within the retained pixels are then used to initiate scarps, which are then routed along "crests" of high $P^*$. $ZK_{thresh}$ then determines a high-pass filter to determine definitive scarps. This step is sensitive to the presence of small marsh scarps. For step (ii), platforms are generated by progressively "filling" the pixels above the scarps over multiple iterations. Pixels in the lower part of the elevation distribution of the newly generated platforms are then eliminated, using $rz_{thresh}$ to determine the percentage of the distribution to eliminate after the lowest point of the elevation distribution. The result of these two steps is a classified raster, with values of 0 for tidal flats and 1 for marsh platforms.

Moricambe Bay is larger than most sites for which the TIP method was tested. Furthermore, while the TIP method was shown to be effective for marsh platforms exhibiting a well-defined scarp, this is not the case everywhere in Moricambe Bay. Hence, we separate the study site into 21 sectors and implement the TIP method on each sector with different parameters. The sectors were defined using GoogleEarth imagery to minimise the overlap of mature and young platforms within any given sector, so as to avoid the TIP method mistaking the younger, lower platforms for tidal flats. Figure 6.13 shows the layout of the sectors and Tables 6.7, 6.8 and 6.9 record the parameters used in each sector. The TIP method tends to exclude pools and disconnected channels from the marsh platform, thus creating complex and discontinuous marsh platforms which do not correspond to the most seaward marsh margin. To keep only the most seaward outlines, we use a negative image of the TIP method's original results (see Figure 6.14a) to identify tidal flats, of which we select only the largest. In Figure 6.14a, this is the

northernmost tidal flat. Any pixel within the area of interest not classified as a tidal flat is then considered a marsh platform, yielding Figure 6.14b. A close-up of marsh platforms for each year are shown in green in Figure 4.3a.

Along the seaward outline of each marsh platform, we generate transverse profiles of 10 m in length, spaced regularly by 20 m, as shown in Figure 4.3a. The length of 10 m was chosen as a compromise to cater for the need to observe the as much of the margin in prograding areas and as little of the non-marginal areas in retreating zones, as well as to speed up profile generation. Each 10 m long profile contains 11 vertices (one each meter, including the starting and ending points). We extract the topography of each individual profile for all 3 years, as shown in Figure 4.3b–d. Each year will have its own set of marsh profiles. This is because the orientation of the marsh edge changes when the marsh outline progrades or retreats: hence, a profile that is orthogonal to the marsh outline in 2009 may not be in 2013 or 2017, thus rendering a direct comparison of profile geometry impossible. An approach using sets of profiles for each year is therefore preferable to one using a single set of profiles for all three years. Indeed, the latter approach, using longer profiles, would be suited to analyse the geometry of entire marsh platforms but not of features with small footprints like scarps. But in addition we record the elevations at every profile vertex for all three years. That means that any set of 11 nodes within an individual year's profile will be associated with 3 topographic profiles.

Each vertex $p_i$ of a profile $p$ is defined by the coordinates $(p_{i,x}, p_{i,z})$, respectively the seaward distance and elevation of $p_i$. The marsh edge $p_{ma}$ is defined as the first 4 vertices of $p$ (green background in Figure 4.3b–d), while the mudflat edge $p_{mu}$ is defined as the last 4 vertices of $p$ (brown background). We introduce this subdivision of the profiles to avoid the influence of fallen blocks when determining the relief $R$, defined in Section 4.5.3. This assumes the landward-to-seaward length of fallen blocs to be under 4 m, which is consistent with field observations at the site. In the example shown in Figure 4.3, profiles in 2009 and 2013 show little signs of a scarp (b,c), hinting at a prograding evolution which is stopped in 2017, as we observe a visible retreat scarp about 1 m further inland

than the scarps in 2013 and 2009 (d).

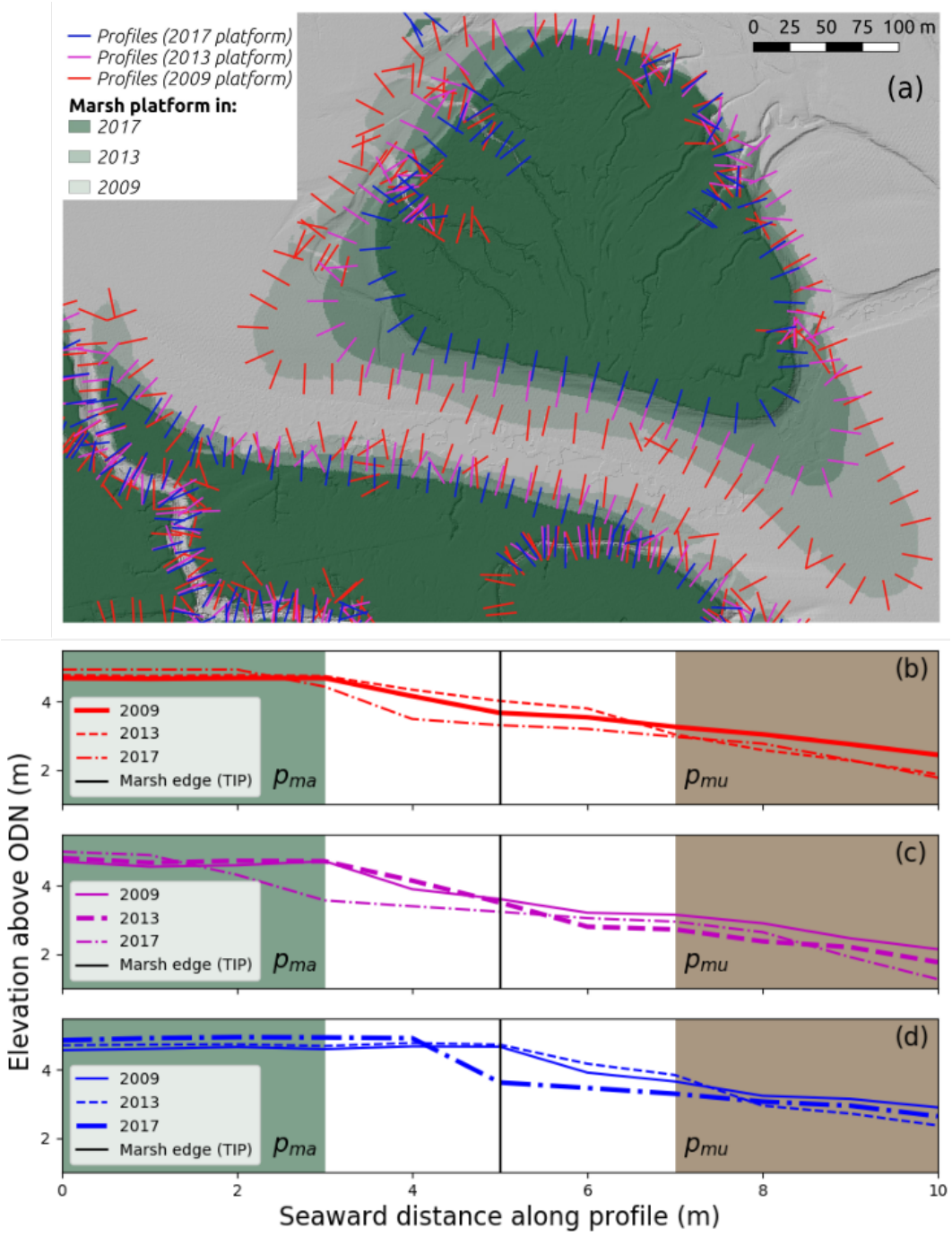


**Figure 4.3:** Evolution of scarp profiles over the years: (**a**) map of marsh platforms near the mouth of the Waver and location of scarp profiles; example of a scarp profile associated with a various marsh outlines, with elevations for all three years; (**b**) 2009 outline; (**c**) 2013 outline; (**d**) 2017 outline. Bold lines indicate the current profile. In (**b–d**) green portions represent the marsh-side of the profile $p_{ma}$ and brown portions represent the mudflat-side of the profile $p_{mu}$.

### 4.4.3 Determination of Change Events

By comparing the marsh platforms generated in Section 4.4.2, we determine the trajectory of each pixel between 2009 and 2017, defined as the record of its classification as marsh platform or mudflat. Each of the 8 possible trajectories for a pixel is shown in Figure 4.4b. For instance, a pixel classified as a marsh platform in 2009, as a mudflat in 2013 and as a marsh platform in 2017 would follow trajectory 8. The trajectory of each pixel as seen in Figure 4.4a is colour-coded according to Figure 4.4b. All pixels except those following trajectories 1 and 2 undergo at least one change of classification between 2009 and 2017.

As illustrated in Figure 4.4a, groups of contiguous pixels tend to follow the same trajectory. Even if pixels do not share a full trajectory, many share partial trajectories. For instance, pixels following trajectories 4 and 8 are both converted to mudflats between 2009 and 2013. In this contribution, we refer to groups of contiguous pixels this conversion as change events ($CE$), indicated as red and blue circles in Figure 4.4b. In this instance, a change event involving the conversion of marsh platforms to mudflats and occurring between 2009 and 2013 may include pixels following trajectories 4 and 8. Likewise, a change event involving the conversion of mudflats to marsh platforms and occurring between 2013 and 2017 will include pixels following trajectories 8 and 5. Thus, a pixel may be involved in up to two change events and each change event is a unique group of contiguous pixels that can be given a unique identification.

We identify all change events larger than 3 contiguous pixels (3 $m^2$), with contiguity being defined within neighbourhoods composed of the eight adjacent pixels (i.e., both cardinal directions and diagonal pixels). Retreat events ($RE$), during which the marsh margin recedes landward, are lined with the most recent profiles on the landward side and the least recent on the seaward side and vice versa for progradation events ($PE$). Thus, each change event accepts as boundaries the marsh outlines that border it and is associated with two sets of profiles: one preceding the change and another resulting from the change (Figure 4.4c). This association between change events and sets of profiles will constitute the basis of our morphological analysis.

Individual change events in each of the 2009–2013 and 2013–2017 periods can be quantified by their total volume $V_{CE}$, surface area $A_{CE}$ and average sediment accumulation $h_{CE}$. Throughout this contribution, we show volumes of change events as positive values to accommodate logarithmic scaling in our figures. However, since retreat events are associated with loss of sediment, change event volume in the figures is such that $V_{CE} = V_{PE}$ for progradation events and $V_{CE} = -V_{RE}$ for retreat events. It is important to note that volume change calculations are subject to lidar error and error caused by vegetation. The latter in particular causes almost exclusively positive error (i.e. ground elevation is overestimated) (Rogers et al., 2016b). Hence, all absolute values of volume and elevation change for both progradation and retreat events are maximum estimates.

### 4.4.4 Profile Comparison and Metrics

In order to understand to what extent change events are correlated with the geometry of marsh margins, we investigate the differences between prograding and retreating profiles. Margin profiles are grouped in sets, each set being associated with a unique change event. To compare the morphology of margin profiles, we define the mean absolute elevation difference $\Delta_{P,N}$ of a set $P$ of $N$ profiles each of length $L$ in Equation (4.2):

$$\Delta_{P,N} = \frac{2}{N(N-1)} * \sum_{\substack{k=1 \\ j<k}}^{N} \sum_{j=1}^{N} \frac{\sum_{i=1}^{L} \sqrt{((pj_{i,z} - pj_{0,z}) - (pk_{i,z} - pk_{0,z}))^2}}{L}, \tag{4.2}$$

where $(pj_{i,z} - pj_{0,z})$ is the elevation of the vertex $pj_i$ of the profile $pj$ relative to the elevation of the first vertex $pj_{0,z}$. The first sum defines the average geometric difference between two profiles by comparing them relatively to their respective most landward elevation. The term $\frac{2}{N(N-1)} * \sum_{\substack{k=1 \\ j<k}}^{N} \sum_{j=1}^{N} X$ is the average of the first sum over all possible combinations of non-identical profiles within $P$. For example, a set $P$ for which $\Delta_{P,N} = 0$ would contain profiles of identical geometry, regardless of their location. $\Delta_{P,2}$ is used further in this chapter to describe the

mean absolute elevation difference in a pair of profiles.

For small events, the close proximity of profiles may play a role in their similarity. Numerous small events may then skew the distribution of $\Delta_{P,N}$ toward lower values. To test this hypothesis, we define the mean inter-profile distance

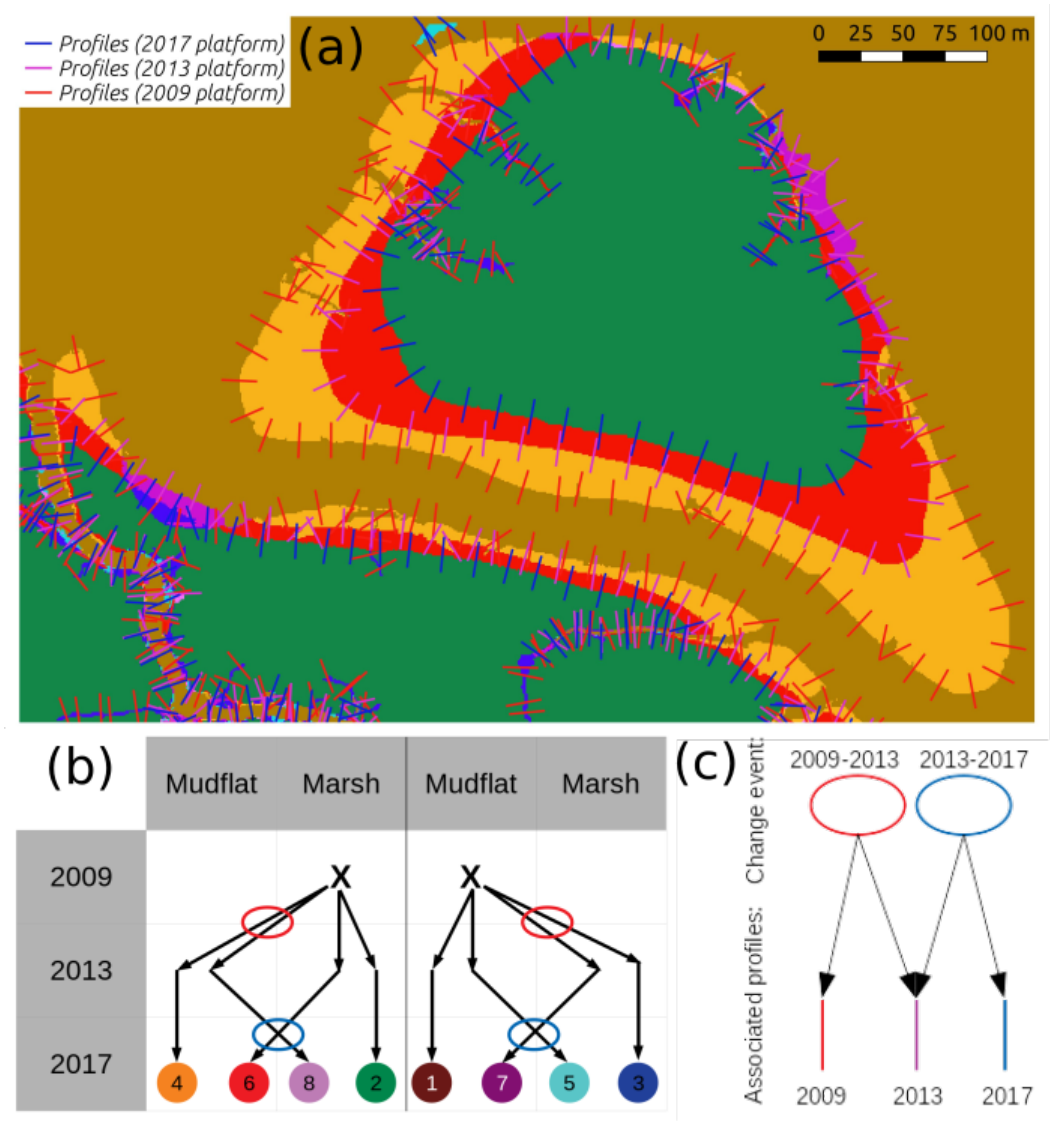


**Figure 4.4:** Diagram showing possible change events: (**a**) map of classified pixel trajectories near the mouth of the Waver and location of scarp profiles; (**b**) colour and number codes for each of the 8 possible pixel trajectories. Ellipses represent retreat or progradation events for each trajectory; (**c**) Diagram showing how change events are associated with profiles. Example: in (**a**), 6 contiguous areas are coded 4, thus generating 6 individual change events; in (**b**), pixel trajectories coded 4 mark retreat between 2009 and 2013 followed by stability; in (**c**), the profiles at the boundaries of the areas coded 4 are 2009 on the seaward side and 2013 and 2017 on the landward side, since there was no evolution between 2013 and 2017.

$D_{P,N}$ of a set $P$ of $N$ profiles in Equation (4.3):

$$D_{P,N} = \frac{2}{N(N-1)} * \sum_{\substack{k=1 \\ j<k}}^{N} \sum_{j=1}^{N} d_{jk}, \tag{4.3}$$

where $d_{jk}$ is the distance between the centre points of profiles $pj$ and $pk$. $D_{P,N}$ therefore expresses the average distance between pairs of profile centroids within a change event. We also define metrics to characterise profile geometry in simple terms: first, the relief $R$ (Figure 4.9a) is defined for a set $P$ of $N$ profiles according to Equation (4.4), where $p_{\tilde{ma},z}$ is the median elevation of the marsh portion of all profiles in the set and $p_{\tilde{mu},z}$ is the median elevation of the mudflat portion of all profiles in the set.

$$R = \tilde{p}_{ma,z} - \tilde{p}_{mu,z}. \tag{4.4}$$

We also define the maximum Slope $Smax$ (Figure 4.9b) of the marsh scarp according to Equation (4.5), where $i \in [3:6]$ and $l = 1m$. This definition ensures that $Smax$ is the closest possible approximation of the real scarp slope.

$$Smax = max(\frac{p_{i,z} - p_{i+1,z}}{l}). \tag{4.5}$$

Finally, we define the slope $S$ (Figure 4.9c,d) of the marsh platform and the mudflat according to Equation (4.6), where $i = 0, j = 3, l = 3m$ (marsh slope $S_{ma}$) and $i = 7, j = 10, l = 3m$ (mudflat slope $S_{mu}$).

$$S = \frac{\widetilde{p_{i,z} - p_{j,z}}}{l}. \tag{4.6}$$

## 4.5 Results and Discussion

### 4.5.1 Location and Properties of Change Events

The elevations of Moricambe Bay in 2009 can be seen in Figure 4.5a,where we show marsh platforms in colour and mudflats in greyscale. The marsh platforms

observed have a maximum elevation range of $4 - 7$ m across the bay. However, western Skinburness Marsh shows visible terracing, indicating a progressive development of the marsh in the shadow of Grune Cast with multiple growth interruptions (Allen, 1989). In this case, the interruptions were caused by the meandering of the River Waver (Singh Chauhan, 2009). Both Skinburness and Newton Marshes show a distinctive increase in elevation with distance upstream of the tidal rivers, indicating a constriction of tidal flows (Leblond, 1978). By 2013, large progradation events have considerably increased the surface area of Newton Marsh (Figure 4.5b), depositing 1 m or more of sediment in some areas. Conversely, Skinburness Marsh has receded under the pressure of the meandering Waver, as have the northernmost portions of Newton Marsh under the influence of the Wampool. We note that most outlines that experienced retreat from their 2009 position are bordered by tidal channels in 2013. Marginal progradation is observed on the Anthorn Marshes. By 2017, Skinburness Marsh has retreated even further under the continued migration of the Waver, while the newly formed marshes of Newton Marsh, well advanced within the bay, are more exposed and show mixed behaviour (Figure 4.5c). This may be attributed to the anabranching of the Wampool along the northern Newton Marsh.

In Figure 4.6a,c, we observe that the surface-area-to-volume ratio $\frac{1}{h_{CE}} = \frac{A_{CE}}{V_{CE}}$ for progradation is larger than for retreat: indeed, between 2009 and 2013, the two largest retreat and progradation events have similar volumes ($\approx 2 \cdot 10^4$ m$^3$ and $\approx 4 \cdot 10^4$ m$^3$). This is in stark contrast with the change in surface area, which for the progradation events is approximately ten times larger. The same trend is observed between 2013 and 2017, although we notice a decrease in the volume and surface area of the largest progradation events. Hence, progradation events deposit less sediment than is eroded during retreat events of the same surface area.

While Figure 4.6a,c seems to show a linear relationship between Figure $V_{CE}$ and $A_{CE}$, panels (b,d) show that $h_{CE}$ appears to be nonlinearly related to the volume of change. The rate of $h_{CE}$ increases with increasing $V_{CE}$ for retreat events, hinting that larger retreat events may be caused by the migration of

deeper creeks or the retreat of higher marsh platforms. During the largest retreat events, which correspond to the migration of the Waver into Skinburness Marsh, approximately 4 m of elevation is removed on average, showing the conversion of

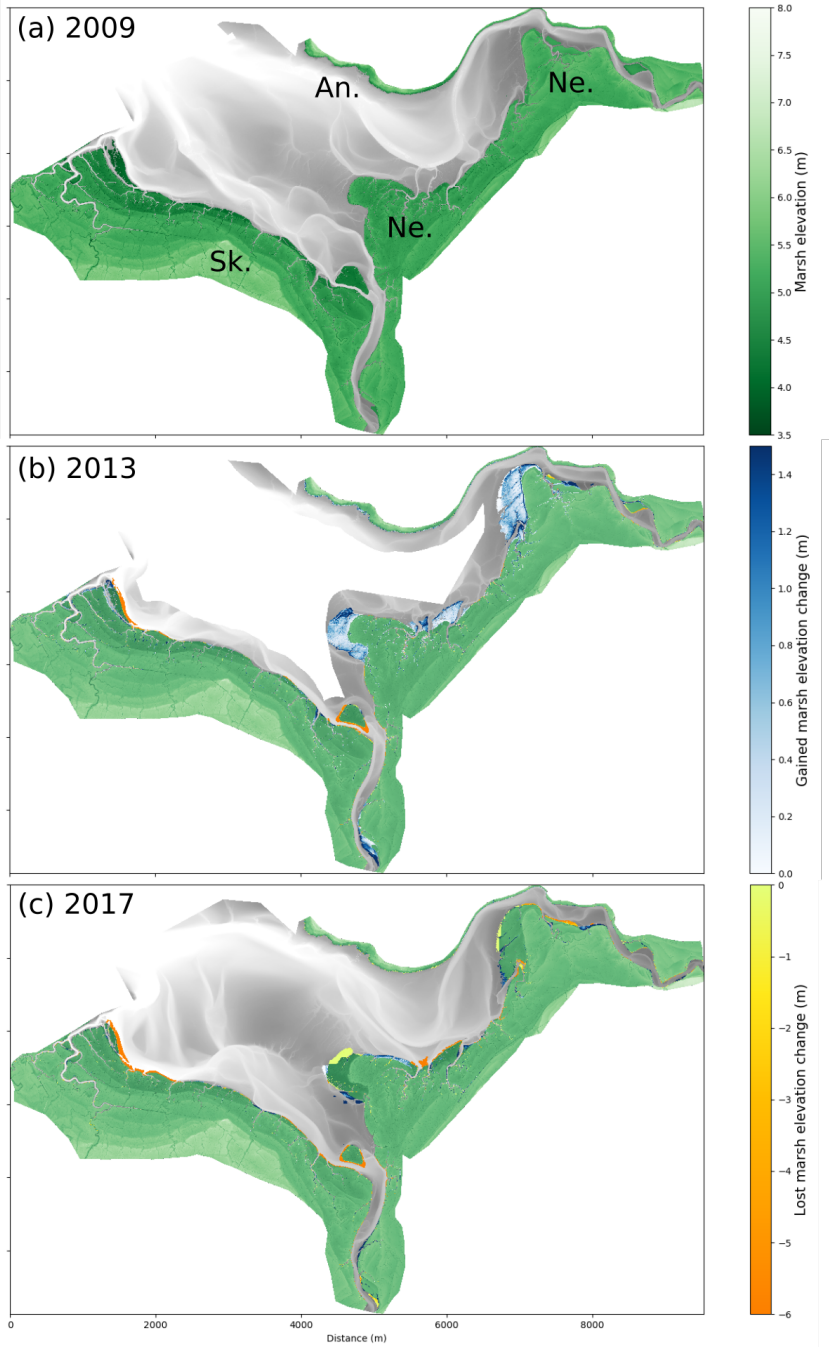


**Figure 4.5:** Elevation and evolution of Moricambe Bay: (**a**) elevation of marsh platforms (greens) and mudflats (greys) in 2009; (**b**) elevation of marsh platforms and mudflats in 2013 and gained (blues) and lost (oranges) marsh platforms in 2013; (**c**) elevation of marsh platforms and mudflats in 2013 and gained (blues) and lost (oranges) marsh platforms in 2017.

a reasonably high marsh platform (see Figure 4.1b.) into a deep tidal creek and not a tidal mudflat.

In prograding sections, $h_{CE}$ increases very slowly with increasing volume of change, only once exceeding 1 m in depth and averaging under 0.3 m. These rates of accretion remain high but are neither impossible (Goodwin and Mudd, 2019) or unheard of for mega-tidal environments with high sediment supply (Leroux, 2013).

### 4.5.2 Geometric Separation between Retreat and Progradation Profiles

Figure 4.7 shows values of $\Delta_{P,N}$ for various cases in groups of six box and violin plots. Each violin plot, within each group, represents the distribution of $\Delta_{P,N}$ for the profiles described in the group. Likewise, boxplots show the first and last ten percentiles (black horizontal line), first and third quartiles (boundaries

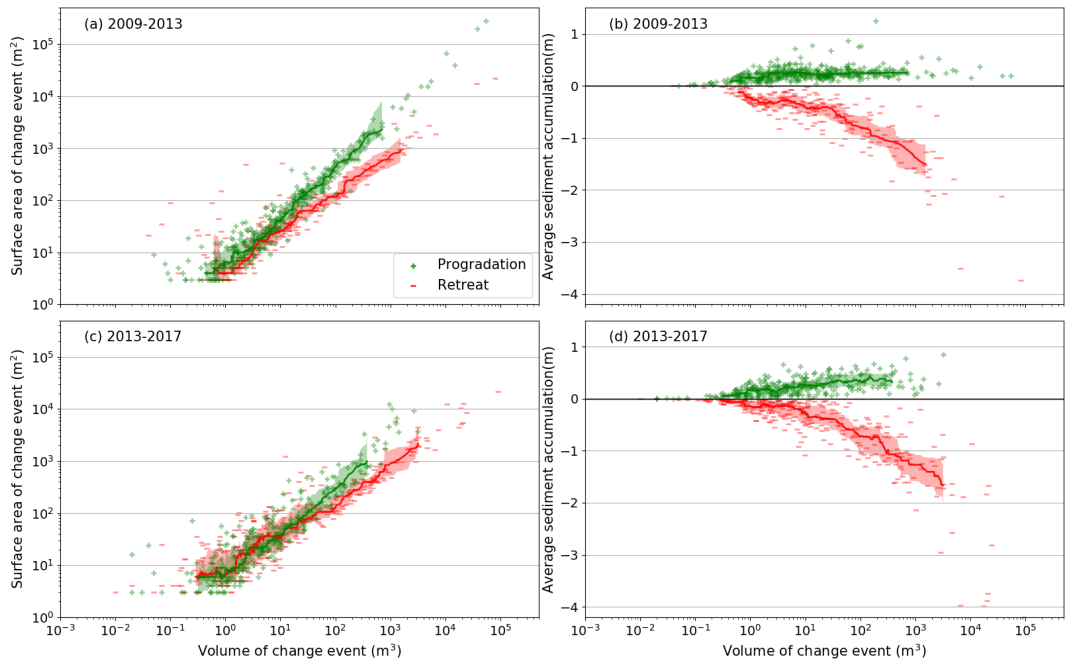


**Figure 4.6:** Properties of change events, expressed as a function of change event volume (the volume of loss events is negative). Surface area gained (green) or lost (red) in the 2009–2013 period (**a**) and 2013–2017 period (**c**); Average sediment depth deposited (green) or eroded (red) in the 2009–2013 period (**b**) and 2013–2017 period (**d**). Thick lines are a running median over 30 elements, surrounded by the 1st and 3rd quartiles (filled).

of the box) and median (orange line) within the distribution illustrated by the violin plots. The first and third groups focus on profiles in 2009 and 2013 about to be affected by change events, while the second and fourth group focus on profiles resulting from change events in 2013 and 2017. Within each group, solid line violin plots and their associated boxplots show the distribution of $\Delta_{P,2}$ for all pairs of retreating profiles (red), prograding profiles (green) or mixed pairs (grey). Dashed lines show the distribution of $\Delta_{P,N}$ for all sets of profiles tied to a retreat or progradation event (respectively red and green). The final (grey) element of each group represents the distribution of $\Delta_{P,N}$ for all combinations of one retreat event to one progradation event. The first three plots within each group are comparisons amongst pairs of all profiles, whereas the second set of three plots within each group are profiles compared amongst other profiles in their change event. We do this to see if there are universal differences in the profiles regardless of the change event (the first three plots) and if profiles within a change event or paired change events are similar (the second three plots within each group).

We observe that the distributions of $\Delta_{P,2}$ between retreating, prograding and mixed pairs are not obviously separable, indicating that the morphology of individual profiles alone is not enough to determine whether a profile has undergone or will undergo retreat or progradation. This result appears to contradict accepted understanding that retreating marsh margins exhibit a visible scarp while prograding margins often do not (Allen, 2000; Friedrichs and Perry, 2001) (see Figure 4.1). This is in fact a spurious byproduct of the gridding process from airborne lidar: DTMs derived in this way offer a nadir-facing perspective that cannot detect the near-vertical surfaces that are erosion scarps. Furthermore, aerial lidar data in our case study are gridded with a 1 $m^2$ cell size, which is larger than the typical footprint of a marsh scarp. Hence, the apparent slope of the scarp on a DTM is limited by the cell size of the DTM and is in effect the difference in elevation between two contiguous pixels containing the scarp. This discrepancy is the reason why the TIP method used to determine the marsh outline constructs lines of local slope maxima to locate marsh scarps and variably places the limit of the marsh margin at the top or the bottom of the scarp, as

can be seen in Figure 4.3d.

Conversely, when grouped into change events, profiles exhibit a far greater degree of similarity, depicted by the latter three plots in each of the four groups in Figure 4.7. The distribution of $\Delta_{P,N}$ for change events of the same nature (retreat or progradation, respectively red and green dashed distributions) spans significantly lower values of $\Delta_{P,N}$ than that of $\Delta_{P,2}$ for paired profiles for change events of the same nature in all four instances shown in Figure 4.7. Furthermore, the distribution of $\Delta_{P,N}$ for pairs of change events of a different nature (grey dashed distributions) span values of $\Delta_{P,N}$ far greater than for profiles grouped by change events of the same nature (i.e., either progradation or retreat). The data therefore suggest that we can distinguish the morphology of marsh outlines affected or generated by change events of the same nature from those generated by different events, confirming the findings of Evans et al. (2019), despite our inability to observe the morphology of the scarp itself. Akin to observations in

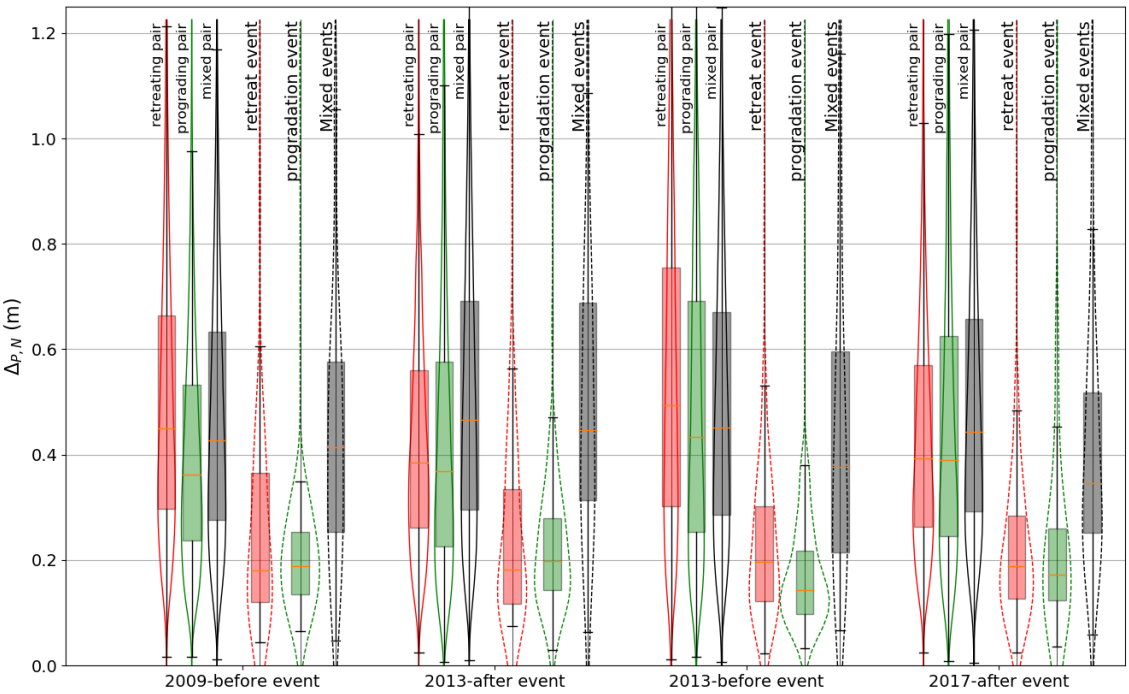


**Figure 4.7:** Boxplots and full distribution of $\Delta_{P,N}$ for various configurations. Distributions with continuous lines are $\Delta_{P,2}$ for pairs containing two retreating (red) or prograding (green) profiles or mixed pairs (grey). Distributions with dashed lines are $\Delta_{P,N}$ for all retreat events (red) and progradation events (green) or paired retreat and progradation events (grey).

mountainous regions (Grieve et al., 2016a), we find that a key feature of salt marsh geomorphology, such as an erosion scarp, may be characterised at grid resolutions greater than its spatial dimension.

This observation alone does not imply an exclusive relationship between the nature of marsh outline mobility and the profile geometry observable through airborne lidar. As shown in Figure 4.6 (a,c), only a dozen change events of either retreat or progradation are larger than 1000 $m^2$ (0.1 ha) and for small events, the close proximity of profiles may play a role in their similarity. Hence, small events can skew the distribution of $\Delta_{P,N}$ toward lower values.

Figure 4.8 shows the relationship between $\Delta_{P,N}$ and various metrics relating to profile proximity. Panels (a,c) express $\Delta_{P,N}$ as a function of $D_{P,N}$ both before and after change events and show no clear relationship between the two quantities, with a 20-point moving median of $\Delta_{P,N}$ remaining relatively stable under 0.3 m for retreat and progradation events. $\Delta_{P,N}$ is also noted to be fairly constant with the surface area of change events (b,d). Both $D_{P,N}$ and $A_{CE}$ cause an increase in the number of profiles $N$: due to their regular spacing of 20 m, $L_P = 20{*}N$ can be used to express the minimum length of the change event's seaward outline and also shows no clear effect on $\Delta_{P,N}$. From this we conclude that the distance between profiles exerts no clear positive or negative influence on $\Delta_{P,N}$, thus confirming that the similitude in geometry observed within change events is likely linked to the nature of their evolution.

### 4.5.3 Event Magnitude and Profile Morphology

Having established that the different geometries of retreating and prograding marsh margins are observable from 1 m gridded lidar data, we investigate the influence of retreat and progradation on four topographic metrics: relief, scarp slope, marsh slope and mudflat slope. Figure 4.9 shows the distribution of the metrics within all sets of profiles that will undergo or underwent retreat or progradation between the identified periods of 2009–2013 and 2013–2017. Violin plots represent the distribution of $\Delta_{P,N}$ for the profiles described in the group. Coloured boxes in the boxplots show the interquartile range, with orange lines showing the

median of the distribution. We show the median elevations of marshes and mudflats for each change event in Figure 6.15.

$R$ (see Equation (4.4)) ranges between 0 and 3.5 m and is noticeably larger for retreat events than progradation events at the same time step. This is in line with photographic evidence provided in Figure 4.1 and consistent with the hypothesis that progradation generates new low marsh platforms which accrete to elevations above the mudflat through time, thus getting more exposed to erosive factors and adopting the typical scarp morphology (Marani et al., 2013; Mariotti et al., 2010). Both profiles about to be affected by change events and those generated by them appear to follow this pattern and also exhibit an increase in $R$ observed after change.

$Smax$ (see Equation (4.5)) follows a pattern similar to $R$ (this is inevitable given their definitions) but $Smax$ highlights the emergent patterns to a greater degree. On the other hand, contrary to $R$, $Smax$ is impacted by the resolution of the DTM. That retreating and prograding profiles show similar differences in

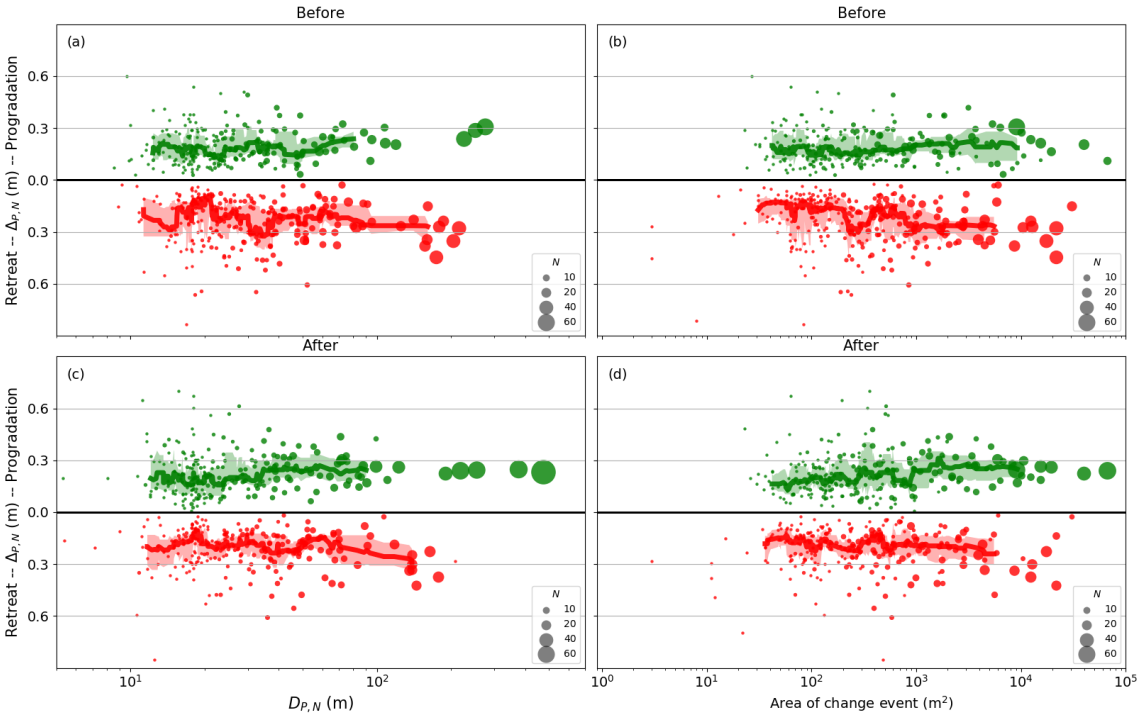


**Figure 4.8:** $\Delta_{P,N}$ for individual retreat and progradation events, expressed as a function of $D_{P,N}$ (**a**,**c**) and area of change event (**b**,**d**). (**a**,**b**) show profiles before events and (**c**,**d**) after events.

$R$ and $Smax$ before and after change events suggests that a retreating profile is likely to conserve its shape and continue to retreat, as a prograding profile is likely to continue to prograde. However this statement appears contrary to the fact that $R$ and $Smax$ values associated to change in events in the 2013–2017 period begin lower than in the 2009–2013 period. We note that not all of the marsh outline is affected by change events in each period. Therefore, Figure 4.9 is not depicting a paradoxical decrease in relief between profiles generated by change events in 2013 and those affected by change events in 2017 but rather the two years' change events sample from a different distribution of profiles. This in turn suggests that positive feedbacks causing marsh outlines to continue evolving in their current direction may be superceded by external forcings more powerful than bank resistance, causing bank erosion.

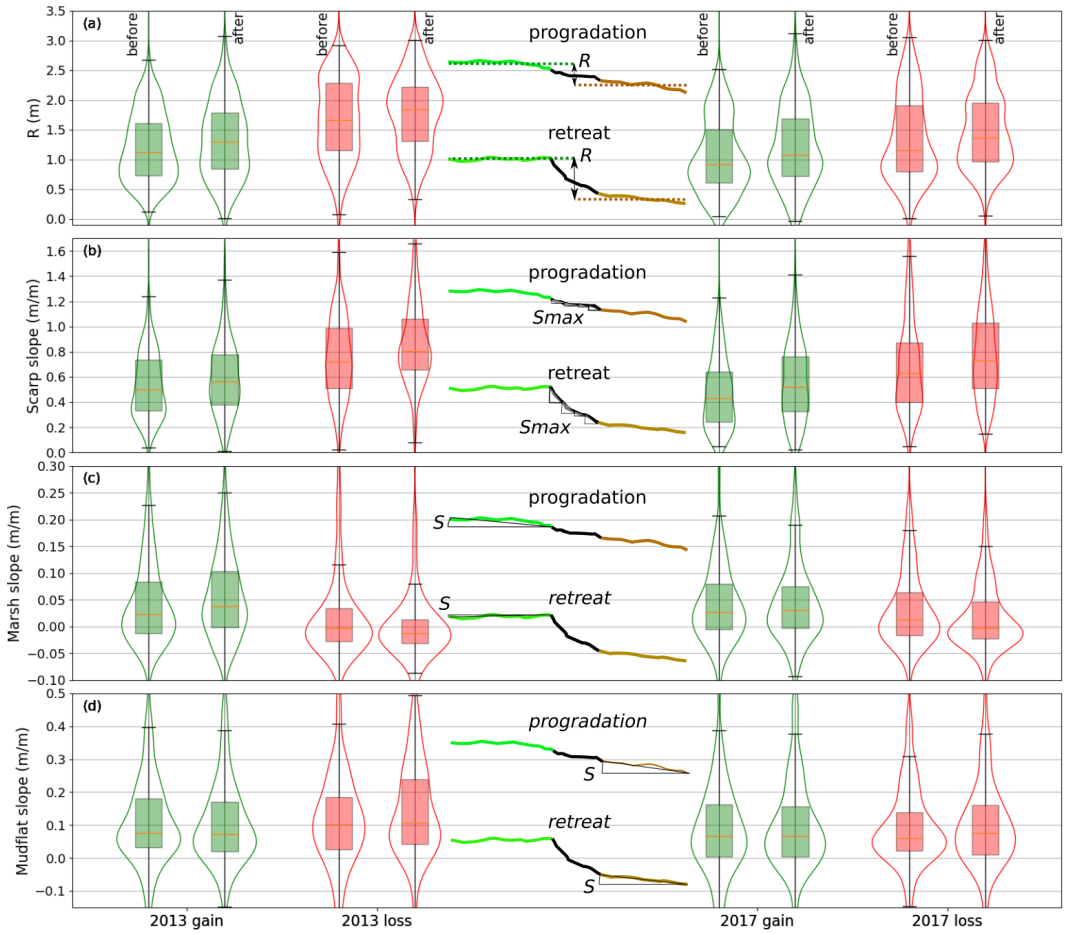


**Figure 4.9:** Boxplots and full distributions of marsh margin relief (**a**), maximum scarp slope (**b**), marsh slope (**c**) and mudflat slope (**d**). Diagrams in the centre of each panel represent the method to obtain the metric.

The distributions of $S_{ma}$ and $S_{mu}$ (see Equation (4.6)) follow different patterns: $S_{ma}$ is consistently higher for progradating profiles than for retreating profiles. Indeed, retreating profiles often display a slope that dips toward the land rather than sloping offshore (e.g., the slope is negative in Figure 4.9c). This landward dip is likely due to higher deposition rates occurring close to creek networks and the marsh edge, predicted by models (Mudd et al., 2004) and observed in the field (Temmerman et al., 2005). This decrease in slope contrasts with the slight increase in $S_{ma}$ for prograding profiles after progradation. For progradation events, the age of the marsh platform before progradation is unknown. After progradation however, the marsh surface is only 4 years old. As shown previously (Marani et al., 2010, 2013), a young marsh platform is a transitional form closer to the original tidal flat than a fully developed marsh platform and therefore has

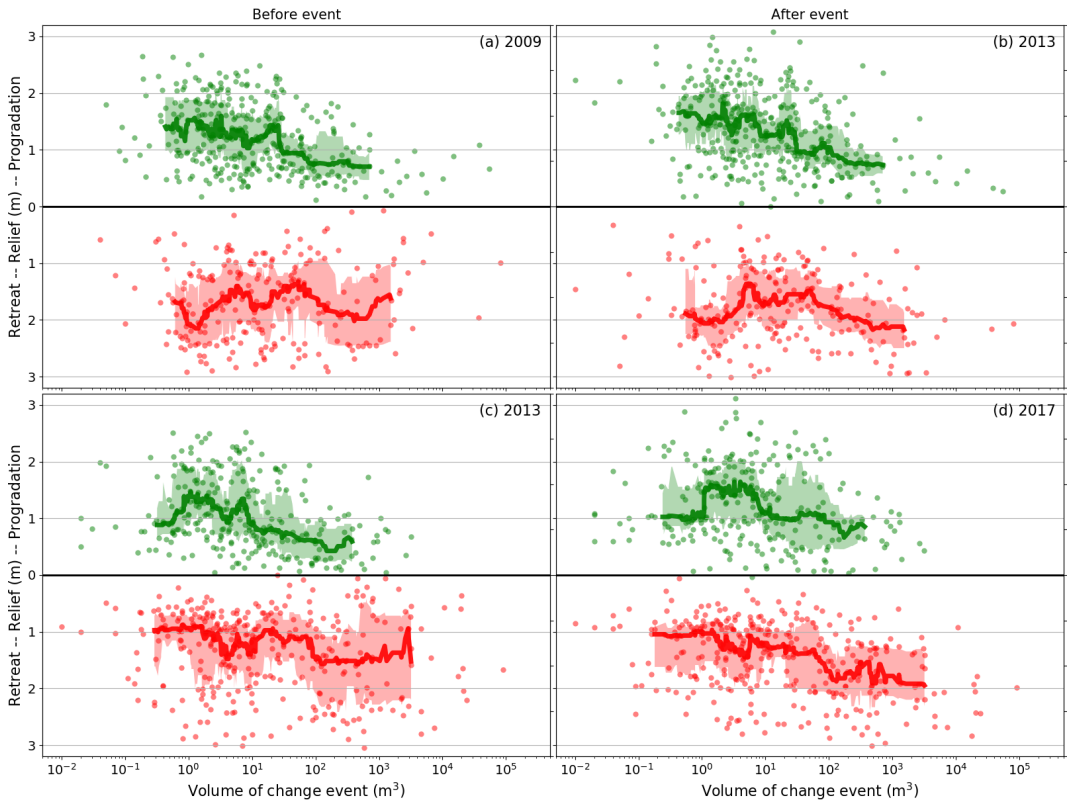


**Figure 4.10:** Marsh margin relief, expressed as a function of change event volume (the volume of loss events is negative) for profiles affected by change events (**a**,**c**) and resulting of change events (**b**,**d**), in the periods 2009–2013 (**a**,**b**) and 2013–2017 (**c**,**d**). Thick lines are a running median over 30 elements, surrounded by the 1st and 3rd quartiles (filled). Relief for prograding profiles (green) and retreating profiles (red) are mirrored through the $y = 0$ line.

a typically steeper slope. While we do not observe a significant difference in $S_{mu}$ between retreating and prograding profiles, we do note that retreating profiles experience an increase in mudflat slope after the retreat, whereas prograding profiles experience either no variation or a decrease in mudflat slope. These differences may be explained by the high likelihood of a creek bordering retreated profiles which causes the mudflat to appear steep.

Figure 4.10 examines more closely the relationship between change event volume and $R$, which is the only metric depicted in Figure 4.9 that is independent of DTM resolution. We observe that relief tends to decrease with increasing progradation event volume, both before and after progradation. Therefore, large progradation events tend to affect marsh outlines with low relief and also generate new outlines with low relief. Notably, the largest progradation events are associated with a post-event relief of less than 0.5 m. Hence, large progradation events produce marsh fronts which are close in elevation to the bordering mudflat. This creates a favourable environment for clonal and sexual colonisation, hydraulic conditions allowing (Hu et al., 2015). This suggests that, barring variations of mudflat elevation, for example due to wind-waves (D'Alpaos et al., 2013; Fagherazzi and Wiberg, 2009), the marsh will prograde until hydraulic and chemical conditions are no longer suitable (Emery et al., 2001; Hu et al., 2015). Conversely, relief shows no consistent trend with change event volume before retreat events, indicating that retreat may affect marsh outlines similarly regardless of their original relief (Figure 4.10a,c). However, after retreat events of more than 100 $m^3$ in 2013 and all retreat events in 2017, relief increases with change event volume. Retreat events of larger volume tend to increase relief because they remove platforms up to larger distances inland and tend to "replace" these high marsh platforms by "tidal flats" which are in effect creek banks, and therefore on average lower than the actual tidal flats preceding them.

### 4.5.4 Marsh Boundary Movement and Vertical Accretion

Figure 4.11 shows the relationship between the median initial marsh platform elevation $\tilde{p}_{ma,z}$ and the median change in $\tilde{p}_{ma,z}$ for profiles in individual change

events between 2009 and 2013 (a) and 2013 and 2017(b). We observe from the distribution of initial elevation that retreat events affect higher marsh platforms than progradation events and that change events between 2013 and 2017 affected lower platforms than in the 2009–2013 period. This result shows that during our study period, higher and therefore older or further upstream platform edges were more likely to undergo retreat. Concurrently, in both periods the decrease in $\tilde{p}_{ma,z}$ with initial elevation are very similar for retreat and progradation events. This implies that the rates of accretion at the platform edge are primarily controlled by their initial elevation rather than the direction of shoreline movement.

The influence of initial elevation on accretion rates has been demonstrated before, notably using single-point models (D'Alpaos et al., 2011; Goodwin and Mudd, 2019; Morris et al., 2002). These models also emphasise the importance of suspended sediment concentration on accretion rates. Our results suggest that,

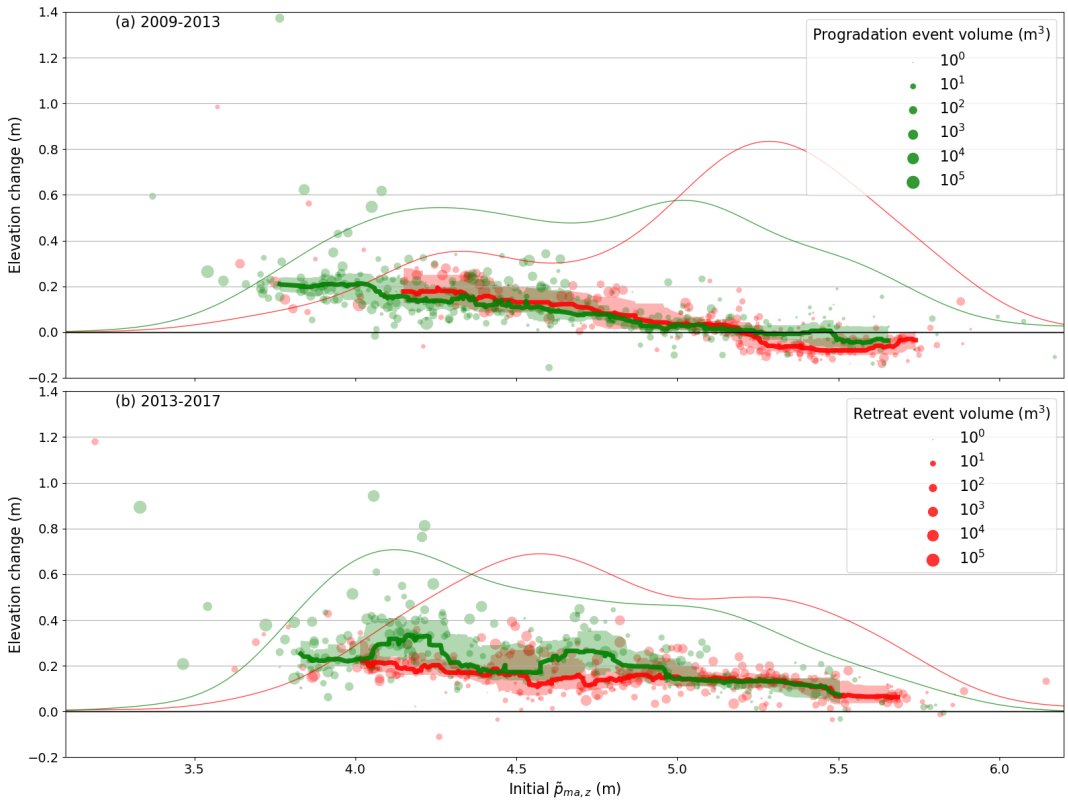


**Figure 4.11:** Vertical accretion of the marsh platform expressed as a function of initial platform elevation in the periods 2009–2013 (**a**) and 2013–2017 (**b**). Thick lines are a running median over 30 elements, surrounded by the 1st and 3rd quartiles (filled). Background red and green lines show the distribution of the initial elevation of change events.

for Moricambe Bay, sediment supply is not significantly larger near prograding platform edges than near retreating platform edges. Hence, despite expected local heterogeneity in sediment dsitribution, we may reject the idea that heterogeneous sediment distribution in Moricambe Bay drives marsh platform progradation. Rather, the drivers of marsh edge evolution are external forcings such as tidal creek meandering that force retreat processes. Consequently, retreating platforms may prograde again as tidal creek thalwegs move away from them, as suggested by (Butzeck et al., 2016). By extension, we infer that Moricambe Bay has sufficient sediment supply to support rapid infilling and conversion of the bay to marshes were it not for the action of meandering creeks.

## 4.6 Conclusions

In this contribution, we examine the morphological properties of both prograding and retreating salt marsh margins in Moricambe Bay, a sheltered mega-tidal bay for which topographic data are available at a grid step of 1 m and a vertical accuracy ranging from 3 to 7 cm. We use the TIP method (Goodwin et al., 2018) to determine the location of salt marsh margins for 3 surveys in 2009, 2013 and 2017. We then design and use a new algorithm to generate 10 m long topographic profiles, regularly spaced every 20 m along each margin. At the time of writing, we found very few quantitative studies aside from Evans et al. (2019) focusing on the morphology and evolution of salt marsh scarps. While some seminal studies refer to marsh margins (Phillips, 1986) and the bordering mudflats (Friedrichs, 2012), they often define margins over several kilometres and ignore the meter scale structures that are scarps. This is, to our knowledge, the first analysis of salt marsh margins to cover a large marsh system at such high spatial resolution and the first to consider the variability of marsh margins in such close proximity to the marsh edge. We have used this dataset to determine whether marsh profile geometry before and after change events correlates with marsh profile evolution and to explore the evolution of simple metrics relating to profile geometry during retreat and progradation events.

We determine spatially contiguous change events (i.e., contiguous areas that have either prograded or retreated) and find that retreat events consistently have a lower surface-area-to-volume ratio than progradation events. That is, for a given area of marsh, a retreat event will excavate a larger volume of sediment compared to the volume of sediment deposited by a progradation event of the same surface area. This result, consistent with our field observations, suggests a morphological difference between retreating and prograding marsh margins. Hence, we analyse the spatial variation in profile geometry for both retreat and progradation events to see if profiles that prograde or retreat in the next timestep are similar. Indeed, if prograding profiles were to look similar and not like retreating profiles, it could be possible to predict which parts of the marsh may retreat or prograde in the future. A necessary caveat to this analysis is that all observations are valid within the time period of obervation and at the time scale of observation. In chapter 5, I further detail the sensitivity of monitoring to the relative time scales of salt marsh evolution and data acquisition.

We find that the difference between pairs of retreating or prograding profiles is not significantly lower than for randomly paired retreating and prograding profiles, precluding predictions for future evolution. This is a product of the difference between the scale of scarps and that of the topographic data used. However, we find profiles within change events to be similar to each other and different from profiles in other change events. We also find this similarity to be uncorrelated to the distance between all transects within a change event, implying that the observed pattern in profile geometry may be linked to marsh margin evolution processes.

A well-documented difference between retreating and prograding profiles is the presence of a sub-vertical scarp. Profiles that have retreated in the previous timestep have scarps, those that prograded do not. Having shown that there is an observable difference between retreating and prograding profiles despite the "invisibility" of scarps at the scale of observation, we proceed to explore four basic metrics of profile morphology. We find that the marsh-to-mudflat relief behaves similarly to the maximum observed scarp slope and is different for retreating and

prograding profiles. In the absence of detailed observations of the scarp, we use this metric as a proxy for scarp height. We observe a noticeable difference between prograding profile marsh slopes, which dip seaward and retreating profile marsh slopes, for which landward dip increases after retreat. This suggests that retreating profiles are mainly observed in older terraces, whereas if left undisturbed, young prograding profiles will continue to prograde. Concurrently, we note that retreating and prograding scarps exhibit very close accretion rates of the marsh surface between time steps. From this we infer that accretion in our site is controlled by the initial elevation of the marsh surface to a greater extent than the loss or gain of marsh surface. This disconnection between vertical and horizontal growth shows that Moricambe Bay does not have a sediment supply deficit and confirms that in the absence of creek-driven erosion, marsh progradation would fill in the Bay.

This contribution highlights the richness of information that may be derived from a close examination of active marsh margins. This wealth has been partially uncovered by the availability of high-resolution lidar, however the limits of nadir-facing topographic data are strained for environments featuring complex sub-vertical structures such as erosion scarps. Previous work stresses the role of scarp geometry in determining wave thrust (Tonelli et al., 2010). We suggest that future research in this field applies itself to oblique observations, as have been seen in morphological analyses of fault scarps (Kokkalas and Koukouvelas, 2005), cliff faces (Rosser et al., 2005) or river banks (Brodu and Lague, 2012). The resulting production of 3D models of marsh edges to better inform existing geomechanical models of scarp failure (Bendoni et al., 2014) and thus improve our predictions of marsh outline evolution.

2454 .

# Chapter 5

# Discussion and Conclusions

# List of Abbreviations

| Abbreviation | Meaning |
|---|---|
| DEM | Digital Elevation Model |
| DSM | Digital Surface Model |
| DTM | Digital Terrain Model |
| NDVI | Normalised Difference Vegetation Index |
| RGB | Red-Green-Blue |
| TIP | Topographic Identification of Platforms |

**Table 5.1:** Abbreviations used in this chapter

# List of Notations

| Notation | Meaning |
|---|---|
| $P_i^*$ | Dimensionless product of a pixel $i$ [$\varnothing$] |
| $Q_{dep,\Delta t}z$ | Deposition fluxes over $\Delta t$ [L] |
| $D_{50}$ | Median grain diameter [L] |
| $C_0$ | Forcing depth-averaged suspended sediment concentration [$\varnothing$] |

**Table 5.2:** Notations used in this chapter

Geomorphological research is driven by two main objectives: (1) to describe and measure the shape of the Earth's surface, and (2) to understand the processes that determine its morphology. These goals are essential to the advancement of the discipline. They also describe necessary steps toward a responsible management of landscapes that are not only subject to natural forcings, but are inexorably affected by human activity. If we wish to preserve environments such as salt marshes, we must strive to understand natural processes as well as the extent of the perturbations we cause. "Soft" environments such as dunes, alluvial plains or salt marshes have a particularly short response time to perturbations compared to "hard" environments like rocky plateaus, cliffs or bedrock rivers. Both types of environments require accurate surveying, with "soft" environments requiring more frequent monitoring, a goal which is often achieved through the analysis of topographic data.

To this end, a large number of tools have been created: software packages to determine hilltop curvature (Hurst et al., 2012), fluvial channel heads (Clubb et al., 2014), catchment properties (Schwanghart and Scherler, 2014; Schwanghart and Kuhn, 2010), tidal creek geometry (Chirol et al., 2018; Fagherazzi et al., 1999; Liu et al., 2015) are now commonly used among researchers. Amid this diversity of tools, one can differentiate those that aim to measure a distributed property of the landscape (i.e. elevation, slope, curvature, etc.) from those that delineate the limits of geographical objects (i.e. rivers, catchments, landslides). The first set of tools is used for quantification, while the second serves the purpose of classification. To fully describe any given type of landscape, be it a beach, salt marsh, river catchment or fault scarp, one must first define its geographical extent with classification tools, then employ quantification tools to describe it within its defined boundaries. Further analysis is then conducted using simulation tools.

In this thesis, I initiated the development of a comprehensive topographic analysis tool to describe a specific type of landscape: salt marshes. Ideally, such a tool will be able to detect all salt marshes contained in an area of interest purely using topographic data (classification), and produce all the relevant metrics to describe them (quantification) and estimate their future behaviour (simulation).

First, I presented the development the TIP method, a numerical method to reproducibly classify salt marsh platforms in a high-resolution DTM of intertidal landscapes (Chapter 2). Then, I demonstrated an application of this method combined with a novel analysis of tidal records to inform numerical simulations of salt marsh accretion rates (Chapter 3). Finally, I developed an additional module to the TIP method to extend the analysis to the marsh edge, showing that retreating and prograding scarps have quantifiably distinct morphologies and that the difference between them can be expressed with simple relief and slope metrics (Chapter 4).

In this final chapter, I reflect on the contribution of this thesis to the wider fields of topographic analysis and geomorphology. First, I describe the advantages and drawbacks of using characteristic topographic features to classify landscapes. Particularly, I reflect on the variability of the topography of the marsh scarp and how it affects the results of the TIP method. I then propose possible solutions to refine the outlining of marsh boundaries without using externally sourced multispectral data. I also discuss various use cases for the TIP method, its developments described in Chapters 3 and 4, and the potential for the emergence of a comprehensive topographic analysis tool for salt marshes, with possible adaptations to other landscapes. Second, I discuss the influence of variable sediment supply and properties on deposition rates, and reflect on directions that future research may take to better constrain deposition parameters. Finally, I discuss the room for improvement in our understanding of the marsh edge and its dynamics. For this, I propose to adapt our vision of topographic analysis to 3-dimensional observations rather than the "2.5" dimensions currently represented by DTMs. I show examples of very high resolution 3D models of a marsh edge and discuss how their use may improve our representation of marsh dynamics.

## 5.1 A landscape-specific topographic analysis tool

### 5.1.1 The use of topographic signature

Identifying salt marshes using exclusively topographic data presupposes the existence within coastal landscapes of topographic features that belong exclusively to salt marshes and separate them from other neighbouring landscape elements. These features may be grouped under the broad class of "topographic signatures".

In Chapter 1, I described how salt marshes elevate above tidal flats in the form of subhorizontal platforms. This growth process produces extensive subhorizontal platforms bordered on the seaward side by sub-vertical scarps. To design the TIP method, I considered this combination features to be the topographic signature of a salt marsh. At an initial stage of reflection, I surmised that areas of high elevation and low slope bordered by areas of high slope were sufficient to identify a salt marsh using a DTM and its derived slope map. However, tidal flats are also sub-horizontal and dissected by creeks, the banks of which may resemble scarps, although they are most often correctly identified as such by observers. Hence, while the seaward boundary of a mature salt marsh may seem obvious to a human observer, with the capacity to see a DTM in its entirety, numerically achieving a similar agility in changing the scale of observation is not as straightforward. This prompted me to develop the $P^*$ metric (Chapter 2), a product of non-dimensional relief and slope within the area of interest. This metric allowed me to distinguish "true" marsh scarps from other common steep features such as tidal flat creek banks without utilising data-intensive procedures such as machine learning. Avoiding reliance on machine learning means that the TIP method requires very little live memory and can run on most laptops, which primarily benefits non-academic users. This makes the TIP method reflective in that it uses the very topographic features generated by the formation of salt marshes to identify them. Such an approach is extremely effective for mature marshes, for which the topographic signature is clearly defined (See Chapter 4).

The TIP method falls victim to its own design for prograding sections, which do not present well defined scarps (See Chapter 4), which may lead ill-informed

users to erroneous results. Chapter 4 provided one possible way to improve on this notable shortcoming by dividing a study site into approximately defined retreating and prograding sections using *a priori* user knowledge and by calibrating the parameters of each prograding section to force the results to match user knowledge. This approach suits the study of a single site, but it is hardly adequate to analyse multiple marshes or large sections of coast. Indeed, relying on user-based knowledge reinstroduces the notion of user expertise and subjectivity in the classification process. While the experience of field experts and expert software users is invaluable to the scientific development of classification methods, the TIP method's aim to achieve full automation is equally important: automation is indeed a crucial step in achieving both reproducibility and objectivity. These two attributes define a scientifically robust method in the sense that the method yields robust results regardless of the user's level of expertise. It also has the added benefit of freeing field experts and expert users for other tasks. Hence, a simple, user independent classification of prograding sections is crucial to the development of a user-friendly topographic analysis tool.

Future iterations of the TIP method may therefore turn to spectral analysis to complement topographic information. In Chapter 2, I discarded the simultane-

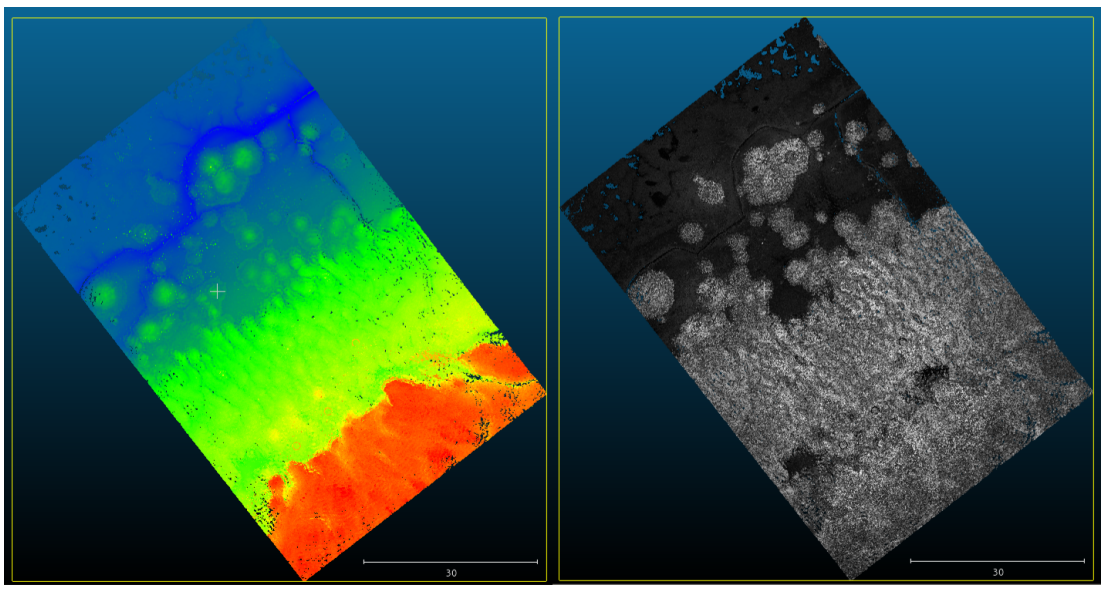

**Figure 5.1:** Composite scans of Campfield marsh in the Solway Firth, UK. Left: colours (blue to red) show elevation; right: colours (black to white) show return intensity.

ous use of multispectral and topographic data for classification purposes, mainly because these data are seldom acquired simultaneously and at comparable resolutions. However, recent developments in the accessibility of aerial or satellite-based spectral imagery, wether from governmental organisations such as NASA or the European Space Agency (ESA) or from private source (www.planet.com) spell an end to the episodic incompatibility of topographic and spectral analyses. Furthermore, the development of Stucture from Motion (SfM) techniques now produces point clouds equivalent in quality to those acquired with ground-based lidar (Godfrey et al., 2020). Given the explosion of the availability of spectral data, a purely topographic approach will soon become obsolete, particularly considering the added value of spectral imagery in the determination of plant assemblages.

Furthermore, using spectral imagery may help compensate the high cost of high-resolution topographic acquisitions. Indeed, the acquisition of high-resolution topography is currently confined to lidar flyovers or SfM from UAV-mounted cameras. The first technique requires the commission of a manned aircraft or of rare UAV-mounted lidar, which means that most lidar acquisitions are funded by governmental bodies at regular intervals (usually of more than a year at best), a frequency which is not adequate to monitoring fast-moving marsh boundaries typically found in macro-tidal areas. The second technique currently requires numerous ground-control points to compensate for the difficulty of locating individual pictures on grassy surfaces like a salt marsh platform, and hence is not adapted to monitoring large areas. Monitoring schemes may therefore be enhanced by using spectral data both in combination with topographic data and as intermediate snapshots of marsh evolution

Though common multispectral metrics such as the Normalised Vegetation Difference Index (NDVI) may not be suited to fully unsupervised classification, it may be possible to use cruder spectral metrics to assist topographic analysis. Indeed, most sources of high-resolution topographic data record at least red or red and green monochromatic pulses (for lidar) or Red-Green-Blue (RGB) (cameras used for SfM). While these data are not as well suited to identify vegetation as the NDVI, they may be combined to topographic analysis to enhance its perfor-

mance. Figure 5.1 shows the different perspectives on the location of salt marshes provided by topography (left) and return intensity (right), typically at 1064 *nm*. At the seaward edge of the marsh (top left on each plot), topographic analysis may struggle to clearly determine the outline of vegetation patches, while return intensity provides a distinct image of patch outlines, thus providing material to complement topographic analysis. I therefore intend to develop the TIP method to incorporate simple spectral return intensity analysis in a topographic package.

### 5.1.2 Modularity and quantification

Like many landscapes, salt marshes exist within a continuum of geographic objects of varying dimensions, and cannot exist without the imports of water, sediment and nutrients from freshwater environments upstream and tidal flats downstream of them. Salt marshes themselves can be subdivided into multiple elements, all of which contribute to their ecological and geomorphic functioning. Among these elements, grassy platforms are the most extensive. They may be divided into a multitude of topographic terraces or, more commonly, into three ecological zones:the high, mid or low marsh. Platforms almost always contain unvegetated depressions which fill with salt water when the platform is submerged. As the water recedes, these depressions may remain flooded, forming pools, or are drained to form salt pans. Tidal creeks are another important elements of a salt marsh landscape, dissecting the platforms and acting as conduits of sediment and nutrients to the platforms. Finally, scarps line the edge of the platforms, marking the limits of the salt marsh landscape and ecosystem with variable clarity.

As previously stated in this chapter, a tool aiming to providing relevant descriptive metrics for salt marshes must allow their identification as well as that of the elements that compose them. Not all of these elements, however, are equally important to all users. From this observation arises the need for a modular tool, which enables the user to select different analysis options. In Chapter 2, I developed the TIP method as the most basic component of a comprehensive marsh analysis tool. This component performs the essential task of defining the limits of salt marshes within an area of interest, and produces simple descriptive

metrics such as the surface area and perimeter of the identified platforms. This component alone can be sufficient for coastal management authorities who wish to monitor the evolution of marsh surface area within their jurisdiction. Using objective topographic analysis to this end is highly dependant on the frequency of data acquisition (see section5.1.1) and at present mostly presents an advantage to reliably identify retreating zones (see Chapter 2). These topographic classifications may also be compared with national or global datasets (Mcowen et al., 2017) to further follow surface area gain or loss. In future developments of the TIP method, notably including spectral analysis, monitoring will be more efficient and less dependant on expensive lidar flyovers.

More advanced projects may require more sophisticated metrics: hence, classification tools should be optionally completed by quantification tools. Chapter 3 focuses on the platforms identified with the TIP method and adds more complex metrics to quantify their elevation. Namely, it defines the distribution of platform elevation within a buffer distance of creeks and scarps as well as the distribution of elevation for platform pixels with the most likely low DTM error. All elevations described in Chapter 3 are relative to representative values of the tidal record. The addition of data sources other than the DTM provides important insight regarding the potential for accretion on the marsh platform. Chapter 3 focused on the distribution of elevation within the tidal frame because this metric is relevant to the application of the 0-dimensional model used to predict the sediment requirements for accretion. However, this description of platforms could be enhanced by many other metrics, such as the direction and magnitude of the greatest slope over the entire marsh platform. Such a metric may provide preliminary information on flow direction and strength for managers wishing to ditch portions of a salt marsh. Ditching may be necessary to manage the grazing of cattle, but influences flow patterns on the marsh, hence the need for an understanding of principal flow directions. For hydrodynamic management projects, however, a more complex description of flows is necessary, and the description of the platform would be enhanced by the addition of a simple flow routing module, for instance inspired by the numerical model EROS (Crave and Davy, 2001).

By adding quantification metrics to the TIP method, Chapter 3 illustrated one possible form of modularity for a comprehensive topographic analysis tool. In contrast, Chapter 4 focused on the edge of marsh platforms, demonstrating that the TIP method may serve as a basis to analyse features other than platforms. In that sense, researchers with an interest in analysing salt marsh scarps may combine the TIP method with the tools presented in Chapter 4. This may be particularly useful to researchers using simplified topography to determine wave thrust on the marsh scarp, or those with an interest in identifying potential spots for vegetation colonisation. More importantly, the description of scarps may be combined with the analysis of platform elevations and surface area to identify narrow strips that are at risk of being eroded. This may allow land managers to better plan protection schemes. Here, we observe that the different tools developed in the research chapters constitute modules of a numerical tool to quantifiably describe salt marsh topography. This tool in development is centred around the TIP method and uses optional modules to provide data that fits the user's requirements.

A precautionary word must however be added concerning the use of quantitative metrics to describe marsh morphology and infer geomorphic processes. Indeed, none of the results described in this thesis are independant of the spatial resolution of topographic data. While the availability of 1 m lidar topography is unconstestably a boon for salt-marsh researchers and allows the detection of features well under 1 m in width (see Chapter 4), we must bear in mind that resolution-induced error will always be present, especially in raster-based analyses. For instance, volume change calculations during retreat events are influenced by the positioning of scarp pixels relative to the real scarp. As expressed by Grieve et al. (2016b), gridded data might not need to capture the entirety of a geomorphically significant landform, nevertheless the determination of the fittest-for-use resolution in salt marsh topographic analysis remains an open question.

### 5.1.3 Future software developments

At the time of writing, the TIP method, the extraction of marsh scarps and the generation of transverse profiles as used in Chapters 2 and 4 are grouped as a coherent series of Python scripts, although they are not packaged. The scripts to calculate descriptive metrics used in Chapters 3 and 4 are however separate from this corpus. Hence, it would be impractical for users to successively run the classification and quantification scripts to describe marshes of interest to them. An important step for future work on this tool set is to package all the relevant scripts. This would partly address an issue of the work I presented and which is common to most open-source software: user-unfriendliness. It must be acknowledged that even for users who are familiar with Linux and Python, using LSDTopoTools (to obtain slope maps), the TIP method (to classify marsh platforms), its option to output scarps, and various quantification scripts to analyse the results requires specific training. Furthermore, at the time of writing, very few people are able to provide such training. It is therefore vital for the distribution of the tools I designed to undergo packaging and be accompanied by a user manual. To further improve user-friendliness, a simple graphical interface can be designed. With these features, I am confident more users will benefit from access to these objective classification and topographic analysis tools.

Even with adequate usability, the work I described in this thesis does not yet perform a comprehensive description of a salt marsh environment. For instance, neither pools, salt pans or creeks are described, meaning that the tools I produced cannot analyse topographic features that are essential to hydraulic flow on the surface and in the soil of salt marshes. To remedy this, it is possible to use published material to identify creek skeletons (Chirol et al., 2018; Fagherazzi et al., 1999; Liu et al., 2015). This solution does not, however, apply to pools, pans, or even prograding margins. Hence, future work will have to address the classification of each feature individually. Combined as modules centered around the basic principles of the TIP method, a corpus of detection and analysis tools aimed at specific topographic features of a salt marsh could consitute a coherent software, usable by scientists and land managers alike. In a long-term approach,

this set of tools may be modified to classify landscapes presenting features similar to salt marshes such as limestone cliffs and mesas, or other landscape features with unique topography such as drumlins or eskers in post-glacial landscapes.

Finally, the most prominent to this software, as stated in Section 5.1.1, is the addition of spectral analysis capabilities. Given the stochastic nature of the drivers marsh change (see Chapter 3), regulat topographic surveys even one year apart may not suffice to capture important retreat or progradation events. Although large organisations like NOAA have the capacity to commandeer lidar flyovers after the landfall of tropical storms, this type of response does not yield worldwide, accessible data. Until high-resolution topography equivalent in accuracy to airborne lidar can be acquired by satellites, topographic data will be too infrequent to appropriately monitor salt marsh evolution. The most important development of the TIP method will therefore be to add the capacity to perform simple spectral analyses such as NDVI-based semi-supervised classification (for sources providing near-infrared bands) or intensity-based semi-supervised classification. More than increasing monitoring capacity, this approach will give the software a more comprehensive view of marsh development, and in time may allow users to compare topographically classified marsh platforms to spectrally classified marsh grasslands.

## 5.2 On the variable mobility of intertidal sediment

In Chapter 3, I observed that sediment supply conditions for the study sites were not well known, despite the availability of satellite records of total suspended matter and field samples of sediment concentration and grain size. I interpreted this lack of knowledge as being due to the spatial and temporal scales of observations: indeed, while the MERIS satellite data enabled long-term monitoring, it did not possess sufficient spatial resolution to observe the spatial variability of sediment supply. I observed the opposite issue for field sampling of suspended sediment: while strategic areas of the salt marsh system may be repeatedly sampled (for instance, the creeks or the marsh platform at various distances from the creeks),

it is costly to implement at high frequency over a long period of time.

Broad scale or point observations are insufficient to describe the sediment in intertidal waters because both the quantity and size of suspended sediment is highly variable. Literature shows variability in sediment concentration between two low tides (Leroux, 2013; Mariotti and Fagherazzi, 2011) and in deposited grain size depending on wave exposure (Fagherazzi et al., 2014). This is often attributed to differences in current or wave shear stress, for example under the influence of storm surges and waves (Mariotti and Fagherazzi, 2013a), but seasonal and stochastic variations in fluvial sediment load may also affect the sediment available in shallow coastal areas. Furthermore, microbial activity in settled intertidal sediment affects its cohesive properties (Valentine et al., 2014): microphytobenthos thus causes seasonal variations in resistance to erosion (Amos et al., 2004; Amos et al., 2010) and may explain variations in sediment delivery to marshes. Sediment supply was also recently shown to influence not only salt marsh vertical development but also lateral extent (Ladd and Edwards, 2019).

Due to the high costs and difficulty of accurately quantifying sediment supply, most predictive models use constant values of sediment concentration and size. In Chapter 3, I demonstrated that variations in tidal elevations cause variations in marsh platform elevations that was not explained by previous models using a constant value of mean high tide for tidal amplitude. Tidal amplitude only affects $Q_{dep,T}$ in that it determines the amount of time the marsh surface remains flooded (see Chapter 3). On the other hand, within the framework described in Chapter 3, we know from Equations 3.2 and 3.3 that $Q_{dep,T} \propto D_{50}^2$. Likewise, we know from Equations 3.2 and 3.5 that $Q_{dep,T} \propto C_0$. Hence, while the influence of sediment properties is mathematically simpler than that of the tide, it also undeniably changes deposition rates even in the simplest 0-dimensional models.

While this thesis does not detail the effects of sediment supply on deposition, topographic analysis may help estimate the patterns of deposition on actively accreting marshes. In such areas as the Mont-Saint-Michel Bay, tidal rhythmites form strata of coarser sediment corresponding to the deposition of sediment during the strongest tides (Tessier, 1993). By extrapolating this principle, one can

conceive that the amount of sediment deposited over a known period of time with known flooding conditions, is only conditioned by the sediment concentration and settling velocity. The latter parameter is in turn conditioned by current velocity, turbulence, grain size distribution and the stability of flocs. Given samples of sediment are collected during that period of time, it is theoretically possible to determine the effective concentration of sediment over the marsh surface during deposition. I believe that this approach, while only theoretical yet, may hold important answers to simplifying sediment supply monitoring. Furthermore, it holds potential in our endeavour to uncover the small, event-based processes that underpin the dynamic equilibrium of salt marsh systems over centuries (Zhou et al., 2017).

## 5.3 Understanding the marsh edge with 3D data

Throughout this thesis, the very definition of marsh platforms is conditioned by the existence of the marsh edge. In Chapter 2, I observed that the variability of the marsh edge topography hinders the accuracy of the TIP method. I suggested in Section 5.1.1 that spectral analysis may compensate for this loss of accuracy. In Chapter 4, I was able to separate prograding and retreating marshes using 4 simple quantitative metrics to describe the marsh margin. While these metrics were sufficient to describe marsh edges in macro-tidal settings with pixel sizes of 1 $m$, the features of a marsh scarp are more complex than can be detected with this pixel size and from a nadir-facing sensor. Hence, I suggested that oblique observations with very high resolutions could further improve our understanding of scarp morphology.

Oblique or horizontal surveys are by no means a novelty in geosciences. Multiplying the angles of observation is indeed crucial to observe near-vertical or rough surfaces, and many geomorphic features with high relief have been surveyed using oblique lidar or SfM. However, the most important advantage of adding an oblique perspective is that it allows the creation of "true" 3-dimensional (3D) topographic models. Conversely, DSMs and DTMs are often referred to as "2.5D",

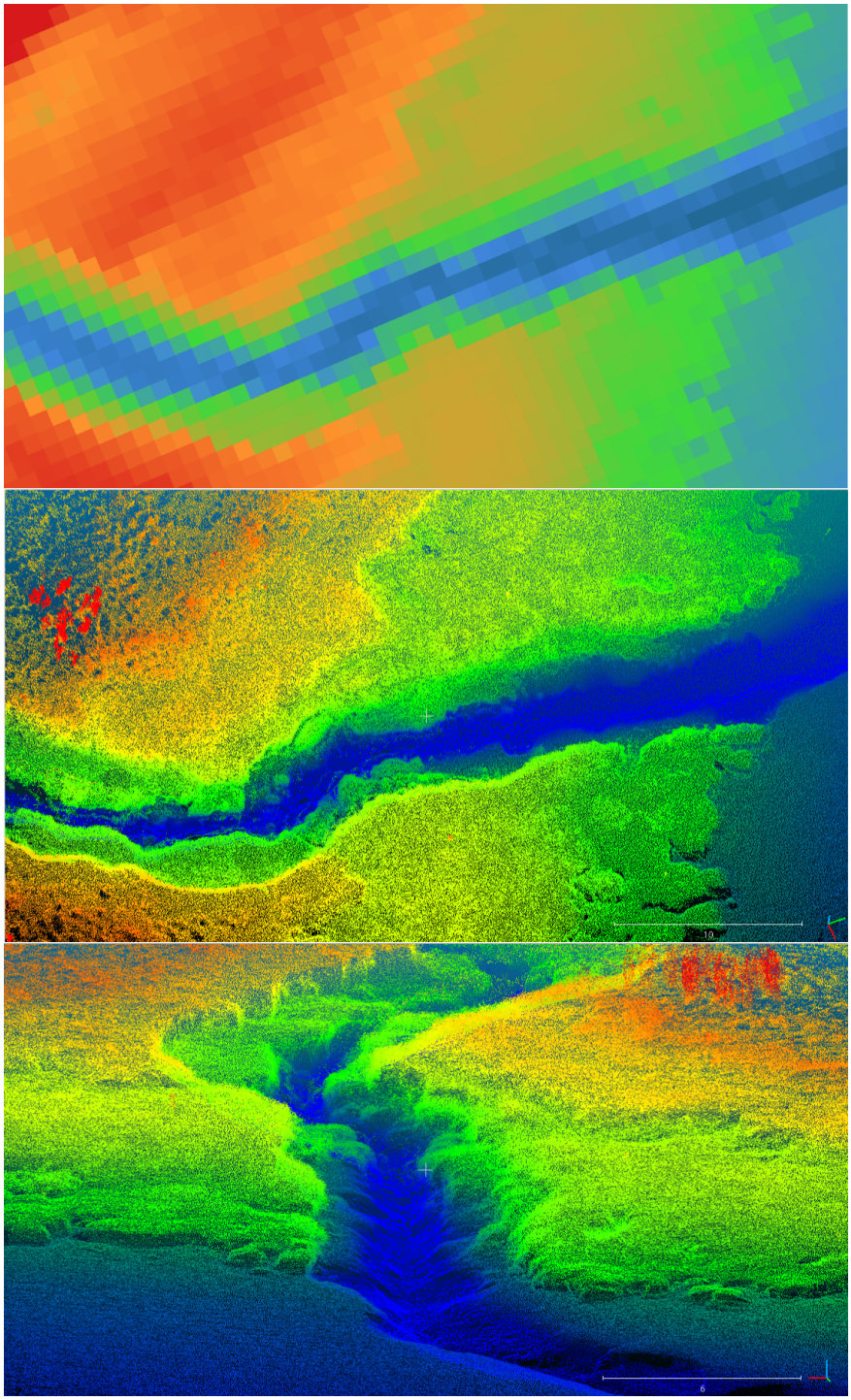

**Figure 5.2:** Comparison of different data sources and view angles for a creek outlet in Campfield Marsh, Cumbria, UK. Top: Environment Agency 2017 DTM from airborne lidar (pixel size, 1 $m$); Centre and bottom: University of Edinburgh point cloud collected with a Terrestrial Laser Scanner (point density $> 10\ pts \cdot cm^{-3}$). Colours represent elevation so as to show the creek and mudflat in blue, the low marsh in green and the high marsh in red.

owing to the fact that spatial coordinates are projected on a plane. 3D data are commonly represented as point clouds and have been used to estimate lateral dune migration (Nagihara et al., 2004) or predict boulder detachment on sea cliffs (Adams and Chandler, 2002; Richter et al., 2013; Rosser et al., 2005). Their use is however limited in salt marsh environments, with only a few descriptions of creek migration (Leroux, 2013) or of the various morphologies and behaviours of marsh edges (Evans et al., 2019). Indeed, acquiring point clouds of a sufficient density to observe small structures like vegetation patches, tussocks or ridge-and-runnel systems is costly and requires multiple man-hours for very low coverage. While high-density point clouds are currently too expensive to acquire and process for large-scale monitoring, their application to research, particularly in the observation of scarp failure or marsh establishment, is only beginning to show its potential. Int the future, there is hope that the development of point cloud generation with fixed cameras (Godfrey et al., 2020) will expand the use of 3D data to operational activities.

Figure 5.2 provides a striking example of the difference between airborne and ground-based topographic surveys: while the DTM (top) show most of the structures visible in the 3D model (centre), confirming the conclusions of Chapter 4, we can also observe that fine elements such as toppled blocs or tension cracks are invisible to airbone surveys. Yet these elements are crucial to our comprehension of creek migration. Furthermore, the oblique view of the point cloud (bottom) clearly shows irregular erosion features which may be attributed to groundwater flow, also invisible on the DEM.

Other examples of point clouds in Figure 5.3 show how very high resolution 3D topography may enable us to pursue and quantify early work on marsh development: the multiple structures defined by Allen (1989) are clearly visible on the point clouds, and may allow us to determine the mode of development of pioneer platforms. 3-dimensional topographic models such as those shown in Figure 5.3 may be used in particle-based hydraulic or hydrodynamic simulations to improve our understanding of flow turbulence but also wave breaking and spilling at the marsh edge, and ultimately inform larger scale models on adequate values

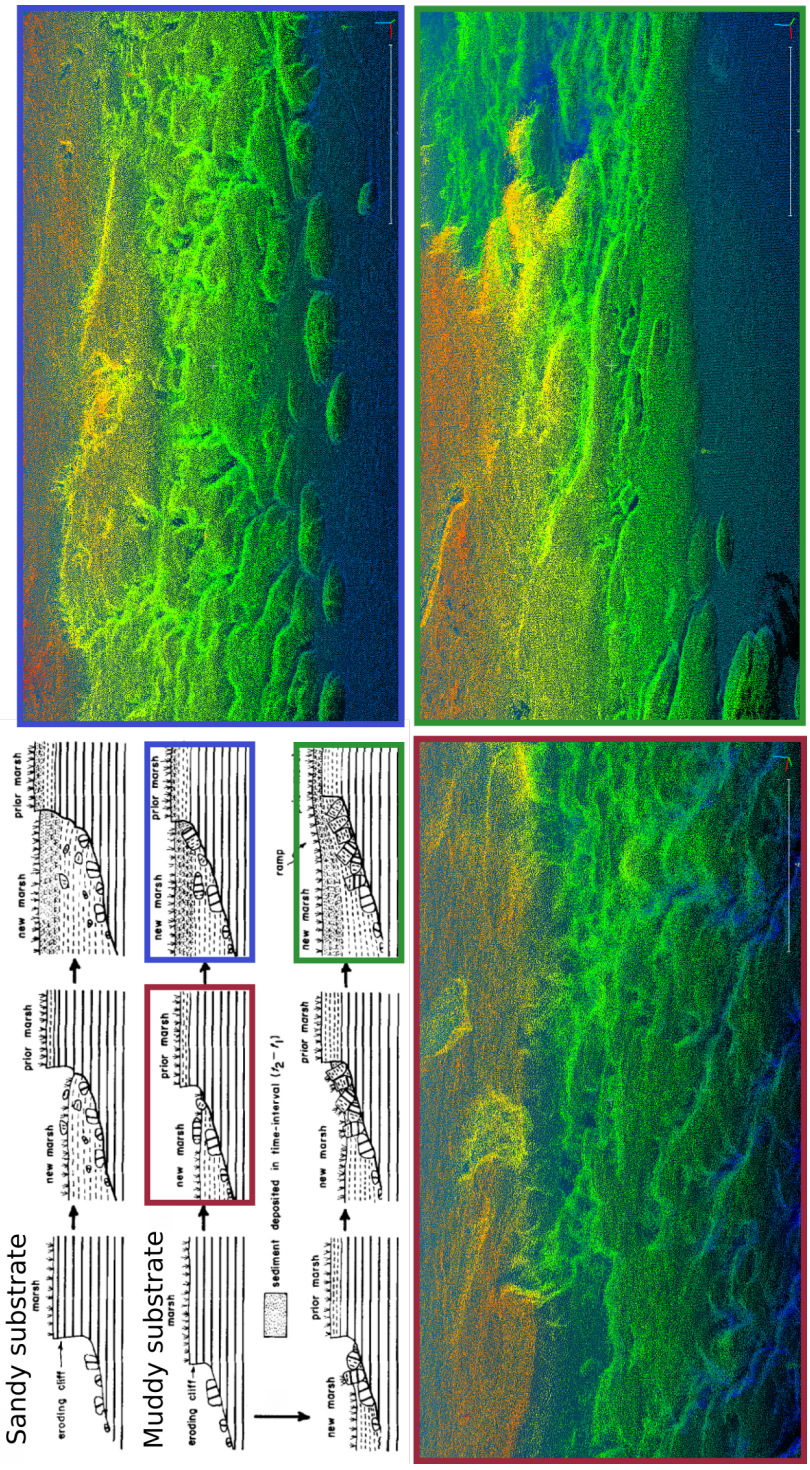


**Figure 5.3:** Top Left: diagrams of cyclical marsh development adapted from Allen (1989). Other panels: very high resolution observations of structures corresponding to various stages in marsh development. Point colours represent elevations (scaled to show the mudflat as blue, the pioneer marsh as green and older marsh terraces as orange or red).

of roughness for flow simulations. Finally, existing topographic analysis methods such as that describe by Balke et al. (2012) may be adapted to 3D models (Figure 5.4). The adaptation of topographic analysis tools to 3D topography may be an important step for the advancement of geomorphology: entire research groups have already devoted their resources to pursuing this avenue, showing impressive flow analysis capacities (Rheinwalt et al., 2019).

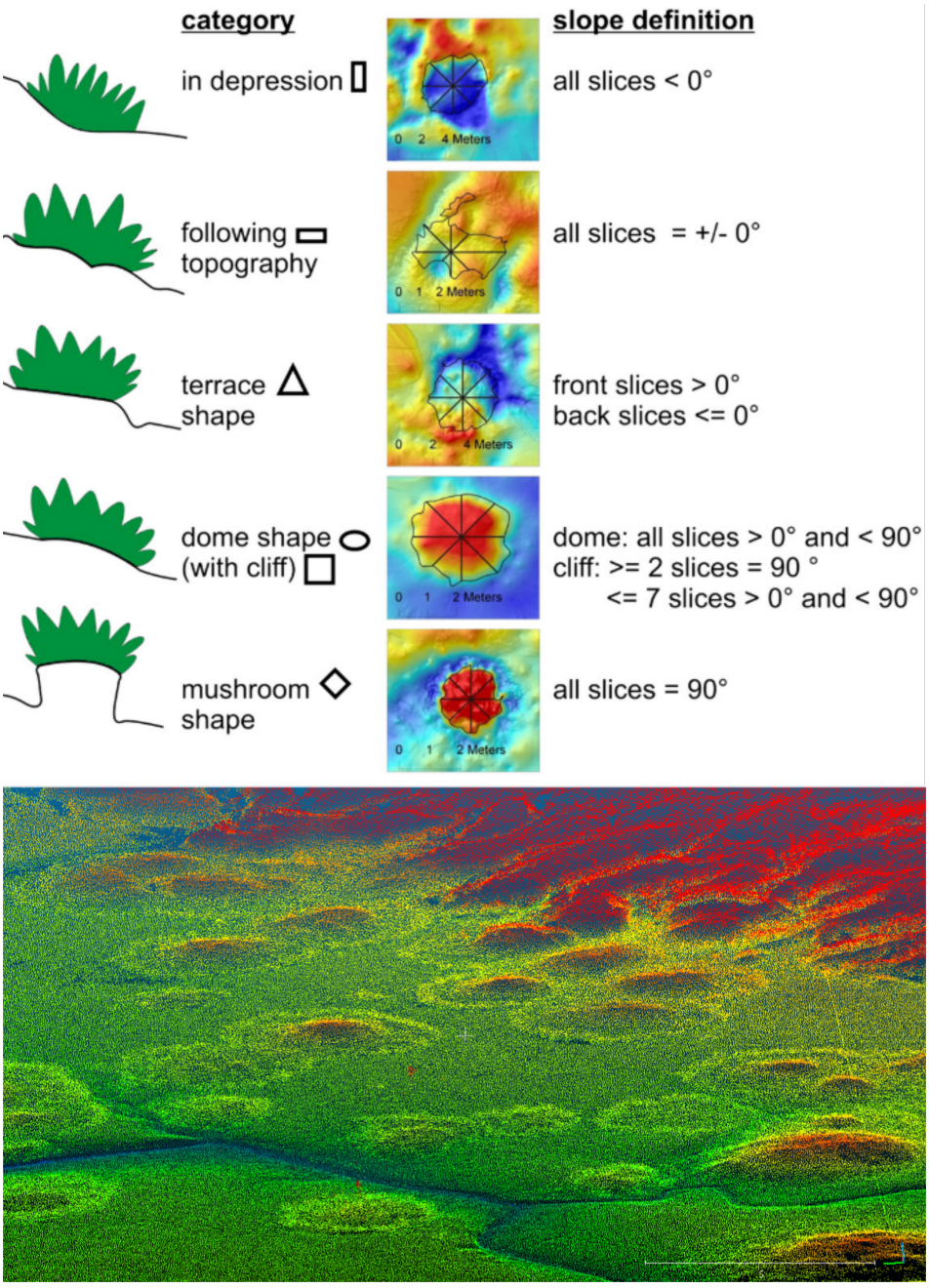


**Figure 5.4:** Top: Different shapes of tussocks observed by Balke et al. (2012); point cloud of vegetation patches in Campfield Marsh.

## 5.4 Conclusions

1. *Salt marsh platforms can be detected on high resolution data from their topographic signature alone*

   Using only a DTM with a resolution of $1 - 3m$, the Topographic Identification of Platforms (TIP) method classifies salt marsh platforms within an intertidal landscape with a success rate above 90%. It encounters difficulty with prograding marsh platforms and can be improved by spectral analyses.

2. *Deposition rates on salt marsh platforms are influenced by tidal extremes and ill-constrained sediment supply conditions*

   The elevation range of mature salt marsh platforms is confined between the mean high tide and highest high tide observations, demonstrating the importance of extreme tidal elevations in accretion processes. Uncertainties in sediment supply and properties estimates propagate to deposition calculations; deposits from monthly tide cycles may help infer sediment delivery.

3. *Retreating and prograding salt marsh platforms can be differenciated on high resolution data using simple topographic metrics*

   Salt marsh seaward margin profiles in a mega-tidal bay can be separated in connected groups of retreating and prograding profiles. Simple topographic metrics such as relief, marsh platform slope and scarp slope may adequately describe the profiles. Prograding platforms do not show signs of increased sediment supply, showing that retreat and progradation in this case are determined by external erosive factors.

4. *Future developments in analysis tools will improve our understanding of salt marsh platform dynamics*

   The development of a comprehensive tool for salt marsh analysis will facilitate the access to objective data for researchers and land managers. The adaptation of topographic analysis tools to 3D point clouds can lead to a better visualisation and quantification of dynamic geomorphic processes such as creek migration, wave-erosion and pioneer marsh colonisation.

# Chapter 6

# Appendix

## 6.1 Appendices to Chapter 2

### 6.1.1 TIP method performance tables

| Resolution (m) | S1 | S2 | S3 | S4 | S5 | S6 |
|---|---|---|---|---|---|---|
| 1.0 | 0.907 | 0.940 | 0.936 | 0.967 | 0.963 | 0.952 |
| 1.5 | 0.876 | 0.934 | 0.948 | 0.926 | 0.953 | 0.950 |
| 2.0 | 0.868 | 0.921 | 0.950 | 0.942 | 0.945 | 0.919 |
| 2.5 | 0.891 | 0.926 | 0.948 | 0.955 | 0.942 | 0.926 |
| 3.0 | 0.646 | 0.897 | 0.944 | 0.954 | 0.946 | 0.935 |
| 4.0 | 0.643 | 0.861 | 0.932 | 0.942 | 0.945 | 0.909 |
| 5.0 | 0.869 | 0.872 | 0.915 | 0.927 | 0.941 | 0.897 |
| 7.5 | 0.778 | 0.682 | 0.804 | 0.806 | 0.942 | 0.376 |
| 10.0 | 0.599 | 0.771 | 0.786 | 0.603 | 0.882 | 0.376 |

**Table 6.1:** Table of Accuracy for sites S1 to S6 (columns) with no Wiener filter, for resolutions varying between 1 and 10 m (rows).

| Resolution (m) | S1 | S2 | S3 | S4 | S5 | S6 |
|---|---|---|---|---|---|---|
| 1.0 | 0.837 | 0.979 | 0.985 | 0.972 | 0.973 | 0.916 |
| 1.5 | 0.763 | 0.970 | 0.977 | 0.974 | 0.953 | 0.910 |
| 2.0 | 0.753 | 0.971 | 0.976 | 0.967 | 0.941 | 0.890 |
| 2.5 | 0.789 | 0.961 | 0.976 | 0.969 | 0.942 | 0.889 |
| 3.0 | 0.518 | 0.959 | 0.975 | 0.974 | 0.943 | 0.880 |
| 4.0 | 0.513 | 0.951 | 0.977 | 0.968 | 0.942 | 0.835 |
| 5.0 | 0.787 | 0.936 | 0.989 | 0.932 | 0.932 | 0.896 |
| 7.5 | 0.765 | 0.908 | 0.988 | 0.956 | 0.949 | 0.376 |
| 10.0 | 0.475 | 0.699 | 0.992 | 0.000 | 0.947 | 0.376 |

**Table 6.2:** Table of Precision for sites S1 to S6 (columns) with no Wiener filter, for resolutions varying between 1 and 10 m (rows).

| Resolution (m) | S1 | S2 | S3 | S4 | S5 | S6 |
|---|---|---|---|---|---|---|
| 1.0 | 0.940 | 0.913 | 0.931 | 0.943 | 0.973 | 0.962 |
| 1.5 | 0.981 | 0.910 | 0.956 | 0.834 | 0.981 | 0.963 |
| 2.0 | 0.974 | 0.883 | 0.959 | 0.882 | 0.981 | 0.895 |
| 2.5 | 0.972 | 0.902 | 0.956 | 0.916 | 0.975 | 0.915 |
| 3.0 | 0.985 | 0.849 | 0.953 | 0.906 | 0.980 | 0.956 |
| 4.0 | 0.992 | 0.786 | 0.934 | 0.882 | 0.979 | 0.945 |
| 5.0 | 0.892 | 0.821 | 0.901 | 0.880 | 0.984 | 0.823 |
| 7.5 | 0.571 | 0.448 | 0.757 | 0.533 | 0.965 | 1.000 |
| 10.0 | 0.996 | 1.000 | 0.731 | nan | 0.870 | 1.000 |

**Table 6.3:** Table of Sensitivity for sites S1 to S6 (columns) with no Wiener filter, for resolutions varying between 1 and 10 m (rows).

| Resolution (m) | S1 | S2 | S3 | S4 | S5 | S6 |
|---|---|---|---|---|---|---|
| 1.0 | 0.900 | 0.943 | 0.948 | 0.961 | 0.950 | 0.948 |
| 1.5 | 0.847 | 0.857 | 0.948 | 0.963 | 0.953 | 0.950 |
| 2.0 | 0.868 | 0.854 | 0.950 | 0.956 | 0.945 | 0.919 |
| 2.5 | 0.890 | 0.938 | 0.948 | 0.964 | 0.942 | 0.923 |
| 3.0 | 0.646 | 0.928 | 0.947 | 0.962 | 0.945 | 0.935 |
| 4.0 | 0.824 | 0.832 | 0.931 | 0.964 | 0.945 | 0.910 |
| 5.0 | 0.717 | 0.882 | 0.904 | 0.961 | 0.941 | 0.910 |
| 7.5 | 0.777 | 0.698 | 0.854 | 0.965 | 0.942 | 0.376 |
| 10.0 | 0.593 | 0.771 | 0.833 | 0.945 | 0.870 | 0.376 |

**Table 6.4:** Table of Accuracy for sites S1 to S6 (columns) with a Wiener filter, for resolutions varying between 1 and 10 m (rows).

| Resolution (m) | S1 | S2 | S3 | S4 | S5 | S6 |
|---|---|---|---|---|---|---|
| 1.0 | 0.816 | 0.978 | 0.976 | 0.963 | 0.948 | 0.900 |
| 1.5 | 0.716 | 0.798 | 0.977 | 0.961 | 0.952 | 0.910 |
| 2.0 | 0.753 | 0.795 | 0.976 | 0.966 | 0.941 | 0.989 |
| 2.5 | 0.787 | 0.774 | 0.976 | 0.962 | 0.942 | 0.889 |
| 3.0 | 0.518 | 0.778 | 0.976 | 0.951 | 0.944 | 0.880 |
| 4.0 | 0.687 | 0.794 | 0.979 | 0.948 | 0.943 | 0.841 |
| 5.0 | 0.571 | 0.846 | 0.993 | 0.953 | 0.932 | 0.887 |
| 7.5 | 0.757 | 0.897 | 0.990 | 0.962 | 0.951 | 0.376 |
| 10.0 | 0.471 | 0.699 | 0.995 | 0.919 | 0.960 | 0.376 |

**Table 6.5:** Table of Precision for sites S1 to S6 (columns) with a Wiener filter, for resolutions varying between 1 and 10 m (rows).

| Resolution (m) | S1 | S2 | S3 | S4 | S5 | S6 |
|---|---|---|---|---|---|---|
| 1.0 | 0.955 | 0.920 | 0.957 | 0.938 | 0.982 | 0.971 |
| 1.5 | 0.993 | 0.997 | 0.956 | 0.945 | 0.981 | 0.963 |
| 2.0 | 0.974 | 0.993 | 0.959 | 0.920 | 0.982 | 0.895 |
| 2.5 | 0.973 | 0.999 | 0.956 | 0.946 | 0.975 | 0.909 |
| 3.0 | 0.985 | 0.961 | 0.955 | 0.953 | 0.977 | 0.956 |
| 4.0 | 0.976 | 0.936 | 0.931 | 0.961 | 0.979 | 0.938 |
| 5.0 | 0.978 | 0.958 | 0.883 | 0.948 | 0.985 | 0.823 |
| 7.5 | 0.581 | 0.489 | 0.834 | 0.950 | 0.964 | 1.000 |
| 10.0 | 0.996 | 1.000 | 0.790 | 0.946 | 0.838 | 1.000 |

**Table 6.6:** Table of Sensitivity for sites S1 to S6 (columns) with a Wiener filter, for resolutions varying between 1 and 10 m (rows).

### 6.1.2 Additional test sites and limitations of the TIP method

Here we present three additional sites that demonstrate the capabilities and limits of the TIP method. Sites were selected based on the availability of gridded 1 m DEMs on OpenTopography (http://www.opentopography.org) and on the variety of tidal ranges and climates present: we analyse Morro Bay, CA (A1), Wax Lake Delta, LA (A2) and Plum Island, MA (A3, see Fig. 6.1). As is common of marshes in the United States, these additional sites have a lower relief than many European marshes, with site A2 displaying a relief of 0.8 m. The performances of the TIP method are recorded in Fig. 6.2. Optimisation parameters were maintained within the ranges described in Fig. 2.7.

Site A1, located in the North-East of Morro Bay, shows an extremely close correspondence between the digitised and TIP-detected platforms, with an accuracy of 97%. It also demonstrates the ability of the TIP method to detect marsh platforms in DEMs where tidal flats exist at higher elevations, as shown by the

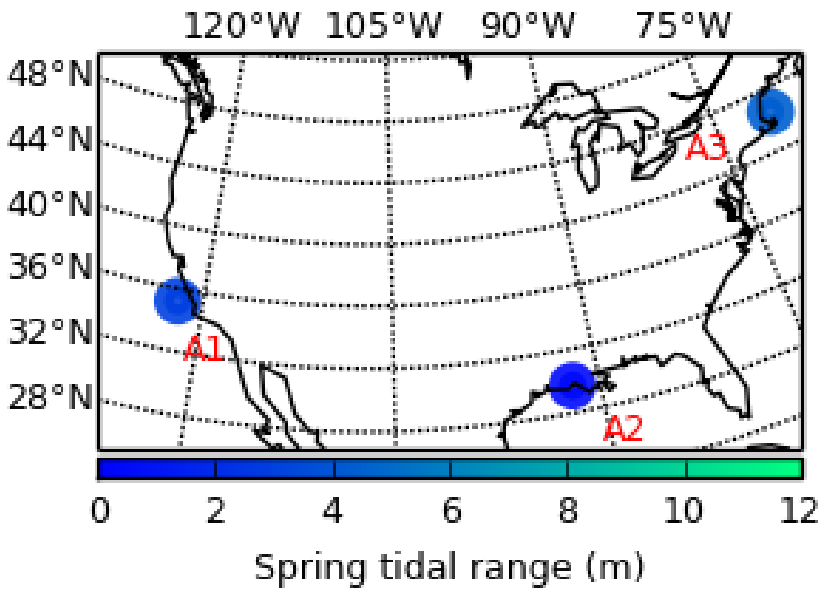


**Figure 6.1:** This map shows the three additional sites selected from the lidar collection of OpenTopography (http://www.opentopography.org), coloured by spring tidal range. The sites are numbered as follows: A1: Morro Bay, California; A2: Wax Lake Delta, Louisiana; A3: Plum Island, Massachusetts.

similar and non-null probability of the TIP-detected and digitised platforms at elevations between 0.3 and 0.9 m (Fig. 6.2b1). To confirm the observations drawn in the body of the article, site A1 displays an abundance of false negatives within tidal creeks (Fig. 6.2a1), adding weight to the argument that these features require independent treatment.

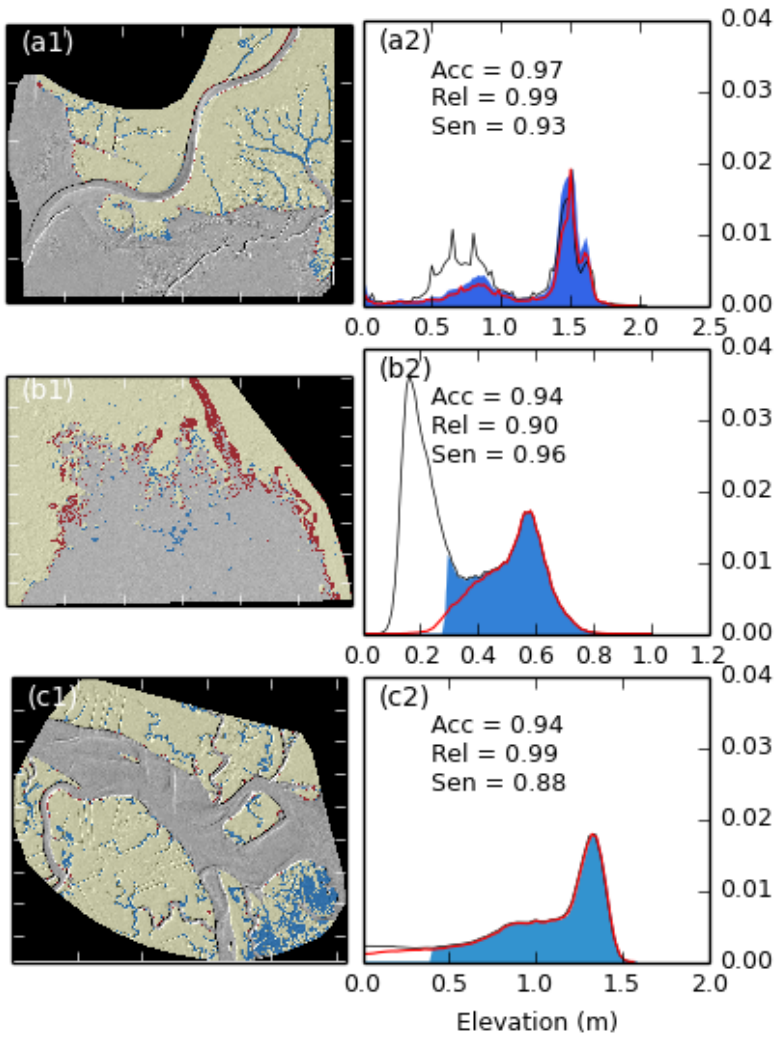


**Figure 6.2:** This figure combines the map found in Fig. 2.10 (a1, b1 and c1) and the probability distribution functions in Fig. 2.9 as well as the values of Accuracy, Precision and Sensitivity for sites A1 to A3 (a2, b2, c2). Each DEM was processed at its native resolution of 1 m.

Site A2 is located on the inside of a marsh island in the rapidly growing Wax Lake Delta. In order to detect the marsh platform with the performance reported in Fig. 6.2b2, the minimum elevation buffer of 20 cm used in step 5 of Fig. 2.1 to fill marsh platforms was reduced to 5 cm. This allows the TIP method to function in a site with very low relief and poorly defined scarps. However, we note in Fig. 6.2b1 that the marginal patches of the marsh are not well identified by the method, as indicated by the relatively large number of false positives on the outline of the marsh. This example therefore demonstrates the difficulties experienced when attempting to detect a prograding marsh by the TIP method. We therefore recommend caution when using the TIP method to monitor prograding marshes, as additional work is needed to fully characterise the topographic signatures of fallen blocks and pioneer zones.

Site A3 is a portion of the well-studied Plum Island, MA. The TIP method yields similar results to site A1, with the notable exception of the bottom right corner of Fig. 6.2c1. In this area, the marsh platform is heavily dissected by wide, shallow pools and channels, which are commonly excluded from the platform ensemble by the TIP method. Furthermore, the excluded area (containing most false negatives) forms a low, shallow concave surface within the marsh, typically associated with seasonally vegetated areas. These features are morphologically similar to a high tidal flat within the platform, and are therefore difficult to identify using the TIP method.

### 6.1.3 Scripts used to implement the TIP method

Here, I included scripts available from https://zenodo.org/record/1007788. These scripts present the TIP method as a functional programme. A new version of the TIP method as an Object-Based programme is under construction and will be made available as soon as it is completed.

**MarshPlatformAnalysis.py**

"""

```
2921 MarshPlatformAnalysis.py
2922 This function drives marsh platform analysis
2923 Authors: Guillaume CH Goodwin, Simon M. Mudd and Fiona J.
2924     Clubb, University of Edinburgh
2925 """
2926
2927 # First import the mecessary modules
2928 import os
2929 import sys
2930 import LSDMarshPlatform as MP
2931
2932 #
2933     ============================================================
2934
2935 # This is just a welcome screen that is displayed if no
2936     arguments are provided.
2937 #
2938     ============================================================
2939
2940 def print_welcome():
2941     print("\n\n
2942         ============================================================
2943         ")
2944     print("Hello! I'm going to run a marsh platform
2945         analysis.")
2946     print("You will need to tell me which directory to
2947         look in.")
2948     print("Use the --dir flag to define the working
2949         directory.")
2950     print("If you don't do this I will assume the data is
2951         in the same directory as this script.")
```

```
2952        print("For help type:")
2953        print("    python MarshPlatformAnalysis.py -h\n")
2954        print("==========================================\n\n
2955            ")
2956
2957    #================================================
2958    # This is the main function that runs the whole thing
2959    #================================================
2960    def main(argv):
2961        # print("On some windows systems you need to set an
2962            environment variable GDAL_DATA")
2963        # print("If the code crashes here it means the
2964            environment variable is not set")
2965        # print("Let me check gdal enviroment for you.
2966            Currently is is:")
2967        # print(os.environ['GDAL_DATA'])
2968        #os.environ['GDAL_DATA'] = os.popen('gdal-config --
2969            datadir').read().rstrip()
2970        #print("Now I am going to get the updated version:")
2971        #print(os.environ['GDAL_DATA'])
2972
2973        # If there are no arguments, send to the welcome
2974            screen
2975        if not len(sys.argv) > 1:
2976            full_paramfile = print_welcome()
2977            sys.exit()
2978
2979        # Get the arguments
2980        import argparse
2981        parser = argparse.ArgumentParser()
2982        # The location of the data files
```

```
2983        parser.add_argument("-dir", "--base_directory", type=
2984            str, help="The base directory with the DEMs for the
2985            marsh analysis. If this isn't defined I'll assume
2986            it's the same as the current directory.")
2987        parser.add_argument("-sites", "--sites",type=str,
2988            default = "", help = "This is a comma delimited
2989            string that gets the list of sites you want for
2990            analysis and plotting. This is a prefix that
2991            preceeds all the other DEM extensions. Default = no
2992            sites")
2993
2994        # What sort of analyses you want
2995        parser.add_argument("-MID", "--MarshID", type=bool,
2996            default=False, help="If this is true, this will run
2997            the marsh ID algorithm")
2998
2999        # What sort of plots you want
3000        parser.add_argument("-MIDP", "--MarshID_plots", type=
3001            bool, default=False, help="If this is true I'll
3002            plot all the platform plots.")
3003
3004        args = parser.parse_args()
3005
3006        sites = []
3007        if not args.sites:
3008            print("WARNING! You haven't supplied your site
3009                names. Please specify this with the flag '-
3010                sites'")
3011            sys.exit()
3012        else:
3013            print("The sites you want to analyse are: ")
```

```
3014            sites = [str(item) for item in args.sites.split(',
3015                ')]; print(sites)
3016
3017        # get the base directory
3018        if args.base_directory:
3019
3020            this_dir = args.base_directory
3021            print("You gave me the base directory:"); print(
3022                this_dir)
3023        else:
3024            this_dir = os.getcwd()
3025            print("You didn't give me a directory. I am using
3026                the current working directory:"); print(
3027                this_dir)
3028
3029        # Run the analysis if you want it
3030        if args.MarshID:
3031            MP.MarshID(Input_dir = this_dir, Output_dir =
3032                this_dir,Sites=sites)
3033
3034        # make the plots depending on your choices
3035        if args.MarshID_plots:
3036            MP.Plot_platform_on_hillshade(Input_dir = this_dir
3037                , Output_dir = this_dir,Sites=sites)
3038            MP.Plot_marsh_outline_on_hillshade(Input_dir =
3039                this_dir, Output_dir = this_dir,Sites=sites)
3040            MP.Plot_Elevation_PDF(Input_dir = this_dir,
3041                Output_dir = this_dir,Sites=sites)
3042
3043    #============================
3044    if __name__ == "__main__":
```

```
3045        main(sys.argv[1:])
```

**LSDMarshPlatform/__init__.py**

```
3047    """
3048    This wraps the LSDMarshPlatform functions
3049    Functions by Guillaume CW Goodwin
3050    """
3051    from __future__ import absolute_import, division,
3052        print_function, unicode_literals
3053    from .LSDMarshPlatform_Marsh_ID import *
3054    from .LSDMarshPlatform_functions import *
3055    from .LSDMarshPlatform_Plots import *
```

**LSDMarshPlatform/LSDMarshPlatform_functions.py**

```
3057    # Load useful Python packages
3058    import os
3059    import sys
3060    import numpy as np
3061    import matplotlib.pyplot as plt
3062    from osgeo import gdal, osr, gdalconst
3063    from osgeo.gdalconst import *
3064    import cPickle
3065
3066    #
3067        ------------------------------------------------------------------------
3068
3069    def ENVI_raster_binary_to_2d_array(file_name, gauge):
3070        """
3071        This function transforms a raster into a numpy array.
3072
3073        Args:
```

```
3074            file_name (ENVI raster): the raster you want to
3075                work on.
3076            gauge (string): a name for your file
3077
3078        Returns:
3079            image_array (2-D numpy array): the array
3080                corresponding to the raster you loaded
3081            pixelWidth (geotransform, inDs) (float): the size
3082                of the pixel corresponding to an element in the
3083                 output array.
3084
3085        Source: http://chris35wills.github.io/python-gdal-
3086            raster-io/
3087        """
3088
3089        print 'Opening %s' % (gauge)
3090        driver = gdal.GetDriverByName('ENVI')
3091        driver.Register()
3092        inDs = gdal.Open(file_name, GA_ReadOnly)
3093        if inDs is None:
3094            print "Couldn't open this file: " + file_name
3095            print "Perhaps you need an ENVI .hdr file? "
3096            sys.exit("Try again!")
3097        else:
3098            print "%s opened successfully" %file_name
3099            #print '~~~~~~~~~~~~~~~'
3100            #print 'Get image size'
3101            #print '~~~~~~~~~~~~~~~'
3102            cols = inDs.RasterXSize
3103            rows = inDs.RasterYSize
3104            bands = inDs.RasterCount
```

```
3105            #print "columns: %i" %cols
3106            #print "rows: %i" %rows
3107            #print "bands: %i" %bands
3108            #print '~~~~~~~~~~~~~~~~';
3109            #print 'Get georeference information'
3110            #print '~~~~~~~~~~~~~~~~';
3111            geotransform = inDs.GetGeoTransform()
3112            originX = geotransform[0]
3113            originY = geotransform[3]
3114            pixelWidth = geotransform[1]
3115            pixelHeight = geotransform[5]
3116            #print "origin x: %i" %originX
3117            #print "origin y: %i" %originY
3118            #print "width: %2.2f" %pixelWidth
3119            #print "height: %2.2f" %pixelHeight
3120
3121            # Set pixel offset.....
3122            print '~~~~~~~~~~~~~~~~';
3123            print 'Convert␣image␣to␣2D␣array'
3124            print '~~~~~~~~~~~~~~~~';
3125            band = inDs.GetRasterBand(1)
3126            image_array = band.ReadAsArray(0, 0, cols, rows)
3127            image_array_name = file_name
3128            print type(image_array)
3129            print image_array.shape
3130
3131            return image_array, pixelWidth, (geotransform,
3132                inDs)
3133
3134    #
3135    ---------------------------------------------------------------------
```

```
3136
3137 def ENVI_raster_binary_from_2d_array(envidata, file_out,
3138     post, image_array):
3139         """
3140         This function transforms a numpy array into a raster.
3141
3142         Args:
3143             envidata: the geospatial data needed to create
3144                 your raster
3145             file_out (string): the name of the output file
3146             post: coordinates for the goegraphical
3147                 transformation
3148             image_array (2-D numpy array): the input raster
3149
3150         Returns:
3151             new_geotransform
3152             new_projection: the projection in which the raster
3153             file_out (ENVI raster): the raster you wanted
3154
3155         Source: http://chris35wills.github.io/python-gdal-
3156             raster-io/
3157         """
3158
3159         driver = gdal.GetDriverByName('ENVI')
3160
3161         original_geotransform, inDs = envidata
3162
3163         rows, cols = image_array.shape
3164         bands = 1
3165
3166         # Creates a new raster data source
```

```
3167        outDs = driver.Create(file_out, cols, rows, bands,
3168            gdal.GDT_Float32)
3169        # Write metadata
3170        originX = original_geotransform[0]
3171        originY = original_geotransform[3]
3172        outDs.SetGeoTransform([originX, post, 0.0, originY,
3173            0.0, -post])
3174        outDs.SetProjection(inDs.GetProjection())
3175        #Write raster datasets
3176        outBand = outDs.GetRasterBand(1)
3177        outBand.WriteArray(image_array)
3178        new_geotransform = outDs.GetGeoTransform()
3179        new_projection = outDs.GetProjection()
3180        print "Output binary saved: ", file_out
3181
3182        return new_geotransform,new_projection,file_out
3183
3184 #
3185     ----------------------------------------------------------------------
3186
3187 def Distribution(Data2D, Nodata_value):
3188        """
3189        This simple function takes a 2-D array (Data2D) and
3190            makes a probability distribution of its values. It
3191            is set to ignore elements with a specific value (
3192            Nodata_value).
3193
3194        Args:
3195            Data2D (2D numpy array): the 2D array you want a
3196                distribution for
3197            Nodata_value (float): The value for ignored
```

```
3198            elements
3199
3200        Returns:
3201            bins [1D numpy array]: the value bins
3202            hist [1D numpy array]: the probability associated
3203                to the bins
3204
3205        Author: GCHG
3206        """
3207
3208        Data1D = Data2D.ravel()
3209
3210        Max_distribution = max(Data1D)
3211        if len(Data1D[Data1D>Nodata_value]) == 0:
3212            Min_distribution = -1
3213        else:
3214            Min_distribution = min(Data1D[Data1D>Nodata_value
3215                ])
3216        bin_size = (Max_distribution - Min_distribution) / 100
3217        X_values = np.arange(Min_distribution,
3218            Max_distribution, bin_size)
3219
3220        hist, bins = np.histogram (Data1D, X_values, density=
3221            True)
3222        hist=hist/sum(hist)
3223        bins=bins[:-1]
3224
3225        return bins,hist
3226
3227    #
3228    ------------------------------------------------------------------------
```

```
3229
3230 def Outline(Raster, Outline_value, Nodata_value):
3231     """
3232     This simple function takes a 2-D array (Raster) and
3233         attributes a specific value (Outline value) to
3234         elements at the limit of a bloc of elements with
3235         identical values. Effectively, it draws an outline
3236         around a group of elements with the same value. It
3237         is set to ignore elements with a specific value (
3238         Nodata_value).
3239
3240     Args:
3241         Raster (2D numpy array): the 2-D array
3242         Outline_value (float): The value associated to the
3243             outline. Be smart and select a different value
3244             from those already in your 2-D array.
3245         Nodata_value (float): The value for ignored
3246             elements
3247
3248     Returns:
3249         Raster (2D numpy array): the 2-D array, with the
3250             outlines given their own value.
3251
3252     Author: GCHG
3253     """
3254
3255     P1 = np.where(Raster[:,1:] != Raster[:,:-1])
3256     Raster[P1] = Outline_value
3257
3258     P2 = np.where(Raster[1:,:] != Raster[:-1,:])
3259     Raster[P2] = Outline_value
```

```
3260     for i in range(len(Raster)):
3261         for j in range(len(Raster[0,:])):
3262             if Raster[i,j] == Outline_value:
3263                 K = kernel (Raster, 3, i, j)
3264                 if np.mean(K) < 0:
3265                     Raster[i,j] = 0
3266 
3267     return Raster
3268 
3269 #
3270     ------------------------------------------------------------------------
3271 
3272 def define_search_space (DEM, Slope, Nodata_value, opt):
3273     """
3274     This function defines a search space (Search_space)
3275         within a 2-D array, based on the combined values of
3276         2 2-D arrays (DEM and Slope) of the same dimensions.
3277          It defines the threshold for the selection of the
3278         search space according to a threshold value (opt).
3279         It is set to ignore elements with a specific value (
3280         Nodata_value).
3281     Args:
3282         DEM (2D numpy array): a 2-D array (here a DEM)
3283             used as a first condition for the definition of
3284              the search space
3285         Slope (2D numpy array): a 2-D array (here a DEM)
3286             used as a second condition for the definition
3287             of the search space
3288         Nodata_value (float): The value for ignored
3289             elements
3290         opt (float): the value of the threshold for the
```

```
3291            selection of the search space
3292
3293        Returns:
3294            Search_space (2D numpy array): The resulting
3295                search space array. Search_space has a value of
3296                 0 for non-selected elements and 1 for selected
3297                 elements.
3298            Crossover (2D numpy array): The array resulting of
3299                 the multiplication of relative slope and
3300                relative relief.
3301            bins (1D array): the value bins for the Crossover
3302                array
3303            hist (1D array): the value hist for the Crossover
3304                array
3305            Inflecion_point(float): the value of the threshold
3306                 for the search space selection.
3307
3308        Author: GCHG
3309        """
3310
3311        print 'Choosing a holiday destination ...'
3312        Height = len(DEM); Width = len(DEM[0,:])
3313        Search_space = np.zeros((Height,Width), dtype=np.float
3314            )
3315
3316        # We calculate the relative relief of the DEM to have
3317            values of elevation between 0 and 1
3318        Relief = DEM-np.amin(DEM[DEM > Nodata_value])
3319        Rel_relief = Relief/np.amax(Relief)
3320        Rel_relief[DEM == Nodata_value] = Nodata_value
3321
```

```
3322    # We then do the same thing for slope
3323    Rel_slope = Slope/np.amax(Slope)
3324    Rel_slope[Slope == Nodata_value] = Nodata_value
3325
3326    # We then multiply these new relative relief and slope
3327        arrays and biologically name them "Crossover"
3328    Crossover = Rel_relief * Rel_slope
3329    Crossover[DEM == Nodata_value] = Nodata_value
3330
3331    # We make a curve of the frequency of values in this
3332        Crossover
3333    # That curve should look like a decreasing exponential
3334        function
3335    data = Crossover.ravel(); data = data[data>0]
3336    step = (max(data) - min(data)) / 100
3337    value = np.arange(min(data), max(data), step)
3338    hist, bins = np.histogram (data, value, density=True)
3339    hist=hist/sum(hist); bins=bins[:-1]
3340
3341    # We now find the slope of that curve
3342    hist_der = np.zeros(len(hist), dtype = np.float)
3343    for j in range(1, len(hist), 1):
3344        hist_der[j] = (hist[j]-hist[j-1])/step
3345
3346    # If the slope gets above the -1 threshold, now that
3347        we have hit the closest point to the origin.
3348    # We call it the inflexion point even though it's not
3349        really an inflexion point.
3350    for j in range(1, len(hist)-1, 1):
3351        if hist_der[j] < opt and hist_der[j+1] >= opt:
3352            Inflexion_point = bins[j]
```

```
3353
3354        # Points within the search space should have a
3355            Crossover value above the inflexion point
3356        Search = np.where(Crossover > Inflexion_point)
3357        Search_space[Search] = 1
3358
3359        # We get rid of the borders of the DEM because
3360            otherwise it will be difficult to work with the
3361            smaller slope array
3362        Search_space[0,:] = 0; Search_space[Height-1,:] = 0;
3363            Search_space[:,0] = 0; Search_space[:,Width-1] = 0
3364
3365        # And update the search locations for the shaved edges
3366        Search = np.where(Search_space == 1)
3367
3368        # If this happens, your landscape is weird
3369        if np.amax(Search_space) == 0:
3370            print "....Your search space is empty! Are you
3371                sure there's a marsh platform here?"
3372            STOP
3373
3374        return Search_space, Crossover, bins, hist,
3375            Inflexion_point
3376
3377 #
3378     ------------------------------------------------------------------------
3379
3380 def kernel (array, kernel_size, x_centre, y_centre):
3381     """
3382     This function defines a square kernel within an array
3383         (array), centred on (x_centre, y_centre). The is of
```

```
3384        a width of kernel_size.
3385    Args:
3386        array (2D numpy array): a 2-D array.
3387        kernel_size (float): the width of the square
3388            defining the size of the kernel. kernel_size
3389            MUST be an ODD number to account for the
3390            central element.
3391        x_centre (int): The index of the element in the 1
3392            st dimension.
3393        y_centre (int): The index of the element in the 2
3394            nd dimension.
3395
3396    Returns:
3397        kernel (2D numpy array): The kernel of selected
3398            elements.
3399
3400    Author: GCHG
3401    """
3402
3403    if (-1)**kernel_size < 0:
3404        X_to_0 = x_centre
3405        X_to_End = len(array)-x_centre
3406        Y_to_0 = y_centre
3407        Y_to_End = len(array[0,:])-y_centre
3408
3409        Lim_left = x_centre - min(np.floor(kernel_size/2),
3410            X_to_0)
3411        Lim_right = x_centre + min(np.floor(kernel_size/2)
3412            +1, X_to_End)
3413        Lim_top = y_centre - min(np.floor(kernel_size/2),
3414            Y_to_0)
```

```
3415            Lim_bottom = y_centre + min(np.floor(kernel_size
3416                /2)+1, Y_to_End)
3417
3418            kernel = array [int(Lim_left):int(Lim_right), int(
3419                Lim_top):int(Lim_bottom)]
3420
3421        else:
3422            print " .... WARNING: you need to choose an odd
3423                kernel size, buddy"
3424            pass
3425
3426        return kernel
3427
3428    #
3429        ------------------------------------------------------------------------
3430
3431    def peak_flag (Slope, Search_space, Order):
3432        """
3433        This function is the first stage of a routing process
3434            used to identify lines of maximum slopes.
3435        This function identifies multiple local maxima in an
3436            array (Slope), within a predefined search space (
3437            Search_space). The identified maxima are given a
3438            value of Order.
3439
3440        Args:
3441            Slope (2D numpy array): the input 2-D array, here
3442                issued from a slope raster.
3443            Search_space (2D numpy array): the search space
3444                array in which to look for local maxima.
3445            Order (int): the value given to the local maxima
```

```
3446            points.
3447
3448        Returns:
3449            Peaks (2D numpy array): a 2-D array where the
3450                local maxima have a value of Order and other
3451                elements are null.
3452            Slope_copy (2D numpy array): a copy of the input
3453                array where the value of the selected local
3454                maxima has been set to 0.
3455
3456        Author: GCHG
3457        """
3458
3459        print 'Finding local slope maxima ...'
3460        Slope_copy = np.copy(Slope) # the copy of the initial
3461            data array
3462        Search = np.where(Search_space == 1) # the searched
3463            locations
3464        Peaks = np.zeros((len(Slope),len(Slope[0,:])),dtype =
3465            np.float)
3466
3467        for i in range(len(Search[0])):
3468            x=Search[0][i]; y=Search[1][i] # coordinates of
3469                the kernel's centre
3470            Kernel_slope = kernel (Slope, 3, x, y)
3471            Kernel_search = kernel(Search_space, 3, x, y)
3472
3473            # if the centre of the kernel is its maximum and
3474                is not an isolated point
3475            if Kernel_slope[1,1] == np.amax(Kernel_slope) and
3476                np.amax(Kernel_search[Kernel_search<=
```

```
3477                Kernel_search[1,1]] > 0):
3478                Peaks[x,y] = Order # The kernel centre becomes
3479                    a local peak
3480                Slope_copy[x,y] = 0 # The slope of the
3481                    modified data array drops to 0
3482
3483        return Peaks, Slope_copy
3484
3485 #
3486     ----------------------------------------------------------------------
3487
3488 def initiate_ridge(Slope, Search_space, Peaks, Order):
3489     """
3490     This function is the second stage of a routing process
3491         used to identify lines of maximum slopes.
3492     This function identifies multiple duplets of elements
3493         in an array (Slope), within a predefined search
3494         space (Search_space) and within the neighbourhood
3495         of the local maxima identified in a second input
3496         array (Peaks). The identified elements are given a
3497         value of Order. To make this function work, the
3498         input array Slope should be the output array
3499         Slope_copy of the function peak_flag.
3500
3501     Args:
3502         Slope (2D numpy array): the input 2-D array, here
3503             issued from a slope raster where the local
3504             maximal values have been replaced by 0.
3505         Search_space (2D numpy array): the search space
3506             array.
3507         Peaks (2D numpy array): A 2-D array containing
```

```
3508            elements with a value of 1. These elements have
3509             the same indices as the elements with a value
3510            of 0 in Slope.
3511        Order (int): the value given to the identified
3512            elements. it should be superior by 1 to the
3513            value of Order in the function peak_flag.
3514
3515    Returns:
3516        Ridges (2D numpy array): a 2-D array where the
3517            identified elements have a value of Order. This
3518             array is modified from the Peaks array and
3519            therefore also contains elements of a value
3520            equal to the Order in the function peak_flag.
3521        Slope_copy (2D numpy array): a copy of the input
3522            array where the value of the selected elements
3523            has been set to 0.
3524
3525    Author: GCHG
3526    """
3527
3528    print '    ... Starting ridges ...'
3529    Slope_copy = np.copy(Slope) # the copy of the initial
3530        data array
3531    Search = np.where(Search_space == 1) # the searched
3532        locations
3533    Search_peaks = np.where(Peaks == Order-1) # the
3534        searched locations where the peaks are
3535    Ridges = np.copy(Peaks)
3536
3537    # Define Kernels
3538    for i in range(len(Search_peaks[0])):
```

```
3539            x=Search_peaks[0][i]; y=Search_peaks[1][i] #
3540                coordinates of the kernel's centre
3541            Kernel_slope = kernel (Slope, 3, x, y)
3542            Kernel_slope_copy = kernel (Slope_copy, 3, x, y)
3543            Kernel_ridges = kernel (Ridges, 3, x, y)
3544            Kernel_search = kernel (Search_space, 3, x, y)
3545
3546            # 1/ If there are no other peaks, we have two
3547                ridge starters
3548            if np.count_nonzero(Kernel_ridges) == 1:
3549                Ridge_starter1 = np.where (Kernel_slope_copy
3550                    == np.amax (Kernel_slope_copy))
3551                X1=Ridge_starter1[0][0]; Y1=Ridge_starter1
3552                    [1][0]
3553
3554                # if it is within the initial search space
3555                if Search_space[x+X1-1, y+Y1-1] != 0:
3556                    Ridges[x+X1-1, y+Y1-1] = Order
3557                    Slope_copy[x+X1-1, y+Y1-1] = 0
3558
3559                    # Look for a second ridge starter
3560                    Ridge_starter2 = np.where (
3561                        Kernel_slope_copy == np.amax (
3562                        Kernel_slope_copy))
3563                    X2=Ridge_starter2[0][0]; Y2=Ridge_starter2
3564                        [1][0]
3565                    Distance = np.sqrt((X2-X1)**2+(Y2-Y1)**2)
3566
3567                    # if it is within the initial search space
3568                        AND not next to the first ridge
3569                        starter
```

```
3570                if Search_space[x+X2-1, y+Y2-1] != 0 and
3571                    Distance > np.sqrt(2):
3572                    Ridges[x+X2-1, y+Y2-1] = Order
3573                    Slope_copy[x+X2-1, y+Y2-1] = 0
3574
3575                # Otherwise, look for second ridge starter
3576                    elsewhere in the kernel
3577                elif Search_space[x+X2-1, y+Y2-1] != 0 and
3578                    Distance <= np.sqrt(2):
3579                    for j in np.arange(0,9,1):
3580                        Kernel_slope_copy[X2, Y2] = 0
3581
3582                        Ridge_starter2 = np.where (
3583                            Kernel_slope_copy == np.amax (
3584                            Kernel_slope_copy))
3585                        X2=Ridge_starter2[0][0]; Y2=
3586                            Ridge_starter2[1][0]
3587                        Distance = np.sqrt((X2-X1)**2+(Y2-
3588                            Y1)**2)
3589
3590                        if Search_space[x+X2-1, y+Y2-1] !=
3591                            0 and Distance > np.sqrt(2):
3592                            Ridges[x+X2-1, y+Y2-1] = Order
3593                            Slope_copy[x+X2-1, y+Y2-1] = 0
3594                            break
3595
3596            # 2/ If there are two peaks, we have one ridge
3597                starter
3598            elif np.count_nonzero(Kernel_ridges) == 2:
3599                Ridge_starter1 = np.where (Kernel_slope_copy
3600                    == np.amax (Kernel_slope_copy))
```

```
3601                X1=Ridge_starter1[0][0]; Y1=Ridge_starter1
3602                    [1][0]
3603
3604                # if it is within the initial search space
3605                if Search_space[x+X1-1, y+Y1-1] != 0:
3606                    Ridges[x+X1-1, y+Y1-1] = Order
3607                    Slope_copy[x+X1-1, y+Y1-1] = 0
3608
3609        return Ridges, Slope_copy
3610
3611 #
3612     ----------------------------------------------------------------------
3613
3614 def Continue_ridge (Slope, Search_space, Peaks, Order):
3615     """
3616     This function is the third and final stage of a
3617         routing process used to identify lines of maximum
3618         slopes.
3619     IMPORTANT: this function is meant to be run several
3620         times! It requires the incrementation of the Order
3621         value with each iteration.
3622     This function identifies multiple elements in an array
3623          (Slope), within a predefined search space (
3624         Search_space) and within the neighbourhood of the
3625         local maxima identified in a second input array (
3626         Peaks). The identified elements are given a value
3627         of Order. To make this function work, the input
3628         array Slope should be the output array Slope_copy
3629         of the function initiate_ridge.
3630
3631     Args:
```

```
3632        Slope (2D numpy array): the input 2-D array, here
3633            issued from a slope raster where the elements
3634            selected in the initiate_ridge function have
3635            been replaced by 0.
3636        Search_space (2D numpy array): the search space
3637            array.
3638        Peaks (2D numpy array): A 2-D array containing
3639            elements with a value of 1. These elements have
3640             the same indices as the elements with a value
3641            of 0 in Slope.
3642        Order (int): the value given to the identified
3643            elements. On the first iteration it should be
3644            superior by 1 to the value of Order in the
3645            function initiate_ridge. the value of Order
3646            then needs to be incremented with every
3647            iteration.
3648
3649    Returns:
3650        Ridges (2D numpy array): a 2-D array where the
3651            identified elements have a value of Order. This
3652             array is modified from the Peaks array and
3653            therefore also contains elements of a value
3654            equal to the Order in the functions peak_flag
3655            and initiate_ridge.
3656        Slope_copy (2D numpy array): a copy of the input
3657            array where the value of the selected elements
3658            has been set to 0.
3659
3660    Author: GCHG
3661    """
3662
```

```
3663        print '    ... Prolongating ridges ...'
3664        Slope_copy = np.copy(Slope) # the copy of the initial
3665            slope array
3666        Search = np.where(Search_space == 1) # the searched
3667            locations
3668        Search_peaks = np.where(Peaks == Order-1) # the
3669            searched locations where the peaks are
3670        Ridges = np.copy(Peaks)
3671
3672        # Define Kernels
3673        for i in range(len(Search_peaks[0])):
3674            x=Search_peaks[0][i]; y=Search_peaks[1][i] #
3675                coordinates of the kernel's centre
3676
3677            Kernel_slope = kernel (Slope, 3, x, y)
3678            Kernel_slope_copy = kernel (Slope_copy, 3, x, y)
3679            Kernel_ridges = kernel (Ridges, 3, x, y)
3680            Kernel_search = kernel (Search_space, 3, x, y)
3681
3682            # Count the number of nonzero points in the kernel
3683                of the ridge array
3684            Ridge_count = np.count_nonzero(Kernel_ridges)
3685
3686            # If there are only the 2 previous ridge points,
3687                draw a third point that is far enough from the
3688                previous point
3689            if Ridge_count == 2:
3690                New_point = np.where (Kernel_slope_copy == np.
3691                    amax (Kernel_slope_copy))
3692                X=New_point[0][0]; Y=New_point[1][0]
3693                Grandad_point = np.where (Kernel_ridges ==
```

```
3694                 Order-2)
3695             Xgd=Grandad_point[0][0]; Ygd=Grandad_point
3696                 [1][0]
3697             Distance = np.sqrt((X-Xgd)**2+(Y-Ygd)**2)
3698
3699             if Search_space[x+X-1, y+Y-1] != 0 and
3700                 Distance > np.sqrt(2):
3701                  Ridges[x+X-1, y+Y-1] = Order
3702                  Slope_copy[x+X-1, y+Y-1] = 0
3703
3704             elif Search_space[x+X-1, y+Y-1] != 0 and
3705                 Distance <= np.sqrt(2):
3706                  for j in np.arange(0,9,1):
3707                      Kernel_slope_copy[X, Y] = 0
3708
3709                      New_point = np.where (
3710                          Kernel_slope_copy == np.amax (
3711                          Kernel_slope_copy))
3712                      X=New_point[0][0]; Y=New_point[1][0]
3713                      Distance = np.sqrt((X-Xgd)**2+(Y-Ygd)
3714                          **2)
3715
3716                      if Search_space[x+X-1, y+Y-1] != 0 and
3717                          Distance > np.sqrt(2):
3718                          Ridges[x+X-1, y+Y-1] = Order
3719                          Slope_copy[x+X-1, y+Y-1] = 0
3720                          break
3721
3722     return Ridges, Slope_copy
3723
3724 #
```

```
3725 ------------------------------------------------------------------------------
3726
3727 def Clean_ridges (Peaks, DEM, Nodata_value, opt):
3728     """
3729     This function eliminates some of the ridges (Peaks)
3730         identified by the trio of functions (peak_flag,
3731         initiate_ridge and continue_ridge). The elimination
3732          process depends on local relief, which uses a DEM
3733         (DEM) and a threshold value (opt). It is set to
3734         ignore elements with a value of  Nodata_value.
3735
3736     Args:
3737         Peaks (2D numpy array): the input 2-D arraym which
3738             is the output of the ridge identification
3739             process.
3740         DEM (2D numpy array): the DEM array used as a base
3741             for the elimination of unnecessary ridges.
3742         Nodata_value (float): The value for ignored
3743             elements.
3744         opt (float): The value of the threshold to
3745             eliminate unnecessary ridges.
3746
3747     Returns:
3748         Peaks (2D numpy array): a 2-D array much like the
3749             input Peaks array, but the unnecessary elemets
3750             have been reset to 0.
3751
3752     Author: GCHG
3753     """
3754
3755     print "Cleaning up ridges ..."
```

```
3756        DEM_copy = np.copy(DEM)
3757        DEM_copy[DEM_copy==Nodata_value] = 0
3758        Search_ridge = np.where (Peaks != 0)
3759
3760        Cutoff = np.percentile(DEM_copy,75)
3761        Threshold = np.amax(DEM_copy[DEM_copy<Cutoff])
3762        DEM_copy[DEM_copy>Threshold]=Threshold
3763
3764        for i in range(len(Search_ridge[0])):
3765            x=Search_ridge[0][i]; y=Search_ridge[1][i] #
3766                coordinates of the kernel's centre
3767            Kernel_DEM = kernel (DEM_copy, 9, x, y)
3768            Kernel_DEM[Kernel_DEM==Nodata_value]=0
3769
3770            if np.amax(Kernel_DEM)/Threshold < opt:
3771                Peaks[x,y] = 0
3772
3773        Search_ridge = np.where (Peaks != 0)
3774        for i in range(len(Search_ridge[0])):
3775            x=Search_ridge[0][i]; y=Search_ridge[1][i] #
3776                coordinates of the kernel's centre
3777            Kernel_ridges = kernel (Peaks, 9, x, y)
3778            # If there aren't at least 8 ridge points in the
3779                neighbourhood of 10 by 10
3780            if np.count_nonzero(Kernel_ridges) < 8:
3781                Peaks[x,y] = 0
3782
3783        return Peaks
3784
3785 #
3786     ---------------------------------------------------------------------
```

```
3787
3788 def Fill_marsh (DEM, Peaks, Nodata_value, opt):
3789     """
3790     This function builds a marsh platform array by using
3791        the Peaks array as a starting point. It uses the
3792        DEM array to establish conditions on the elements
3793        to select. the opt parameter sets a threshold value
3794         to eliminate superfluous elements. It is set to
3795        ignore elements with a value of Nodata_value.
3796
3797     Args:
3798         DEM (2D numpy array): the DEM array.
3799         Peaks (2D numpy array): the 2-D array of ridge
3800            elements, which is the output of the ridge
3801            identification and cleaning process.
3802         Nodata_value (float): The value for ignored
3803            elements.
3804         opt (float): The value of the threshold to
3805            eliminate unnecessary elements.
3806
3807     Returns:
3808         Marsh (2D numpy array): a 2-D array where the
3809            marsh platform elements are identified by
3810            strictly positive values. Other elements have a
3811             valuof 0 or Nodata_value.
3812
3813     Author: GCHG
3814     """
3815
3816     print "Initiate platform ..."
3817     DEM_copy = np.copy(DEM)
```

```
3818    Marsh = np.zeros((len(DEM), len(DEM[0,:])), dtype = np
3819        .float)
3820
3821    Counter = 1
3822    Search_ridges = np.where (Peaks > 0)
3823    for i in range(len(Search_ridges[0])):
3824        x=Search_ridges[0][i]; y=Search_ridges[1][i]
3825        Kernel_ridges = kernel (Peaks, 3, x, y)
3826        Kernel_DEM = kernel (DEM, 3, x, y)
3827
3828        Marsh_point = np.where (np.logical_and (Kernel_DEM
3829            >= Kernel_DEM[1,1], Kernel_ridges == 0))
3830        for j in range(len(Marsh_point[0])):
3831            X=Marsh_point[0][j]; Y=Marsh_point[1][j]
3832            Marsh[x+X-1, y+Y-1] = Counter
3833
3834    Search_marsh_start = np.where (Marsh == 1)
3835    for i in range(len(Search_marsh_start[0])):
3836        x=Search_marsh_start[0][i]; y=Search_marsh_start
3837            [1][i]
3838        Kernel_marsh = kernel (Marsh, 3, x, y)
3839        Kernel_ridges = kernel (Peaks, 3, x, y)
3840        if np.count_nonzero(Kernel_marsh) <=2:
3841            Marsh[x,y] = 0
3842
3843    print '....Build platform...'
3844    while Counter < 100:
3845        Counter = Counter+1
3846        Search_marsh = np.where (Marsh == Counter-1)
3847        for i in range(len(Search_marsh[0])):
3848            x = Search_marsh[0][i]; y = Search_marsh[1][i]
```

```
3849                Kernel_DEM = kernel (DEM, 3, x, y)
3850                Kernel_DEM_copy = kernel (DEM_copy, 3, x, y)
3851                Kernel_ridges = kernel (Peaks, 3, x, y)
3852                Kernel_marsh = kernel (Marsh, 3, x, y)
3853                Big_Kernel_DEM = kernel (DEM, 11, x, y)
3854                Big_Kernel_DEM_copy = kernel (DEM_copy, 11, x,
3855                    y)
3856
3857
3858                Conditions = np.zeros((len(Kernel_DEM), len(
3859                    Kernel_DEM[0,:])), dtype = np.float)
3860                # 1: free space
3861                Condition_1 = np.where (np.logical_and(
3862                    Kernel_ridges == 0, Kernel_marsh == 0));
3863                    Conditions[Condition_1] = 1
3864                # 2: not topped
3865                Condition_2 = np.where (np.logical_and(
3866                    Kernel_DEM_copy > np.amax(
3867                    Big_Kernel_DEM_copy)-0.2, Conditions == 1))
3868                    ; Conditions[Condition_2] = 2
3869
3870
3871                #This is a distance thing to make sure you don
3872                    't cross the ridges agin
3873                Here_be_ridges = np.where (Kernel_ridges != 0)
3874                Here_be_parents = np.where (Kernel_marsh ==
3875                    Counter-1)
3876
3877                for j in range(len(Condition_2[0])):
3878                    X=Condition_2[0][j]; Y=Condition_2[1][j]
3879                    Distance_to_ridges = []
```

```
3880                Distance_to_parents = []
3881
3882                for k in range(len(Here_be_ridges[0])):
3883                    Xr=Here_be_ridges[0][k]; Yr=
3884                        Here_be_ridges[1][k]
3885                    Distance = np.sqrt((X-Xr)**2+(Y-Yr)
3886                        **2)
3887                    Distance_to_ridges.append(Distance)
3888
3889                for k in range(len(Here_be_parents[0])):
3890                    Xp=Here_be_parents[0][k]; Yp=
3891                        Here_be_parents[1][k]
3892                    Distance = np.sqrt((X-Xp)**2+(Y-Yp)
3893                        **2)
3894                    Distance_to_parents.append(Distance)
3895
3896                if len(Distance_to_ridges)>0:
3897                    if min(Distance_to_ridges) > min(
3898                        Distance_to_parents):
3899                         Marsh[x+X-1, y+Y-1] = Counter
3900                else:
3901                    Marsh[x+X-1, y+Y-1] = Counter
3902                    DEM_copy[x+X-1, y+Y-1] = 0
3903
3904    print '    ...    defining    the    elimination    of    low    platforms
3905        ...'
3906    Platform = np.copy(Marsh)
3907    Platform[Platform > 0] = DEM [Platform > 0]
3908    Platform_bins, Platform_hist = Distribution(Platform
3909        ,0)
3910
```

```
3911        #1. Find the highest and biggest local maximum of
3912            frequency distribution
3913        # Initialize Index
3914        Index = len(Platform_hist)-1
3915        # Initiate Cutoff_Z value
3916        Cutoff_Z = 0
3917
3918        for j in range(1,len(Platform_hist)-1):
3919            if Platform_hist[j]>0.9*max(Platform_hist) and
3920               Platform_hist[j]>Platform_hist[j-1] and
3921               Platform_hist[j]>Platform_hist[j+1]:
3922                Index  = j
3923
3924        #2. Now run a loop from there toward lower elevations.
3925        Counter = 0
3926        for j in range(Index,0,-1):
3927            # See if you cross the mean value of frequency.
3928               Count for how many indices you are under.
3929            if Platform_hist[j] < np.mean(Platform_hist):
3930                Counter = Counter + 1
3931            # Reset the counter value if you go above average
3932               again
3933            else:
3934                Counter = 0
3935
3936            #If you stay long enough under (10 is arbitrary
3937               for now), initiate cutoff and stop the search
3938            if Counter > opt:
3939                Cutoff = j
3940                Cutoff_Z = Platform_bins[Cutoff]
3941                break
```

```
3942
3943        # If you stay under for more than 5, set a Cutoff_Z
3944            value but keep searching
3945        if Counter > opt/2:
3946            Cutoff = j
3947            Cutoff_Z = Platform_bins[Cutoff]
3948
3949        Marsh[Platform<Cutoff_Z] = 0
3950
3951        print "....Fill high areas left blank..."
3952        Search_marsh_condition = np.zeros((len(DEM), len(DEM
3953            [0,:])), dtype = np.float)
3954        Search_marsh = np.where (DEM >= Platform_bins[Index])
3955        Search_marsh_condition [Search_marsh] = 1
3956        Search_marsh_2 = np.where (np.logical_and(Marsh == 0,
3957            Search_marsh_condition == 1))
3958        Marsh[Search_marsh_2] = 3
3959
3960        print '....Fill the interior of pools...'
3961        for Iteration in np.arange(0,10,1):
3962            Counter = 100
3963            while Counter > 2:
3964                Counter = Counter-1
3965                Search_marsh = np.where (Marsh == Counter+1)
3966                Non_filled = 0
3967                for i in range(len(Search_marsh[0])):
3968                    x = Search_marsh[0][i]; y = Search_marsh
3969                        [1][i]
3970                    Kernel_DEM = kernel (DEM, 3, x, y)
3971                    Kernel_ridges = kernel (Peaks, 3, x, y)
3972                    Kernel_marsh = kernel (Marsh, 3, x, y)
```

```
3973
3974                    if Non_filled <len(Search_marsh[0]):
3975                        if np.count_nonzero(Kernel_marsh) > 6:
3976                            Condition = np.where (np.
3977                                logical_and(Kernel_marsh == 0,
3978                                Kernel_ridges == 0))
3979                            for j in range(len(Condition[0])):
3980                                X=Condition[0][j]; Y=Condition
3981                                    [1][j]
3982                                Marsh[x+X-1, y+Y-1] = Counter
3983                        else:
3984                            Non_filled = Non_filled + 1
3985
3986        # Reapply the cutoff because the straight line thing
3987            is ugly
3988        Platform = np.copy(Marsh)
3989        Platform[Platform > 0] = DEM [Platform > 0]
3990        Marsh[Platform<Cutoff_Z] = 0
3991
3992        # We fill in the wee holes
3993        Search_marsh = np.where (np.logical_and(Marsh == 0,
3994            Peaks == 0))
3995        for i in range(len(Search_marsh[0])):
3996            x = Search_marsh[0][i]; y = Search_marsh[1][i]
3997            Kernel_marsh = kernel (Marsh, 3, x, y)
3998            if np.count_nonzero(Kernel_marsh) == 8:
3999                Marsh[x,y] = 105
4000
4001        print '    ....Adding the ridges'
4002        # We get rid of scarps that do not have a marsh next
4003            to them
```

```
4004        Search_false_scarp = np.where (Peaks > 0)
4005        for i in range(len(Search_false_scarp[0])):
4006            x = Search_false_scarp[0][i]; y =
4007                Search_false_scarp[1][i]
4008            Kernel_marsh = kernel (Marsh, 3, x, y)
4009            if np.count_nonzero (Kernel_marsh) == 0:
4010                Peaks[x, y] = 0
4011
4012        # We get rid of the sticky-outy bits
4013        Search_ridge = np.where (Peaks > 0)
4014        for i in range(len(Search_ridge[0])):
4015            x=Search_ridge[0][i]; y=Search_ridge[1][i]
4016            Kernel_ridges = kernel (Peaks, 9, x, y)
4017            if np.count_nonzero(Kernel_ridges) < 8:
4018                Peaks[x,y] = 0
4019
4020        # We put the scarps in the platform
4021        Search_side = np.where (Peaks > 0)
4022        Marsh[Search_side] = 110
4023
4024        print " .... eliminate patches of empty elements ..."
4025        Search_marsh_condition = np.zeros((len(DEM), len(DEM
4026            [0,:])), dtype = np.float)
4027        Search_marsh = np.where (DEM >= Platform_bins[Index])
4028        Search_marsh_condition [Search_marsh] = 1
4029        Search_marsh_2 = np.where (np.logical_and(Marsh == 0,
4030            Search_marsh_condition == 1))
4031        Marsh[Search_marsh_2] = 3
4032
4033        print ' .... Fill the interior of pools ... '
4034        for Iteration in np.arange(0,10,1):
```

```
4035            Counter = 110
4036            while Counter > 2:
4037                Counter = Counter-1
4038                Search_marsh = np.where (Marsh == Counter+1)
4039                Non_filled = 0
4040                for i in range(len(Search_marsh[0])):
4041                    x = Search_marsh[0][i]; y = Search_marsh
4042                        [1][i]
4043                    Kernel_DEM = kernel (DEM, 3, x, y)
4044                    Kernel_ridges = kernel (Peaks, 3, x, y)
4045                    Kernel_marsh = kernel (Marsh, 3, x, y)
4046
4047                    if Non_filled <len(Search_marsh[0]):
4048                        if np.count_nonzero(Kernel_marsh) > 6:
4049                            Condition = np.where (np.
4050                                logical_and(Kernel_marsh == 0,
4051                                Kernel_ridges == 0))
4052                            for j in range(len(Condition[0])):
4053                                X=Condition[0][j]; Y=Condition
4054                                    [1][j]
4055                                Marsh[x+X-1, y+Y-1] = Counter
4056                        else:
4057                            Non_filled = Non_filled + 1
4058
4059        print '....defining the elimination of low platforms
4060            ...'
4061        Platform = np.copy(Marsh)
4062        Platform[Platform > 0] = DEM [Platform > 0]
4063        Marsh[Platform<Cutoff_Z] = 0
4064        Marsh[DEM == Nodata_value] = Nodata_value
4065
```

```
4066     return Marsh
4067
4068 #
4069     ----------------------------------------------------------------------
4070
4071 def MARSH_ID (DEM, Slope, Nodata_value, opt1, opt2, opt3):
4072     """
4073     This is the master function for marsh identification.
4074         It defines in which order the functions
4075         define_search_space, peak_flag, initiate_ridge,
4076         Continue_ridge, Clean_ridges, Fill_marsh are
4077         executed. It is set to repeat the iteration of the
4078         Continue_ridge function 50 times.
4079
4080     Args:
4081         DEM (2D numpy array): the input DEM array.
4082         Slope (2D numpy array): the input Slope array.
4083         Nodata_value (float): The value for ignored
4084             elements.
4085         opt1 (float): The value of the threshold used in
4086             the define_search_space function.
4087         opt2 (float): The value of the threshold used in
4088             the Clean_ridges function.
4089         opt3 (float): The value of the threshold used in
4090             the Fill_marsh function.
4091
4092     Returns:
4093         Search_space (2D numpy array): The output search
4094             space of the define_search_space function.
4095         Ridge (2D numpy array): The output ridges of the
4096             peak_flag, initiate_ridge, Continue_ridge,
```

```
4097            Clean_ridges functions.
4098        Marsh (2D numpy array): The output marsh platform
4099            of the Fill_marsh function.
4100
4101    Author: GCHG
4102    """
4103
4104    DEM_work = np.copy(DEM); Slope_work = np.copy(Slope);
4105
4106    Platform = np.copy(DEM_work)
4107    Ridge = np.copy(DEM_work)
4108    Marsh = np.copy(DEM_work)
4109
4110    Platform[Platform != Nodata_value] = 0
4111    Summit = np.where (Platform==np.amax(Platform))
4112    Platform[Summit] = 1
4113
4114    Search_space, Crossover, bins, hist, Inflexion_point =
4115        define_search_space (DEM_work, Slope_work,
4116        Nodata_value,opt1)
4117
4118    Order = 1
4119    Ridge, Slope_temp = peak_flag (Slope_work,
4120        Search_space, Order)
4121
4122    Order = Order+1
4123    Ridge, Slope_temp = initiate_ridge (Slope_temp,
4124        Search_space, Ridge, Order)
4125
4126    while Order < 50:
4127        Order = Order+1
```

```
4128            Ridge, Slope_temp = Continue_ridge (Slope_temp,
4129                Search_space, Ridge, Order)
4130
4131        Ridge = Clean_ridges (Ridge, DEM_work, Nodata_value,
4132            opt2)
4133        Marsh = Fill_marsh (DEM_work, Ridge, Nodata_value,
4134            opt3)
4135        print "My hovercraft is full of eels!"
4136
4137        return Search_space, Ridge, Marsh
4138
4139    #
4140    ----------------------------------------------------------------------
4141
4142    def Confusion (Subject, Reference, Nodata_value):
4143        """
4144        This function compares a Subject 2-D array to a
4145            Reference 2-D array and returns an array of
4146            differences, which we call a confusion array or
4147            confusion map if it look like a map. It then
4148            calculates a number of metrics relative to the
4149            adequation between the subject and the reference.
4150            It is set to ignore elements with a value of
4151            Nodata_value.
4152
4153        To learn more about confusion matrices and their
4154            associated metrics, please visit the Wikipedia page
4155            : https://en.wikipedia.org/wiki/Confusion_matrix
4156
4157        Args:
4158            Subject (2D numpy array): the input array. This is
```

```
4159                the one you want to test
4160            Reference (2D numpy array): the reference array.
4161                This one is supposed to contain correct
4162                information
4163            Nodata_value (float): The value for ignored
4164                elements.
4165
4166        Returns:
4167            Confusion_matrix (2D numpy array): an array
4168                containing the values 1 (True Positive), 2 (
4169                True Negative), -1 (False Positive) and -2 (
4170                False Negative).
4171            Performance (1D numpy array): the number of (
4172                respectively) True Positives, True Negatives,
4173                False Positives and False Negatives in
4174                Confusion_matrix.
4175            Metrix (1D numpy array): The values of (
4176                respectively) Accuracy, Reliability,
4177                Sensitivity, F1 derived from the Performance
4178                array.
4179
4180        Author: GCHG
4181        """
4182
4183        Height = len(Subject[:,0]); Width = len(Subject[0,:])
4184        Height_R = len(Reference[:,0]); Width_R = len(
4185            Reference[0,:])
4186
4187        print Height, Width
4188        print Height_R, Width_R
4189
```

```
4190        H = min (Height, Height_R)
4191        W = min (Width, Width_R)
4192
4193        Confusion_matrix = Nodata_value*np.ones((Height, Width
4194            ), dtype = np.float)
4195
4196        Subject_marsh = np.where (np.logical_and(Subject != 0,
4197             Subject != Nodata_value))
4198        Reference_marsh = np.where (np.logical_and(Reference
4199           != 0, Reference != Nodata_value))
4200
4201        Subject[Subject_marsh] = 1.
4202        Reference[Reference_marsh] = 1.
4203
4204        for i in range (H):
4205            for j in range (W):
4206                if Subject[i,j] == 1 and Reference[i,j] == 1:
4207                   # TRUE POSITIVE
4208                    Confusion_matrix[i,j] = 1
4209                elif Subject[i,j] == 0 and Reference[i,j] ==
4210                   0: # TRUE NEGATIVE
4211                    Confusion_matrix[i,j] = 2
4212                elif Subject[i,j] == 1 and Reference[i,j] ==
4213                   0: # FALSE POSITIVE
4214                    Confusion_matrix[i,j] = -1
4215                elif Subject[i,j] == 0 and Reference[i,j] ==
4216                   1: # FALSE NEGATIVE
4217                    Confusion_matrix[i,j] = -2
4218
4219        True_positive = np.sum(Confusion_matrix[
4220           Confusion_matrix == 1])
```

```
4221        True_negative = np.sum(Confusion_matrix[
4222            Confusion_matrix == 2])/2
4223        False_positive = -np.sum(Confusion_matrix[
4224            Confusion_matrix == -1])
4225        False_negative = -np.sum(Confusion_matrix[
4226            Confusion_matrix == -2])/2
4227
4228        Reliability = True_positive / (True_positive+
4229            False_positive)
4230        Sensitivity = True_positive / (True_positive+
4231            False_negative)
4232        Accuracy = (True_positive+True_negative) / (
4233            True_positive+True_negative+False_positive+
4234            False_negative)
4235        F1 = 2*True_positive/(2*True_positive+False_positive+
4236            False_negative)
4237
4238        Performance = np.array([True_positive,True_negative,
4239            False_positive,False_negative])
4240        Metrix = np.array([Accuracy, Reliability, Sensitivity,
4241             F1])
4242
4243        return Confusion_matrix, Performance, Metrix
```

**LSDMarshPlatform/LSDMarshPlatform_Marsh_ID.py**

```
4245 """
4246 LSDMarshPlatform_Marsh_ID.py
4247
4248 This is your driver file to run the marsh platform
4249     extraction.
4250 Please read the README and the instructions in this script
```

```
4251     before you run it.
4252 Authors: Guillaume GH Goodwin and Simon Marius Mudd
4253
4254 """
4255
4256 #
4257     ------------------------------------------------------------------------
4258
4259 #0. Set up display environment if you are working on a
4260     terminal with no GUI.
4261 import matplotlib
4262 matplotlib.use('Agg')
4263
4264 #
4265     ------------------------------------------------------------------------
4266
4267 # Useful Python packages
4268 import numpy as np
4269 import cPickle
4270 import timeit
4271 import os
4272
4273 # A very useful package
4274 from LSDMarshPlatform_functions import
4275     ENVI_raster_binary_to_2d_array
4276 from LSDMarshPlatform_functions import
4277     ENVI_raster_binary_from_2d_array
4278
4279 # The main functions for the marsh identification
4280 from LSDMarshPlatform_functions import MARSH_ID
4281 from LSDMarshPlatform_functions import Confusion
```

```
4282
4283 # Retained directories from Guillaume
4284 # "//csce.datastore.ed.ac.uk/csce/geos/users/s1563094/
4285     Software/LSDTopoTools/LSDTopoTools_MarshPlatform/
4286     Example_data/"
4287
4288 #----------------------------------------------------------------------
4289 def MarshID(Input_dir =  "/LSDTopoTools/
4290     LSDTopoTools_MarshPlatform/Example_data/",
4291                 Output_dir = "/LSDTopoTools/
4292                     LSDTopoTools_MarshPlatform/Example_data/",
4293                 Sites = ["FEL_DEM_clip"], opt1 = -2.0, opt2 =
4294                     0.85, opt3 = 8.0,
4295                     compare_with_digitised_marsh = False):
4296     """
4297     This function wraps all the marsh ID scripts in one
4298         location
4299
4300     Args:
4301         Input_dir (str): Name your data input directory
4302         Output_dir (str): Name your results output
4303             directory
4304         Sites (str list): A list of strings. The file
4305             names are modified based on these sites
4306         opt1 (flt): first optimisation
4307         opt2 (flt): 2nd optimisation
4308         opt3 (flt): 3rd optimisation
4309         compare_with_digitised_marsh (bool): If true, this
4310             will compare the data with a digitised marsh
4311             platform
4312
```

```
4313        Author:
4314            GCHG, Modified by SMM 02/10/2017
4315        """
4316
4317        #
4318            ------------------------------------------------------------------------
4319
4320        print("Welcome to the marsh ID program!")
4321        print("I am opening the file: "+Input_dir)
4322
4323        # Set the value for empty DEM cells
4324        Nodata_value = -9999
4325
4326        # Timing
4327        Start = timeit.default_timer()
4328        for site in Sites:
4329            print("Loading input data from site: "+site)
4330            # NB: When loading input data, please make sure
4331                the naming convention shown here is respected.
4332            print(" Loading DEM")
4333            DEM, post_DEM, envidata_DEM =
4334                ENVI_raster_binary_to_2d_array (Input_dir+"%s.
4335                bil" % (site), site)
4336            print " Loading Slopes"
4337            # check to get the correct slope raster
4338            slope_fname = site+"_slope.bil"
4339            if not os.path.isfile(Input_dir+slope_fname):
4340                 slope_fname = site+"_SLOPE.bil"
4341            Slope, post_Slope, envidata_Slope =
4342                ENVI_raster_binary_to_2d_array (Input_dir+
4343                slope_fname, site)
```

```
4344
4345            # Here begins the detection process
4346            print "Identifying the platform and scarps"
4347            DEM_work = np.copy(DEM)
4348            Search_space, Scarps, Platform = MARSH_ID(DEM,
4349                Slope, Nodata_value, opt1, opt2, opt3)
4350            Platform_work = np.copy(Platform)
4351            Scarps[Scarps == 0] = Nodata_value
4352
4353            # Here is where you save your output files for use
4354                in a GIS software
4355            print "Saving marsh features"
4356            new_geotransform, new_projection, file_out =
4357                ENVI_raster_binary_from_2d_array (envidata_DEM,
4358                 Output_dir+"%s_Search_space.bil" % (site),
4359                post_DEM, Search_space)
4360            new_geotransform, new_projection, file_out =
4361                ENVI_raster_binary_from_2d_array (envidata_DEM,
4362                 Output_dir+"%s_Scarps.bil" % (site), post_DEM,
4363                 Scarps)
4364            new_geotransform, new_projection, file_out =
4365                ENVI_raster_binary_from_2d_array (envidata_DEM,
4366                 Output_dir+"%s_Marsh.bil" % (site), post_DEM,
4367                Platform)
4368
4369            # Disable the following section if you do not wish
4370                to compare your results to a reference marsh
4371            if compare_with_digitised_marsh:
4372                # NB When loading input data, please make sure
4373                    the naming convention shown here is
4374                   respected.
```

```
4375            print "␣Loading␣detected␣Marsh"
4376            Platform_work, post_Platform,
4377                envidata_Platform =
4378                ENVI_raster_binary_to_2d_array (Output_dir+
4379                "%s_Marsh.bil" % (site), site)
4380            print "Loading␣reference␣marsh"
4381            Reference, post_Reference, envidata_Reference
4382                = ENVI_raster_binary_to_2d_array (
4383                Input_dir+"%s_ref.bil" % (site), site)
4384            print "Evaluating␣the␣performance␣of␣the␣
4385                detection"
4386            Confusion_matrix, Performance, Metrix =
4387                Confusion (Platform_work, Reference,
4388                Nodata_value)
4389            new_geotransform, new_projection, file_out =
4390                ENVI_raster_binary_from_2d_array (
4391                envidata_Platform, Output_dir+"%s_Confusion
4392                .bil" % (site),
4393
4394                post_Platform, Confusion_matrix)
4395
4396            cPickle.dump(Performance,open(Output_dir+"%
4397                s_Performance.pkl" % (site), "wb"))
4398            cPickle.dump(Metrix,open(Output_dir+"%s_Metrix
4399                .pkl" % (site), "wb"))
4400
4401    # Comment these 2 lines if you don't want to know how
4402        long the script run for.
4403    Stop = timeit.default_timer()
4404    print 'Runtime␣=␣', Stop - Start , 's'
```

## 6.2 Appendices to Chapter 3

### 6.2.1 Detailed platform elevations

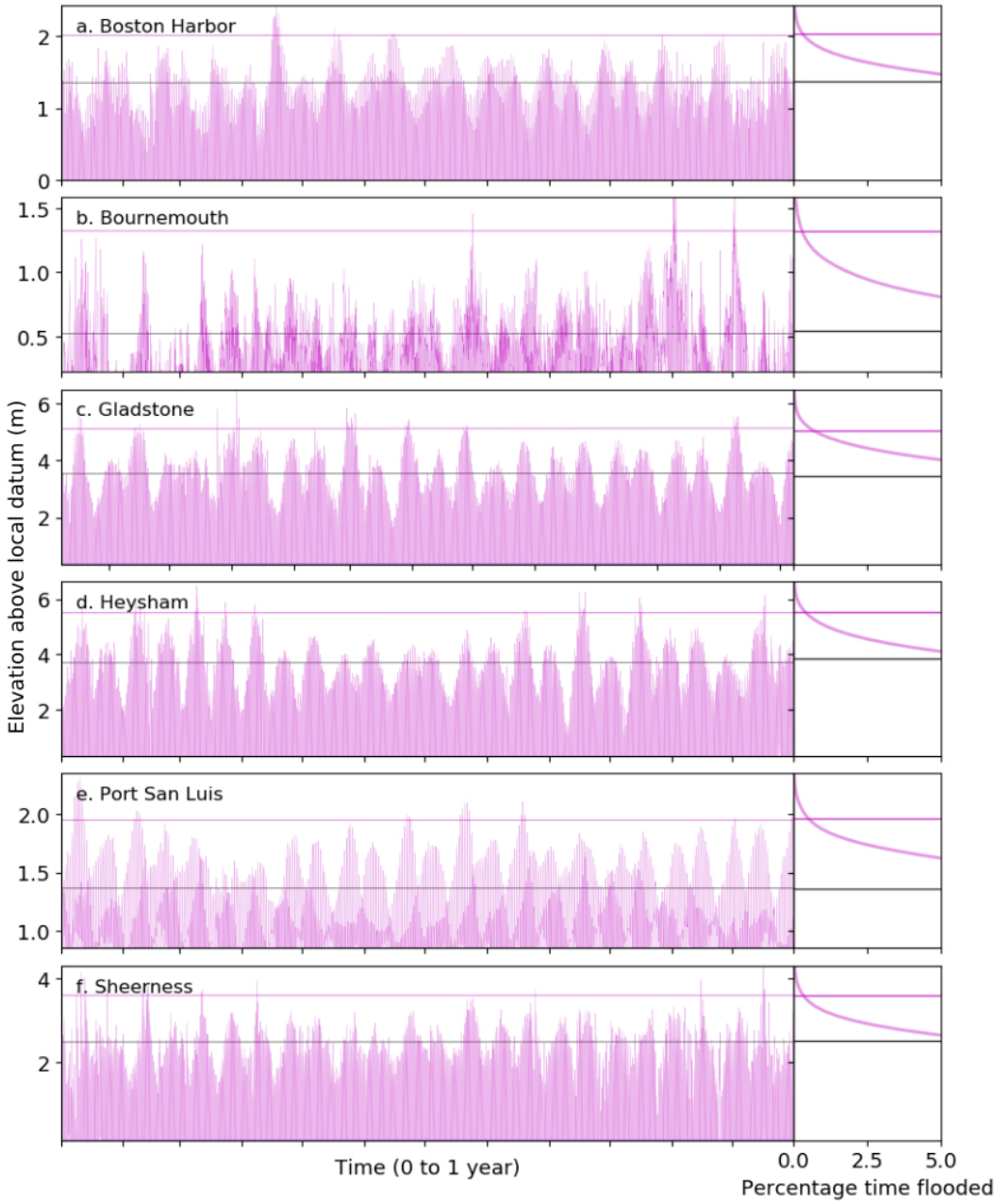


**Figure 6.3:** Detail of sea levels used for each tide station to calculate mineral deposition fluxes over a year. Left panel shows sea levels above Mean Sea Level. Black and purple lines are respectively $MHT$ ad $OHHT$. Right panel shows the percentage time flooded above $MHT$.

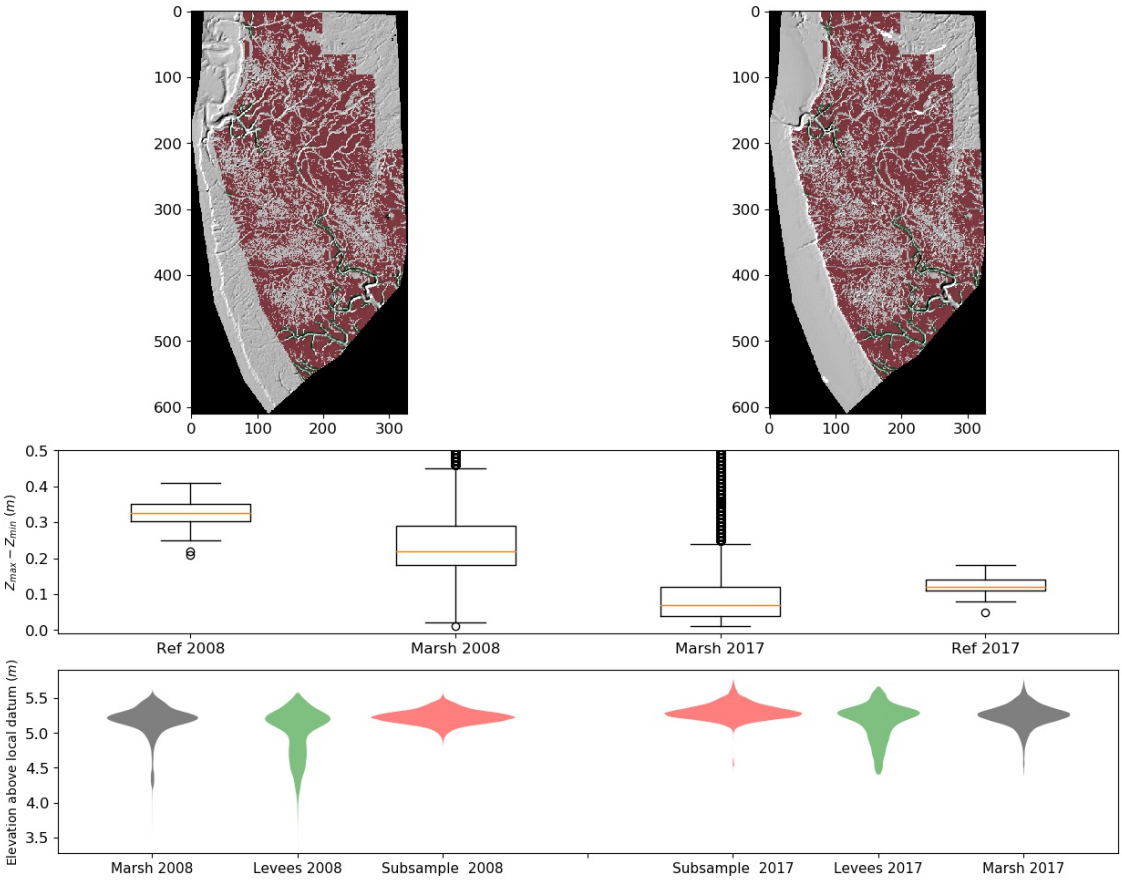


**Figure 6.4:** Equivalent of Figure 6.3 for Morecambe Bay.

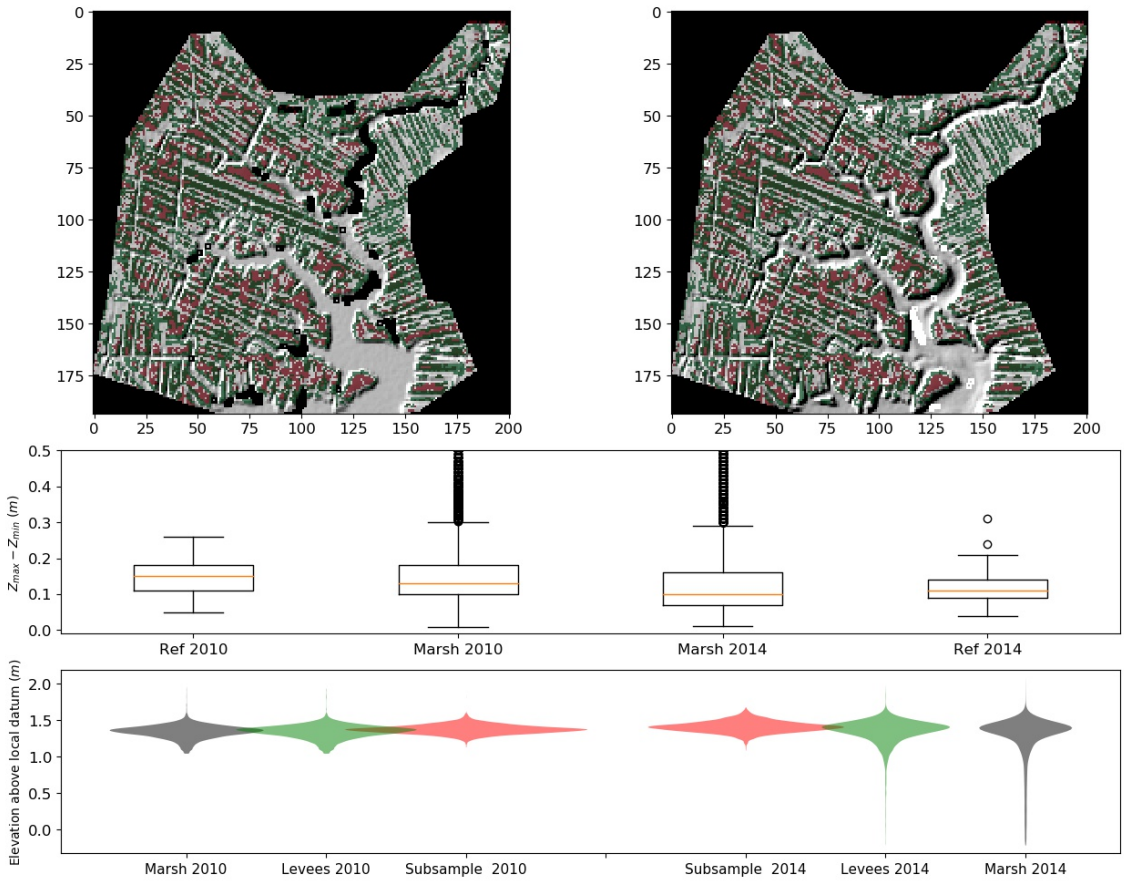


**Figure 6.5:** Equivalent of Figure 6.3 for Boston Harbor.

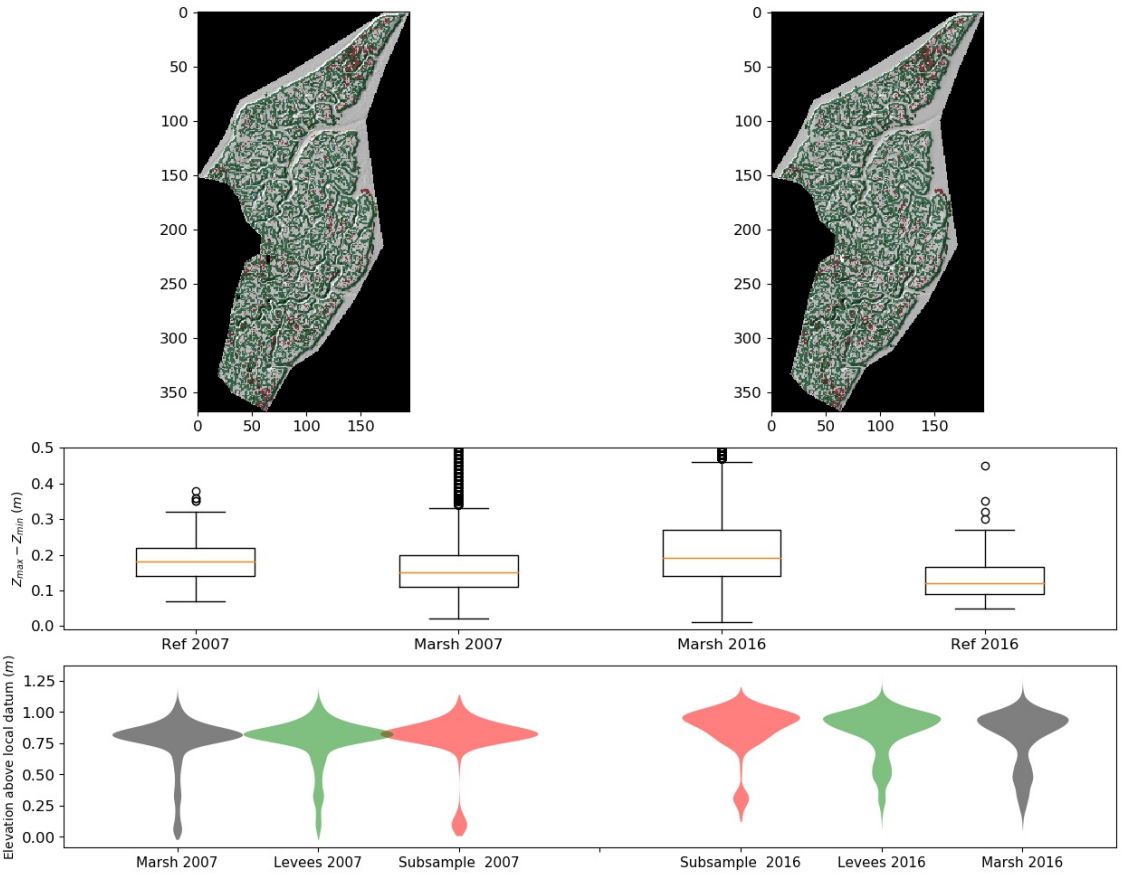


**Figure 6.6:** Equivalent of Figure 6.3 for Arne Bay.

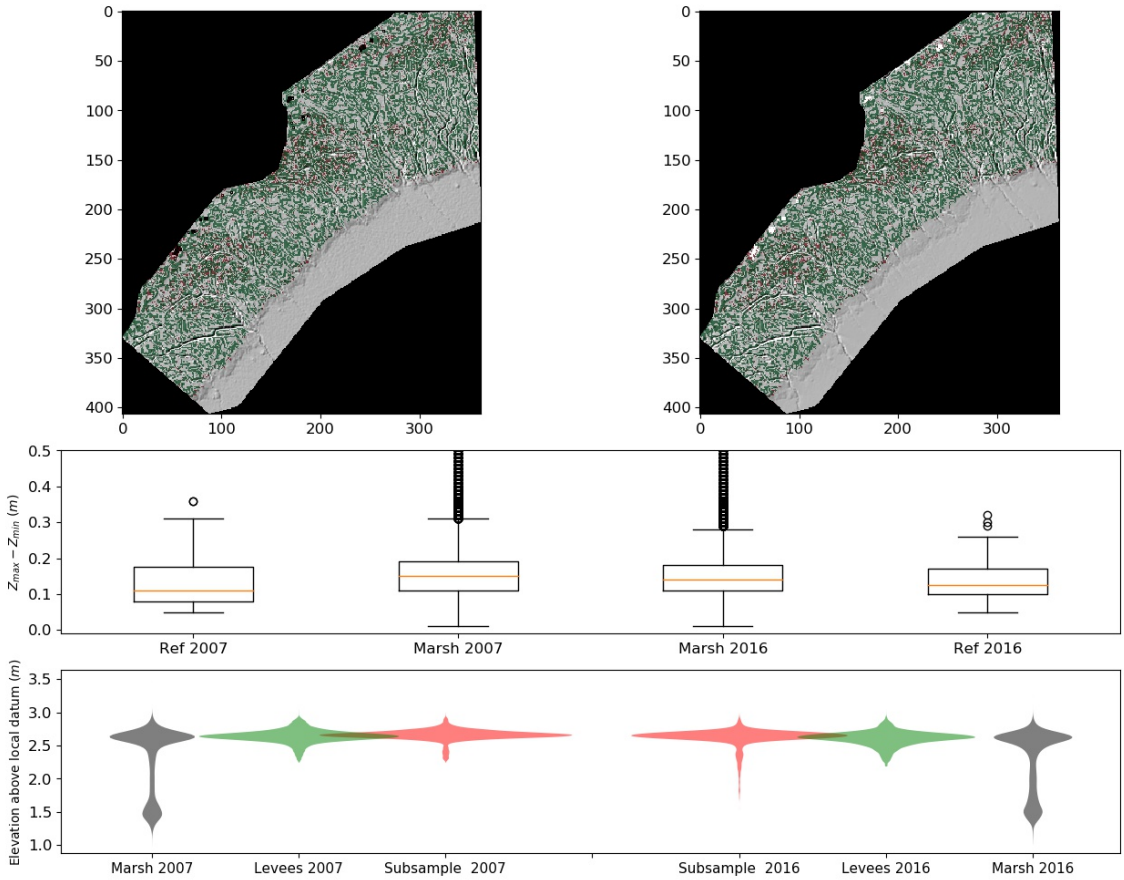


**Figure 6.7:** Equivalent of Figure 6.3 for the Swale Estuary.

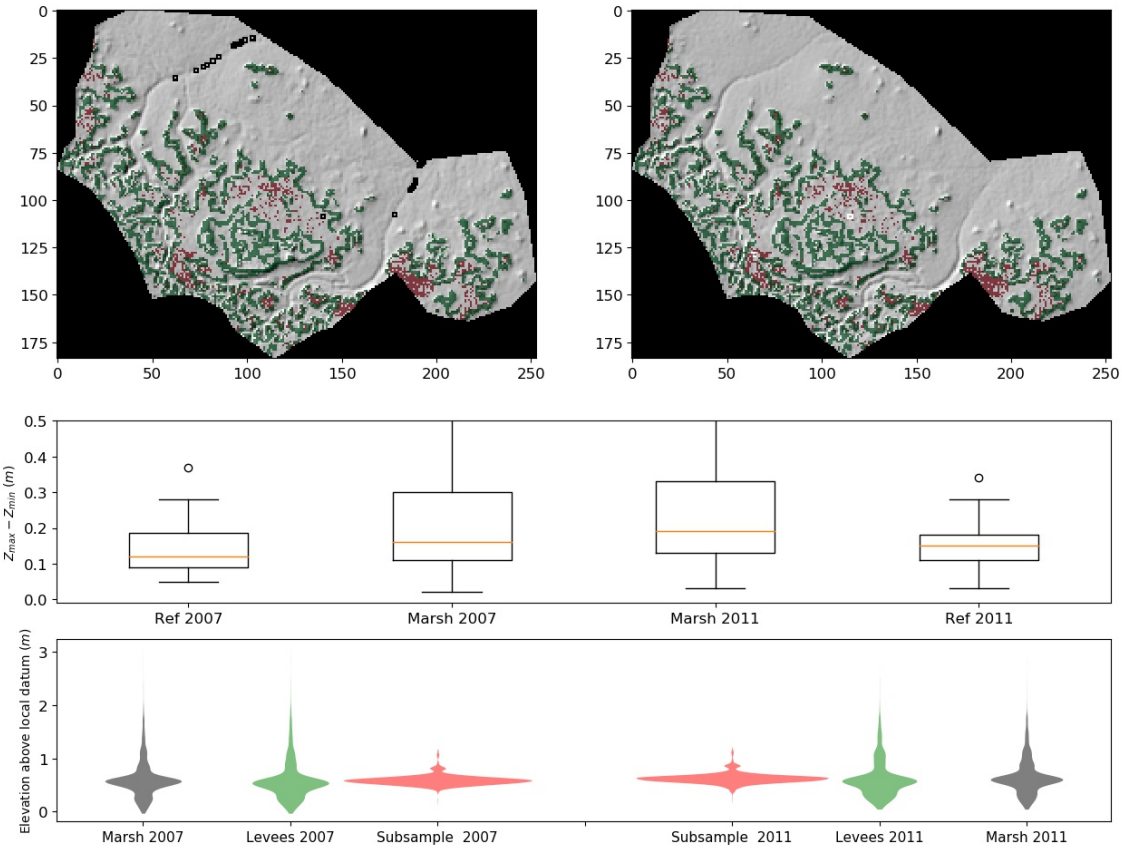


**Figure 6.8:** Equivalent of Figure 6.3 for Shell Bay.

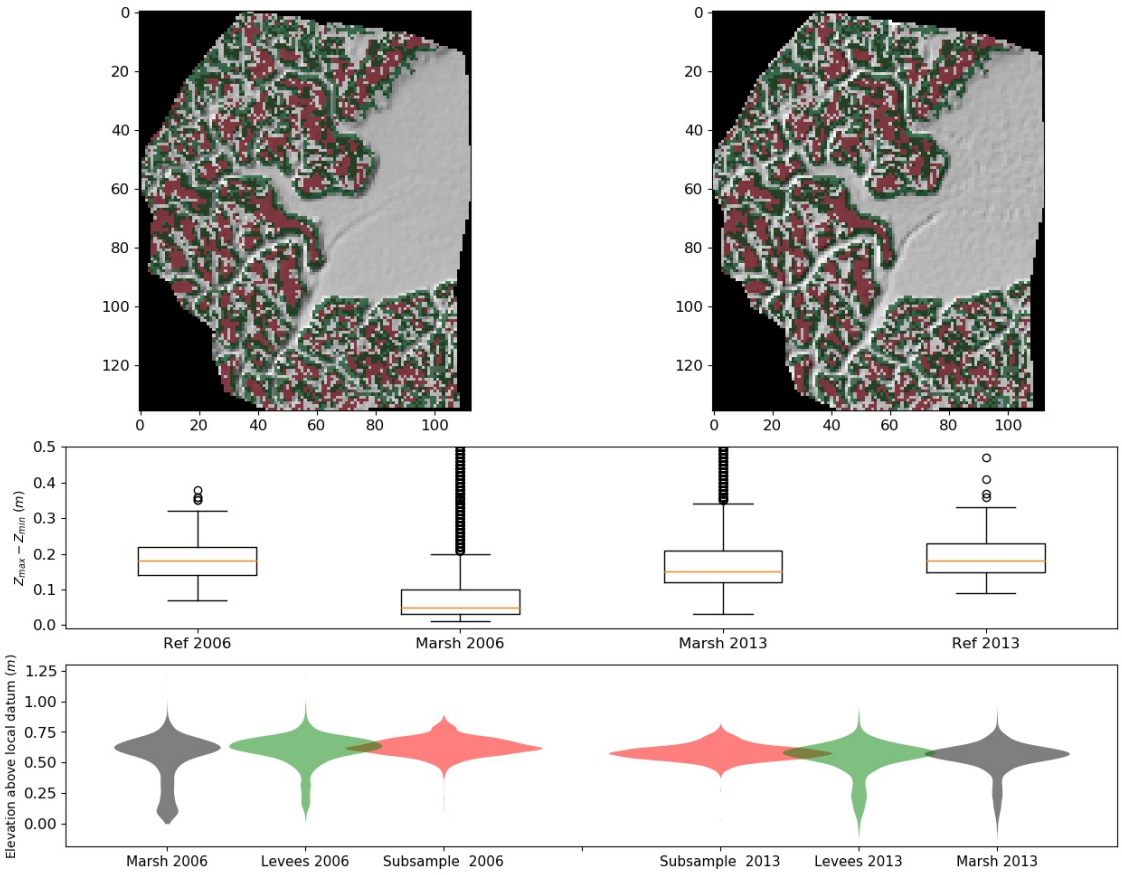


**Figure 6.9:** Equivalent of Figure 6.3 for Arne Bay.

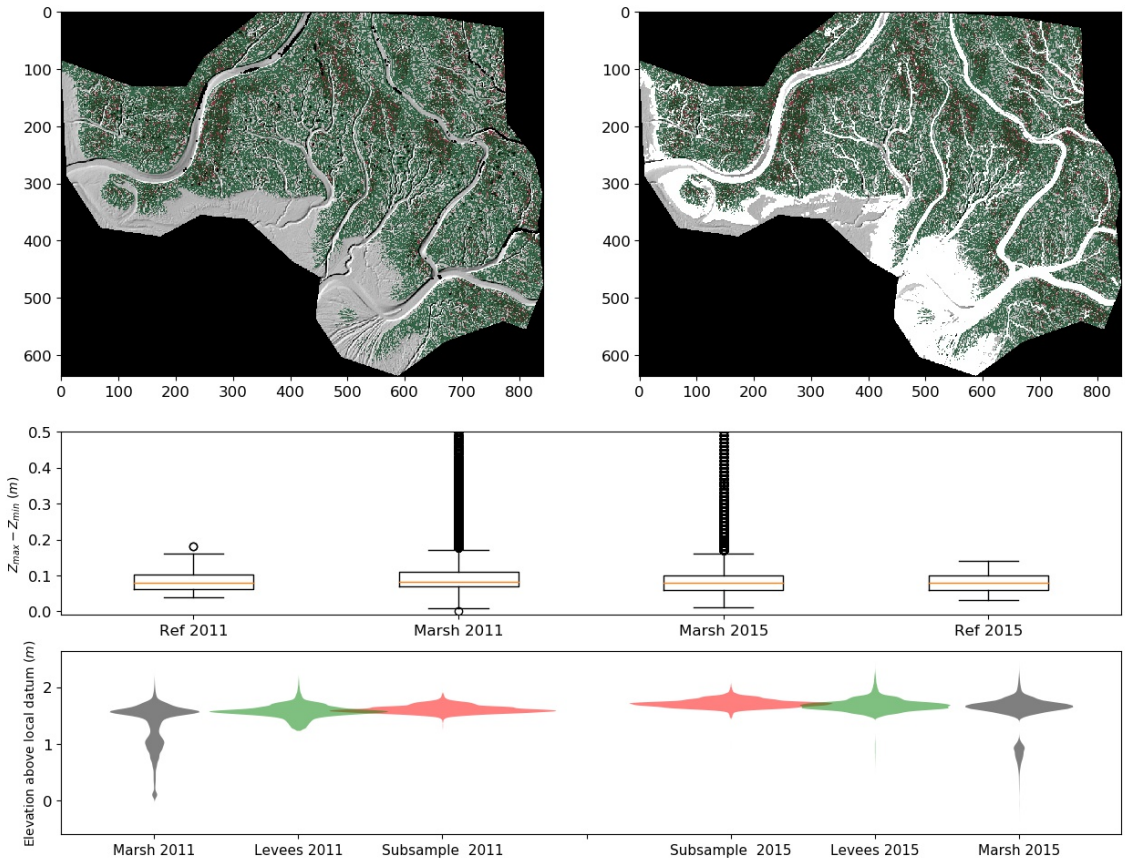


**Figure 6.10:** Equivalent of Figure 6.3 for Morro Bay.

## 6.3 Appendices to Chapter 4

### 6.3.1 Dtm Offset

### 6.3.2 Ground-Truthing

### 6.3.3 Sectors and Parameters Used for the Tip Method

### 6.3.4 Raw Elevation Data

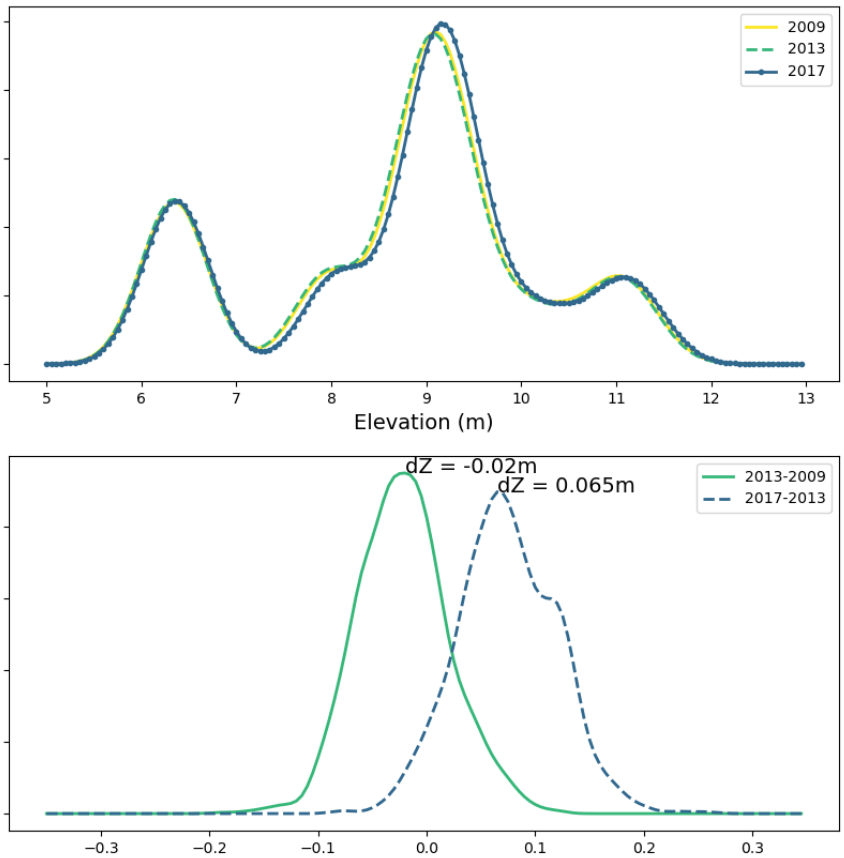


**Figure 6.11:** (**top**) Distribution of elevations for ground-truthing points in Moricambe Bay. (**bottom**) distribution of elevation offset between DTM point elevations at the location of ground-truthing points at different dates.

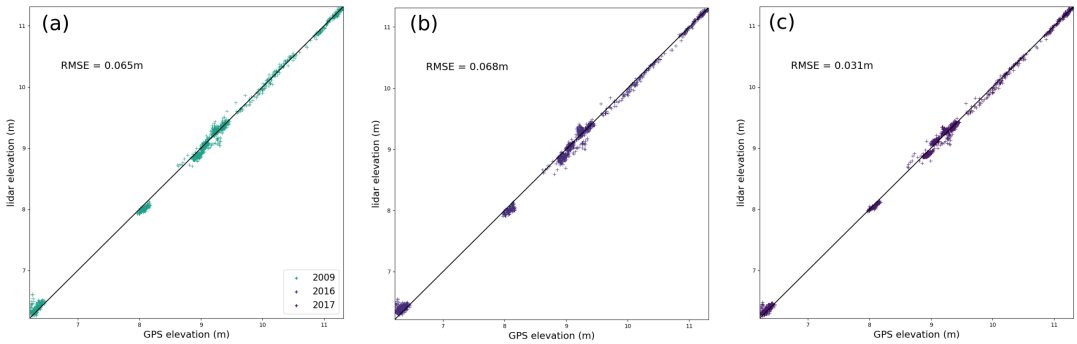


**Figure 6.12:** Comparative plot of elevations at ground-truthing points between the DTM and ground-truthing data of the same year or a close year. (**a**) the DTM year is 2009 and the ground-truthing year is 2009; (**b**) the DTM year is 2013 and the ground-truthing year is 2016; (**c**) the DTM year is 2017 and the ground-truthing year is 2017.

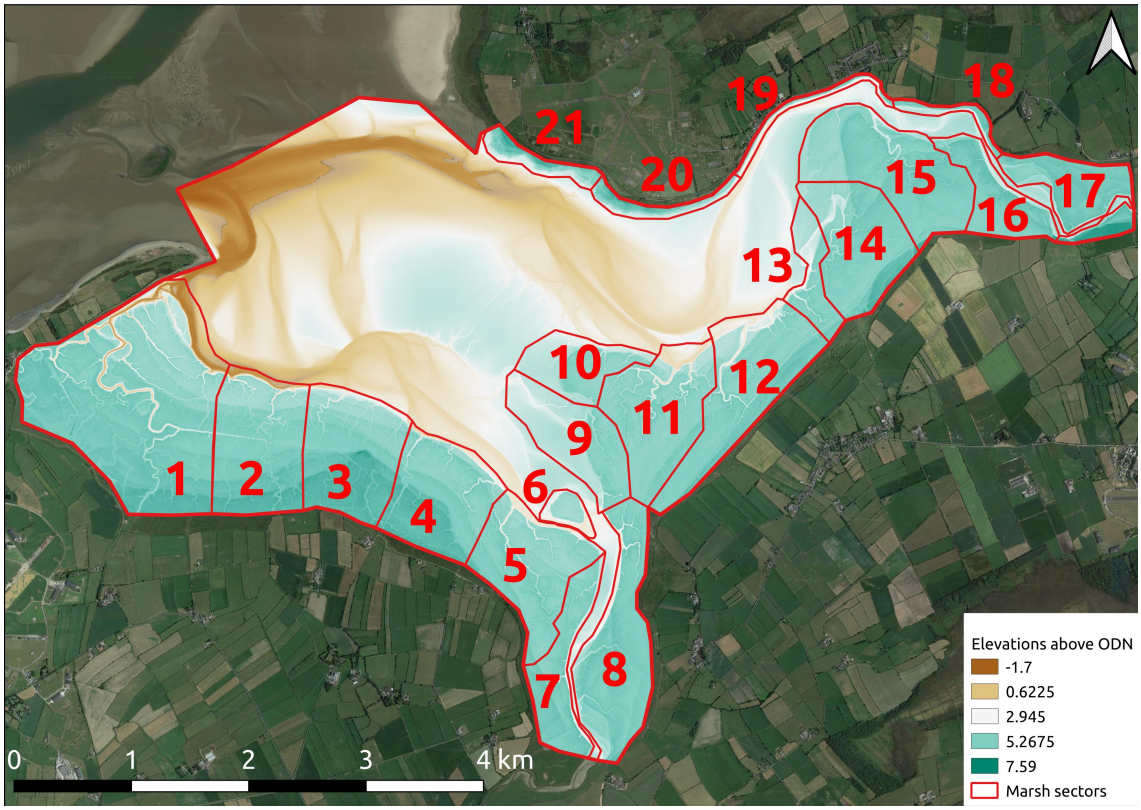


**Figure 6.13:** Map of the sectors used to implement the TIP method, overlain on the 2017 DTM of Moricambe Bay.

**Table 6.7:** The parameters used in the TIP method for each of the 21 sectors in the 2009 DTM.

| Sector | $Sp_{thresh}$ | $ZK_{thresh}$ | $rz_{thresh}$ |
|---|---|---|---|
| 1 | −2.0 | 0.85 | 8 |
| 2 | −2.0 | 0.85 | 8 |
| 3 | −2.0 | 0.85 | 8 |
| 4 | −2.0 | 0.85 | 8 |
| 5 | −2.0 | 0.85 | 8 |
| 6 | −2.0 | 0.85 | 8 |
| 7 | −2.0 | 0.85 | 8 |
| 8 | −2.0 | 0.85 | 8 |
| 9 | −2.0 | 0.85 | 8 |
| 10 | −2.0 | 0.85 | 8 |
| 11 | −2.0 | 0.85 | 8 |
| 12 | −2.0 | 0.35 | 24 |
| 13 | −2.0 | 0.85 | 14 |
| 14 | −2.0 | 0.85 | 2 |
| 15 | −2.0 | 0.85 | 1 |
| 16 | −2.0 | 0.85 | 1 |
| 17 | −2.0 | 0.85 | 8 |
| 18 | −2.0 | 0.85 | 10 |
| 19 | −2.0 | 0.85 | 12 |
| 20 | −3.0 | 0.4 | 22 |
| 21 | −2.0 | 0.85 | 14 |

**Table 6.8:** The parameters used in the TIP method for each of the 21 sectors in the 2013 DTM. Stars indicate manual modification of the marsh outline was performed.

| Sector | $Sp_{thresh}$ | $ZK_{thresh}$ | $rz_{thresh}$ |
|---|---|---|---|
| 1 | −2.0 | 0.85 | 8 |
| 2 | −2.0 | 0.85 | 8 |
| 3 | −2.0 | 0.85 | 8 |
| 4 | −2.0 | 0.85 | 8 |
| 5 | −2.0 | 0.85 | 8 |
| 6 | −2.0 | 0.85 | 8 |
| 7 | −2.0 | 0.85 | 8 |
| 8 | −2.0 | 0.85 | 8 |
| 9 | −2.0 | 0.85 | 20 |
| 10 | −2.0 | 0.85 | 13 |
| 11 | −2.0 | 0.85 | 12 |
| 12 | −2.0 | 0.35 | 12 |
| 13 | −2.0 | 0.85 | 12 |
| 14 | −2.0 | 0.85 | 7 |
| 15 | −2.0 | 0.85 | 6 |
| 16 | −2.0 | 0.85 | 1 |
| 17 | −2.0 | 0.85 | 8 |
| 18 | −2.0 | 0.85 | 10 |
| 19 | −2.0 | 0.85 | 20 * |
| 20 | −3. | 0.4 | 22 |
| 21 | −2.0 | 0.5 | 12 |

**Table 6.9:** The parameters used in the TIP method for each of the 21 sectors in the 2017 DTM. Stars indicate manual modification of the marsh outline was performed.

| Sector | $Sp_{thresh}$ | $ZK_{thresh}$ | $rz_{thresh}$ |
|---|---|---|---|
| 1 | $-2$ | 0.85 | 8 |
| 2 | $-2.0$ | 0.85 | 8 |
| 3 | $-2.0$ | 0.85 | 8 |
| 4 | $-2.0$ | 0.85 | 8 |
| 5 | $-2.0$ | 0.85 | 8 |
| 6 | $-2.0$ | 0.85 | 8 |
| 7 | $-2.0$ | 0.85 | 8 |
| 8 | $-2.0$ | 0.85 | 8 |
| 9 | $-2.0$ | 0.85 | 16 |
| 10 | $-2.0$ | 0.85 | 10 |
| 11 | $-3.0$ | 0.5 | 13 |
| 12 | $-3.0$ | 0.5 | 13 |
| 13 | $-2.0$ | 0.1 | 10 |
| 14 | $-2.0$ | 0.9 | 4 |
| 15 | $-2.0$ | 0.85 | 6 |
| 16 | $-2.0$ | 0.85 | 3 |
| 17 | $-2.0$ | 0.85 | 1 |
| 18 | $-2.0$ | 0.85 | 10 |
| 19 | $-2.0$ | 0.85 | 30 * |
| 20 | $-0.3$ | 0.4 | 22 |
| 21 | $-2.0$ | 0.5 | 16 |

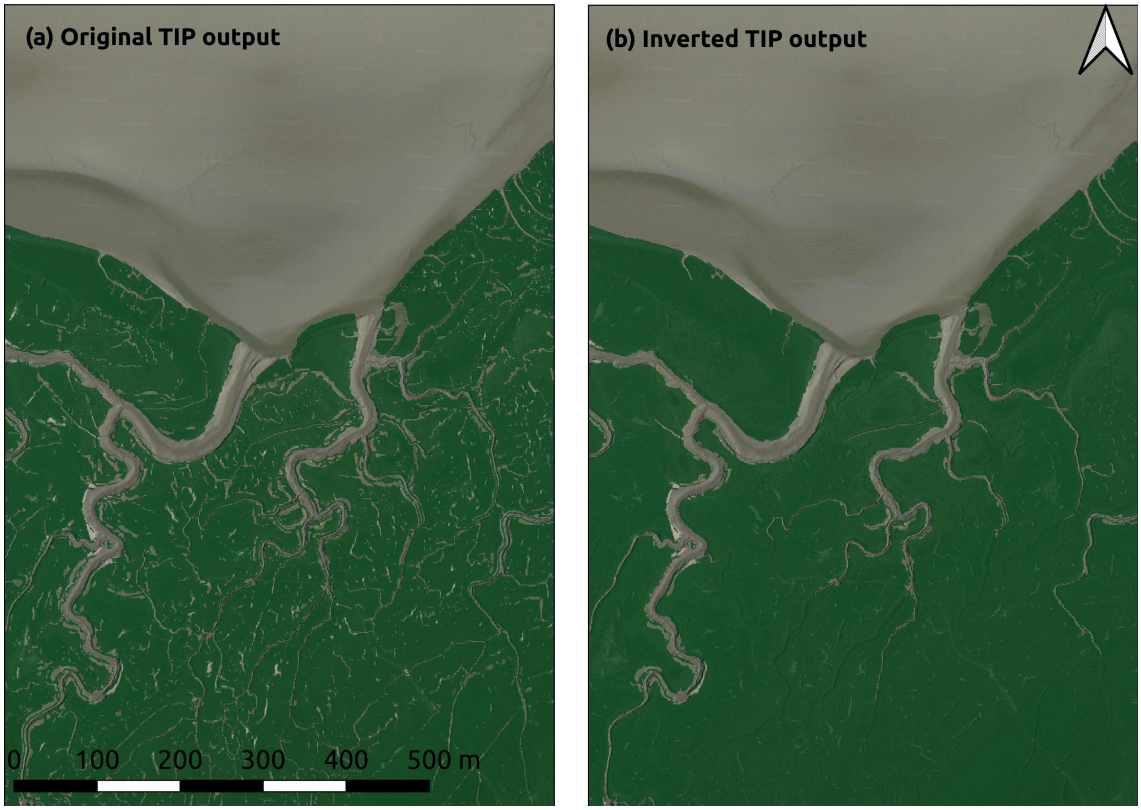


**Figure 6.14:** Example outputs of the TIP method, used in its original form (**a**) and "inverted" output, filled by considering as a marsh platform all pixels that are not part of the largest contiguous mudflat, in this case at the top of the panel (**b**). Marsh platforms are overlain over the Google Earth image of Figure 4.2.

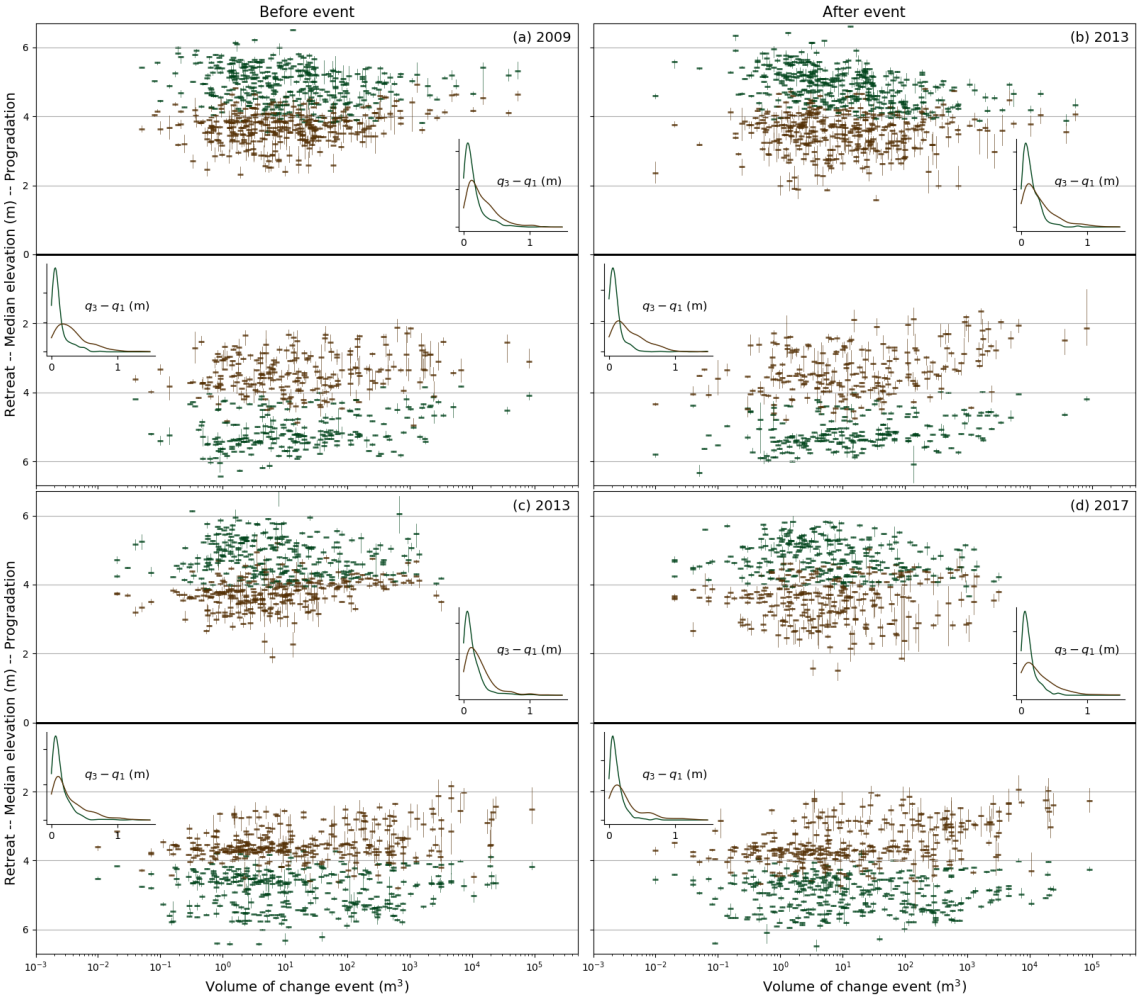


**Figure 6.15:** Median elevation (and surrounding quartiles) of the marsh (**green**) and mudflat (**brown**) portion of a group of profiles for individual change events. Progradation events are shown upward in each panel and retreat events are shown mirrorred along the $y = 0$ line. Insets show the distribution of the interquartile range for marsh and mudflat portions of profiles.

# Bibliography


Adams, J. C. and J. H. Chandler (2002). "EVALUATION OF LIDAR AND MEDIUM SCALE PHOTOGRAMMETRY FOR DETECTING SOFT-CLIFF COASTAL CHANGE". In: *Photogrammetric Record* 17.April, pp. 405–418.

Ahmad, M. F., P. Dong, M. Mamat, W. B. W. Nik, and M. H. Mohd (2011). "The critical shear stresses for sand and mud mixture". In: *Applied Mathematical Sciences* 5.2, pp. 53–71. URL: http://www.doaj.org/doaj?func=openurl%7B%5C&%7Dissn=1312885X%7B%5C&%7Ddate=2011%7B%5C&%7Dvolume=5%7B%5C&%7Dissue=2%7B%5C&%7Dspage=53%7B%5C&%7Dgenre=article.

Aldridge, J. N. (1997). "Hydrodynamic Model Predictions of Tidal Asymmetry Morecambe Bay". In: *Estuarine Coastal and Shelf Science*, pp. 39–56.

Allen, J. R. L. and J. E. Rae (1988). "Vertical salt-marsh accretion since the Roman Period in the Severn Estuary, southwest Britain". In: *Marine Geology* 83.1-4, pp. 225–235. DOI: 10.1016/0025-3227(88)90059-X.

Allen, J. R. L. (2000). "Morphodynamics of Holocene salt marshes: A review sketch from the Atlantic and Southern North Sea coasts of Europe". In: *Quaternary Science Reviews* 19.12, pp. 1155–1231. DOI: 10.1016/S0277-3791(99)00034-7.

Allen, J. R. (1989). "EVOLUTION OF SALT-MARSH CLIFFS IN MUDDY AND SANDY SYSTEMS : A QUALITATIVE COMPARISON OF BRITISH WEST-COAST ESTUARIES". In: *Earth Surface Processes and Landforms* 14.3, pp. 85–92.

Alves, J.-h. G. M. (2006). "Numerical modeling of ocean swell contributions to the global wind-wave climate". In: *Ocean Modelling* 11.243, pp. 98–122. DOI: 10.1016/j.ocemod.2004.11.007.

Amos, C. L. and T. T. Alfoldi (1979). "The determination of suspended sediment concentration in a macrotidal system using landsat data". In: *Journal of Sedimentary Petrology* 49.1, pp. 159–174.

Amos, C. L., A. Bergamasco, G. Umgiesser, S. Cappucci, D. Cloutier, L. Denat, et al. (2004). "The stability of tidal flats in Venice Lagoon - The results of in-situ measurements using two benthic, annular flumes". In: *Journal of Marine Systems* 51.1-4 SPEC. ISS. Pp. 211–241. DOI: 10.1016/j.jmarsys.2004.05.013.

Amos, C. L., G. Umgiesser, C. Ferrarin, C. E. L. Thompson, R. J. S. Whitehouse, T. F. Sutherland, et al. (2010). "The erosion rates of cohesive sediments in Venice lagoon, Italy". In: *Continental Shelf Research* 30.8, pp. 859–870. DOI: 10.1016/j.csr.2009.12.001.

Anisfeld, S. C., T. D. Hill, and D. R. Cahoon (2016). "Elevation dynamics in a restored versus a submerging salt marsh in Long Island Sound". In: *Estuarine, Coastal and Shelf Science* 170, pp. 145–154. DOI: 10.1016/j.ecss.2016.01.017.

Balke, T., T. J. Bouma, E. M. Horstman, E. L. Webb, P. L. A. Erftemeijer, and P. M. J. Herman (2011). "Windows of opportunity: Thresholds to mangrove seedling es-

tablishment on tidal flats". In: *Marine Ecology Progress Series* 440, pp. 1–9. DOI: 10.3354/meps09364.

Balke, T., P. C. Klaassen, A. Garbutt, D. Van der Wal, P. M. J. Herman, and T. J. Bouma (2012). "Conditional outcome of ecosystem engineering: A case study on tussocks of the salt marsh pioneer Spartina anglica". In: *Geomorphology* 153-154, pp. 232–238. DOI: 10.1016/j.geomorph.2012.03.002.

Balke, T., P. M. J. Herman, and T. J. Bouma (2014). "Critical transitions in disturbance-driven ecosystems: Identifying Windows of Opportunity for recovery". In: *Journal of Ecology*, pp. 700–708. DOI: 10.1111/1365-2745.12241.

Balke, T., M. Stock, K. Jensen, T. J. Bouma, and M. Kleyer (2016). "A global analysis of the seaward salt marsh extent: The importance of tidal range". In: *Water Resources Research* 52.5, pp. 3775–3786. DOI: 10.1002/2015WR018318. arXiv: 2014WR016527 [10.1002].

Barbier, E. B., S. D. Hacker, C. Kennedy, E. W. Koch, a. C. Stier, and B. R. Silliman (2011). "The value of estuarine and coastal ecosystem services". In: *Ecological Monographs* 81.2, pp. 169–193. DOI: 10.1890/10-1510.1.

Barrot, G., A. Mangin, and S. Pinnock (2007). *GlobColour Global Ocean Colour for Carbon Cycle Research Product User Guide*. Tech. rep.

Bartholdy, J., A. T. Bartholdy, D. Kim, and J. B. T. Pedersen (2014). "On autochthonous organic production and its implication for the consolidation of temperate salt marshes". In: *Marine Geology* 351, pp. 53–57. DOI: 10.1016/j.margeo.2014.03.015.

Bauer, B. O., M. S. Lorang, and D. J. Sherman (2002). "Estimating boat-wake-induced levee erosion using sediment suspension measurements". In: *Journal of Waterway, Port, Coastal and Ocean Engineering* 128.4, pp. 152–162. DOI: 10.1061/(ASCE)0733-950X(2002)128:4(152).

Beaumont, N. J., M. C. Austen, S. C. Mangi, and M. Townsend (2008). "Economic valuation for the conservation of marine biodiversity". In: *Marine Pollution Bulletin* 56, pp. 386–396. DOI: 10.1016/j.marpolbul.2007.11.013.

Belliard, J. P., N. Di Marco, L. Carniello, and M. Toffolon (2016). "Sediment and vegetation spatial dynamics facing sea-level rise in microtidal salt marshes: Insights from an ecogeomorphic model". In: *Advances in Water Resources* 93, pp. 249–264. DOI: 10.1016/j.advwatres.2015.11.020.

Belliard, J. P., S. Temmerman, and M. Toffolon (2017). "Ecogeomorphic relations between marsh surface elevation and vegetation properties in a temperate multi-species salt marsh". In: *Earth Surface Processes and Landforms* 42.6, pp. 855–865. DOI: 10.1002/esp.4041.

Belluco, E., M. Camuffo, S. Ferrari, L. Modenese, S. Silvestri, A. Marani, et al. (2006). "Mapping salt-marsh vegetation by multispectral and hyperspectral remote sensing". In: *Remote Sensing of Environment* 105.1, pp. 54–67. DOI: 10.1016/j.rse.2006.06.006.

Bendoni, M., S. Francalanci, L. Cappietti, and L. Solari (2014). "On salt marshes retreat: Experiments and modeling toppling failures induced by wind waves". In: *Journal of Geophysical Research: Earth Surface* 119, pp. 603–620. DOI: 10.1002/2013JF003000.Received.

Bertness, M. D., C. P. Brisson, T. C. Coverdale, M. C. Bevil, S. M. Crotty, and E. R. Suglia (2014). "Experimental predator removal causes rapid salt marsh die-off". In: *Ecology Letters* 17.7, pp. 830–835. DOI: 10.1111/ele.12287.

Borchert, S. M., M. J. Osland, N. M. Enwright, and K. T. Griffith (2018). "Coastal wetland adaptation to sea level rise : Quantifying potential for landward migration

and coastal squeeze". In: *Journal of Applied Ecology* March, pp. 2876–2887. DOI: 10.1111/1365-2664.13169.

Bouma, T. J., J. V. Belzen, T. Balke, J. V. Dalen, P. Klaassen, A. M. Hartog, et al. (2016). "Short-term mudflat dynamics drive long-term cyclic salt marsh dynamics". In: *Limnology and Oceanography* 61, pp. 2261–2275. DOI: 10.1002/lno.10374.

Bouma, T. J., L. A. van Duren, S. Temmerman, T. Claverie, A. Blanco-Garcia, T. Ysebaert, et al. (2007). "Spatial flow and sedimentation patterns within patches of epibenthic structures: Combining field, flume and modelling experiments". In: *Continental Shelf Research* 27.8, pp. 1020–1045. DOI: 10.1016/j.csr.2005.12.019.

Bouma, T. J., S. Temmerman, L. A. van Duren, E. Martini, W. Vandenbruwaene, D. P. Callaghan, et al. (2013). "Organism traits determine the strength of scale-dependent bio-geomorphic feedbacks: A flume study on three intertidal plant species". In: *Geomorphology* 180-181, pp. 57–65. DOI: 10.1016/j.geomorph.2012.09.005.

Brain, M. J., A. C. Kemp, B. P. Horton, S. J. Culver, A. C. Parnell, and N. Cahill (2015). "Quantifying the contribution of sediment compaction to late Holocene salt-marsh sea-level reconstructions, North Carolina, USA". In: *Quaternary Research (United States)* 83.1, pp. 41–51. DOI: 10.1016/j.yqres.2014.08.003. arXiv: arXiv:0811.2183v2.

Breugem, W. a. and L. H. Holthuijsen (2007). "Generalized Shallow Water Wave Growth from Lake George". In: *Journal of Waterway, Port, Coastal, and Ocean Engineering* 133.June, pp. 173–182. DOI: 10.1061/(ASCE)0733-950X(2007)133:3(173).

Brienen, Phillips, Feldpausch, Gloor, Baker, Lloyd, et al. (2015). "Long-term decline of the Amazon carbon sink". In: *Nature* 519.7543, pp. 344–348. DOI: 10.1038/nature14283.

Brodu, N. and D. Lague (2012). "3D terrestrial lidar data classification of complex natural scenes using a multi-scale dimensionality criterion: Applications in geomorphology". In: *ISPRS Journal of Photogrammetry and Remote Sensing* 68.1, pp. 121–134. DOI: 10.1016/j.isprsjprs.2012.01.006. arXiv: 1107.0550.

Bromirski, P. D., A. J. Miller, R. E. Flick, and G. Auad (2011). "Dynamical suppression of sea level rise along the Pacific coast of North America: Indications for imminent acceleration". In: *Journal of Geophysical Research: Oceans* 116.7, pp. 1–13. DOI: 10.1029/2010JC006759.

Brooks, H., I. Möller, S. Carr, C. Chirol, E. Christie, B. Evans, et al. (2020). "State of Science Resistance of salt marsh substrates to near-instantaneous hydrodynamic forcing". In: *Earth Surface Processes and Landforms*. DOI: 10.1002/esp.4912.

Butzeck, C., U. Schröder, J. Oldeland, S. Nolte, and K. Jensen (2016). "Vegetation succession of low estuarine marshes is affected by distance to navigation channel and changes in water level". In: *Journal of Coastal Conservation* 20.3, pp. 221–236. DOI: 10.1007/s11852-016-0432-1.

Buynevich, I. V., D. M. Fitzgerald, L. B. J. Smith, and A. J. Doughertyt (2001). "Stratigraphic Evidence for Historical Position of the East Cambridge Shoreline , Boston". In: *Journal of Coastal Research*, pp. 15–20.

Cahoon, D. R. and D. J. Reed (1995). "Relationships among Marsh Surface Topography, Hydroperiod , and Soil Accretion in a Deteriorating Louisiana Salt Marsh". In: *Journal of Coastal Research* 11.2, pp. 357–369.

Cahoon, D. R., J. C. Lynch, P. Hensel, R. Boumans, B. C. Perez, B. Segura, et al. (2001). "HIGH-PRECISION MEASUREMENTS OF WETLAND SEDIMENT ELEVATION : I . RECENT IMPROVEMENTS TO THE SEDIMENTATION – EROSION TABLE". In: *Journal of sedimentary research* 1993, pp. 730–733.

Cahoon, D. R., P. F. Hensel, T. Spencer, D. J. Reed, K. L. Mckee, and N. Saintilan (2006). "Coastal Wetland Vulnerability to Relative Sea-Level Rise : Wetland Elevation Trends and Process Controls". In: *Ecological Studies* 190.

Cahoon, D. R., J. C. Lynch, and A. N. Powell (1996). "Marsh Vertical Accretion in a Southern California Estuary, U.S.A." In: *Estuarine, Coastal and Shelf Science* 43.1, pp. 19–32. DOI: 10.1006/ecss.1996.0055.

Cahoon, D. R., J. R. French, T. Spencer, D. J. Reed, and I. Moller (2000). "Vertical accretion versus elevational adjustment in UK saltmarshes : an evaluation of alternative methodologies". In: *Coastal and Estuarine Environments. sedimentology, geomorphology and geoarchaeology*, pp. 223–238.

Cahoon, D. R. (2015). "Estimating Relative Sea-Level Rise and Submergence Potential at a Coastal Wetland". In: *Estuaries and Coasts* 38.3, pp. 1077–1084. DOI: 10.1007/s12237-014-9872-8.

Cain, M. R. and P. F. Hensel (2018). "Wetland Elevations at Sub-Centimeter Precision: Exploring the Use of Digital Barcode Leveling for Elevation Monitoring". In: *Estuaries and Coasts* 41.2, pp. 582–591. DOI: 10.1007/s12237-017-0282-6.

Carniello, L., A. Defina, S. Fagherazzi, and L. D'Alpaos (2005). "A combined wind wave-tidal model for the Venice lagoon, Italy". In: *Journal of Geophysical Research: Earth Surface* 110.4, pp. 1–15. DOI: 10.1029/2004JF000232.

Carniello, L., A. Defina, and L. D'Alpaos (2009). "Morphological evolution of the Venice lagoon: Evidence from the past and trend for the future". In: *Journal of Geophysical Research: Earth Surface* 114.4, pp. 1–10. DOI: 10.1029/2008JF001157.

Carniello, L., A. D'Alpaos, G. Botter, and A. Rinaldo (2016). "Statistical characterization of spatiotemporal sediment dynamics in the Venice lagoon". In: *Journal of Geophysical Research F: Earth Surface* 121.5, pp. 1049–1064. DOI: 10.1002/2015JF003793.

Castagno, K. A., A. M. Jiménez-robles, and J. P. Donnelly (2018). "Intense Storms Increase the Stability of Tidal Bays". In: *Geophysical Research Letters*, pp. 5491–5500. DOI: 10.1029/2018GL078208.

Chassereau, J. E., J. M. Bell, and R. Torres (2011). "A comparison of GPS and lidar salt marsh DEMs". In: *Earth Surface Processes and Landforms* 36.13, pp. 1770–1775. DOI: 10.1002/esp.2199.

Chirol, C., I. D. Haigh, N. Pontee, C. E. Thompson, and S. L. Gallop (2018). "Remote Sensing of Environment Parametrizing tidal creek morphology in mature saltmarshes using semi- automated extraction from lidar". In: *Remote Sensing of Environment* 209.March, pp. 291–311. DOI: 10.1016/j.rse.2017.11.012.

Chmura, G. L., S. C. Anisfeld, D. R. Cahoon, and J. C. Lynch (Dec. 2003a). "Global carbon sequestration in tidal, saline wetland soils". In: *Global Biogeochemical Cycles* 17.4, p. 1111. DOI: 10.1029/2002GB001917.

Chmura, G. L., S. C. Anisfeld, D. R. Cahoon, and J. C. Lynch (2003b). "Global carbon sequestration in tidal, saline wetland soils". In: *Global Biogeochemical Cycles* 17.4, p. 12. DOI: 111110.1029/2002gb001917. arXiv: 715796.

Clubb, F. J., S. M. Mudd, D. T. Milodowski, D. A. Valters, L. J. Slater, M. D. Hurst, et al. (2017). "Geomorphometric delineation of floodplains and terraces from objectively defined topographic thresholds". In: *Earth Surface Dynamics* 5, pp. 369–385.

Clubb, F. J., S. M. Mudd, D. T. Milodowski, M. D. Hurst, and L. J. Slater (2014). "Objective extraction of channel heads fromhigh-resolution topographic data". In: *Water Resources Research* 1, pp. 4840–4847. DOI: 10.1002/2015WR017273.Received.

Collin, A., B. Long, and P. Archambault (2010). "Salt-marsh characterization, zonation assessment and mapping through a dual-wavelength LiDAR". In: *Remote Sensing of Environment* 114.3, pp. 520–530. DOI: 10.1016/j.rse.2009.10.011.

Costanza, R., R. Arge, R. D. Groot, S. Farberk, M. Grasso, B. Hannon, et al. (1997). "The value of the world ' s ecosystem services and natural capital". In: *Nature* 387.May, pp. 253–260. DOI: 10.1038/387253a0. arXiv: 9809069v1 [arXiv:gr-qc].

Coverdale, T. C., C. P. Brisson, E. W. Young, S. F. Yin, J. P. Donnelly, and M. D. Bertness (2014). "Indirect human impacts reverse centuries of carbon sequestration and salt marsh accretion". In: *PLoS ONE* 9.3, pp. 1–7. DOI: 10.1371/journal.pone.0093296.

Cowell, P. J. and B. G. Thom (1994). "Morphodynamics of coastal evolution". In: *Coastal evolution: late Quaternary shoreline morphodynamics*, pp. 33–86.

Cox, R., R. A. Wadsworth, and A. G. Thomson (2003). "Long-term changes in salt marsh extent affected by channel deepening in a modified estuary". In: *Continental Shelf Research* 23.17-19, pp. 1833–1846. DOI: 10.1016/j.csr.2003.08.002.

Crave, A. and P. Davy (2001). "A stochastic " precipiton " model for simulating erosion / sedimentation dynamics". In: 27, pp. 815–827.

Crooks, S., J. Schutten, G. D. Sheern, K. Pye, and A. J. Davy (2002). "Drainage and elevation as factors in the restoration of salt marsh in Britain". In: *Restoration Ecology* 10.3, pp. 591–602. DOI: 10.1046/j.1526-100X.2002.t01-1-02036.x.

Crosby, S. C., D. F. Sax, M. E. Palmer, H. S. Booth, L. A. Deegan, M. D. Bertness, et al. (2016). "Salt marsh persistence is threatened by predicted sea-level rise". In: *Estuarine, Coastal and Shelf Science* 181, pp. 93–99. DOI: 10.1016/j.ecss.2016.08.018.

Cundy, A. B., L. Hopkinson, R. Lafite, K. Spencer, J. A. Taylor, B. Ouddane, et al. (2005). "Heavy metal distribution and accumulation in two Spartina sp . -dominated macrotidal salt marshes from the Seine estuary ( France ) and the Medway estuary ( UK )". In: *Applied Geochemistry* 20, pp. 1195–1208. DOI: 10.1016/j.apgeochem.2005.01.010.

D'Alpaos, A., S. M. Mudd, and L. Carniello (2011). "Dynamic response of marshes to perturbations in suspended sediment concentrations and rates of relative sea level rise". In: *Journal of Geophysical Research: Earth Surface* 116.4. DOI: 10.1029/2011JF002093.

D'Alpaos, A., S. Lanzoni, M. Marani, S. Fagherazzi, and A. Rinaldo (2005). "Tidal network ontogeny: Channel initiation and early development". In: *Journal of Geophysical Research: Earth Surface* 110.2, pp. 1–14. DOI: 10.1029/2004JF000182.

D'Alpaos, A., S. Lanzoni, M. Marani, and A. Rinaldo (2007a). "Landscape evolution in tidal embayments: Modeling the interplay of erosion, sedimentation, and vegetation dynamics". In: *Journal of Geophysical Research: Earth Surface* 112.1, pp. 1–17. DOI: 10.1029/2006JF000537.

D'Alpaos, A., S. Lanzoni, M. Marani, A. Bonometto, G. Cecconi, and A. Rinaldo (2007b). "Spontaneous tidal network formation within a constructed salt marsh: Observations and morphodynamic modelling". In: *Geomorphology* 91.3-4, pp. 186–197. DOI: 10.1016/j.geomorph.2007.04.013.

D'Alpaos, A., S. Lanzoni, M. Marani, and A. Rinaldo (2010). "On the tidal prism-channel area relations". In: *Journal of Geophysical Research: Earth Surface* 115.1, pp. 1–13. DOI: 10.1029/2008JF001243.

D'Alpaos, A., L. Carniello, and A. Rinaldo (2013). "Statistical mechanics of wind wave-induced erosion in shallow tidal basins: Inferences from the Venice Lagoon". In: *Geophysical Research Letters* 40.13, pp. 3402–3407. DOI: 10.1002/grl.50666.

D'Alpaos, A. and M. Marani (2016). "Reading the signatures of biologic-geomorphic feedbacks in salt-marsh landscapes". In: *Advances in Water Resources* 93, pp. 265–275. DOI: 10.1016/j.advwatres.2015.09.004.

Da Lio, C., A. D'Alpaos, and M. Marani (2013). "The secret gardener: vegetation and the emergence of biogeomorphic patterns in tidal environments." In: *Philosophical transactions. Series A, Mathematical, physical, and engineering sciences* 371.2004, p. 20120367. DOI: 10.1098/rsta.2012.0367.

Dalyander, P. S., B. Butman, C. R. Sherwood, R. P. Signell, and J. L. Wilkin (2013). "Characterizing wave- and current- induced bottom shear stress: U.S. middle Atlantic continental shelf". In: *Continental Shelf Research* 52, pp. 73–86. DOI: 10.1016/j.csr.2012.10.012.

Dame, R. and J. Lefeuvre (1994). "Tidal exchange: import-Tidal exchange: import-export of nutrients and organic matter in new and old world salt marshes: conclusions." In: *Global wetlands: old world and new*, pp. 303–305.

Day Jr., J. W., D. F. Boesch, E. J. Clairain, G. P. Kemp, S. B. Laska, W. J. Mitsch, et al. (2007). "Restoration of the Mississippi Delta: lessons from Hurricanes Katrina and Rita". In: *Science* 315.2007, pp. 1679–84. DOI: 10.1126/science.1137030.

Day, J. W., L. D. Britsch, S. R. Hawes, G. P. Shaffer, D. J. Reed, D. Cahoon, et al. (2000). "Pattern and process of land loss in the Mississippi Delta: A spatial and temporal analysis of wetland habitat change". In: *Estuaries* 23.4, p. 425. DOI: 10.2307/1353136.

Day, J. W., G. P. Kemp, D. J. Reed, D. R. Cahoon, R. M. Boumans, J. M. Suhayda, et al. (2011). "Vegetation death and rapid loss of surface elevation in two contrasting Mississippi delta salt marshes: The role of sedimentation, autocompaction and sea-level rise". In: *Ecological Engineering* 37.2, pp. 229–240. DOI: 10.1016/j.ecoleng.2010.11.021.

Defina, A., L. Carniello, S. Fagherazzi, and L. D'Alpaos (2007). "Self-organization of shallow basins in tidal flats and salt marshes". In: *Journal of Geophysical Research: Earth Surface* 112.3, pp. 1–11. DOI: 10.1029/2006JF000550.

Dijkema, K. S. (1997). "Impact prognosis for salt marshes from subsidence by gas extraction in the Wadden Sea". In: *Journal of Coastal Research* 13.4, pp. 1294–1304. URL: http://www.jstor.org/stable/10.2307/4298739.

Dobson, M. J. (1989). "History of malaria in England". In: *Journal of the Royal Society of Medicine* 82.17, pp. 3–7.

Donatelli, C., N. K. Ganju, X. Zhang, S. Fagherazzi, and N. Leonardi (2018). "Salt Marsh Loss Affects Tides and the Sediment Budget in Shallow Bays". In: *Journal of Geophysical Research: Earth Surface* 2002, pp. 2647–2662. DOI: 10.1029/2018JF004617.

Donnelly, J. P. (2006). "A Revised Late Holocene Sea-Level Record for Northern Massachusetts, USA". In: *Journal of Coastal Research* 225.5, pp. 1051–1061. DOI: 10.2112/04-0207.1.

Duarte, C. M., W. C. Dennison, R. J. W. Orth, and T. J. B. Carruthers (2008). "The charisma of coastal ecosystems: Addressing the imbalance". In: *Estuaries and Coasts* 31.2, pp. 233–238. DOI: 10.1007/s12237-008-9038-7.

Eisma, D. (1986). "Flocculation and De-Flocculation of suspended matter in estuaries". In: *Netherlands Journal of Sea Research* 20, pp. 183–199.

Elschot, K., T. J. Bouma, S. Temmerman, and J. P. Bakker (2013). "Effects of long-term grazing on sediment deposition and salt-marsh accretion rates". In: *Estuarine, Coastal and Shelf Science* 133, pp. 109–115. DOI: 10.1016/j.ecss.2013.08.021.

Emery, N. C., P. J. Ewanchuk, and M. D. Bertness (2001). "Competition and Salt-Marsh Plant Zonation : Stress Tolerators May Be Dominant Competitors". In: *Ecology* 82.9, pp. 2471–2485.

Eugene Turner, R., C. S. Milan, and E. M. Swenson (2006). "Recent volumetric changes in salt marsh soils". In: *Estuarine, Coastal and Shelf Science* 69.3-4, pp. 352–359. DOI: 10.1016/j.ecss.2006.05.005.

Evans, B. R., I. Möller, T. Spencer, and G. Smith (2019). "Dynamics of salt marsh margins are related to their three-dimensional functional form". In: *Earth Surface Processes and Landforms*. DOI: 10.1002/esp.4614.

Fagherazzi, S. and A. M. Priestas (2010). "Sediments and water fl uxes in a muddy coastline : interplay between waves and tidal channel hydrodynamics". In: *Earth Surface Processes and Landforms* 293.January, pp. 284–293. DOI: 10.1002/esp.1909.

Fagherazzi, S. and P. L. Wiberg (2009). "Importance of wind conditions, fetch, and water levels on wave-generated shear stresses in shallow intertidal basins". In: *Journal of Geophysical Research: Solid Earth* 114.3, pp. 1–12. DOI: 10.1029/2008JF001139.

Fagherazzi, S., G. Mariotti, A. T. Banks, E. J. Morgan, and R. W. Fulweiler (2014). "The relationships among hydrodynamics, sediment distribution, and chlorophyll in a mesotidal estuary". In: *Estuarine, Coastal and Shelf Science* 144, pp. 54–64. DOI: 10.1016/j.ecss.2014.04.003.

Fagherazzi, S., A. Bortoluzzi, W. E. Dietrich, A. Adami, S. Lanzoni, M. Marani, et al. (1999). "Tidal networks 1. Automatic network extraction and preliminary scaling features from digital terrain maps". In: *Water Resources Research* 35.12, pp. 3891–3904. DOI: 10.1029/1999WR900236.

Fagherazzi, S., L. Carniello, L. D'Alpaos, and A. Defina (2006). "Critical bifurcation of shallow microtidal landforms in tidal flats and salt marshes". In: *Proceedings of the National Academy of Sciences* 103.22, pp. 8337–8341. DOI: 10.1073/pnas.0508379103.

Fagherazzi, S., M. L. Kirwan, S. M. Mudd, G. R. Guntenspergen, S. Temmerman, J. M. Rybczyk, et al. (2012). "Numerical models of salt marsh evolution: Ecological, geormorphic, and climatic factors". In: *Review of Geophysics* 50.2011, pp. 1–28. DOI: 10.1029/2011RG000359.1.INTRODUCTION.

Fagherazzi, S., S. C. Anisfeld, L. K. Blum, E. V. Long, R. A. Feagin, A. Fernandes, et al. (2019). "Sea Level Rise and the Dynamics of the Marsh-Upland Boundary". In: *Frontiers in Environmental Science* 7.February, pp. 1–18. DOI: 10.3389/fenvs.2019.00025.

Farris, A. S., Z. Defne, and N. K. Ganju (2019). "Identifying Salt Marsh Shorelines from Remotely Sensed Elevation Data and Imagery". In: *Remote Sensing* 11.

Fawcett, T. (2006). "An introduction to ROC analysis". In: *Pattern Recognition Letters* 27.6, pp. 861–874. DOI: 10.1016/j.patrec.2005.10.010. arXiv: /dx.doi.org/10.1016/j.patrec.200 [http:].

Feagin, R. A., M. L. Martinez, G. Mendoza-Gonzalez, and R. Costanza (2010). "Salt marsh zonal migration and ecosystem service change in response to global sea level rise: A case study from an urban region". In: *Ecology & Society* 15.4, pp. 1–15. URL: http://proxying.lib.ncsu.edu/index.php?url=http://search.ebscohost.com/login.aspx?direct=true%7B%5C&%7Ddb=eih%7B%5C&%7DAN=66785167%

7B%5C&%7Dsite=ehost-live%7B%5C&%7Dscope=site%7B%5C%%7D5Cnhttp://pdxscholar.library.pdx.edu/iss%7B%5C_%7Dpub/35%7B%5C%%7D5Cnhttp://www.ecologyandsociety.org/vol15/iss4/art14/%7B%5C%%7D5Cn.

Finnigan, J. J., R. H. Shaw, and E. G. Patton (2009). "Turbulence structure above a vegetation canopy". In: *Journal of Fluid Mechanics* 637, p. 387. DOI: 10.1017/S0022112009990589.

Francalanci, S., M. Bendoni, M. Rinaldi, and L. Solari (2013). "Ecomorphodynamic evolution of salt marshes: Experimental observations of bank retreat processes". In: *Geomorphology* 195, pp. 53–65. DOI: 10.1016/j.geomorph.2013.04.026.

French, J. (2006). "Tidal marsh sedimentation and resilience to environmental change: Exploratory modelling of tidal, sea-level and sediment supply forcing in predominantly allochthonous systems". In: *Marine Geology* 235.1-4 SPEC. ISS. Pp. 119–136. DOI: 10.1016/j.margeo.2006.10.009.

Friedrichs, C. T. (2012). *Tidal Flat Morphodynamics: A Synthesis*. Vol. 3. Elsevier Inc., pp. 137–170. ISBN: 9780080878850. DOI: 10.1016/B978-0-12-374711-2.00307-7.

Friedrichs, C. T. and J. E. Perry (2001). "Tidal Salt Marsh Morphodynamics: A Synthesis". In: *Journal of Coastal Research* 27, pp. 7–37. DOI: 10.2307/25736162.

Gailleton, B., S. M. Mudd, F. J. Clubb, D. Peifer, and M. D. Hurst (2019). "A segmentation approach for the reproducible extraction and quantification of knickpoints from river long profiles". In: *Earth Surface Dynamics* 7, pp. 211–230.

Ganju, N. K., Z. Defne, M. L. Kirwan, S. Fagherazzi, A. D'Alpaos, and L. Carniello (2017). "Spatially integrative metrics reveal hidden vulnerability of microtidal salt marshes". In: *Nature Communications* 8, p. 14156. DOI: 10.1038/ncomms14156.

Gao, A. S. and M. B. Collins (1994). "Analysis of Grain Size Trends , for Defining Sediment Transport Pathways in Marine Environments". In: *Journal of Coastal Research* 10.1, pp. 70–78.

Gartner, J. W. (2004). "Estimating suspended solids concentrations from backscatter intensity measured by acoustic Doppler current profiler in San Francisco Bay , California". In: *Marine Geology* 211, pp. 169–187. DOI: 10.1016/j.margeo.2004.07.001.

Gedan, K. B., B. R. Silliman, and M. D. Bertness (2009). "Centuries of human-driven change in salt marsh ecosystems." In: *Annual review of marine science* 1, pp. 117–141. DOI: 10.1146/annurev.marine.010908.163930.

Gedan, K. B., M. L. Kirwan, E. Wolanski, E. B. Barbier, and B. R. Silliman (2011). "The present and future role of coastal wetland vegetation in protecting shorelines: Answering recent challenges to the paradigm". In: *Climatic Change* 106.1, pp. 7–29. DOI: 10.1007/s10584-010-0003-7.

Godfrey, S., J. Cooper, F. Bezombes, and A. Plater (2020). "Monitoring coastal morphology : the potential of low-cost fixed array action cameras for 3D reconstruction". In: *Earth Surface Processes and Landforms*. DOI: 10.1002/esp.4892.

Goodwin, G. C. H. and S. M. Mudd (2019). "High Platform Elevations Highlight the Role of Storms and Spring Tides in Salt Marsh Evolution". In: *Frontiers in Environmental Science* 7.May, pp. 1–14. DOI: 10.3389/fenvs.2019.00062.

Goodwin, G. C., S. M. Mudd, and F. J. Clubb (2018). "Unsupervised detection of salt marsh platforms: A topographic method". In: *Earth Surface Dynamics* 6.1, pp. 239–255. DOI: 10.5194/esurf-6-239-2018.

Goodwin, G. C. and S. M. Mudd (2020). "Detecting the Morphology of Prograding and Retreating Marsh Margins — Example of a Mega-Tidal Bay". In: *Remote Sensing* 12.13. DOI: 10.3390/rs12010013.

Gray, A. J. and R. Scott (1977). "The Ecology of Morecambe Bay . VII . The Distribution of Puccinellia maritima , Festuca rubra and Agrostis stolonifera in the Salt Marshes". In: *British Ecological Society* 14.1, pp. 229–241.

Green, F. H. W. (1940). *Poole Harbour - a hydrographic survey 1938-9*.

Grieve, S. W. D., S. M. Mudd, D. T. Milodowski, F. J. Clubb, and D. J. Furbish (2016a). "How does grid-resolution modulate the topographic expression of geomorphic processes ?" In: *Earth Surface Dynamics* 4, pp. 627–653. DOI: 10.5194/esurf-4-627-2016.

Grieve, S. W. D., S. M. Mudd, D. T. Milodowski, F. J. Clubb, and D. J. Furbish (2016b). "How does grid-resolution modulate the topographic expression of geomorphic processes ?" In: *Earth Surface Dynamics* 4, pp. 627–653. DOI: 10.5194/esurf-4-627-2016.

Haas, H. L., K. a. Rose, B. Fry, T. J. Minello, and L. P. Rozas (2004). "Brown Shrimp on the Edge : Linking Habitat to Survival Using an Individual-Based Simulation Model". In: *Ecological Applications* 14.4, pp. 1232–1247.

Hasselmann, K., T. P. Barnett, E. Bouws, H. Carlson, D. E. Cartwright, K. Enke, et al. (1973). "Measurements of Wind-Wave Growth and Swell Decay during the Joint North Sea Wave Project (JONSWAP)". In: *Ergnzungsheft zur Deutschen Hydrographischen Zeitschrift Reihe* A(8).8 0, p.95. DOI: citeulike-article-id:2710264.

Hayden, B. P., M. C. F. V. Santos, G. Shao, and R. C. Kochel (1995). "Geomorphological controls on coastal vegetation at the virginia Coast Reserve". In: *Geomorphology* 13, pp. 283–300.

Hladik, C. and M. Alber (2012a). "Accuracy assessment and correction of a LIDAR-derived salt marsh digital elevation model". In: *Remote Sensing of Environment* 121, pp. 224–235. DOI: 10.1016/j.rse.2012.01.018.

Hladik, C. and M. Alber (2012b). "Accuracy assessment and correction of a LIDAR-derived salt marsh digital elevation model". In: *Remote Sensing of Environment* 121, pp. 224–235. DOI: 10.1016/j.rse.2012.01.018.

Hladik, C., J. Schalles, and M. Alber (2013). "Salt marsh elevation and habitat mapping using hyperspectral and LIDAR data". In: *Remote Sensing of Environment* 139, pp. 318–330. DOI: 10.1016/j.rse.2013.08.003.

Hladik, C. and M. Alber (2014). "Classification of salt marsh vegetation using edaphic and remote sensing-derived variables". In: *Estuarine, Coastal and Shelf Science* 141, pp. 47–57. DOI: 10.1016/j.ecss.2014.01.011.

Holdaway, G. P., P. D. Thorne, D. Flatt, S. E. Jones, and D. Prandle (1999). "Comparison between ADCP and transmissometer measurements of suspended sediment concentration". In: *Continental Shelf Research* 19, pp. 421–441.

Hopkinson, C., J. T. Morris, S. Fagherazzi, W. M. Wollheim, and P. A. Raymond (2018a). "Lateral Marsh Edge Erosion as a Source of Sediments for Vertical Marsh Accretion". In: *Journal of Geophysical Research G: Biogeosciences*, pp. 2444–2465. DOI: 10.1029/2017JG004358.

Hopkinson, C., J. T. Morris, S. Fagherazzi, W. M. Wollheim, and P. A. Raymond (2018b). "Lateral Marsh Edge Erosion as a Source of Sediments for Vertical Marsh Accretion". In: *Journal of Geophysical Research G: Biogeosciences*, pp. 2444–2465. DOI: 10.1029/2017JG004358.

Houwing, E.-J. J. (1999). "Determination of the critical erosion threshold of cohesive sediments on intertidal mudflats along the Dutch Wadden Sea coast". In: *Esuarine, Coastal and Shelf Science* 49, pp. 545–555. DOI: 10.1006/ecss.1999.0518.

Hu, Z., J. Van Belzen, D. Van Der Wal, T. Balke, Z. B. Wang, M. Stive, et al. (2015). "Windows of opportunity for salt marsh vegetation establishment on bare tidal flats: The importance of temporal and spatial variability in hydrodynamic forcing". In: *Journal of Geophysical Research G: Biogeosciences* 120.7, pp. 1450–1469. DOI: 10.1002/2014JG002870.

Hubbard, J. . C. . E. . (1965). "Spartina Marshes in Southern England : VI . Pattern of Invasion in Poole Harbour". In: *British Ecological Society* 53.3, pp. 799–813.

Hurst, M. D., S. M. Mudd, R. Walcott, M. Attal, and K. Yoo (2012). "Using hilltop curvature to derive the spatial distribution of erosion rates". In: *Journal of Geophysical Research: Earth Surface* 117.2, pp. 1–19. DOI: 10.1029/2011JF002057.

Ipcc, I. P. o. C. C. (2014). "Coastal Systems and Low-Lying Areas". In: *Climate Change 2014: Impacts, Adaptation, and Vulnerability. Part A: Global and Sectoral Aspects. Contribution of Working Group II to the Fifth Assessment Report of the Intergovernmental Panel on Climate Change*, pp. 361–409.

Jankowski, K. L., T. E. Törnqvist, and A. M. Fernandes (2017). "Vulnerability of Louisiana's coastal wetlands to present-day rates of relative sea-level rise". In: *Nature Communications* 8, pp. 1–7. DOI: 10.1038/ncomms14792.

Jonkman, S. N., B. Maaskant, E. Boyd, and M. L. Levitan (2009). "Loss of life caused by the flooding of New Orleans after hurricane Katrina: Analysis of the relationship between flood characteristics and mortality". In: *Risk Analysis* 29.5, pp. 676–698. DOI: 10.1111/j.1539-6924.2008.01190.x.

Jucke van Beijma, S. (2015). "Remote Sensing - Based Mapping and Modelling of Coastal Salt Marsh Habitats Based on Optical , Lidar and Sar Data". PhD thesis, p. 206.

Julian, J. P. and R. Torres (2006). "Hydraulic erosion of cohesive riverbanks". In: *Geomorphology* 76.1-2, pp. 193–206. DOI: 10.1016/j.geomorph.2005.11.003.

Karimpour, A., Q. Chen, and R. R. Twilley (2017). "Wind Wave Behavior in Fetch and Depth Limited Estuaries". In: *Scientific Reports* 7.April 2016, p. 40654. DOI: 10.1038/srep40654.

Kearney, W. S. and S. Fagherazzi (2016). "Salt marsh vegetation promotes efficient tidal channel networks". In: *Nature Communications* 7, pp. 1–7. DOI: 10.1038/ncomms12287.

Kennish, M. J. (2001). "Coastal Salt Marsh Systems in the U . S .: A Review of Anthropogenic Impacts". In: 17.3, pp. 731–748.

Kirwan, M. and S. Temmerman (2009). "Coastal marsh response to historical and future sea-level acceleration". In: *Quaternary Science Reviews* 28.17-18, pp. 1801–1808. DOI: 10.1016/j.quascirev.2009.02.022.

Kirwan, M. L. and G. R. Guntenspergen (2010). "Influence of tidal range on the stability of coastal marshland". In: *Journal of Geophysical Research: Earth Surface* 115.F2, F02009. DOI: 10.1029/2009jf001400.

Kirwan, M. L. and S. M. Mudd (2012). "Response of salt-marsh carbon accumulation to climate change." In: *Nature* 489.7417, pp. 550–3. DOI: 10.1038/nature11440. arXiv: 9809069v1 [arXiv:gr-qc].

Kirwan, M. L. and A. B. Murray (2008). "Tidal marshes as disequilibrium landscapes? Lags between morphology and Holocene sea level change". In: *Geophysical Research Letters* 35.24, pp. 1–5. DOI: 10.1029/2008GL036050.

Kirwan, M. L., G. R. Guntenspergen, A. D'Alpaos, J. T. Morris, S. M. Mudd, and S. Temmerman (2010). "Limits on the adaptability of coastal marshes to rising sea level". In: *Geophysical Research Letters* 37.23, pp. 1–5. DOI: 10.1029/2010GL045489.

Kirwan, M. L., A. B. Murray, J. P. Donnelly, and D. R. Corbett (2011). "Rapid wetland expansion during European settlement and its implication for marsh survival under modern sediment delivery rates". In: *Geology* 39.5, pp. 507–510. DOI: 10.1130/G31789.1.

Kirwan, M. L. and J. P. Megonigal (2013). "Tidal wetland stability in the face of human impacts and sea-level rise". In: *Nature* 504.7478, pp. 53–60. DOI: 10.1038/nature12856.

Kirwan, M. L., S. Temmerman, E. E. Skeehan, G. R. Guntenspergen, and S. Fagherazzi (2016a). "Overestimation of marsh vulnerability to sea level rise". In: *Nature Climate Change* 6.3, pp. 253–260. DOI: 10.1038/nclimate2909.

Kirwan, M. L., S. Temmerman, E. E. Skeehan, G. R. Guntenspergen, and S. Fagherazzi (2016b). "Overestimation of marsh vulnerability to sea level rise". In: *Nature Climate Change* 6.3, pp. 253–260. DOI: 10.1038/nclimate2909.

Kokkalas, S. and I. K. Koukouvelas (2005). "Fault-scarp degradation modeling in central Greece : The Kaparelli and Eliki faults ( Gulf of Corinth ) as a case study". In: *Journal of Geodynamics* 40, pp. 200–215. DOI: 10.1016/j.jog.2005.07.006.

Kuhn, N. and J. B. Zedler (1997). "Differential Effects of Salinity and Soil Saturation on Native and Exotic Plants of a Coastal Salt Marsh". In: *Estuaries* 20.2, pp. 391–403.

Kvale, E. P. (2006). "The origin of neap-spring tidal cycles". In: *Marine Geology* 235.1-4 SPEC. ISS. Pp. 5–18. DOI: 10.1016/j.margeo.2006.10.001.

Ladd, C. J. T. and M. F. D. Edwards (2019). "Sediment Supply Explains Long - Term and Large - Scale Patterns in Salt Marsh Lateral Expansion and Erosion". In: *Geophysical Research Letters* 46, pp. 1–10. DOI: 10.1029/2019GL083315.

Lafleur, E., D. Yeates, and A. Aysen (2002). "Estimating the Economic Impact of the Wild Shrimp, Penaeus sp., Fishery: A Study of Terrebonne Parsih, Louisiana". In: *Marine Fisheries review*, pp. 28–43.

Lagomasino, D., D. R. Corbett, and J. P. Walsh (2013). "Influence of Wind-Driven Inundation and Coastal Geomorphology on Sedimentation in Two Microtidal Marshes, Pamlico River Estuary, NC". In: *Estuaries and Coasts* 36.6, pp. 1165–1180. DOI: 10.1007/s12237-013-9625-0.

Leblond, P. H. (1978). "On Tidal Propagation in Shallow Rivers". In: *Journal of Geophysical Research* 83.8, pp. 4717–4721.

Leonardi, N. and S. Fagherazzi (2014). "How waves shape salt marshes". In: *Geology* 42.10, pp. 887–890. DOI: 10.1130/G35751.1.

Leonardi, N., N. K. Ganju, and S. Fagherazzi (2016a). "A linear relationship between wave power and erosion determines salt-marsh resilience to violent storms and hurricanes". In: *Proceedings of the National Academy of Sciences* 113.1, pp. 64–68. DOI: 10.1073/pnas.1510095112.

Leonardi, N., Z. Defne, N. K. Ganju, and S. Fagherazzi (2016b). "Salt marsh erosion rates and boundary features in a shallow Bay". In: *Journal of Geophysical Research : Earth Surface*, pp. 1–15. DOI: 10.1002/2016JF003975.Received.

Lerberg, S. (2016). "Assessing tidal marsh resilience to sea-level rise at broad geographic scales with multi-metric indices". In: *Biological Conservation* 204, pp. 263–275. DOI: 10.1016/j.biocon.2016.10.015.

Leroux, J. (2013). "Chenaux tidaux et dynamique des prés- salés en régime méga-tidal : approche multi-temporelle du siècle à l'évènement de marée". In: p. 216.

Liu, Y., M. Zhou, S. Zhao, W. Zhan, K. Yang, and M. Li (2015). "Automated extraction of tidal creeks from airborne laser altimetry data". In: *Journal of Hydrology* 527, pp. 1006–1020. DOI: 10.1016/j.jhydrol.2015.05.058.

Ma, Z., T. Ysebaert, D. van der Wal, D. J. de Jong, X. Li, and P. M. J. Herman (2014). "Long-term salt marsh vertical accretion in a tidal bay with reduced sediment supply". In: *Estuarine, Coastal and Shelf Science* 146, pp. 14–23. DOI: 10.1016/j.ecss.2014.05.001.

Mallet, C. and F. Bretar (2009). "ISPRS Journal of Photogrammetry and Remote Sensing Full-waveform topographic lidar : State-of-the-art". In: *ISPRS Journal of Photogrammetry and Remote Sensing* 64.1, pp. 1–16. DOI: 10.1016/j.isprsjprs.2008.09.007.

Manning, A. J., J. V. Baugh, J. R. Spearman, and R. J. S. Whitehouse (2010). "Flocculation settling characteristics of mud : sand mixtures". In: *Ocean Dynamics*, pp. 237–253. DOI: 10.1007/s10236-009-0251-0.

Marani, M., A. D'Alpaos, S. Lanzoni, and M. Santalucia (2011). "Understanding and predicting wave erosion of marsh edges". In: *Geophysical Research Letters* 38.21, pp. 1–5. DOI: 10.1029/2011GL048995.

Marani, M., A. D'Alpaos, S. Lanzoni, L. Carniello, and A. Rinaldo (2007). "Biologically-controlled multiple equilibria of tidal landforms and the fate of the Venice lagoon". In: *Geophysical Research Letters* 34.11, pp. 1–5. DOI: 10.1029/2007GL030178.

Marani, M., A. D'Alpaos, S. Lanzoni, L. Carniello, and A. Rinaldo (2010). "The importance of being coupled: Stable states and catastrophic shifts in tidal biomorphodynamics". In: *Journal of Geophysical Research: Earth Surface* 115.4, pp. 1–15. DOI: 10.1029/2009JF001600.

Marani, M., C. Da Lio, and A. D'Alpaos (2013). "Vegetation engineers marsh morphology through multiple competing stable states." In: *Proceedings of the National Academy of Sciences of the United States of America* 110.9, pp. 3259–63. DOI: 10.1073/pnas.1218327110. arXiv: arXiv:1408.1149.

Mariotti, G., S. Fagherazzi, P. L. Wiberg, K. J. McGlathery, L. Carniello, and A. Defina (2010). "Influence of storm surges and sea level on shallow tidal basin erosive processes". In: *Journal of Geophysical Research: Oceans* 115.11, pp. 1–17. DOI: 10.1029/2009JC005892.

Mariotti, G. and S. Fagherazzi (2011). "Asymmetric fluxes of water and sediments in a mesotidal mudflat channel". In: *Continental Shelf Research* 31.1, pp. 23–36. DOI: 10.1016/j.csr.2010.10.014.

Mariotti, G. and S. Fagherazzi (2010). "A numerical model for the coupled long-term evolution of salt marshes and tidal flats". In: *Journal of Geophysical Research: Earth Surface* 115.1, pp. 1–15. DOI: 10.1029/2009JF001326.

Mariotti, G. and S. Fagherazzi (2013a). "Critical width of tidal flats triggers marsh collapse in the absence of sea-level rise." In: *Proceedings of the National Academy of Sciences of the United States of America* 110.14, pp. 5353–6. DOI: 10.1073/pnas.1219600110. arXiv: arXiv:1408.1149.

Mariotti, G. and S. Fagherazzi (2013b). "Wind waves on a mudflat: The influence of fetch and depth on bed shear stresses". In: *Continental Shelf Research* 60, S99–S110. DOI: 10.1016/j.csr.2012.03.001.

Marques, B., A. I. Lillebø, E. Pereira, and A. C. Duarte (2011). "Mercury cycling and sequestration in salt marshes sediments: An ecosystem service provided by Juncus maritimus and Scirpus maritimus". In: *Environmental Pollution* 159.7, pp. 1869–1876. DOI: 10.1016/j.envpol.2011.03.036.

McLoughlin, S. M., P. L. Wiberg, I. Safak, and K. J. McGlathery (2015). "Rates and Forcing of Marsh Edge Erosion in a Shallow Coastal Bay". In: *Estuaries and Coasts* 38, pp. 620–638. DOI: 10.1007/s12237-014-9841-2.

Mcowen, C., L. Weatherdon, J.-W. Bochove, E. Sullivan, S. Blyth, C. Zockler, et al. (2017). "A global map of saltmarshes". In: *Biodiversity Data Journal* 5, e11764. DOI: 10.3897/BDJ.5.e11764.

Mehta, A. J., K. N. Hwang, and Y. P. Khare (2015). "Critical shear stress for mass erosion of organic-rich fine sediments". In: *Estuarine, Coastal and Shelf Science* 165, pp. 97–103. DOI: 10.1016/j.ecss.2015.08.020.

Mo, Y., B. Momen, and M. S. Kearney (2015). "Quantifying moderate resolution remote sensing phenology of Louisiana coastal marshes". In: *Ecological Modelling* 312, pp. 191–199. DOI: http://dx.doi.org/10.1016/j.ecolmodel.2015.05.022.

Moffett, K. B., D. A. Robinson, and S. M. Gorelick (2010). "Relationship of Salt Marsh Vegetation Zonation to Spatial Patterns in Soil Moisture, Salinity, and Topography". In: *Ecosystems* 13.8, pp. 1287–1302. DOI: 10.1007/s10021-010-9385-7.

Moffett, K. B., S. M. Gorelick, R. G. McLaren, and E. A. Sudicky (2012). "Salt marsh ecohydrological zonation due to heterogeneous vegetation-groundwater-surface water interactions". In: *Water Resources Research* 48.2. DOI: 10.1029/2011WR010874.

Molinaroli, E., S. Guerzoni, A. Sarretta, M. Masiol, and M. Pistolato (2009). "Thirty-year changes (1970 to 2000) in bathymetry and sediment texture recorded in the Lagoon of Venice sub-basins, Italy". In: *Marine Geology* 258.1-4, pp. 115–125. DOI: 10.1016/j.margeo.2008.12.001.

Möller, I. (2006). "Quantifying saltmarsh vegetation and its effect on wave height dissipation: Results from a UK East coast saltmarsh". In: *Estuarine, Coastal and Shelf Science* 69.3-4, pp. 337–351. DOI: 10.1016/j.ecss.2006.05.003.

Möller, I. and T. Spencer (2002). "Wave dissipation over macro-tidal saltmarshes: Effects of marsh edge typology and vegetation change". In: *Journal of Coastal Research* 36.36, pp. 506–521. DOI: ISSN:0749-0208.

Möller, I., M. Kudella, F. Rupprecht, T. Spencer, M. Paul, B. K. van Wesenbeeck, et al. (2014). "Wave attenuation over coastal salt marshes under storm surge conditions". In: *Nature Geoscience* 7.September, pp. 727–731. DOI: 10.1038/ngeo2251.

Montané, J. M. and R. Torres (2006). "Accuracy Assessment of Lidar Saltmarsh Topographic Data Using RTK GPS". In: *Photogrammetric Engineering & Remote Sensing* August, pp. 961–967. DOI: 0099-1112/06/7208âĂŞ0961.

Morris, J. T., K. Sundberg, and C. S. Hopkinson (2013). "Salt Marsh Primary Production and Its Response to Relative Sea Level and Nutrients in Estuaries at Plum Island, Massachusets, and North Inlet, South Carolina, USA". In: *Oceanography* 26.3, pp. 78–84. DOI: âĂŃ10.5670/oceanog.2013.48.

Morris, J. T., P. V. Sundareshwar, C. T. Nietch, B. Kjerfve, and D. R. Cahoon (2002). "Responses of Coastal Wetlands to Rising Sea Level". In: *Ecology* 83.10, pp. 2869–2877. DOI: 10.1890/0012-9658(2002)083[2869:ROCWTR]2.0.CO;2.

Morris, J. T., D. Porter, M. Neet, P. a. Noble, L. Schmidt, L. a. Lapine, et al. (2005). "Integrating LIDAR elevation data, multi-spectral imagery and neural network modelling for marsh characterization". In: *International Journal of Remote Sensing* 26.23, pp. 5221–5234. DOI: 10.1080/01431160500219018.

Morris, J. T. (2007). "Estimating primary production of salt marsh macrophytes". In: *Principles and Standards for Measuring Primary Production*. Vol. 6. 38, pp. 45–66. ISBN: 9780199682676. DOI: 10.1093/acprof. arXiv: 0402594v3 [arXiv:cond-mat].

Morris, J. T., D. C. Barber, J. C. Callaway, R. Chambers, S. C. Hagen, C. S. Hopkinson, et al. (2016). "Contributions of organic and inorganic matter to sediment volume and accretion in tidal wetlands at steady state". In: *Earth's Future* 4.4, pp. 110–121. DOI: 10.1002/2015EF000334.

Mossman, H. L., A. J. Davy, and A. Grant (2011). "Quantifying local variation in tidal regime using depth-logging fish tags". In: *Estuarine, Coastal and Shelf Science* 96, pp. 122–128. DOI: 10.1016/j.ecss.2011.10.019.

Mudd, S. M., M. Attal, D. T. Milodowski, S. W. D. Grieve, and D. A. Valters (2014). "A statistical framework to quantify spatial variation in channel gradients using the integral method of channel pro fi le analysis". In: *Journal of Geophysical Research : Earth Surface* 119, pp. 138–152. DOI: 10.1002/2013JF002981.

Mudd, S. M., F. J. Clubb, B. Gailleton, and M. D. Hurst (2018). "How concave are river channels ?" In: *Earth Surface Dynamics* 6, pp. 505–523.

Mudd, S. M., S. M. Howell, and J. T. Morris (2009). "Impact of dynamic feedbacks between sedimentation, sea-level rise, and biomass production on near-surface marsh stratigraphy and carbon accumulation". In: *Estuarine, Coastal and Shelf Science* 82.3, pp. 377–389. DOI: 10.1016/j.ecss.2009.01.028.

Mudd, S. M., A. D'Alpaos, and J. T. Morris (2010). "How does vegetation affect sedimentation on tidal marshes? Investigating particle capture and hydrodynamic controls on biologically mediated sedimentation". In: *Journal of Geophysical Research: Earth Surface* 115.3. DOI: 10.1029/2009JF001566.

Mudd, S. M., S. Fagherazzi, J. T. Morris, and D. J. Furbish (2004). "Flow, sedimentation, and biomass production on a vegetated salt marsh in South Carolina: toward a predictive model of marsh morphologic and ecologic evolution". In: *American Geophysical Union*, pp. 165–187. DOI: 10.1029/CE059p0165.

Muller, H., L. Pineau-Guillou, D. Idier, and F. Ardhuin (2014). "Atmospheric storm surge modeling methodology along the French (Atlantic and English Channel) coast". In: *Ocean Dynamics* 64.11, pp. 1671–1692. DOI: 10.1007/s10236-014-0771-0.

Mulligan, R. P., J. P. Walsh, and H. M. Wadman (2014). "Storm Surge and Surface Waves in a Shallow Lagoonal Estuary during the Crossing of a Hurricane". In: *Journal of Waterway, Port, Coastal, and Ocean Engineering* 141.4, A5014001. DOI: 10.1061/(ASCE)WW.1943-5460.0000260.

Munk, W. H. (1950). "Origin and generation of waves". In: *Proceedings of the first Conference on Coastal Engineering* 531, pp. 1–4. DOI: 10.9753/icce.v1.1.

Nagihara, S., K. R. Mulligan, and W. Xiong (2004). "TECHNICAL COMMUNICATION USE OF A THREE-DIMENSIONAL LASER SCANNER TO DIGITALLY CAPTURE THE TOPOGRAPHY OF SAND DUNES IN HIGH SPATIAL RESOLUTION". In: *Earth Surface Processes and Landforms* 398.February, pp. 391–398. DOI: 10.1002/esp.1026.

Nardin, W. and D. A. Edmonds (2014). "Optimum vegetation height and density for inorganic sedimentation in deltaic marshes". In: *Nature Geoscience* 7.10, pp. 722–726. DOI: 10.1038/ngeo2233.

Nelson, J. L. and E. S. Zavaleta (2012). "Salt marsh as a coastal filter for the oceans: Changes in function with experimental increases in Nitrogen loading and sea-level rise". In: *PLoS ONE* 7.8. DOI: 10.1371/journal.pone.0038558.

Nepf, H. M. (1999). "Drag, turbulence, and diffusion in flow through emergent vegetation". In: *Water Resources Research* 35.2, pp. 479–489. DOI: 10.1029/1998WR900069.

Nepf, H. M. (2012). "Flow and Transport in Regions with Aquatic Vegetation". In: *Annual Review of Fluid Mechanics* 44.1, pp. 123–142. DOI: 10.1146/annurev-fluid-120710-101048.

Neubauer, S. C. (2008). "Contributions of mineral and organic components to tidal freshwater marsh accretion". In: *Estuarine, Coastal and Shelf Science* 78.1, pp. 78–88. DOI: 10.1016/j.ecss.2007.11.011.

Neumeier, U. and P. Ciavola (2004). "Flow resistance and associated sedimentary processes in a Spartina maritima salt-marsh". In: *Journal of Coastal Conservation* 20.2, pp. 435–447. DOI: 10.2112/1551-5036(2004)020.

Nienhuis, J. H., A. D. Ashton, and L. Giosan (2015). "What makes a delta wave-dominated?" In: *Geology* 43.6, pp. 511–514. DOI: 10.1130/G36518.1.

Nikuradse, J. (1950). "Laws of Flow in Rough Pipes". In: *Journal of Applied Physics* 3.November, p. 399. DOI: 10.1063/1.1715007.

Nolte, S., E. C. Koppenaal, P. Esselink, K. S. Dijkema, M. Schuerch, A. V. De Groot, et al. (2013). "Measuring sedimentation in tidal marshes: A review on methods and their applicability in biogeomorphological studies". In: *Journal of Coastal Conservation* 17.3, pp. 301–325. DOI: 10.1007/s11852-013-0238-3.

Ouyang, X. and S. Y. Lee (2014). "Updated estimates of carbon accumulation rates in coastal marsh sediments". In: *Biogeosciences* 11.18, pp. 5057–5071. DOI: 10.5194/bg-11-5057-2014.

Packard, R. (2016). *The Making of a Tropical Disease A Short History of Malaria*. 1, p. 320. ISBN: 9781421403960.

Padilla-Hernández, R. and J. Monbaliu (2001). "Energy balance of wind waves as a function of the bottom friction formulation". In: *Coastal Engineering* 43.2, pp. 131–148. DOI: 10.1016/S0378-3839(01)00010-2.

Parrish, C. E., J. N. Rogers, and B. R. Calder (2014). "Assessment of waveform features for lidar uncertainty modeling in a coastal salt marsh environment". In: *IEEE Geoscience and Remote Sensing Letters* 11.2, pp. 569–573. DOI: 10.1109/LGRS.2013.2280182.

Pawlowicz, R., B. Beardsley, and S. Lentz (2002). "Classical tidal harmonic analysis including error estimates in MATLAB using T TIDE". In: *Computers and Geosciences* 28, pp. 929–937.

Pendleton, L., D. C. Donato, B. C. Murray, S. Crooks, W. A. Jenkins, S. Sifleet, et al. (2012). "Estimating Global "Blue Carbon" Emissions from Conversion and Degradation of Vegetated Coastal Ecosystems". In: *PLoS ONE* 7.9. DOI: 10.1371/journal.pone.0043542.

Pennings, S. C., E. R. Selig, L. T. Houser, and M. D. Bertness (2003). "Geographic Variation in Positive and Negative Interactions among Salt Marsh Plants". In: *Ecology* 84.6, pp. 1527–1538.

Pennings, S. C., M. B. Grant, and M. D. Bertness (2005). "Plant zonation in low-latitude salt marshes: Disentangling the roles of flooding, salinity and competition". In: *Journal of Ecology* 93.1, pp. 159–167. DOI: 10.1111/j.1365-2745.2004.00959.x.

Phillips, J. D. (1986). "Coastal Submergence and Marsh Fringe Erosion". In: *Journal of Coastal Research* 2.4, pp. 427–436.

Priestas, A., G. Mariotti, N. Leonardi, and S. Fagherazzi (2015). "Coupled Wave Energy and Erosion Dynamics along a Salt Marsh Boundary, Hog Island Bay, Virginia, USA". In: *Journal of Marine Science and Engineering* 3, pp. 1041–1065. DOI: 10.3390/jmse3031041.

Pringle, A. W. (1995). "Erosion of a cyclic saltmarsh in Morecambe Bay, North-West England". In: *Earth Surface Processes and Landforms* 20.5, pp. 387–405. DOI: 10.1002/esp.3290200502.

Ravens, T. M. and P. M. Gschwend (1999). "FLUME MEASUREMENTS OF SEDIMENT ERODIBILITY IN BOSTON HARBOR". In: *JOURNAL OF HYDRAULIC ENGINEERING* 125.10, pp. 998–1005.

Reed, D. and D. Cahoon (1992). "The relationship between marsh surface topography, hydroperiod, and growth of Spartina alterniflora in a deteriorating Louisiana salt marsh". In: *Journal of Coastal Research* 8.1, pp. 77–87. URL: http://www.jstor.org/stable/10.2307/4297954.

Reef, R., T. O. M. Spencer, I. M. Ller, and C. E. Lovelock (2017). "The effects of elevated CO 2 and eutrophication on surface elevation gain in a European salt marsh". In: *Global Change Biology* 23, pp. 881–890. DOI: 10.1111/gcb.13396.

Rheinwalt, A., B. Goswami, and B. Bookhagen (2019). "A network-based flow accumulation algorithm for point clouds : Facet-Flow Networks ( FFN )". In: *Journal of Geophysical Research : Earth Surface*, pp. 1–31.

Richter, A., D. Faust, and H. Maas (2013). "Dune cliff erosion and beach width change at the northern and southern spits of Sylt detected with multi-temporal Lidar". In: *Catena* 103, pp. 103–11. DOI: 10.1016/j.catena.2011.02.007.

Roberts, W., P. Le Hir, and R. J. S. Whitehouse (2000). "Investigation using simple mathematical models of the effect of tidal currents and waves on the profile shape of intertidal mudflats". In: *Continental Shelf Research* 20.10-11, pp. 1079–1097. DOI: 10.1016/S0278-4343(00)00013-3.

Robinson, E. A. and S. Treitel (1967). "Principles of Digital Wiener Filtering". In: *Geophysical Prospecting* 15.3, pp. 311–332. DOI: 10.1111/j.1365-2478.1967.tb01793.x.

Rogers, J. N., C. E. Parrish, L. G. Ward, and D. M. Burdick (2016a). "Assessment of Elevation Uncertainty in Salt Marsh Environments using Discrete-Return and Full-Waveform Lidar". In: *Journal of Coastal Research* 76, pp. 107–122. DOI: 10.2112/SI76-010.

Rogers, J. N., C. E. Parrish, L. G. Ward, and D. M. Burdick (2016b). "Assessment of Elevation Uncertainty in Salt Marsh Environments using Discrete-Return and Full-Waveform Lidar". In: *Journal of Coastal Research* 76, pp. 107–122. DOI: 10.2112/SI76-010.

Rogers, J. N., C. E. Parrish, L. G. Ward, and D. M. Burdick (2018). "Improving salt marsh digital elevation model accuracy with full-waveform lidar and nonparametric predictive modeling". In: *Estuarine, Coastal and Shelf Science* 202, pp. 193–211. DOI: 10.1016/j.ecss.2017.11.034.

Roner, M., A. D'Alpaos, M. Ghinassi, M. Marani, S. Silvestri, E. Franceschinis, et al. (2016). "Spatial variation of salt-marsh organic and inorganic deposition and organic carbon accumulation: Inferences from the Venice lagoon, Italy". In: *Advances in Water Resources* 93, pp. 276–287. DOI: 10.1016/j.advwatres.2015.11.011.

Rosser, N. J., D. N. Petley, M. Lim, S. A. Dunning, and R. J. Allison (2005). "Terrestrial laser scanning for monitoring the process of". In: *Quarterly Journal of Engineering, Geology and Hydrology*, pp. 363–375.

Saco, P. M., S. Sandi, N. Saintilan, and G. Riccardi (2017). "Potential increase in coastal wetland vulnerability to sea-level rise suggested by considering hydrodynamic attenuation effects". In: *Nature Communications* May. DOI: 10.1038/ncomms16094.

Sadro, S., M. Gastil-Buhl, and J. Melack (2007). "Characterizing patterns of plant distribution in a southern California salt marsh using remotely sensed topographic and hyperspectral data and local tidal fluctuations". In: *Remote Sensing of Environment* 110.2, pp. 226–239. DOI: 10.1016/j.rse.2007.02.024.

Saintilan, N., N. C. Wilson, K. Rogers, A. Rajkaran, and K. W. Krauss (2014). "Mangrove expansion and salt marsh decline at mangrove poleward limits". In: *Global Change Biology* 20.1, pp. 147–157. DOI: 10.1111/gcb.12341.

Schmid, K. A., B. C. Hadley, and N. Wijekoon (2011). "Vertical Accuracy and Use of Topographic LIDAR Data in Coastal Marshes". In: *Journal of Coastal Research* 275.6, pp. 116–132. DOI: 10.2112/JCOASTRES-D-10-00188.1.

Schroder, A., L. Persson, A. M. de Roos, and P. Lundbery (2005). "Direct Experimental Evidence for Alternative Stable States: A Review". In: 110.1, pp. 3–19.

Schuerch, M., A. Vafeidis, T. Slawig, and S. Temmerman (2013). "Modeling the influence of changing storm patterns on the ability of a salt marsh to keep pace with sea level rise". In: *Journal of Geophysical Research: Earth Surface* 118.1, pp. 84–96. DOI: 10.1029/2012JF002471.

Schuerch, M., T. Spencer, S. Temmerman, M. L. Kirwan, C. Wolff, D. Lincke, et al. (2018). "Future response of global coastal wetlands to sea-level rise". In: *Nature* 561.7722, pp. 231–234. DOI: 10.1038/s41586-018-0476-5.

Schwanghart, W. and D. Scherler (2014). "Short Communication : TopoToolbox 2 – MATLAB-based software for topographic analysis and modeling in Earth surface sciences". In: *Earth Surface Dynamics*, pp. 1–7. DOI: 10.5194/esurf-2-1-2014.

Schwanghart, W. and N. J. Kuhn (2010). "Environmental Modelling & Software Topo-Toolbox : A set of Matlab functions for topographic analysis". In: *Environmental Modelling and Software* 25.6, pp. 770–781. DOI: 10.1016/j.envsoft.2009.12.002.

Schwarz, C., T. Cox, T. van Engeland, D. van Oevelen, J. van Belzen, J. van de Koppel, et al. (2017). "Field estimates of floc dynamics and settling velocities in a tidal creek with significant along-channel gradients in velocity and SPM". In: *Estuarine, Coastal and Shelf Science* 197, pp. 221–235. DOI: 10.1016/j.ecss.2017.08.041. arXiv: arXiv:0910.5333v1.

Sebag, D., C. Di Giovanni, S. Ogier, V. Mesnage, F. Laggoun-Défarge, and A. Durand (2006). "Inventory of sedimentary organic matter in modern wetland (Marais Vernier, Normandy, France) as source-indicative tools to study Holocene alluvial deposits (Lower Seine Valley, France)". In: *International Journal of Coal Geology* 67.1-2, pp. 1–16. DOI: 10.1016/j.coal.2005.08.002.

Shennan, I. A. N. and B. E. N. Horton (2002). "Holocene land- and sea-level changes in Great Britain". In: *Journal of Quaternary Science* 17, pp. 511–526. DOI: 10.1002/jqs.710.

Shennan, I. A. N., G. Milne, and S. Bradley (2012). "Late Holocene vertical land motion and relative sea- level changes : lessons from the British Isles". In: 27, pp. 64–70. DOI: 10.1002/jqs.1532.

Shepard, C. C., C. M. Crain, and M. W. Beck (2011). "The protective role of coastal marshes: A systematic review and meta-analysis". In: *PLoS ONE* 6.11. DOI: 10.1371/journal.pone.0027374.

Silinski, A., M. Heuner, J. Schoelynck, S. Puijalon, U. Schröder, E. Fuchs, et al. (2015). "Effects of wind waves versus ship waves on tidal marsh plants: A flume study on different life stages of scirpus maritimus". In: *PLoS ONE* 10.3, pp. 1–16. DOI: 10.1371/journal.pone.0118687.

Silvestri, S., M. Marani, and A. Marani (2003). "Hyperspectral remote sening of salt marsh vegetation, morphology and soil topography". In: *Physics and Chemistry of the Earth* 28, pp. 15–25.

Silvestri, S., A. Defina, and M. Marani (2005). "Tidal regime, salinity and salt marsh plant zonation". In: *Estuarine, Coastal and Shelf Science* 62.1-2, pp. 119–130. DOI: 10.1016/j.ecss.2004.08.010.

Singh Chauhan, P. P. (2009). "Autocyclic erosion in tidal marshes". In: *Geomorphology* 110.3-4, pp. 45–57. DOI: 10.1016/j.geomorph.2009.03.016.

Soulsby, R. and S. Clarke (2005). "Bed Shear-stresses Under Combined Waves and Currents on Smooth and Rough Beds". In: *Hydraulics Research Report* 1905.August, TR 137.

Spivak, A. C., J. Sanderman, J. L. Bowen, E. A. Canuel, and C. S. Hopkinson (2019). "Global-change controls on soil-carbon accumulation and loss in coastal vegetated ecosystems". In: *Nature Geoscience* 12.September, pp. 685–692. DOI: 10.1038/s41561-019-0435-2.

Stark, J., Y. Plancke, S. Ides, P. Meire, and S. Temmerman (2016). "Coastal flood protection by a combined nature-based and engineering approach: Modeling the effects of marsh geometry and surrounding dikes". In: *Estuarine, Coastal and Shelf Science* 175, pp. 34–45. DOI: 10.1016/j.ecss.2016.03.027.

Stopford, S. (1951). "An Ecological Survey of the Cheshire Foreshore of the Dee Estuary". In: *British Ecological Society* 20.1, pp. 103–122.

Strom, K. and A. Keyvani (2011). "AN EXPLICIT FULL-RANGE SETTLING VELOCITY EQUATION FOR MUD FLOCS". In: *Journal of sedimentary research* 81, pp. 921–934. DOI: 10.2110/jsr.2011.62.

Suchrow, S. and K. Jensen (2010). "Plant Species Responses to an Elevational Gradient in German North Sea Salt Marshes". In: *Wetlands* 30, pp. 735–746. DOI: 10.1007/s13157-010-0073-3.

Syvitski, J. P., A. J. Kettner, I. Overeem, E. W. H. Hutton, M. T. Hannon, G. R. Brakenridge, et al. (2009). "Sinking deltas due to human activites". In: *Nature Geoscience* 2.10, pp. 681–686. DOI: 10.1038/ngeo629.

Tambroni, N. and G. Seminara (2012). "A one-dimensional eco-geomorphic model of marsh response to sea level rise: Wind effects, dynamics of the marsh border and equilibrium". In: *Journal of Geophysical Research: Earth Surface* 117.3, pp. 1–25. DOI: 10.1029/2012JF002363.

Temmerman, S., G. Govers, P. Meire, and S. Wartel (2003). "Modelling long-term tidal marsh growth under changing tidal conditions and suspended sediment concentrations, Scheldt estuary, Belgium". In: *Marine Geology* 193.1-2, pp. 151–169. DOI: 10.1016/S0025-3227(02)00642-4.

Temmerman, S., T. J. Bouma, J. Van de Koppel, D. Van der Wal, M. B. De Vries, and P. M. J. Herman (2007). "Vegetation causes channel erosion in a tidal landscape". In: *Geology* 35.7, pp. 631–634. DOI: 10.1130/G23502A.1.

Temmerman, S., T. J. Bouma, G. Govers, and D. Lauwaet (2005). "Flow paths of water and sediment in a tidal marsh: Relations with marsh developmental stage and tidal inundation height". In: *Estuaries* 28.3, pp. 338–352. DOI: 10.1007/BF02693917.

Tessier, B. (1993). "Upper intertidal rhythmites in the Mont-Saint-Michel Bay (NW France): Perspectives for paleoreconstruction". In: *Marine Geology* 110.3-4, pp. 355–367. DOI: 10.1016/0025-3227(93)90093-B.

Tonelli, M., S. Fagherazzi, and M. Petti (2010). "Modeling wave impact on salt marsh boundaries". In: *Journal of Geophysical Research: Oceans* 115.9, pp. 1–17. DOI: 10.1029/2009JC006026.

Törnqvist, T. E., D. J. Wallace, J. E. a. Storms, J. Wallinga, R. L. van Dam, M. Blaauw, et al. (2008). "Mississippi Delta subsidence primarily caused by compaction of Holocene strata". In: *Nature Geoscience* 1.3, pp. 173–176. DOI: 10.1038/ngeo129.

Tuxen, K. A., L. M. Schile, M. Kelly, and S. W. Siegel (2008). "Vegetation colonization in a restoring tidal marsh: A remote sensing approach". In: *Restoration Ecology* 16.2, pp. 313–323. DOI: 10.1111/j.1526-100X.2007.00313.x.

Valentine, K., G. Mariotti, and S. Fagherazzi (2014). "Repeated erosion of cohesive sediments with biofilms". In: *Advances in Geosciences* 39, pp. 9–14. DOI: 10.5194/adgeo-39-9-2014.

Van der Nat, A., P. Vellinga, R. Leemans, and E. van Slobbe (2016). "Ranking coastal flood protection designs from engineered to nature-based". In: *Ecological Engineering* 87, pp. 80–90. DOI: 10.1016/j.ecoleng.2015.11.007.

Voss, C. M., R. R. Christian, and J. T. Morris (2013). "Marsh macrophyte responses to inundation anticipate impacts of sea-level rise and indicate ongoing drowning of North Carolina marshes". In: *Marine Biology* 160.1, pp. 181–194. DOI: 10.1007/s00227-012-2076-5.

Wang, C., M. Menenti, M. P. Stoll, E. Belluco, and M. Marani (2007). "Mapping mixed vegetation communities in salt marshes using airborne spectral data". In: *Remote Sensing of Environment* 107.4, pp. 559–570. DOI: 10.1016/j.rse.2006.10.007.

Wang, C., M. Menenti, M. P. Stoll, A. Feola, E. Belluco, and M. Marani (2009). "Separation of ground and low vegetation signatures in LiDAR measurements of salt-marsh environments". In: *IEEE Transactions on Geoscience and Remote Sensing* 47.7, pp. 2014–2023. DOI: 10.1109/TGRS.2008.2010490.

Webb, E. L., D. A. Friess, K. W. Krauss, D. R. Cahoon, G. R. Guntenspergen, and J. Phelps (2013). "A global standard for monitoring coastal wetland vulnerability to accelerated sea-level rise". In: *Nature Climate Change* 3.5, pp. 458–465. DOI: 10.1038/nclimate1756.

Wentworth, C. K. (1922). "A Scale of Grade and Class Terms for Clastic Sediments". In: *The Journal of Geology* 30.5, pp. 377–392.

Weston, N. B., S. C. Neubauer, D. J. Velinsky, and M. A. Vile (2014). "Net ecosystem carbon exchange and the greenhouse gas balance of tidal marshes along an estuarine salinity gradient". In: *Biogeochemistry* 120.1-3, pp. 163–189. DOI: 10.1007/s10533-014-9989-7.

Wharfe, J. R. (1977). "THE INTERTIDAL SEDIMENT HABITATS OF THE LOWER MEDWAY ESTUARY". In: *Environmental Pollution* 13.

Wiberg, P. L. and J. D. Smith (1987). "Calculations of the Critical Shear Stress for Motion of Uniform and Heterogeneous Sediments". In: *Water Resources Research* 23.8, pp. 1471–1480.

Wiener, N. (1949). *Extrapolation, Interpolation, and Smoothing of Stationary Time Series With Engineering Applications*.

Woodworth, P. L., J. R. Hunter, M. Marcos, P. Caldwell, M. Menéndez, and I. Haigh (2016). "Towards a global higher-frequency sea level dataset". In: *Geoscience Data Journal* 3.2, pp. 50–59. DOI: 10.1002/gdj3.42.

Yang, S. L., H. Li, T. Ysebaert, T. J. Bouma, W. X. Zhang, Y. Y. Wang, et al. (2008). "Spatial and temporal variations in sediment grain size in tidal wetlands, Yangtze Delta: On the role of physical and biotic controls". In: *Estuarine, Coastal and Shelf Science* 77.4, pp. 657–671. DOI: 10.1016/j.ecss.2007.10.024.

Young, I. and L. Verhagen (1996). "The growth of fetch limited waves in water of finite depth. Part 2: Spectral evolution". In: *Coastal Engineering* 29, pp. 79–99.

Young, I. (1999). *Wind generated ocean waves*.

Ysebaert, T., S. L. Yang, L. Zhang, Q. He, T. J. Bouma, and P. M. J. Herman (2011). "Wave attenuation by two contrasting ecosystem engineering salt marsh macrophytes in the intertidal pioneer zone". In: *Wetlands* 31.6, pp. 1043–1054. DOI: 10.1007/s13157-011-0240-1.

Zedler, J. B. and S. Kercher (2005). "WETLAND RESOURCES: Status, Trends, Ecosystem Services, and Restorability". In: *Annual Review of Environment and Resources* 30.1, pp. 39–74. DOI: 10.1146/annurev.energy.30.050504.144248. arXiv: arXiv:1011.1669v3.

Zhang, X., N. Leonardi, C. Donatelli, and S. Fagherazzi (2019). "Advances in Water Resources Fate of cohesive sediments in a marsh-dominated estuary". In: *Advances in Water Resources* 125.June 2018, pp. 32–40. DOI: 10.1016/j.advwatres.2019.01.003.

Zhou, J. and N. Broodbank (2013). "Sediment-water interactions of pharmaceutical residues in the river environment". In: *Water Research* 48, pp. 61–70. DOI: 10.1016/j.watres.2013.09.026.

Zhou, Z., G. Coco, I. Townend, M. Olabarrieta, M. van der Wegen, Z. Gong, et al. (2017). "Is "Morphodynamic Equilibrium" an oxymoron?" In: *Earth-Science Reviews* 165, pp. 257–267. DOI: 10.1016/j.earscirev.2016.12.002.